

The Role of Iron Sulfide Polymorphism in Localized Corrosion of Mild Steel

A dissertation presented to  
the faculty of  
the Russ College of Engineering and Technology of Ohio University

In partial fulfillment  
of the requirements for the degree  
Doctor of Philosophy

Jing Ning

December 2016

© 2016 Jing Ning. All Rights Reserved.

This dissertation titled  
The Role of Iron Sulfide Polymorphism in Localized Corrosion of Mild Steel

by

JING NING

has been approved for  
the Department of Chemical and Biomolecular Engineering  
and the Russ College of Engineering and Technology by

Srdjan Nešić

Professor of Chemical and Biomolecular Engineering

Dennis Irwin

Dean, Russ College of Engineering and Technology

**ABSTRACT**

NING JING, Ph.D., December 2016, Chemical Engineering

The Role of Iron Sulfide Polymorphism in Localized Corrosion of Mild Steel

Director of Dissertation: Srdjan Nešić

H<sub>2</sub>S localized corrosion, occurring at discrete sites on a steel surface, can result in fast penetration of pipeline walls and loss of containment. This mode of metal attack is generally considered to be the main cause for catastrophic corrosion failures of facilities in the oil and gas industry. Hence, the prediction and control of H<sub>2</sub>S localized corrosion is a significant challenge for assuring asset integrity in oil and gas fields containing H<sub>2</sub>S. The purpose of this dissertation project is to explore, heretofore poorly understood, localized corrosion mechanisms related to the formation of iron sulfide polymorphs and related phases.

In order to make this investigation possible, a thermodynamic model was initially developed as a tool to determine experimental conditions that could potentially replicate localized corrosion associated with iron sulfide polymorphism in an aqueous H<sub>2</sub>S system. Equilibrium expressions for H<sub>2</sub>S solubility and dissociation constants were reviewed and compared. Models to predict water chemistry of an H<sub>2</sub>S-H<sub>2</sub>O system were built and verified against experimental measurements. In order to predict the formation and dissolution of iron sulfides, their solubility limits were experimentally measured in an H<sub>2</sub>S-H<sub>2</sub>O-Fe<sup>2+</sup> system. At 25°C, the measured pK<sub>sp,2</sub> values were observed to change with time as the identity of the observed iron sulfide type changed. The pK<sub>sp,2</sub> of mackinawite at 25°C was measured as 3.6 ± 0.2. Pyrite and greigite were observed at 60°C. Greigite

was dominant around pH 5 with a  $pK_{sp,2} 9.8 \pm 0.5$ , while pyrite was dominant around pH 3.5 with  $pK_{sp,2} 6.5 \pm 0.5$ .

The electrochemical thermodynamics of an  $H_2S-H_2O-Fe$  system were then investigated, with iron sulfides selected in relation to the oil and gas industry. Mackinawite, pyrrhotite, greigite, and pyrite were taken into consideration for Pourbaix diagram generation, accompanied by a complete accounting of all the assumptions, underlying thermodynamic data, and reaction mechanisms. Generated Pourbaix diagrams were validated by long-term experiments at different temperatures ( $25^\circ C$  and  $80^\circ C$ ) and by adjusting solution pH.

Following the establishment of the thermodynamic model, experimental conditions leading to the formation of different iron sulfides as corrosion products in a sour environment were established. A strong correlation between the formation of greigite and/or pyrite on a steel surface and onset of localized corrosion was observed. Localized corrosion was absent when neither greigite nor pyrite formed. Consequently, the formation of greigite and/or pyrite was hypothesized to play an important role in the initiation of localized corrosion. Novel experiments involving deposition of pyrite on the steel surface were then designed and conducted. It was found that the galvanic coupling between pyrite particles and steel is the dominant mechanism for this type of localized corrosion.

Finally, a descriptive model was built to answer when, where, and how this type of localized corrosion occurs in a sour environment. This model can provide guidance for the mitigation of localized corrosion in field conditions.

**DEDICATION**

*To*

*My parents, Guangxin Ning and Guizhi Zhang*

*My husband, Yougui Zheng*

*And all other family members*

*For their love, care, inspiration, and support*

## ACKNOWLEDGMENTS

It has been a privilege to study, grow, and pursue my Ph.D. degree in the Institute for Corrosion and Multiphase Technology at Ohio University. I have been very lucky to have Professor Srdjan Nešić as my advisor. Taking this opportunity, I would like to give my deepest gratitude to Professor Srdjan Nešić for his supervision, advice, support, passion, patience, and encouragement throughout my Ph.D. study over the past six years. Besides being an academic advisor, he also has been a mentor for my professional career and my personal life. He has given me valuable suggestions on my career, shared his tremendous expertise with me, and inspired me to always take the positive side of things in life. Under his guidance, I have become a more professional, mature, and optimistic person, and moreover, I have well prepared for challenges in the future.

I would like to thank my project leader, Dr. Bruce Brown, for always being there for me throughout my Ph.D. study. I could not have completed my study without Dr. Brown's continued help and support. I also appreciate Dr. David Young for his dedication to my project, providing wonderful ideas, and reviewing my proposal, papers, and dissertation. Great thanks go to Prof. Marc Singer, Dr. Yoon-Seok Choi, Ms. Becky Gill, Mr. Al Schubert, Mr. Cody Shafer, Mr. Phil Bullington, Mr. Alexis Barxias, and former technician Mr. Steve Upton, for their assistance and care during my academic study and experimentation in the laboratory. Special thanks go to technicians Mr. Phil Bullington, Mr. Cody Shafer, and Mr. Alexis Barxias, and former students Dr. Yougui Zheng, Dr. Najmiddin Yaakob, and Dr. Peng Jin, who have been "buddies" for my hydrogen sulfide experiments.

I am very grateful to my committee members, Prof. Howard Dewald, Prof. Dina Lopez, Prof. Kevin Crist, Prof. Monica Burdick, and Prof. David Young for serving on my dissertation committee. I highly appreciate their contribution and time.

I would also like to express my acknowledgements to Mr. Stephen Smith, Prof. David Shoemith at Western University, Prof. David Rickard at Cardiff University, Dr. Bert Pots, Dr. Richard Woollam at BP America, Dr. Raymundo Case at ConocoPhillips, Prof. Brian Kinsella at Curtin University, Prof. Bernard Tribollet at Pierre and Marie Curie University, Dr. Bruce Craig, Dr. Nihal Obeyesekere at Clariant, and Dr. Jose Vera at DNV, for discussion with me and giving valuable suggestions for my research. Many thanks also go to Dr. Dan Wang in the Center for Electrochemical Engineering Research at Ohio University for his assistance in XRD analysis.

I appreciate two industrial internship opportunities with ConocoPhillips and ExxonMobil, from which I have had great chances to learn and grow. I would like to thank Dr. Mohsen Achour, Dr. Raymundo Case, Dr. Yuxiu Liu, and Dr. Sonja Richter for their supervision and help during my internship with the Corrosion, Inspection & Materials team at ConocoPhillips in Bartlesville, Oklahoma. Great thanks also go to Dr. Shalawn Jackson, Dr. Jorge Pacheco, Dr. Yao Xiong, Dr. David Fischer, Dr. Sanket Desai, Dr. Amit Kumar, Dr. Dennis Enning, and Dr. Monica Canalizo-Hernandez with the Corrosion team at ExxonMobil Upstream Research Company, Houston, and Dr. Victor Wang, Dr. Wei Sun, Dr. Chong Li, and Ms. Conchita Mendez at ExxonMobil Development Company, Houston, for supervising and supporting me during my internship. Special thanks to Dr. Yao Xiong for being such a dedicated mentor during my internship. Thanks for his patience, support, and believing in my potential.

I also take this great opportunity to thank my parents Guangxin Ning and Guizhi Zhang, my husband Dr. Yougui Zheng, my brothers Bo and Tao, and all other family members, for all they have done for me for so many years throughout my education. I have dedicated 6 years to the Ph.D. program beyond my Master and Bachelor degrees. I am sure that I could not have made it without their unconditional love, support, inspiration, and care. Thanks to my parents, who have inspired me to be enthusiastic, energetic, independent, and industrious. I am very grateful to my husband for going through this journey with me over the past six years in America, his words of wisdom, and his unwavering love.

Last but not least, please allow me to express sincere appreciation to the following industrial sponsors for their financial support: Anadarko, Baker Hughes, BP, Chevron, Clariant Oil Services, CNPC Tubular Goods, ConocoPhillips, DNV GL, Hess, INPEX Corporation, M-I SWACO, Multi-Chem, Nalco Champion, Occidental Oil Company, Petrobras, Petroleum Development Oman, Petroleum Institute (GRC), Petronas, PTT, Saudi Aramco, Sinopec, TransCanada, TOTAL, and Wood Group Integrity Management.

## TABLE OF CONTENTS

	Page
Abstract.....	3
Dedication.....	5
Acknowledgments.....	6
List of Tables .....	14
List of Figures.....	16
Chapter 1. Introduction.....	26
1.1 Background.....	26
1.2 Goals .....	28
1.3 Publications.....	28
1.3.1 Journal Publications.....	29
1.3.2 Conference Papers & Oral Presentations.....	29
Chapter 2. Chemical Thermodynamics of an H <sub>2</sub> S-H <sub>2</sub> O System .....	31
2.1 Introduction.....	31
2.2 Objectives .....	31
2.3 Literature Review.....	32
2.3.1 The H <sub>2</sub> S Solubility Constant <i>KH<sub>2</sub>S</i> .....	33
2.3.2 The First Dissociation Constant <i>K<sub>a,1</sub></i> .....	34
2.3.3 The Second Dissociation Constant <i>K<sub>a,2</sub></i> .....	35
2.4 Water Chemistry Modeling of an H <sub>2</sub> S-H <sub>2</sub> O System.....	38
2.4.1 Definitions of Open System and Closed System .....	38
2.4.2 Comparison of Water Chemistry between an Open System and a Closed System.....	39
2.4.3 Establishment of Water Chemistry Model for an Open System and a Closed System.....	41
2.4.4 Comparison of Water Chemistry of an Open System and a Closed System .....	43
2.5 Experimental Validation .....	45
2.5.1 Experimental .....	45
2.5.2 Results and Discussion .....	47
2.6 Summary.....	49
Chapter 3. Chemical Thermodynamics of H <sub>2</sub> S-H <sub>2</sub> O-Fe <sup>2+</sup> System .....	51

	10
3.1	Introduction..... 51
3.2	Objectives ..... 51
3.3	Literature Review..... 52
3.3.1	Polymorphism of Iron Sulfides..... 52
3.3.2	The Various Expressions for Solubility Limit of Iron Sulfides..... 54
3.3.3	The Solubility Limit of Iron Sulfides..... 58
3.4	Experimental..... 61
3.4.1	Apparatus ..... 61
3.4.2	Methodology..... 61
3.4.3	Procedure ..... 61
3.5	Results and Discussion ..... 62
3.5.1	Measured $pK_{sp,2}$ Values of Iron Sulfide Formed at 25 °C ..... 62
3.5.2	Measured $pK_{sp,2}$ Values of Iron Sulfide Formed at 60 °C ..... 65
3.5.3	Recalculation of $pK_{sp,2}$ Values of Greigite and Pyrite ..... 70
3.6	Summary..... 72
Chapter 4.	Electrochemical Thermodynamics of the H <sub>2</sub> S-H <sub>2</sub> O-Fe System ..... 73
4.1	Introduction..... 73
4.2	Classification of Polymorphous Iron Sulfide in H <sub>2</sub> S Corrosion of Mild Steel. 75
4.2.1	Amorphous Iron Sulfide (FeS)..... 75
4.2.2	Mackinawite (FeS)..... 76
4.2.3	Cubic Iron Sulfide (FeS)..... 76
4.2.4	Pyrrhotite (Fe <sub>1-x</sub> S (x = 0 to 0.17)) and Troilite (FeS) ..... 77
4.2.5	Smythite (Fe <sub>3+x</sub> S <sub>4</sub> (x = 0 to 0.3))..... 78
4.2.6	Greigite (Fe <sub>3</sub> S <sub>4</sub> )..... 78
4.2.7	Pyrite (FeS <sub>2</sub> )..... 78
4.2.8	Marcasite (FeS <sub>2</sub> )..... 79
4.2.9	Summary..... 80
4.3	Thermodynamic Background..... 81
4.3.1	Electrochemical Thermodynamics..... 81
4.3.2	Thermodynamic Data..... 85
4.4	Pourbaix Diagrams..... 90



	12
6.4.1 Apparatus .....	151
6.4.2 Material .....	151
6.4.3 Procedure .....	151
6.5 Experimental Results .....	154
6.5.1 Experiment Set #1: Reproducible Occurrence of Localized Corrosion with Spontaneous Formation of Polymorphous Iron Sulfides .....	154
6.5.2 Experiment Set #2: Localized Corrosion Triggered by Facilitating Formation of Greigite/Pyrite at Low Temperature .....	167
6.5.3 Experiment Set #3: Adjusting Solution pH without Formation of Greigite/Pyrite .....	176
6.6 Discussion .....	186
6.6.1 Electrochemical Half Reactions .....	186
6.6.2 Electrical Conductivity of Polymorphous Iron Sulfides .....	188
6.7 Summary .....	190
Chapter 7. The Role of Pyrite in Localized Corrosion .....	191
7.1 Introduction .....	191
7.2 Experimental .....	191
7.2.1 Apparatus .....	191
7.2.2 Materials .....	193
7.2.3 Procedure .....	193
7.2.4 Characterization of Deposits .....	194
7.2.5 Test Matrix .....	196
7.3 Results and Discussion .....	201
7.3.1 Test Series #1: Pyrite/Silica Sand UDC Test in an Aqueous H <sub>2</sub> S Environment .....	201
7.3.2 Test Series #2: Impact of Pyrite Particle Size on Corrosion .....	213
7.3.3 Test Series #3: Investigating Potential Mechanisms for Localized Corrosion .....	219
7.3.4 Test Series #4: Pyrite/Silica Sand UDC Test in an Aqueous CO <sub>2</sub> Environment .....	225
7.4 Summary .....	231
Chapter 8. A Descriptive Model for Localized Corrosion in Sour Environments ...	232
8.1 Introduction .....	232

	13
8.2 Understanding of Physiochemical Processes of Localized Corrosion Related to Iron Sulfide Polymorphism.....	232
8.2.1 Where are the Pit Locations in Relation to Pyrite?.....	232
8.2.2 When and How Does Localized Corrosion Occur?.....	236
8.3 A Descriptive Model for Localized Corrosion .....	240
8.3.1 Scenario with Pyrite Deposits on the Steel Surface.....	240
8.3.2 Scenario with Pyrite Spontaneously Formed in Sour Systems.....	242
8.4 An Application of the Model to Field.....	244
8.4.1 The Effects of Parameters on Pyrite Formation.....	245
8.4.2 Pyrite Stability T - pH <sub>2</sub> S Map at Different pH .....	246
8.4.3 The Impact of Oxygen Ingress on Pyrite Stability Map .....	250
8.5 Summary .....	252
Chapter 9. Conclusions & Recommendations for Future Work.....	254
9.1 Conclusions.....	254
9.2 Recommendations for Future Work.....	254
References.....	256
Appendix A: Analytical Techniques.....	275
Appendix B: Surface pH Measurement .....	280
Appendix C: Validation of Pourbaix Diagrams by Electrochemical Polarization .....	292

## LIST OF TABLES

	Page
Table 1 Expressions for solubility constant $K_{H_2S}$ from multiple sources. ....	33
Table 2 Expressions for the first dissociation constant $K_{a,1}$ from multiple sources. ....	34
Table 3 Values of the second dissociation constant $K_{a,2}$ at 25 °C. ....	37
Table 4 Values for the second dissociation constant $pK_{a,2}$ at 25 °C determined by non-calorimetric methodologies. ....	37
Table 5 Expressions for the second dissociation constant $K_{a,2}$ determined by non-calorimetric methodologies from multiple sources. ....	37
Table 6 Combinations of $K_{H_2S}$ , $K_{a,1}$ and $K_{a,2}$ in pH value prediction models. ....	48
Table 7 Polymorphous iron sulfides. ....	52
Table 8 $pK_{sp,2}$ values for mackinawite from literature at 25 °C. ....	58
Table 9 Best estimates of $pK_{sp,2}$ values for polymorphous iron sulfides at 25 °C [51]. ...	60
Table 10 Test matrix. ....	62
Table 11 Thermodynamic data of the species considered for a $H_2S$ - $H_2O$ -Fe system. ....	90
Table 12 Equilibria of electrochemical reactions occurring in the $H_2O$ -Fe system. ....	92
Table 13 Equilibria of electrochemical reactions occurring in the $H_2S$ - $H_2O$ -Fe system. .	95
Table 14 Chemical composition of 5L X65 carbon steel used in experiment (wt. %). .	111
Table 15 Test matrix. ....	113
Table 16 XRD quantitative analysis of the formed corrosion products layer at 80 °C (The steel phase was detected by XRD, but was removed from the quantitative analysis). ...	131
Table 17 XRD quantitative analysis of the formed corrosion products layer with pH adjustment. ....	136
Table 18 Gibbs free energy and dissociation constants of polysulfides. ....	144
Table 19 A summary of peers' work on iron sulfide under deposit corrosion. ....	149
Table 20 Test matrix. ....	153
Table 21 XRD quantitative analysis of corrosion products formed in Exp. #1. ....	160
Table 22. XRD quantitative analysis of corrosion products formed in Exp. #2. ....	171
Table 23 XRD quantitative analysis of corrosion products formed in Exp. #3. ....	182
Table 24 XRD quantitative analysis of the pyrite powder. ....	196
Table 25 Test matrix for test series #1. ....	197
Table 26 Test matrix for test series #2. ....	198

	15
Table 27 Properties of the insulating mesh.....	199
Table 28 Test matrix for test series #3.....	200
Table 29 Test matrix for test series #4.....	201
Table 30 Properties of the mesh.....	281
Table 31 Test matrix. ....	282

## LIST OF FIGURES

	Page
Figure 1. Temperature dependency of the solubility constant KH <sub>2</sub> S. ....	34
Figure 2. Temperature dependency of the first dissociation constant K <sub>a, 1</sub> . ....	35
Figure 3. Temperature dependency of the second dissociation constant K <sub>a, 2</sub> . ....	38
Figure 4. An open system vs. a closed system. ....	39
Figure 5. Graphical interpretation of water chemistry behavior in an open system vs. a closed system. ....	41
Figure 6. Equilibrium concentrations of species as a function of pH for open and closed H <sub>2</sub> S-H <sub>2</sub> O systems (T = 25 °C, p <sub>H<sub>2</sub>S</sub> = 0.1 bar). ....	44
Figure 7. Experimental glass cell setup. ....	46
Figure 8. Comparison of experimental pH values with model predicted pH values at 25°C. ....	48
Figure 9. Comparison of experimental pH values with model predicted pH values at 60°C. ....	49
Figure 10. Comparison of experimental pH values with model predicted pH values at 80°C. ....	49
Figure 11. Conceptual corrosion product diagram (reproduced from [58]). ....	54
Figure 12. Iron sulfide reaction pathways from Smith and Miller [5], and Morse <i>et al.</i> [13]. ....	54
Figure 13. Calculated saturation values using pK <sub>sp,2</sub> values in Table 8 for the selected environment (25 °C, p <sub>H<sub>2</sub>S</sub> = 0.97 mbar, [Fe <sup>2+</sup> ] = 10 ppm, pH = 6.0). ....	60
Figure 14. Measured pK <sub>sp,2</sub> at 200 ppm H <sub>2</sub> S with adding HCl at 25 °C. ....	63
Figure 15. XRD of precipitate (pK <sub>sp,2</sub> was 3.48). ....	64
Figure 16. Measured pK <sub>sp,2</sub> at 200 ppm H <sub>2</sub> S without adding HCl at 25 °C. ....	65
Figure 17. Summary of time dependence of pK <sub>sp,2</sub> at 25 °C. ....	65
Figure 18. Measured pK <sub>sp,2</sub> at 200 ppm H <sub>2</sub> S with adding HCl at 60 °C. ....	66
Figure 19. Measured pK <sub>sp,2</sub> at 200 ppm H <sub>2</sub> S with adding HCl/NaOH at 60 °C. ....	67
Figure 20. XRD of precipitate (pK <sub>sp,2</sub> was 3.02). ....	67
Figure 21. XRD of precipitate (pK <sub>sp,2</sub> was 3.88). ....	68
Figure 22. Measured pK <sub>sp,2</sub> at 1000 ppm H <sub>2</sub> S without adding HCl at 60 °C. ....	69
Figure 23. Measured pK <sub>sp,2</sub> at 1000 ppm H <sub>2</sub> S with adding HCl/NaOH at 60 °C. ....	69
Figure 24. XRD of precipitate (pK <sub>sp,2</sub> was 6.45). ....	70

	17
Figure 25. XRD of precipitate ( $pK_{sp,2}$ was 6.30). .....	70
Figure 26. Summary of pH-recalculated $pK_{sp,2}$ at 60 °C. ....	71
Figure 27. Crystal structures of: (a) Mackinawite; (b) Cubic iron sulfide; (c) Pyrrhotite; (d) Troilite; (e) Greigite; (f) Pyrite generated by CrystalMaker. ....	80
Figure 28. The collection of data for $H_2S_{(g)}$ from various sources: (a) standard molar entropy at 25 °C, $S_{298,15}^{\circ}$ ; (b) heat capacity, $C_p$ . ....	86
Figure 29. The collection of data of $S_{298,15}^{\circ}$ for (a) $Fe^{2+}_{(aq)}$ ; (b) $Fe^{3+}_{(aq)}$ from various sources. ....	87
Figure 30. The collection of data for pyrrhotite <sub>(s)</sub> group from various sources: (a) $S_{298,15}^{\circ}$ ; (b) $C_p$ . ....	87
Figure 31. Heat capacity of metal sulfides: (a) MS; (b) MS <sub>2</sub> ; (c) M <sub>3</sub> S <sub>4</sub> . ....	88
Figure 32. Pourbaix diagram for H <sub>2</sub> O-Fe system (T = 25 °C, $[Fe^{2+}] = 10$ ppm, $[Fe^{3+}] = 10^{-6}$ mol/L, $pH_2 = pO_2 = 1$ bar). ....	92
Figure 33. Pourbaix diagram for H <sub>2</sub> S-H <sub>2</sub> O-Fe system with (a) Mackinawite; (b) Mackinawite / Greigite; (c) Mackinawite / Greigite / Pyrrhotite; (d) Mackinawite / Greigite / Pyrrhotite / Pyrite (T = 25 °C, $pH_2S = 0.1$ bar, $[Fe^{2+}] = 10$ ppm, $[Fe^{3+}] = 10^{-6}$ mol/L, $pH_2 = pO_2 = 1$ bar). ....	97
Figure 34. Pourbaix diagrams for H <sub>2</sub> S-H <sub>2</sub> O-Fe system showing step changes in temperature up to 250 °C (T = 25 °C ~ 250 °C, $[H_2S]_{aq} = 9.4 \times 10^{-3}$ M, $[Fe^{2+}] = 10$ ppm, $[Fe^{3+}] = 10^{-6}$ M): (a) Mackinawite; (b) Mackinawite / Greigite; (c) Mackinawite / Greigite / Pyrrhotite; (d) Mackinawite / Greigite / Pyrrhotite / Pyrite. ....	101
Figure 35. Pourbaix diagrams for H <sub>2</sub> S-H <sub>2</sub> O-Fe system showing step changes in H <sub>2</sub> S partial pressure ( $pH_2S = 0.0001 \sim 10$ bar, T = 80 °C, $[Fe^{2+}] = 10$ ppm, $[Fe^{3+}] = 10^{-6}$ M): (a) Mackinawite; (b) Mackinawite / Greigite; (c) Mackinawite / Greigite / Pyrrhotite; (d) Mackinawite / Greigite / Pyrrhotite / Pyrite. ....	103
Figure 36. Pourbaix diagrams for H <sub>2</sub> S-H <sub>2</sub> O-Fe system showing step changes in ferrous ion concentration ( $[Fe^{2+}] = 1 \sim 100$ ppm, T = 80 °C, $pH_2S = 0.24$ bar, $[Fe^{3+}] = 10^{-6}$ M): (a) Mackinawite; (b) Mackinawite / Greigite; (c) Mackinawite / Greigite / Pyrrhotite; (d) Mackinawite / Greigite / Pyrrhotite / Pyrite. ....	106
Figure 37. Experimental setup. ....	111
Figure 38. Experimental design for pH adjustment. ....	114
Figure 39. (a) Measured bulk pH, surface pH, and $[Fe^{2+}]$ ; (b) Corrosion rate and OCP during experiment at 25 °C. ....	116
Figure 40. Corrosion product layer after 1 day of exposure at 25 °C: (a) Surface morphology with x100 magnification; (b) Surface morphology with 2,000x magnification; (c) XRD pattern. ....	118

Figure 41. Verification of Pourbaix diagram after 1 day of exposure (Pourbaix diagram was generated at $T = 25\text{ }^{\circ}\text{C}$ , $\text{pH}_2\text{S} = 0.097\text{ bar}$ , $[\text{Fe}^{2+}] = 2.5\text{ ppm}$ , $[\text{Fe}^{3+}] = 1.0 \times 10^{-6}\text{ M}$ ). .....	118
Figure 42. Corrosion product layer after 4 days of exposure at $25\text{ }^{\circ}\text{C}$ : (a) SEM image of surface morphology with 100x magnification; (b) SEM image of surface morphology with 2,000x magnification; (c) XRD pattern. ....	120
Figure 43. Verification of Pourbaix diagram after 4 days of exposure (Pourbaix diagram was generated at $T = 25\text{ }^{\circ}\text{C}$ , $\text{pH}_2\text{S} = 0.097\text{ bar}$ , $[\text{Fe}^{2+}] = 0.44\text{ ppm}$ , $[\text{Fe}^{3+}] = 1.0 \times 10^{-6}\text{ M}$ ): (a) Mackinawite; (b) Mackinawite / Greigite / Pyrrhotite / Pyrite.....	120
Figure 44. Corrosion product layer after 7 days of exposure at $25\text{ }^{\circ}\text{C}$ : (a) SEM image of surface morphology with 100x magnification; (b) SEM image of surface morphology with 2,000x magnification; (c) XRD pattern. ....	122
Figure 45. Verification of Pourbaix diagram after 7 days of exposure (Pourbaix diagram was generated at $T = 25\text{ }^{\circ}\text{C}$ , $\text{pH}_2\text{S} = 0.097\text{ bar}$ , $[\text{Fe}^{2+}] = 0.52\text{ ppm}$ , $[\text{Fe}^{3+}] = 1.0 \times 10^{-6}\text{ M}$ ): (a) Mackinawite; (b) Mackinawite / Greigite / Pyrrhotite / Pyrite.....	122
Figure 46. (a) Measured bulk pH and $[\text{Fe}^{2+}]$ ; (b) Corrosion rate and OCP during experiment at $80\text{ }^{\circ}\text{C}$ .....	124
Figure 47. Corrosion product layer after 1 day of exposure at $80\text{ }^{\circ}\text{C}$ : (a) SEM image of surface morphology with 100x magnification; (b) SEM image of surface morphology with 2,000x magnification; (c) XRD pattern. ....	125
Figure 48. Verification of Pourbaix diagram after 1 day of exposure (Pourbaix diagram was generated at $T = 80\text{ }^{\circ}\text{C}$ , $\text{pH}_2\text{S} = 0.053\text{ bar}$ , $[\text{Fe}^{2+}] = 0.1\text{ ppm}$ , $[\text{Fe}^{3+}] = 1.0 \times 10^{-6}\text{ M}$ ). .....	126
Figure 49. Corrosion product layer after 4 days of exposure at $80\text{ }^{\circ}\text{C}$ : (a) SEM image of surface morphology with 100x magnification; (b) SEM image of surface morphology with 2,000x magnification; (c) XRD pattern. ....	127
Figure 50. Verification of Pourbaix diagram after 4 days of exposure (Pourbaix diagram was generated at $T = 80\text{ }^{\circ}\text{C}$ , $\text{pH}_2\text{S} = 0.053\text{ bar}$ , $[\text{Fe}^{2+}] = 0.045\text{ ppm}$ , $[\text{Fe}^{3+}] = 1.0 \times 10^{-6}\text{ M}$ ): (a) Mackinawite; (b) Mackinawite / Greigite / Pyrrhotite / Pyrite.....	128
Figure 51. Corrosion product layer after 7 days of exposure at $80\text{ }^{\circ}\text{C}$ : (a) SEM image of surface morphology with 100x magnification; (b) SEM image of surface morphology with 2,000x magnification; (c) XRD pattern. ....	130
Figure 52. Verification of Pourbaix diagram after 7 days of exposure (Pourbaix diagram was generated at $T = 80\text{ }^{\circ}\text{C}$ , $\text{pH}_2\text{S} = 0.053\text{ bar}$ , $[\text{Fe}^{2+}] = 0.115\text{ ppm}$ , $[\text{Fe}^{3+}] = 1.0 \times 10^{-6}\text{ M}$ ): (a) Mackinawite; (b) Mackinawite / Greigite / Pyrrhotite / Pyrite.....	130
Figure 53. Hypothesis of verification of Pourbaix diagram by adjusting pH (Pourbaix diagram was generated at $T = 25\text{ }^{\circ}\text{C}$ , $\text{pH}_2\text{S} = 0.097\text{ bar}$ , $[\text{Fe}^{2+}] = 0.52\text{ ppm}$ , $[\text{Fe}^{3+}] = 1.0 \times 10^{-6}\text{ M}$ ): (a) Mackinawite / Greigite; (b) Mackinawite / Greigite / Pyrrhotite / Pyrite. ..	132
Figure 54. (a) Measured bulk pH, surface pH, and $[\text{Fe}^{2+}]$ ; (b) Corrosion rate and OCP during experiment. ....	134

Figure 55. Corrosion product layer after 8 days of exposure at 25 °C: (a) SEM image of surface morphology with 50x magnification; (b) SEM image of surface morphology with 4,000x magnification; (c) XRD pattern. ....	135
Figure 56. Verification of Pourbaix diagram after 8 days (Pourbaix diagram was generated at T = 25 °C, pH <sub>2</sub> S = 0.097 bar, [Fe <sup>2+</sup> ] = 0.52 ppm, [Fe <sup>3+</sup> ] = 1.0 x 10 <sup>-6</sup> M): (a) Mackinawite / Greigite; (b) Mackinawite / Greigite / Pyrrhotite / Pyrite. ....	137
Figure 57. Experimental design for Experiment set #1. ....	153
Figure 58. Experimental design for Experiment set #2. ....	154
Figure 59. Experimental design for Experiment set #3. ....	154
Figure 60. OCP and corrosion rates monitored throughout Experiment #1. ....	155
Figure 61. Bulk pH and [Fe <sup>2+</sup> ] monitored throughout Experiment #1. ....	156
Figure 62. Surface morphologies of samples: (a) after 1 day; (b) after 4 days; (c) after 7 days; (d) after 9 days; (e) after 11 days. ....	157
Figure 63. XRD pattern of corrosion product layer formed on samples in Exp. #1: (a) after 1 day; (b) after 4 days; (c) after 7 days; (d) after 9 days; (e) after 11 days. ....	159
Figure 64. Cross section images of samples: (a) after 1 day; (b) after 4 days; (c) after 7 days; (d) after 9 days; (e) after 11 days. ....	162
Figure 65. SEM images with 5, 000x magnification: (a) surface view after 4 days; (b) surface view after 7 days; (c) cross section after 4 days; (d) cross section after 7 days. ....	163
Figure 66. Surface profilometry of samples after removing corrosion product layer: (a) after 4 days; (b) after 7 days; (c) after 9 days; (d) after 11 days. ....	165
Figure 67. Nyquist plot (5000 ~ 0.003Hz). ....	166
Figure 68. Bode plots (Phase Angle vs. Log ω) (5000 ~ 0.003Hz). ....	166
Figure 69. Bode plots (Log Z vs. Log ω) (5000 ~ 0.003Hz). ....	167
Figure 70. Bulk pH, surface pH, and [Fe <sup>2+</sup> ] measured throughout experiment #2. ....	168
Figure 71. Corrosion rate and OCP monitored during experiment #2. ....	168
Figure 72. XRD pattern of corrosion product layer formed on samples in Exp. #2: (a) after 1 day; (b) after 4 days; (c) after 7 days; (d) after 8 days; (e) after 11 days. ....	170
Figure 73. Surface morphologies of samples: (a) after 1 day; (b) after 4 days; (c) after 7 days; (d) after 8 days; (e) after 10 days; (f) after 11 days. ....	172
Figure 74. Cross section images of samples: (a) after 1 day; (b) after 4 days; (c) after 7 days; (d) after 8 days. ....	173
Figure 75. Surface profilometry of samples after removing corrosion product layer: (a) after 4 days; (b) after 7 days; (c) after 9 days; (d) after 11 days. ....	174
Figure 76. Nyquist plots in Exp. #2. ....	175
Figure 77. Bode plots (Phase Angle vs. Log ω) in Exp. #2. ....	176

Figure 78. Bode plots (Log Z vs. Log $\omega$ ) in Exp. #2. ....	176
Figure 79. (a) pH values monitored during Exp. #3; (b) comparison of pH values between Exp. #2 and Exp. #3. ....	178
Figure 80. OCP and corrosion rate throughout experiment #3; (b) Comparisons of corrosion rate and OCP between Exp. #2 and Exp. #3. ....	179
Figure 81. Surface morphologies of samples in chronological order: (a) after 1 day; (b) after 2 days; (c) after 3 days; (d) after 5 days. ....	180
Figure 82. XRD pattern of corrosion product layer formed on samples in Exp. #3: (a) after 1 day; (b) after 2 days; (c) after 3 days; (d) after 5 days. ....	182
Figure 83. Cross section images of samples in Exp. #3: (a) after 1 day with 2000x magnification;(b) after 3 days with 2000x magnification; (c-1) after 5 days with 500x magnification; (c-2) after 5 days with 2000x magnification. ....	183
Figure 84. Surface profilometry of samples in Exp. #3: (a) 2 days; (b) 3 days; (c) 5 days. ....	184
Figure 85. Nyquist plots in Exp. #3. ....	185
Figure 86. Bode plots (Phase Angle vs. Log $\omega$ ) in Exp. #3. ....	186
Figure 87. Discussion of electrochemical half reactions. ....	188
Figure 88. Resistivity data of pyrite from various experimental sources (Schieck [145], Caban-Acevedo [146], Abraitis [147], Pearce [144]) (reproduced from [148]). ....	190
Figure 89. UDC sample holder [149]. ....	192
Figure 90. Experimental glass cell setup. ....	192
Figure 91. (a) Sample holder with a layer of silica sand deposit; (b) Sample holder with a layer of pyrite particles deposit. ....	194
Figure 92. (a) 150 ~ 400 $\mu\text{m}$ silica sand; (b) 150 ~ 400 $\mu\text{m}$ pyrite particles; (c) 1000 ~ 2000 $\mu\text{m}$ pyrite particles. ....	195
Figure 93. XRD pattern of the pyrite powder. ....	196
Figure 94. Experimental setup with: (a) 150 ~ 400 $\mu\text{m}$ pyrite particles; (b) 1000 ~ 2000 $\mu\text{m}$ pyrite particles. ....	198
Figure 95. A SEM image of the insulating mesh. ....	199
Figure 96. Procedure for introducing the insulating mesh: (a) a steel sample prepared and introduced into the sample holder; (b) a non-conductive mesh used over the sample surface; (c) the deposit holder placed over the mesh. ....	200
Figure 97. Corrosion rate and OCP using 2 mm thickness of silica sand deposit in the initial hours of Test #1. ....	202
Figure 98. Corrosion rate and OCP using 2 mm thickness of silica sand deposit for a week in Test #1. ....	203

Figure 99. Corrosion rate and OCP using 2 mm thickness of pyrite particle deposit in the initial hours of Test #2. ....	204
Figure 100. Corrosion rate and OCP using 2 mm thickness of pyrite particle deposit for a week of Test #2. ....	204
Figure 101. Nyquist plots using 2 mm thickness of silica sand deposit in Test #1. ....	205
Figure 102. Nyquist plots using 2 mm thickness of pyrite particle deposit in Test #2...	206
Figure 103. pH and $S_{\text{mackinawite}}$ with: (a) silica sand deposit in Test #1; (b) pyrite particles deposit in Test #2. ....	207
Figure 104. Surface morphologies of the sample with corrosion product layer in place using silica sand deposit in Test #1: (a) 50x SEM image; (b) 2,000x SEM image; (c) EDX analysis of the corrosion product layer. ....	208
Figure 105. Surface morphologies of the sample with corrosion product layer in place using pyrite particle deposit in Test #2: (a) 50x SEM image; (b) 2,000x SEM image; (c) EDX analysis of the crystals. ....	209
Figure 106. Surface morphologies of the sample after removing the corrosion product layer using silica sand deposit in Test #1: (a) 50x SEM image; (b) 1,000x SEM image. ....	210
Figure 107. Surface morphologies of the sample after removing the corrosion product layer using pyrite particle deposit in Test #2. ....	210
Figure 108. Locations of localized corrosion on the specimen using pyrite particle deposit in Test #2. ....	211
Figure 109. (a) Profilometry feature with sand deposit in Test #1; (b) Profilometry feature with pyrite deposit in Test #2; (c) Maximum pit depth with sand deposit in Test #1; (d) Maximum pit depth with pyrite deposit in Test #2. ....	212
Figure 110. Comparison of corrosion rates between sand deposit and pyrite deposit....	212
Figure 111. Corrosion rate and OCP using 1000 ~ 2000 $\mu\text{m}$ pyrite particle deposit in the initial five hours of Test #3. ....	214
Figure 112. Corrosion rate and OCP during the test of a week using 1000 ~ 2000 $\mu\text{m}$ pyrite particle deposit in Test #3. ....	214
Figure 113. Comparison of (a) OCP and (b) corrosion rates between two different pyrite particle sizes. ....	215
Figure 114. Nyquist plots with 1000 ~ 2000 $\mu\text{m}$ pyrite particle deposit in Test #3. ....	216
Figure 115. pH and $S_{\text{mackinawite}}$ during Test #3 using 1000 ~ 2000 $\mu\text{m}$ pyrite particles. .	216
Figure 116. Surface morphologies of the sample with the corrosion product layer in place using 1000 ~ 2000 $\mu\text{m}$ pyrite particle deposit in Test #3: (a) 50x SEM image; (b) 1,000x SEM image; (c) 5,000x SEM image; (d) EDX analysis of crystals. ....	217
Figure 117. Locations of localized attack on the sample using 1000 ~ 2000 $\mu\text{m}$ pyrite particle deposit in Test #3. ....	218

Figure 118. (a) Profilometry feature using 1000 ~ 2000 $\mu\text{m}$ pyrite particle deposit; (b) the maximum pit depth found on sample in Test #3.....	218
Figure 119. Comparison of corrosion rates between different pyrite particle sizes. ....	219
Figure 120. SEM image of 150 ~ 400 $\mu\text{m}$ pyrite particles deposited on the mesh.....	221
Figure 121. Corrosion rate and OCP with 150 ~ 400 $\mu\text{m}$ pyrite particles deposited on the mesh in the initial hours of Test #4.....	221
Figure 122. Corrosion rate and OCP using 1000 ~ 2000 $\mu\text{m}$ pyrite particles deposited on the mesh in the initial hours of Test #5.....	222
Figure 123. Corrosion rate and OCP using 1000 ~ 2000 $\mu\text{m}$ pyrite particles deposited on the mesh for a week in Test #5. ....	223
Figure 124. Surface morphologies of the sample with the corrosion product layer in place using 1000 ~ 2000 $\mu\text{m}$ pyrite particles deposited on the mesh in Test #5: (a) 100x SEM image; (b) 500x SEM image; (c) 4,000x SEM image; (d) EDX analysis of crystals. ....	223
Figure 125. Surface morphologies of the sample after removing corrosion product layer using 1000 ~ 2000 $\mu\text{m}$ pyrite particles deposited on the mesh in Test #5.....	224
Figure 126. Profilometry feature of the specimen after removing corrosion product layer using 1000 ~ 2000 $\mu\text{m}$ pyrite particles deposited on the mesh in Test #5.....	224
Figure 127. Corrosion rate and OCP using 150 ~ 400 $\mu\text{m}$ silica sand deposit in a solution purged with $\text{CO}_2$ in the initial hours of Test #6.....	225
Figure 128. Corrosion rate and OCP using 150 ~ 400 $\mu\text{m}$ silica sand deposit in a solution purged with $\text{CO}_2$ for a week in Test #6.....	226
Figure 129. Corrosion rate and OCP using 150 ~ 400 $\mu\text{m}$ pyrite particle deposit in a solution purged with $\text{CO}_2$ in the initial hours of Test #7.....	226
Figure 130. Corrosion rate and OCP using 150 ~ 400 $\mu\text{m}$ pyrite particle deposit in a solution purged with $\text{CO}_2$ for a week in Test #7.....	227
Figure 131. Surface morphologies of the sample with the corrosion product layer in place using 150 ~ 400 $\mu\text{m}$ silica sand deposit in an aqueous $\text{CO}_2$ solution in Test #6: (a) 50x SEM image; (b) 200x SEM image.....	228
Figure 132. Surface morphologies of the sample with the corrosion product layer in place using 150 ~ 400 $\mu\text{m}$ pyrite particle deposit in an aqueous $\text{CO}_2$ solution in Test #7: (a) 50x SEM image; (b) 50x SEM image.....	228
Figure 133. Surface morphologies of the sample after removing the corrosion product layer using 150 ~ 400 $\mu\text{m}$ silica sand deposit in an aqueous $\text{CO}_2$ solution in Test #7: (a) 50x SEM image; (b) 200x SEM image.....	229
Figure 134. Surface morphologies of the sample after removing the corrosion product layer using 150 ~ 400 $\mu\text{m}$ pyrite particle deposit in an aqueous $\text{CO}_2$ solution in Test #7.....	229

Figure 135. Locations of localized attack on the sample after removing the corrosion product layer using 150 ~ 400 $\mu\text{m}$ pyrite particle deposit in an aqueous $\text{CO}_2$ solution in Test #7.....	230
Figure 136. (a) Profilometry feature using 150 ~ 400 $\mu\text{m}$ pyrite particle deposit in an aqueous $\text{CO}_2$ solution; (b) The maximum pit depth found on the sample in Test #7.....	230
Figure 137. Comparison of corrosion rates between silica sand deposit and pyrite particle deposit in an aqueous $\text{CO}_2$ solution. ....	231
Figure 138. The pit locations in relation to pyrite: (a) pit is underneath the pyrite particle; (b) pit is adjacent to pyrite particle; (c) pit is far away from the pyrite particle.....	233
Figure 139. (a-1) A SEM image of 5mm x 5mm pyrite particles deposited on steel surface at $T = 25\text{ }^\circ\text{C}$ , $p\text{CO}_2 = 0.97\text{ bar}$ , and initial pH 6.0; (a-2) Surface profilometry of the sample shown in (a-1); (b) Surface profilometry of the sample in the presence of 5mm x 5mm pyrite particles at $T = 80\text{ }^\circ\text{C}$ , $p\text{CO}_2 = 0.54\text{ bar}$ , and initial pH 6.0.....	234
Figure 140. Surface profilometry of different locations of specimen in the presence of 1000 ~ 2000 $\mu\text{m}$ pyrite particles at $T = 25\text{ }^\circ\text{C}$ , $p\text{H}_2\text{S} = 0.1\text{ bar}$ , and initial pH 4.0.....	235
Figure 141. Surface profilometry of specimen in the presence of 150 ~ 400 $\mu\text{m}$ pyrite particles at $T = 25\text{ }^\circ\text{C}$ , $p\text{H}_2\text{S} = 0.1\text{ bar}$ , and initial pH 4.0.....	236
Figure 142. Pourbaix diagram for Fe- $\text{H}_2\text{S}$ - $\text{H}_2\text{O}$ system ( $T = 25\text{ }^\circ\text{C}$ , $p\text{H}_2\text{S} = 0.1\text{ bar}$ , $[\text{Fe}^{2+}] = 10\text{ ppm}$ , $[\text{Fe}^{3+}] = 10^{-6}\text{ M}$ ) with (a) Fe + Mackinawite + greigite + pyrrhotite + pyrite; (b) Fe + pyrite.....	238
Figure 143. The relationship between solution conductivity and sodium chloride concentration (data reproduced from literature [153], [154]).....	239
Figure 144. Macroscopic scenario of pyrite particles deposited on steel surface.....	241
Figure 145. Microscopic scenario of localized corrosion in the presence of pyrite particles deposited on steel surface. ....	242
Figure 146. A descriptive model for localized corrosion in the presence of pyrite formed at favorable conditions: (a) Formation of mackinawite; (b) Formation of pyrite; (c) Localized corrosion.....	244
Figure 147. Pyrite stability T- $p\text{H}_2\text{S}$ map at pH 3 generated by ThermoCORP ( $E = -0.65\text{ V}$ vs. $\text{Ag}/\text{AgCl}$ (sat'd $\text{KCl}$ ), $\text{pH} = 3$ , $[\text{Fe}^{2+}] = 10\text{ ppm}$ , $[\text{Fe}^{3+}] = 1\text{ ppm}$ ).....	247
Figure 148. Pyrite stability T- $p\text{H}_2\text{S}$ map at pH 4 generated by ThermoCORP ( $E = -0.65\text{ V}$ vs. $\text{Ag}/\text{AgCl}$ (sat'd $\text{KCl}$ ), $\text{pH} = 4$ , $[\text{Fe}^{2+}] = 10\text{ ppm}$ , $[\text{Fe}^{3+}] = 1\text{ ppm}$ ).....	248
Figure 149. Pyrite stability T- $p\text{H}_2\text{S}$ map at pH 5 generated by ThermoCORP ( $E = -0.65\text{ V}$ vs. $\text{Ag}/\text{AgCl}$ (sat'd $\text{KCl}$ ), $\text{pH} = 5$ , $[\text{Fe}^{2+}] = 10\text{ ppm}$ , $[\text{Fe}^{3+}] = 1\text{ ppm}$ ).....	248
Figure 150. Pyrite stability T- $p\text{H}_2\text{S}$ map at pH 6 generated by ThermoCORP ( $E = -0.65\text{ V}$ vs. $\text{Ag}/\text{AgCl}$ (sat'd $\text{KCl}$ ), $\text{pH} = 5$ , $[\text{Fe}^{2+}] = 10\text{ ppm}$ , $[\text{Fe}^{3+}] = 1\text{ ppm}$ ): (a) $T = 0 \sim 250\text{ }^\circ\text{C}$ , $p\text{H}_2\text{S} = 0 \sim 20\text{ bar}$ ; (b) $T = 0 \sim 100\text{ }^\circ\text{C}$ , $p\text{H}_2\text{S} = 0 \sim 1\text{ bar}$ .....	250

Figure 151. Comparison of corrosion potentials between two tests (80 °C, pCO <sub>2</sub> = 0.5 bar, O <sub>2</sub> concentration = 1 ppm in liquid, pH = 6.6, 1 wt.% NaCl) (Reproduced from [157]).....	252
Figure 152. Pyrite stability T-pH <sub>2</sub> S map with oxygen ingress at pH 6 generated by ThermoCORP (E = -0.45 V vs. Ag/AgCl (sat'd KCl), pH = 3, [Fe <sup>2+</sup> ] = 10 ppm, [Fe <sup>3+</sup> ] = 1 ppm).....	252
Figure 153. Multipoint standard curve plots: (a) for FerroZine <sup>®</sup> reagent; (b) for FerroVer <sup>®</sup> reagent.....	276
Figure 154. Mesh-capped flat pH probe.....	280
Figure 155. A SEM image of mesh.....	281
Figure 156. Surface pH with 100 ppm H <sub>2</sub> S / N <sub>2</sub> at bulk pH 3.0.....	283
Figure 157. Surface pH with 100 ppm H <sub>2</sub> S / N <sub>2</sub> at bulk pH 4.0.....	283
Figure 158. Surface pH with 100 ppm H <sub>2</sub> S / N <sub>2</sub> at bulk pH 5.0.....	284
Figure 159. Surface pH with 1% H <sub>2</sub> S / N <sub>2</sub> at bulk pH 3.0.....	284
Figure 160. Surface pH with 1% H <sub>2</sub> S / N <sub>2</sub> at bulk pH 4.0.....	285
Figure 161. Surface pH with 1% H <sub>2</sub> S / N <sub>2</sub> at bulk pH 5.0.....	285
Figure 162. Surface pH with 10% H <sub>2</sub> S / N <sub>2</sub> at bulk pH 3.0.....	286
Figure 163. Surface pH with 10% H <sub>2</sub> S / N <sub>2</sub> at bulk pH 4.0.....	286
Figure 164. Surface pH with 10% H <sub>2</sub> S / N <sub>2</sub> at bulk pH 5.0.....	287
Figure 165. Summary of measured surface pH at bulk pH 4.0.....	287
Figure 166. Surface pH affected by flow in N <sub>2</sub> purged solution.....	288
Figure 167. Surface pH affected by flow in CO <sub>2</sub> purged solution.....	289
Figure 168. Surface pH affected by flow in 100 ppm H <sub>2</sub> S / N <sub>2</sub> purged solution.....	289
Figure 169. Surface pH affected by flow in 1% H <sub>2</sub> S / N <sub>2</sub> purged solution.....	290
Figure 170. Surface pH affected by flow in 10 % H <sub>2</sub> S / N <sub>2</sub> purged solution.....	290
Figure 171. Schematic of experimental apparatus.....	293
Figure 172. Experimental glass cell setup.....	293
Figure 173. Experimental hypothesis of polarization.....	294
Figure 174. Surface pH with polarization at mesh at -0.35 V vs. Ag/AgCl (Sat'd KCl) (Polarized 0.36 V above OCP, 25 °C, pH <sub>2</sub> S = 0.01bar, stirring 400rpm, initial bulk pH 6.0).....	295
Figure 175. Surface pH with polarization of mesh/sample at -0.35 V vs. Ag/AgCl (Sat'd KCl) (Polarized 0.36 V above OCP, pH <sub>2</sub> S=0.01 bar H <sub>2</sub> S, 400 rpm, initial bulk pH 6.0).....	296

Figure 176. Surface morphology (SEM) and composition analysis (EDX) of steel sample. .....	297
Figure 177. XRD pattern of corrosion product layer formed on steel sample.....	297
Figure 178. Verification of Pourbaix diagrams generated according to experimental conditions at the beginning of experiment (a) Mackinawite / Greigite; (b) Mackinawite / Greigite / Pyrrhotite (25 °C, pH <sub>2</sub> S = 0.01bar, [Fe <sup>3+</sup> ] = 10 <sup>-6</sup> M, [Fe <sup>2+</sup> ] = 10 ppm). ....	298
Figure 179. Verification of Pourbaix diagrams generated according to experimental conditions at the end of experiment (a) Mackinawite / Greigite; (b) Mackinawite / Greigite / Pyrrhotite (25 °C, pH <sub>2</sub> S = 0.01bar, [Fe <sup>3+</sup> ] = 10 <sup>-6</sup> M, [Fe <sup>2+</sup> ] = 0.8 ppm).....	299
Figure 180. Surface pH with polarization at mesh/sample at -0.1 V vs. Ag/AgCl (Sat'd KCl) (Polarize 0.61 V above OCP, pH <sub>2</sub> S = 0.01 bar H <sub>2</sub> S, stirring 400rpm, initial bulk pH 6.0). ....	300
Figure 181. Surface morphologies (SEM images) and composition analysis (EDX) of steel sample after experiment.....	301
Figure 182. XRD pattern of corrosion product layer formed on sample. ....	301
Figure 183. Verification of Pourbaix diagrams generated according to experimental conditions in the beginning of experiment (a) Mackinawite / Greigite; (b) Mackinawite / Greigite / Pyrrhotite (25 °C, pH <sub>2</sub> S = 0.01 bar, [Fe <sup>3+</sup> ] = 10 <sup>-6</sup> M, [Fe <sup>2+</sup> ]=10 ppm).....	302
Figure 184. Verification of Pourbaix diagrams generated according to the experimental conditions at the end of experiment (a) Mackinawite / Greigite; (b) Mackinawite / Greigite / Pyrrhotite (25 °C, pH <sub>2</sub> S = 0.01bar, [Fe <sup>3+</sup> ]=10 <sup>-6</sup> M, [Fe <sup>2+</sup> ]=1.1 ppm). ....	302
Figure 185. Surface pH with polarization at mesh/sample at +0.2 V vs. Ag/AgCl (Sat'd KCl) (Polarized 0.91 V above OCP, pH <sub>2</sub> S = 0.01 bar H <sub>2</sub> S, stirring 400 rpm, initial bulk pH 6.0). ....	304
Figure 186. Surface morphology (SEM) and composition analysis (EDX) of steel sample. .....	304
Figure 187. XRD pattern of corrosion product layer formed on the steel sample.....	305
Figure 188. Verification of Pourbaix diagrams generated according to experimental conditions in the beginning of experiment (a) Mackinawite / Greigite; (b) Mackinawite / Greigite / Pyrrhotite (25 °C, pH <sub>2</sub> S = 0.01 bar, [Fe <sup>3+</sup> ] = 10 <sup>-6</sup> M, [Fe <sup>2+</sup> ] = 10 ppm).....	305
Figure 189. Verification of Pourbaix diagrams generated at the end of experiment (a) Mackinawite / Greigite; (b) Mackinawite / Greigite / Pyrrhotite (25 °C, pH <sub>2</sub> S = 0.01 bar, [Fe <sup>3+</sup> ] = 10 <sup>-6</sup> M, [Fe <sup>2+</sup> ] = 1.3 ppm). ....	306

## CHAPTER 1. INTRODUCTION

### 1.1 Background

One of the most challenging issues for the oil and gas industry is infrastructure failure. This can lead to the release of hydrocarbons into the environment, with associated risk of fire/explosion, as well as financial loss. Although corrosion resistant alloys (CRAs) are widely used, carbon steel remains the preferred construction material in the oil and gas industry. Carbon steel possesses high strength, is easily used in fabrication, inexpensive (compared to CRAs), available, and can be readily used in conjunction with appropriate corrosion mitigation options.

CO<sub>2</sub> and H<sub>2</sub>S corrosion of carbon steel are amongst the most frequently encountered materials degradation processes associated with production and transportation of oil and gas [1], [2]. The CO<sub>2</sub> corrosion mechanism is generally well defined, however, complications arise when H<sub>2</sub>S is present. H<sub>2</sub>S is a highly hazardous, flammable, and extremely explosive gas. It acts as a weak acid when dissolved in water and can cause serious corrosion. However, in some cases, it can form a protective iron sulfide layer on the steel surface preventing further corrosion [3]–[6]. The prediction and control of H<sub>2</sub>S corrosion is a significant challenge to oil and gas producers.

H<sub>2</sub>S corrosion attack can be classified into two categories, localized corrosion and general corrosion, based on the appearance of the corroded steel. Due to recent studies [3], [7]–[12], mechanisms associated with H<sub>2</sub>S general corrosion have become better understood. An electrochemical model of general corrosion [11], including water chemistry and electrochemistry of the Fe-H<sub>2</sub>S system, including growth of protective iron sulfide layers (mackinawite), has been developed to take into account different key

operating parameters:  $p\text{H}_2\text{S}$ ,  $p\text{CO}_2$ , temperature, flow rate, and pH. Compared to  $\text{H}_2\text{S}$  general corrosion, there is minimal understanding of  $\text{H}_2\text{S}$  localized corrosion. Mechanisms of  $\text{H}_2\text{S}$  localized corrosion are unclear and the causes of  $\text{H}_2\text{S}$  localized corrosion are uncertain. However, it is commonly suspected that localized corrosion is related to the type and nature of the corrosion product layers formed on the steel surface. In  $\text{CO}_2$  corrosion in oil and gas production environments, siderite ( $\text{FeCO}_3$ ) is almost always the favored corrosion product. However, in  $\text{H}_2\text{S}$  corrosion of carbon steel, various types, or polymorphs, of iron sulfide and related phases have been reported. These include amorphous ferrous sulfide ( $\text{FeS}$ ), mackinawite ( $\text{FeS}$ ), cubic ferrous sulfide ( $\text{FeS}$ ), troilite ( $\text{FeS}$ ), pyrrhotites ( $\text{Fe}_{1-x}\text{S}$ ), smythite ( $\text{Fe}_{3+x}\text{S}_4$ ), greigite ( $\text{Fe}_3\text{S}_4$ ), and pyrite ( $\text{FeS}_2$ ) [3]–[5]. Each has its own unique set of physicochemical properties. Therefore, it is of great interest to study the role of iron sulfide phases in localized corrosion of carbon steel. A thermodynamic model to predict the formation and transformation of these different types of iron sulfides is an essential prerequisite for any study of localized  $\text{H}_2\text{S}$  corrosion. In the corrosion science community, Pourbaix diagrams are frequently used for predicting the stability of aqueous and solid corrosion products in a corrosion system. Thermodynamic studies, primarily by geochemists [13]–[17], of aqueous  $\text{H}_2\text{S}$  systems and polymorphous iron sulfides have been conducted, published, and in some cases transformed into commercial software. However, inconsistencies exist in reported aqueous sulfide thermochemistry in the literature and are reflected in the output from various commercial software packages. Therefore, a thermodynamic model to predict corrosion products for an  $\text{H}_2\text{S}$ - $\text{H}_2\text{O}$ - $\text{Fe}$  system with a relatively narrow focus on the oil and gas industry for corrosion engineers is also needed.

## 1.2 Goals

The main goal of the present project has been the study of the role of iron sulfide polymorphs in localized corrosion of carbon steel. In order to achieve this goal, the chemical thermodynamics of  $\text{H}_2\text{S-H}_2\text{O}$  and  $\text{H}_2\text{S-H}_2\text{O-Fe}^{2+}$  systems and electrochemical thermodynamics of an  $\text{H}_2\text{S-H}_2\text{O-Fe}$  system were first investigated to develop a thermodynamic model in the form of Pourbaix diagrams [18], [19]. Thereafter, this thermodynamic model was verified by conducting experiments and comparing corrosion products formed in experiments with the predictions made by the Pourbaix diagrams. Experimental conditions, leading to the formation of different iron sulfides as corrosion products in sour environments, were then determined in accordance with this thermodynamic model. The subsequent influence of corrosion product layers containing polymorphous iron sulfides on the localized corrosion of steel was then studied with the focus on pyrite. Meanwhile, novel experiments in the presence of pyrite deposits were designed and performed to further understand the impact on  $\text{H}_2\text{S}$  localized corrosion. Finally, a descriptive model was developed to outline localized corrosion in a sour environment when conditions lead to the formation of pyrite.

## 1.3 Publications

All of the work presented in this dissertation has been reported in the Ohio University Corrosion Center Joint Industry Project (CC-JIP) Advisory Board Meetings, from January 2010 through March 2015. In addition, parts of this work have been published at National Association of Corrosion Engineers (NACE) International Conferences and have been or will be published in the Corrosion Journal. The author's publication list is shown below.

### 1.3.1 Journal Publications

1. J. Ning, Y. Zheng, D. Young, B. Brown, S. Nešić, “The Role of Iron Sulfide Polymorphism in Localized H<sub>2</sub>S Corrosion of Mild Steel,” *Corrosion*, doi: <http://dx.doi.org/10.5006/2030>.
2. Y. Zheng, J. Ning, D. Young, B. Brown, S. Nešić, “Investigation of Cathodic Reaction Mechanisms of H<sub>2</sub>S Corrosion Using a Passive SS304 Rotating Cylinder Electrode,” *Corrosion*, doi: <http://dx.doi.org/10.5006/2005>.
3. Y. Zheng, J. Ning, B. Brown, S. Nešić, “Advancement in Predictive Modeling of Mild Steel Corrosion in CO<sub>2</sub> and H<sub>2</sub> S Containing Environments,” *Corrosion* 72, 5, pp. 679-691, 2016.
4. J. Ning, Y. Zheng, D. Young, B. Brown, S. Nešić, “A Thermodynamic Model for the Prediction of Mild Steel Corrosion Products in an Aqueous Hydrogen Sulfide Environment,” *Corrosion* 71, 8 pp. 945-960, 2015.
5. Y. Zheng, J. Ning, B. Brown, S. Nešić, “Electrochemical Model of Mild Steel Corrosion in a Mixed H<sub>2</sub>S/CO<sub>2</sub> Aqueous Environment”, *Corrosion* 71, 3, pp. 316-325, 2015.
6. J. Ning, Y. Zheng, D. Young, B. Brown, S. Nešić, “A Thermodynamic Study of Hydrogen Sulfide Corrosion of Mild Steel,” *Corrosion* 70, 4, pp. 375-389, 2014.
7. Y. Zheng, J. Ning, B. Brown, D. Young, S. Nešić, “Mechanistic Study of Hydrogen Sulfide Corrosion with Iron Sulfide Layer Growth,” *Corrosion*, Submitted, 2015.

### 1.3.2 Conference Papers & Oral Presentations

1. J. Ning, Y. Zheng, D. Young, B. Brown, S. Nešić, “The Role of Iron Sulfide Polymorphism in Localized Corrosion of Mild Steel,” CORROSION/2016, Vancouver, paper no. 7502
2. Y. Zheng, J. Ning, B. Brown, S. Nešić, “Investigation of Electrochemical Reaction Kinetics of Direct H<sub>2</sub>S Reduction Using 316L RCE” CORROSION/2016, Vancouver, paper no. 7340
3. J. Ning, “The Role of Iron Sulfide Polymorphism in Localized Corrosion of Mild Steel”, Invited Speaker at Sour Gas Corrosion Workshop, CORROSION/2015, Dallas, TX

4. J. Ning, Y. Zheng, B. Brown, D. Young, S. Nešić, “Construction and Verification of Pourbaix Diagrams for Hydrogen Sulfide Corrosion of Mild Steel”, CORROSION/2015, Dallas, TX, paper no. 5507
5. Y. Zheng, J. Ning, B. Brown, D. Young, S. Nešić, “Mechanistic Study of H<sub>2</sub>S Corrosion of Carbon Steel with Iron Sulfide Layer Growth”, CORROSION/2015, Dallas, TX, paper no. 5933
6. R. Case, M. Achour, J. Ning, “Effect of Corrosion Inhibition on the Mitigation of Preferential Weld Corrosion in Seawater Transport Systems”, CORROSION/2015, Dallas, TX , paper no. 5641
7. S. Nešić, Y. Zheng, B. Brown, J. Ning, “Predictive Modelling in CO<sub>2</sub> and H<sub>2</sub>S Containing Environment”, CORROSION/2015, Dallas, TX, paper no. 6146
8. Y. Zheng, J. Ning, B. Brown, S. Nešić, “Electrochemical Model of Mild Steel Corrosion in Mixed H<sub>2</sub>S/CO<sub>2</sub> Environment”, CORROSION/2014, San Antonio, TX, paper no. 3907
9. J. Ning, Y. Zheng, D. Young, B. Brown, S. Nešić, “A Thermodynamic Study of Hydrogen Sulfide Corrosion of Mild Steel”, CORROSION/2013, Orlando, FL, paper no. 2462

## CHAPTER 2. CHEMICAL THERMODYNAMICS OF AN H<sub>2</sub>S-H<sub>2</sub>O SYSTEM

### 2.1 Introduction

Aqueous sulfide thermochemistry has received extensive attention since sulfides are widely present in many aqueous systems relating to geochemistry, oceanography, the oil and gas industry, the pulp and paper industry, water treatment, medical and biological engineering, environmental sciences, and inorganic chemistry. The understanding of thermochemistry of aqueous sulfides is particularly important to fundamental studies and industrial operations in oil and gas industry due to the fact that H<sub>2</sub>S gas has frequently been encountered in the fluids produced in the oil and gas fields. The dissolution and dissociations of gaseous H<sub>2</sub>S make the water acidic and corrosive, causing internal corrosion of production tubing and pipelines [1]–[3].

However, there is confusion and inconsistencies in the literature as regards aqueous sulfide thermochemistry. In the present Chapter, the inconsistencies in prevailing expressions for H<sub>2</sub>S solubility constant ( $K_{H_2S}$ ), the first dissociation constant ( $K_{a,1}$ ), and the second dissociation constant ( $K_{a,2}$ ) are reviewed. Further, the expressions for  $K_{H_2S}$ ,  $K_{a,1}$ , and  $K_{a,2}$  are selected for models to predict water chemistry of an H<sub>2</sub>S-H<sub>2</sub>O system. By comparing with experimental data, the best prediction model for H<sub>2</sub>S solubility and dissociation in an H<sub>2</sub>S-H<sub>2</sub>O system is identified.

### 2.2 Objectives

- Evaluate existing expressions for H<sub>2</sub>S solubility constant and dissociation constants in order to select the most reliable ones for modeling water chemistry of an aqueous H<sub>2</sub>S system.

- Generate thermodynamic models for predicting water chemistry of an H<sub>2</sub>S-H<sub>2</sub>O system by using selected expressions for solubility and dissociations constants.
- Verify a best prediction model for H<sub>2</sub>S solubility and dissociation in an H<sub>2</sub>S-H<sub>2</sub>O system by comparing experimental and predicted pH values.

### 2.3 Literature Review

When gaseous H<sub>2</sub>S is in the presence of water, it readily dissolves in water and dissociates. The chemical reactions and the corresponding expressions for equilibrium constants associated with each reaction defining H<sub>2</sub>S solubility and dissociations in an H<sub>2</sub>S-H<sub>2</sub>O system are shown as Reaction (1) through to Equation (6) [3].

Solubility is directly related to the partial pressure of H<sub>2</sub>S ( $p_{\text{H}_2\text{S}}$ ) according to Henry's Law:



$$K_{\text{H}_2\text{S}} = \frac{[\text{H}_2\text{S}]}{p_{\text{H}_2\text{S}}} \quad (2)$$

Aqueous H<sub>2</sub>S is a weak acid, hence it only partially dissociates. The partial dissociations occur in two steps; the first dissociation (Reaction (3) and corresponding equilibrium Equation (4)) is followed by the second dissociation (Reaction (5) and corresponding equilibrium Equation (6)):



$$K_{a,1} = \frac{[H^+][HS^-]}{[H_2S]} \quad (4)$$



$$K_{a,2} = \frac{[H^+][S^{2-}]}{[HS^-]} \quad (6)$$

Various equations for the  $H_2S$  solubility constant ( $K_{H_2S}$ ), the first dissociation constant ( $K_{a,1}$ ) and the second dissociation constant ( $K_{a,2}$ ) were used for calculating the equilibrium concentrations of species in an  $H_2S$ - $H_2O$  system [3]. These are reviewed below.

### 2.3.1 The $H_2S$ Solubility Constant $K_{H_2S}$

Five equations used for predicting  $K_{H_2S}$  are shown in Table 1. The  $K_{H_2S}$  change with temperature predicted by these five equations is shown in Figure 1, where all the five predicted curves are in good agreement.

Table 1 Expressions for solubility constant  $K_{H_2S}$  from multiple sources.

Equations	Values at 25°C	Sources
$K_{H_2S} = 10^{-[634.27+0.2709T_k-(0.11132 \times 10^{-3} T_k^2)-(16719/T_k)-(261.9 \log T_k)]}$	0.097	Suleimenov[20]
$K_{H_2S} = 10^{-0.71742672-(0.012145427T_c)+(5.6659982 \times 10^{-5})T_c^2-(8.1902716 \times 10^{-8})T_c^3}$	0.103	IUPAC[21],[22]
$K_{H_2S} = \exp[-41.0563 + 66.4005(\frac{100}{T_k}) + 15.1060 \ln(\frac{T_k}{100})]$	0.102	Weiss[23]
$K_{H_2S} = 1/[10 \times \exp(-3.3747 + 0.072437T_k - 1.10765 \times 10^{-4}T_k^2 - \frac{1549.159}{T_k} + 0.144237 \ln(T_k)) - 1]/0.018$	0.102	Carroll[24]
$K_{H_2S} = 10^{[82.7622+0.00831109T_k-(3898.56/T_k)-12.4914 \ln(T_k)]}$	0.102	Roberts[25]

\*  $T_c$  is temperature in degrees Celsius,  $T_k$  is absolute temperature in Kelvin.

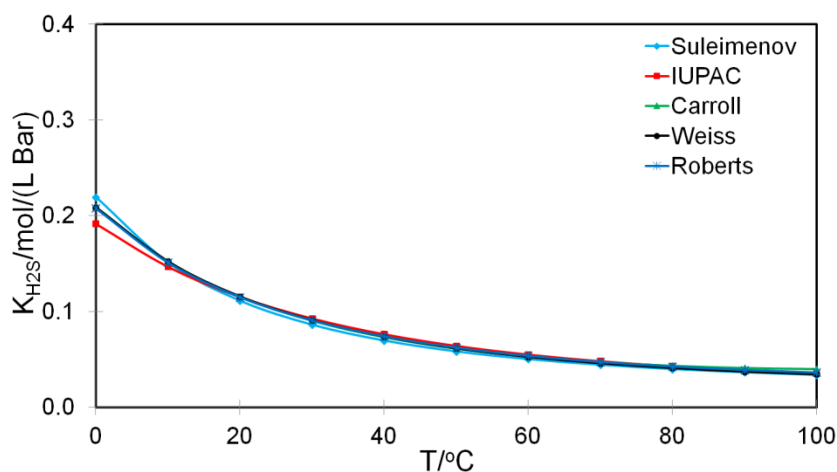


Figure 1. Temperature dependency of the solubility constant  $K_{H_2S}$ .

### 2.3.2 The First Dissociation Constant $K_{a,1}$

Three equations for predicting  $K_{a,1}$  are shown in Table 2. Figure 2 shows  $K_{a,1}$  dependency with temperature as predicted by each of these equations. The curves predicted by Suleimenov [26] and Millero [28] are in agreement, but Kharaka [27] shows a different trend as temperature increases.

Table 2 Expressions for the first dissociation constant  $K_{a,1}$  from multiple sources.

Equations	Value at 25°C	Sources
$K_{a,1} = 10^{782.43945+0.361261T_K-(1.6722 \times 10^{-4})T_K^2-(20565.7315/T_K)-(142.741722 \ln T_K)}$	$1.052 \times 10^{-7}$	Suleimenov[26]
$K_{a,1} = 10^{-[15.345-0.045676T_K+(5.9666 \times 10^{-5})T_K^2]}$	$9.319 \times 10^{-8}$	Kharaka[27]
$K_{a,1} = 10^{-[32.55+(1519.44/T_K)-(15.672 \log T_K)-0.02722T_K]}$	$1.041 \times 10^{-7}$	Millero[28]

\*  $T_K$  is absolute temperature in Kelvin.

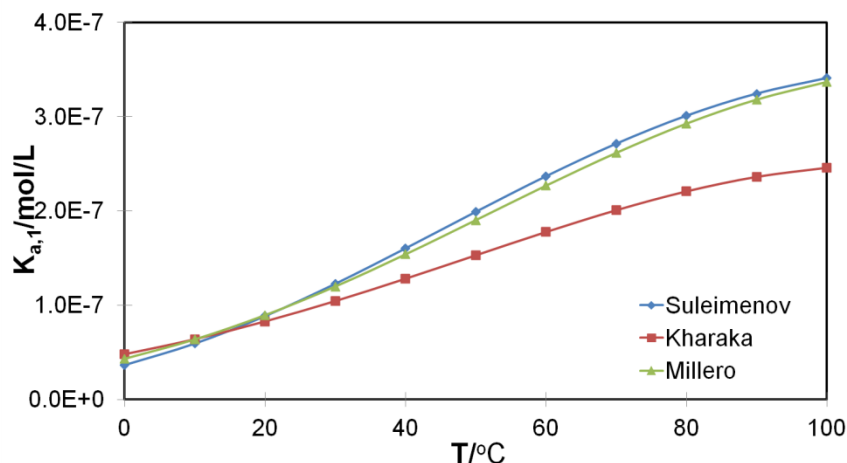


Figure 2. Temperature dependency of the first dissociation constant  $K_{a,1}$ .

### 2.3.3 The Second Dissociation Constant $K_{a,2}$

The values for  $K_{a,2}$  at 25 °C were experimentally measured or estimated by many researchers, as listed in Table 3. There is a large variation of  $K_{a,2}$  values [27], [29]–[35] as shown in Table 3 with the order of magnitude changing from  $10^{-19}$  to  $10^{-12}$ , resulting in a large uncertainty in predicting sulfide ionic concentration in solution. Consequently, using  $K_{a,2}$  to calculate sulfide ion concentration should be avoided. However, the large uncertainty of the values for  $K_{a,2}$  does not necessarily affect predictions of concentrations of other species in the solution, such as  $H_2S$  (it is only related to  $K_{H_2S}$  and  $pH_2S$ ),  $H^+$ , and  $HS^-$  ions, due to  $K_{a,2}$  being much smaller than  $K_{a,1}$  ( $10^{-12} \sim 10^{-19}$  mol/L for  $K_{a,2}$  vs.  $10^{-7}$  mol/L for  $K_{a,1}$  at 25 °C). To be more specific, the small magnitude of  $K_{a,2}$  reveals that reactant is extremely favored over products in the second dissociation reaction, as shown in Equation (5). That is, the second dissociation is negligible compared to the first dissociation process. The values for  $pK_{a,2}$  ( $pK_{a,2} = -\log(K_{a,2})$ ) at 25 °C, 50 °C, and 70 °C were estimated to be 17.4, 15.7, and 14.5 by Migdisov, *et al.* [36]. They also

concluded that the sulfide ion is never a dominant species over the whole range of pH values that one can find in nature because of the miniscule equilibrium constant for the second dissociation reaction.

The issues described above pertaining to the second dissociation step makes the needed experimental measurements hard to conduct accurately, and thus causes uncertainty in values for  $K_{a,2}$ . Moreover, it is noted that these values are also affected by methodologies employed for determining  $K_{a,2}$ . There is a significant inconsistency among the values for  $K_{a,2}$  determined by calorimetric methods. For instance, Stephens and Cobble [33] reported a value of  $1.585 \times 10^{-14}$  mol/L at 25 °C and Wagman, *et al.* [34] reported  $1.200 \times 10^{-13}$  mol/L at 25 °C. In contrast, the values for  $K_{a,2}$  at 25 °C obtained from non-calorimetric methods are relatively consistent.

Table 4 shows values for  $pK_{a,2}$  at 25 °C obtained from non-calorimetric methods such as by vibrational spectroscopy [30], [38], by UV absorption spectra [37], and by differential densitometric analysis [31]. As a result, these values are in relatively good agreement, with an average of  $pK_{a,2} = 17 \pm 0.3$ . Three equations for predicting values for  $K_{a,2}$  obtained from non-calorimetric methods are given in Table 5. Figure 3 shows  $K_{a,2}$  changing with temperature predicted by these three equations. The variation of the values for  $K_{a,2}$  is reduced to a range with the order of magnitude from  $10^{-17}$  to  $10^{-15}$  over a wide range of temperature.

Table 3 Values of the second dissociation constant  $K_{a,2}$  at 25 °C.

$K_{a,2}$ Value at 25 °C	Sources
$1.000 \times 10^{-19}$	Myers [29]
$8.710 \times 10^{-18}$	Kharaka [27]
$1.000 \times 10^{-17}$	Ellis [30]
$1.000 \times 10^{-16}$	Licht [31]
$1.000 \times 10^{-15}$	Skoog [32]
$1.585 \times 10^{-14}$	Stephens [33]
$1.200 \times 10^{-13}$	Wagman [34]
$1.000 \times 10^{-12}$	Su [35]

Table 4 Values for the second dissociation constant  $pK_{a,2}$  at 25 °C determined by non-calorimetric methodologies.

$pK_{a,2}$ value at 25°C	Methodology	Sources
$17 \pm 0.2$	UV absorption spectra	Giggenbach [37]
17	Spectrophotometric	Ellis [30]
$17 \pm 1.0$	Raman	Meyer [38]
$17.6 \pm 0.3$	pH measurement in highly concentrated alkaline solutions	Licht [39]
$17.4 \pm 0.3$	Extrapolation	Schoonen [40]
17.1	Calculated	Kharaka [27]
$17.1 \pm 0.3$	Differential densitometric analysis	Licht [[31]
$17.4 \pm 0.3$	Surface sulfidation of crystalline sulfur	Migdisov [36]

Table 5 Expressions for the second dissociation constant  $K_{a,2}$  determined by non-calorimetric methodologies from multiple sources.

Equations	Sources
$K_{a,2} = 10^{\frac{31286}{T_K} + 94.9734 \ln T_K - 0.097611 T_K - \frac{2.17087 \times 10^6}{T_K^2} - 607.722}$	Derived from Giggenbach [37]
$K_{a,2} = 10^{-(23.93 - 0.030446 T_K + 2.4831 \times 10^{-5} T_K^2)}$	Kharaka [27]
$K_{a,2} = 10^{(0.0646 T_K - 36.631)}$	Derived from Migdisov [36]

\*  $T_k$  is absolute temperature in Kelvin.

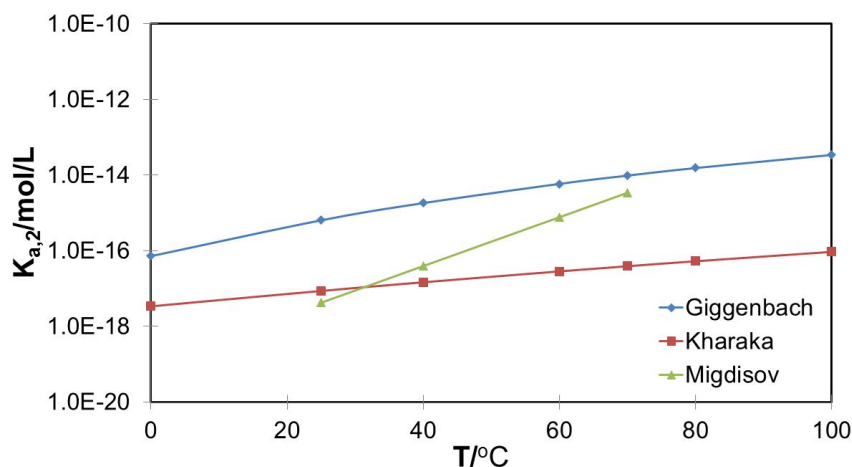


Figure 3. Temperature dependency of the second dissociation constant  $K_{a,2}$ .

## 2.4 Water Chemistry Modeling of an $H_2S$ - $H_2O$ System

The equilibrium concentrations of species present in the solution of a system, , can be predicted by a water chemistry model. One should define the type of system considered prior to modeling and calculating its water chemistry. In general, two types of systems are considered, which are *open* or *closed*. The water chemistry models of both open and closed  $H_2S$ - $H_2O$  systems is described below. The water chemistries predicted by these two models are then compared.

### 2.4.1 Definitions of Open System and Closed System

Examples of an open system and a closed system are given in Figure 4. The glass cell frequently used in the laboratory, which is continually purged with gas (for instance  $H_2S$ /balance  $N_2$  gas), is considered to be an open system. The autoclave shown in Figure 4, which is closed after initially purging with gas of designated partial pressures, is usually considered to be a closed system. The significant difference between these two systems is the constant  $H_2S$  partial pressure for an open system and the conservation of

moles of sulfur-species (includes sulfides in the gaseous and aqueous phases) for a closed system.

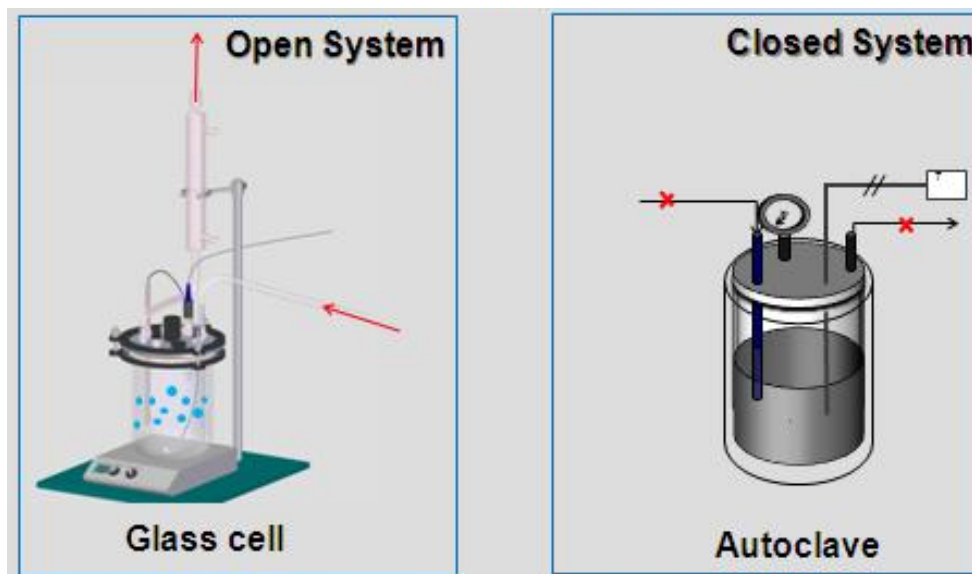
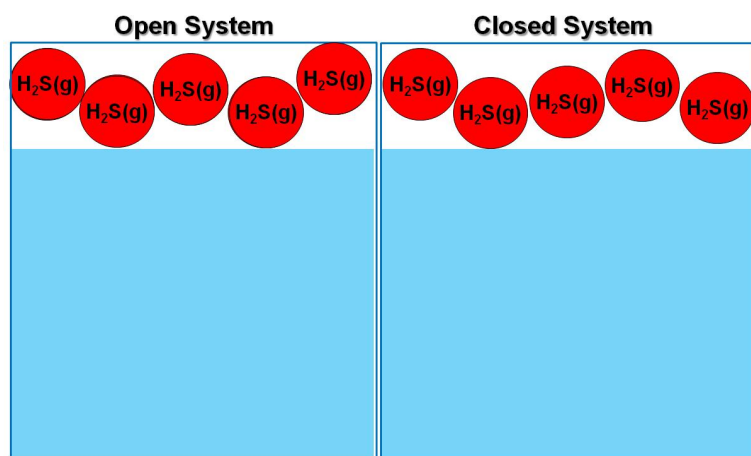


Figure 4. An open system vs. a closed system.

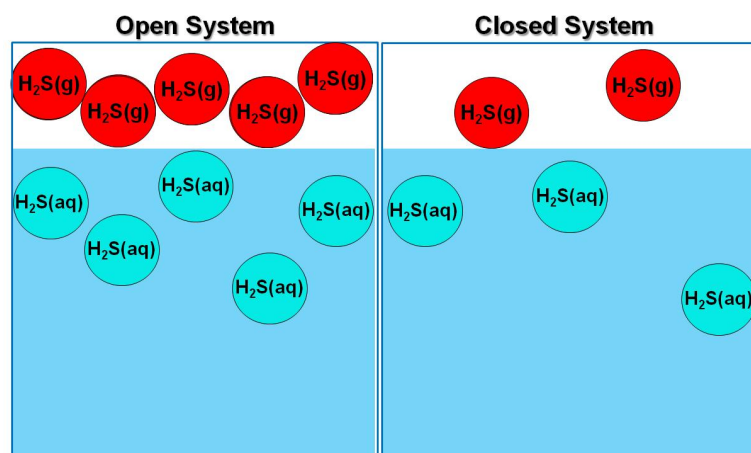
#### 2.4.2 Comparison of Water Chemistry between an Open System and a Closed System

The schematic in Figure 5 shows the processes of the dissolution of gaseous  $\text{H}_2\text{S}$  and its first and second dissociation steps in both an open and closed systems. Figure 5 (a) shows the initial conditions for both systems. For illustrative purposes, the same number of  $\text{H}_2\text{S}$  gas molecules (five) is shown in both systems; these represent the same initial  $\text{H}_2\text{S}$  partial pressure. Figure 5 (b) shows the dissolution of gaseous  $\text{H}_2\text{S}$ . In an open system, as shown in the left image of Figure 5 (b),  $\text{H}_2\text{S}$  partial pressure is constant, so the gaseous  $\text{H}_2\text{S}$  molecules dissolved into water would be replenished by an external reservoir (source). In the closed system shown in the right image of Figure 5 (b), the gaseous  $\text{H}_2\text{S}$  molecules dissolved into water is not replenished. The amount of gaseous  $\text{H}_2\text{S}$  molecules continually decreases until the equilibrium between concentrations of  $\text{H}_2\text{S}$

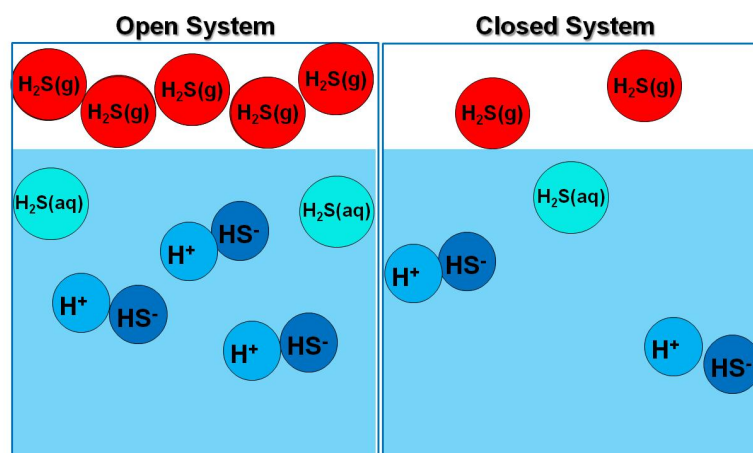
in the gaseous phase and aqueous phase is achieved. Figure 5 (c) and (d) show the first and second dissociation reactions of the dissolved  $\text{H}_2\text{S}$  for the two systems, which reach equilibrium. A constant amount of gaseous  $\text{H}_2\text{S}$  molecules in the gas phase is observed in the open system as shown in the final state (d), which indicates a constant  $\text{H}_2\text{S}$  partial pressure. However, a constant total amount of sulfide species is observed in the closed system, as shown in the final state (d), indicative of the constant total molar amount of sulfide species in a closed system.



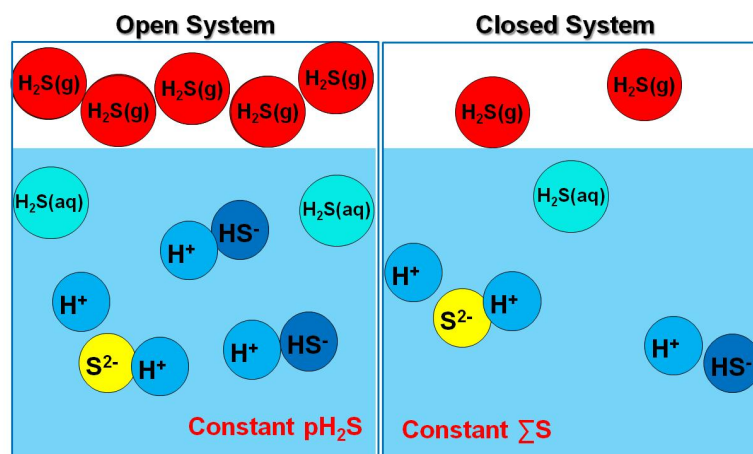
(a) The initial conditions



(b) Solubility



(c) The first dissociation



(d) The second dissociation and the final state

Figure 5. Graphical interpretation of water chemistry behavior in an open system vs. a closed system.

### 2.4.3 Establishment of Water Chemistry Model for an Open System and a Closed System

The well-known equilibrium reactions and equations used for calculating water chemistry for an  $\text{H}_2\text{S}$ - $\text{H}_2\text{O}$  open system are shown in Reaction (1) through to Equation (6). In addition, two more equations, water dissociation shown in Equations (7) and (8) as well as the overall electro-neutrality equation for the system shown in Equation (9), are also considered.



$$K_w = [H^+][OH^-] \quad (8)$$

$$[H^+] = [HS^-] + 2[S^{2-}] + [OH^-] \quad (9)$$

In total, there are six concentrations of species ( $pH_2S$ ,  $[H_2S]$ ,  $[HS^-]$ ,  $[S^{2-}]$ ,  $[OH^-]$ , and  $[H^+]$ ) considered as shown above. For an  $H_2S$ - $H_2O$  open system  $pH_2S$  is constant and usually known, hence, the remaining five concentrations are unknown. Five equations involving these five unknown concentrations of species are shown in Equation (2), (4), (6), (8), and (9). Accordingly, there is a system consisting of five equations involving five unknown variables. Therefore, these five unknown concentrations can be obtained as a solution of the set of equations.

Water chemistry for a closed system are calculated following a similar practice. A major difference from the open system is that  $H_2S$  partial pressure is allowed to change in a closed system, therefore, there is one more unknown variable,  $pH_2S$ , for the calculation of water chemistry of a closed system. In order to compute these six unknown concentrations of species in a closed system, one more equation related to these unknowns is needed. Thus, the conservation of moles of sulfide species, Equation (10), is added into the existing five equations for calculating water chemistry for an  $H_2S$ - $H_2O$  closed system.

$$N_{Sulfur,total} = V_g [H_2S_g]_{initial} = V_g [H_2S_g] + V_{aq} [H_2S_{aq}] + V_{aq} [HS^-] + V_{aq} [S^{2-}] \quad (10)$$

where  $V_g$  represents gaseous volume and  $V_{aq}$  represents aqueous volume in a closed system. The ratio of gaseous volume to aqueous volume in a closed system,  $\frac{V_g}{V_{aq}}$ , is considered to be a significant factor of the water chemistry.

#### 2.4.4 Comparison of Water Chemistry of an Open System and a Closed System

In order to illustrate the difference in water chemistry between an open system and a closed system, the expressions of different equilibrium constants,  $K_{H_2S}$ ,  $K_{a,1}$ , and  $K_{a,2}$  were arbitrarily selected for the modeling and calculations for both systems. The expression for the constant  $K_{H_2S}$  was taken from Suleimenov [20] as shown in Table 1, the expression for  $K_{a,1}$  was taken from Suleimenov [26] as shown in Table 2, and the expression for  $K_{a,2}$  was taken from Kharaka [27] as shown in in Table 5.

The computed equilibrium concentrations of species in an open system are shown as solid lines in Figure 6. The concentrations of  $[H_2S]_{aq}$  and  $[H_2S]_g$  are not dependent on pH in an open system due to  $H_2S$  gas being continually supplied. The species  $HS^-$  and  $S^{2-}$  could be dominant at very high pH values, such as pH values higher than 12.

In addition, the equilibrium concentrations in a closed system at the same conditions were calculated for comparison. The effect of using different values of  $\frac{V_g}{V_{aq}}$  in a closed system on the equilibrium concentrations was studied. First, a value of 1000/1 was used for  $\frac{V_g}{V_{aq}}$ , which simulates a scenario of gas transport line with a negligible amount of water. The equilibrium concentrations of species are shown as dashed lines in

Figure 6. It is observed that the equilibrium concentrations are quite similar to results for an open system, which suggests a closed system with a very small liquid phase can be treated as an open system. The equilibrium concentrations in a closed system with the ratio  $\frac{V_g}{V_{aq}}$  equal to 1 are shown as dotted lines in Figure 6. All concentrations decrease dramatically when pH is higher than 7. Finally,  $\frac{V_g}{V_{aq}}$  changed to 1/1000 representing a closed system with a very small gas phase, and the predicted equilibrium concentrations are shown as dashed-dotted lines in Figure 6. A significant decrease in all the equilibrium concentrations is noticed as compared to previous systems, and the concentrations decrease dramatically when pH is higher than 6. The water chemistry of a closed system greatly depends on the ratio of gaseous volume to aqueous volume in the closed system, and could be very different from the equivalent open system.

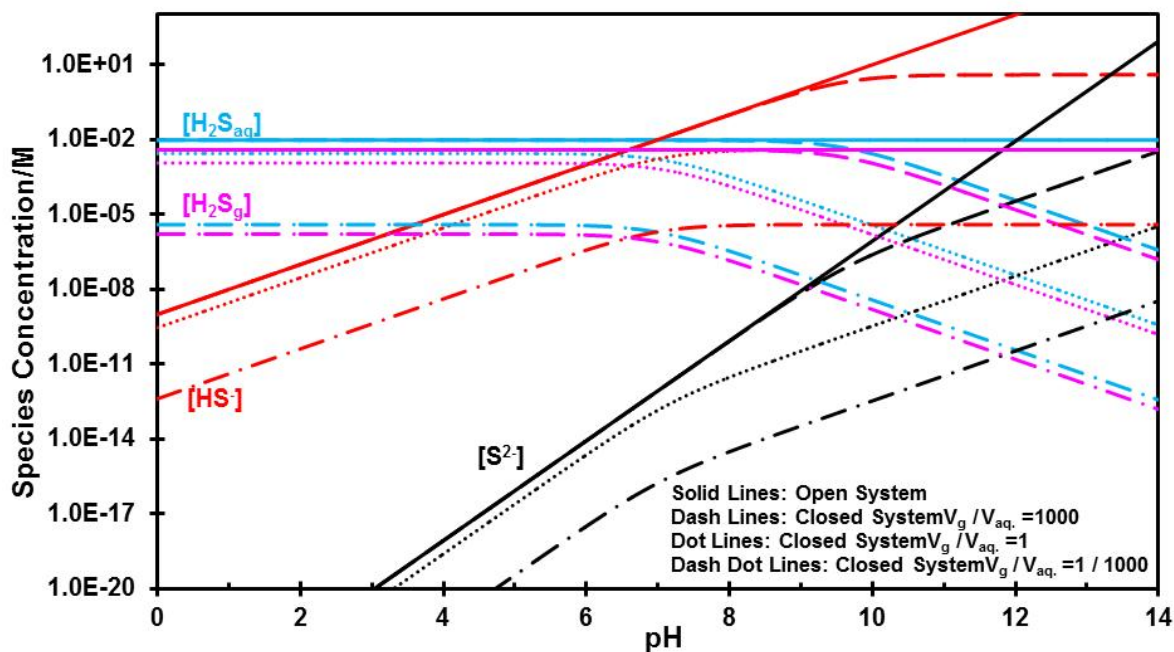


Figure 6. Equilibrium concentrations of species as a function of pH for open and closed H<sub>2</sub>S-H<sub>2</sub>O systems (T = 25 °C, p<sub>H<sub>2</sub>S</sub> = 0.1 bar).

## 2.5 Experimental Validation

As stated above, water chemistry models were built for both the open system and the closed system. Due to the inconsistencies of prevailing expressions for H<sub>2</sub>S solubility and dissociation constants, in the present study, a glass cell set-up with continuous sparging of H<sub>2</sub>S gas was used to validate the water chemistry model for an open system. The experimental pH values were measured for verification purposes to check literature expressions and values for  $K_{H_2S}$ ,  $K_{a,1}$  and  $K_{a,2}$ .

### 2.5.1 *Experimental*

#### 2.5.1.1 *Apparatus*

The experimental apparatus used for this investigation is shown in Figure 7. A magnetic stirring bar was used to mix solution at 400 rpm stirring speed during the experiment. A regular pH probe was used to measure bulk solution pH. The concentration of H<sub>2</sub>S in the mixed H<sub>2</sub>S/N<sub>2</sub> gas was adjusted by using a gas rotameter, and measured by a gas sample pump with H<sub>2</sub>S detector tubes. Sodium hydroxide (NaOH) solution and a carbon scrubber were used to remove H<sub>2</sub>S from the gas coming out of the glass cell.

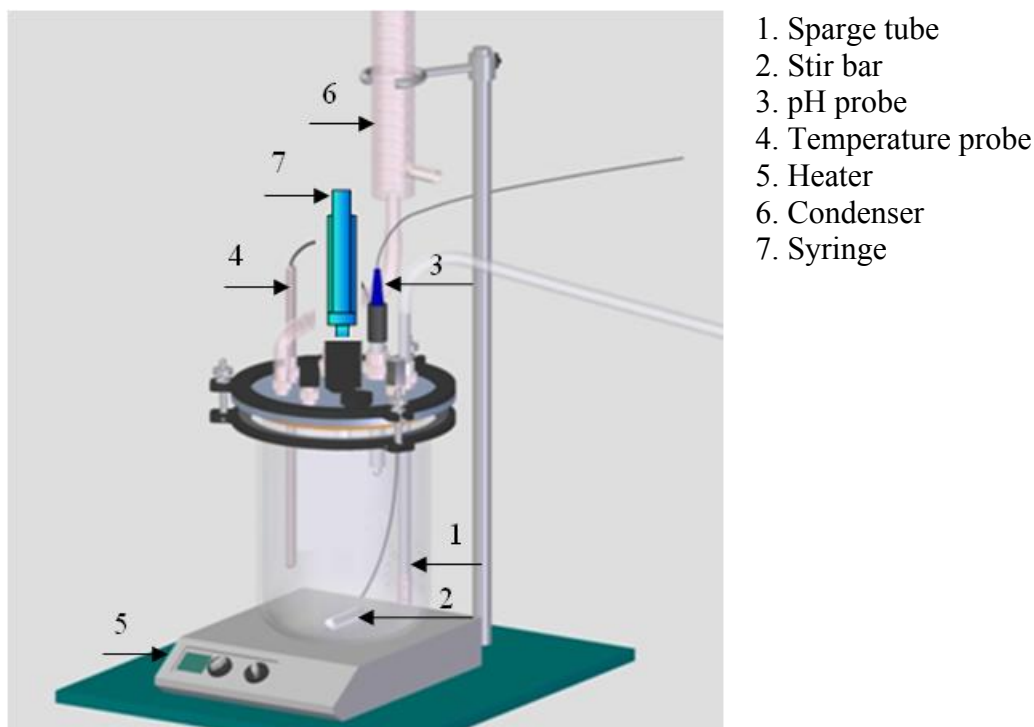


Figure 7. Experimental glass cell setup.

### 2.5.1.2 Procedure

The glass cell was filled with 2 liters of 1 wt. % NaCl (analytical grade) solution. Experiments were conducted after purging this solution with  $N_2$  until saturation (typically a few hours). The  $H_2S$  and  $N_2$  pre-mixed gas was then sparged into the solution at a desired partial pressure  $p_{H_2S}$ . After the pH value stabilized, another pre-mixed gas with higher  $p_{H_2S}$  was then sparged into the solution, and the process was repeated. Experiments were performed for  $H_2S$  concentrations ranging from 40 ppm ( $p_{H_2S} = 0.0387$  mbar at  $25^\circ C$ ) to 8000 ppm ( $p_{H_2S} = 7.75$  mbar at  $25^\circ C$ ) at  $25^\circ C$ ,  $60^\circ C$ , and  $80^\circ C$ .

The resolution of the pH meter display was 0.01 units, and the overall accuracy of the meter was  $\pm 0.02$  pH units. The pH meter/probe was checked using buffer solutions (pH 4.00 and pH 7.00) at the desired temperature prior to every usage, to ensure that any

pH drift was within  $\pm 0.01$  pH unit. Otherwise re-calibration was done at that temperature using the same pH buffer solutions (pH 4.00 and pH 7.00).

### 2.5.2 Results and Discussion

Expressions for  $\text{H}_2\text{S}$  solubility and dissociation constants were selected for incorporating into models, which were then experimentally validated to determine the best model for predicting water chemistry for a  $\text{H}_2\text{S}$ - $\text{H}_2\text{O}$  system.

Five prevalent equations used for predicting  $K_{\text{H}_2\text{S}}$  are listed in Table 1 and the curves as a function of temperature predicted by those equations are shown in Figure 1. It is clear that all the five predicted curves are in excellent agreement. Arbitrarily, the expression of Suleimenov [20] was selected for further use.

As shown in Figure 2, the curves of  $K_{\text{a},1}$  as a function of temperature predicted by Suleimenov [26] and Millero [28] are in agreement, but Kharaka [27] shows a different trend as temperature increases. Therefore, the Suleimenov [26] expression was selected arbitrarily from the two agreeing expressions (Suleimenov [26] and Millero [28]), and the Kharaka [27] expression was also selected to be used in two different versions of the pH prediction model in order to find the more appropriate expression for this equilibrium constant.

The large variation of the literature values for  $K_{\text{a},2}$  was reviewed in section 2.3.3. Any model used to predict pH is affected only slightly by this variation of  $K_{\text{a},2}$ , due to the fact that most of the hydrogen ions are formed by the first dissociation step (see Reaction (3)). The equation for  $K_{\text{a},2}$  proposed by Kharaka [27], as shown in Table 5, was used in the pH prediction models.

As discussed above, two pH value prediction models were obtained by combining these expressions for  $K_{H_2S}$ ,  $K_{a,1}$  and  $K_{a,2}$ , as shown in Table 6. Comparison of experimental pH with model predicted pH values at 25°C, 60°C and 80°C are shown in Figure 8, Figure 9, and Figure 10, respectively. The comparison shows clearly that Model 1 is superior to Model 2.

Table 6 Combinations of  $K_{H_2S}$ ,  $K_{a,1}$  and  $K_{a,2}$  in pH value prediction models.

Models	$K_{H_2S}$	$K_{a,1}$	$K_{a,2}$
Model 1	Suleimenov [20]	Suleimenov [26]	Kharaka [27]
Model 2	Suleimenov [20]	Kharaka [27]	Kharaka [27]

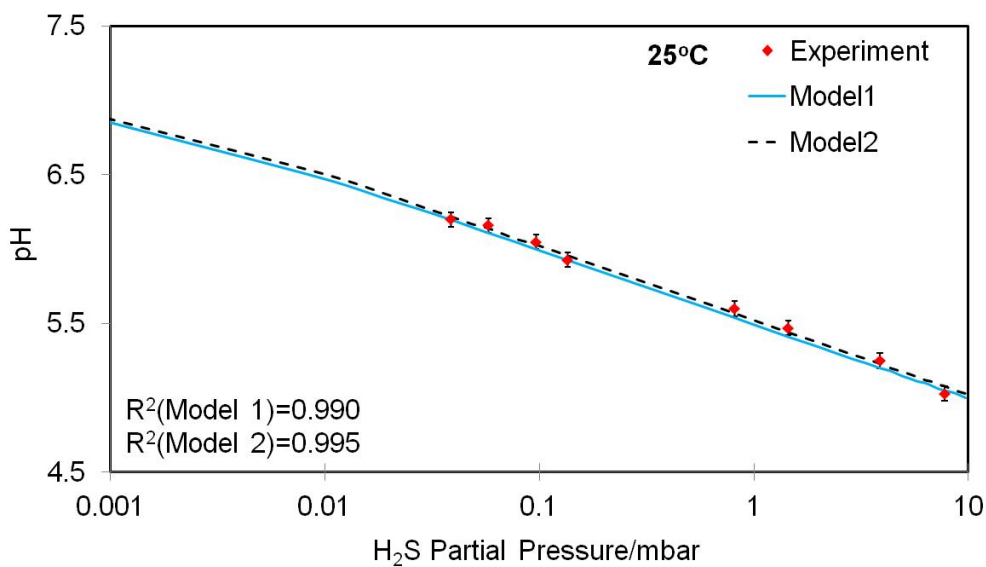


Figure 8. Comparison of experimental pH values with model predicted pH values at 25°C.

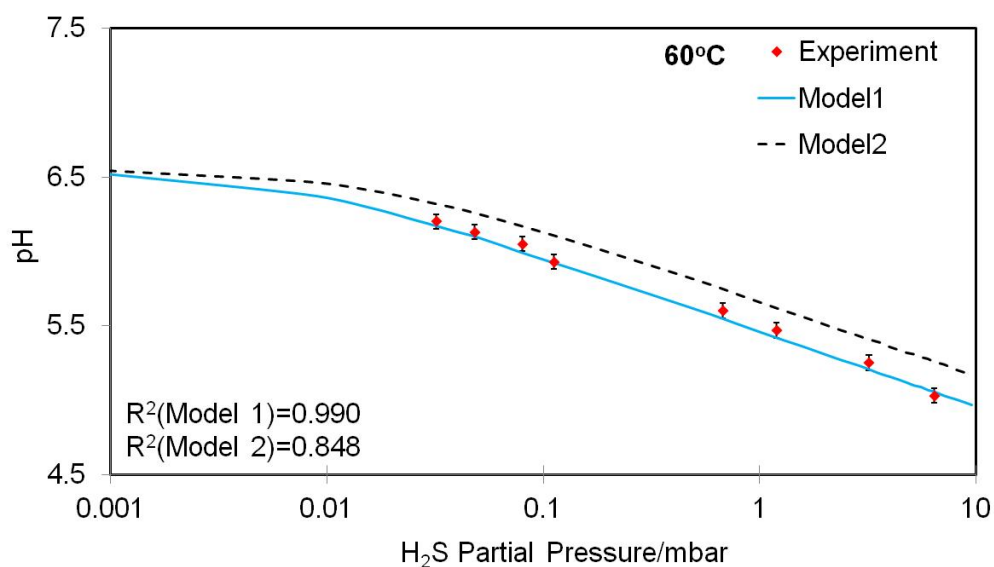


Figure 9. Comparison of experimental pH values with model predicted pH values at 60°C.

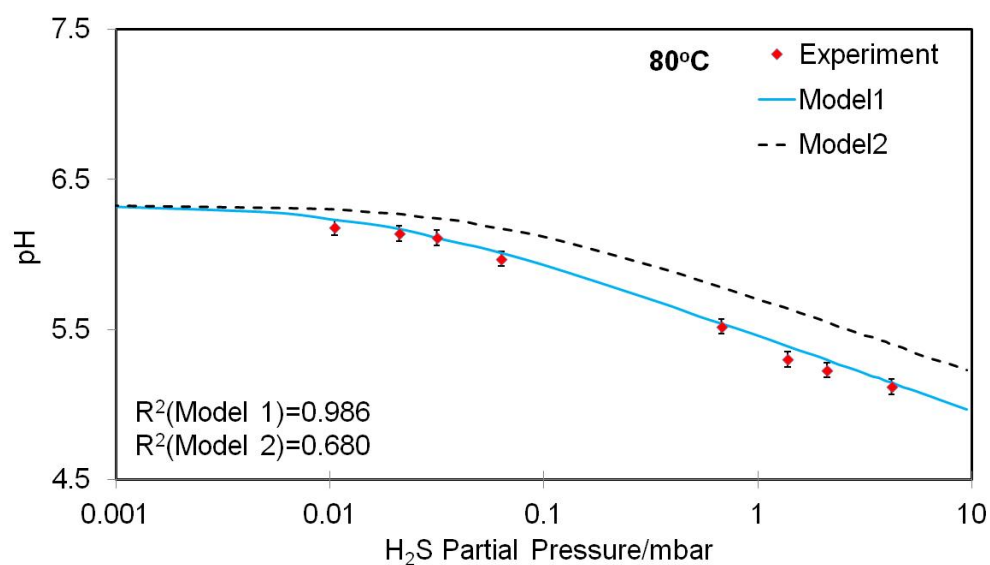


Figure 10. Comparison of experimental pH values with model predicted pH values at 80°C.

## 2.6 Summary

The published expressions for H<sub>2</sub>S solubility and dissociation constants were reviewed and evaluated in the present study. Expressions were selected for a model to

predict water chemistry of an H<sub>2</sub>S-H<sub>2</sub>O system. Experiments were conducted to verify a best model to predict water chemistry of an aqueous H<sub>2</sub>S system. Comparison of experimental pH values with predicted pH values based primarily on the correlations provided by Suleimenov (1994 & 1997) showed excellent agreement. Therefore, this model was selected to calculate water chemistry for H<sub>2</sub>S-H<sub>2</sub>O systems.

## CHAPTER 3. CHEMICAL THERMODYNAMICS OF H<sub>2</sub>S-H<sub>2</sub>O-Fe<sup>2+</sup> SYSTEM

### 3.1 Introduction

In Chapter 2, chemical thermodynamics of an H<sub>2</sub>S-H<sub>2</sub>O system was discussed, and a water chemistry model was developed to predict the equilibrium concentrations of species present. It is also necessary to investigate the more complicated H<sub>2</sub>S-H<sub>2</sub>O-Fe<sup>2+</sup> system, as ferrous ion (Fe<sup>2+</sup>) is present due to corrosion of mild steel. Moreover, when the product of the ferrous ion concentration and sulfide ion concentration exceeds the solubility limit of iron sulfide, iron sulfide polymorphs and related phases can form as corrosion products. These play an important role in the corrosion of the steel underneath [41]–[43]. Therefore, it is critical to know the solubility limits of various iron sulfides in order to predict their formation.

As a starting point, the existing solubility limits of various iron sulfides were reviewed to gain a better understanding of the formation and dissolution of a given iron sulfide layer, and how this may be related to its protectiveness. Experiments were then conducted involving addition of ferrous ions to H<sub>2</sub>S saturated solutions to investigate the formation and solubility limits of the precipitated iron sulfides formed at equilibrium.

### 3.2 Objectives

- Review literature relating to the formation and transformation of iron sulfides.
- Clarify discrepancies between existing expressions for solubility of iron sulfides and review their existing solubility values.
- Design novel experiments to measure solubility limits for iron sulfides formed in an aqueous H<sub>2</sub>S saturated system at various conditions (such as at different temperature, pH<sub>2</sub>S, and pH values).

### 3.3 Literature Review

#### 3.3.1 Polymorphism of Iron Sulfides

The characteristic that distinguishes iron sulfide from other corrosion products of mild steel, such as oxides (*i.e.* Fe<sub>2</sub>O<sub>3</sub>, Fe<sub>3</sub>O<sub>4</sub>), hydroxides (*i.e.* Fe(OH)<sub>2</sub>, Fe(OH)<sub>3</sub>), and iron carbonate (FeCO<sub>3</sub>), is its rich polymorphism. Various polymorphs of iron sulfide can form as corrosion products in H<sub>2</sub>S corrosion of mild steel. These include amorphous ferrous sulfide (FeS), mackinawite (FeS), cubic ferrous sulfide (FeS), troilite (FeS), pyrrhotites (Fe<sub>1-x</sub>S), smythite (Fe<sub>3+x</sub>S<sub>4</sub>), greigite (Fe<sub>3</sub>S<sub>4</sub>), pyrite (FeS<sub>2</sub>) and marcasite (FeS<sub>2</sub>) [3]–[5]. Select physicochemical properties of each are listed in Table 7.

Table 7 Polymorphous iron sulfides.

Name	Chemical Formula	Crystal Structure	Properties
Amorphous	FeS	nano-crystalline	unstable, converts into mackinawite quickly
Mackinawite	FeS	tetragonal, 2D layer	metastable, the initial corrosion product
Cubic FeS	FeS	cubic	very unstable, can transform into mackinawite, troilite or pyrrhotite, never found naturally
Troilite	FeS	hexagonal	stoichiometric end member of the Fe <sub>1-x</sub> S group(x=0)
Pyrrhotite	Fe <sub>1-x</sub> S (x = 0 to 0.17)	monoclinic Fe <sub>7</sub> S <sub>8</sub> or hexagonal Fe <sub>10</sub> S <sub>11</sub>	thermodynamically stable, the most abundant iron sulfide
Smythite	Fe <sub>3+x</sub> S <sub>4</sub> (x = 0 to 0.3)	trigonal-hexagonal	metastable, related to the Fe <sub>1-x</sub> S group
Greigite	Fe <sub>3</sub> S <sub>4</sub>	cubic	metastable spinel-type sulfide
Pyrite	FeS <sub>2</sub>	cubic	thermodynamically stable iron disulfide, the most abundant mineral
Marcasite	FeS <sub>2</sub>	orthorhombic	metastable, present in hydrothermal system and sedimentary rocks

In older scientific literature mackinawite is called hydrotroilite, kansite [44], precipitated FeS, amorphous FeS, and tetragonal FeS [45]. Berner [46] confirmed that XRD patterns of such iron sulfides are identical. Evans *et al.* [47] proposed the term

“mackinawite” for this type of iron sulfide because it was found as a mineral from the Mackinaw Mine in Snohomish County, Washington in 1964. It is broadly agreed that mackinawite is the initial iron sulfide formed in H<sub>2</sub>S corrosion of mild steel due to its fast formation kinetics. Rickard [48] designed a novel apparatus that is able to accurately assess the kinetics of the initial 130 ms of precipitation of mackinawite. By using this apparatus, Rickard [49] reported that the rate of initial precipitation of mackinawite at room temperature from the reaction between ferrous ion and sulfide species is only dependent on the total concentration of sulfide species with a first-order reaction rate constant of  $48 \pm 9 \text{ s}^{-1}$ .

However, mackinawite is a thermodynamically metastable product. Thus, it can transform into more thermodynamically stable iron sulfides such as greigite (Fe<sub>3</sub>S<sub>4</sub>), cubic ferrous sulfide (FeS), troilite (FeS), pyrrhotite (Fe<sub>1-x</sub>S), smythite (Fe<sub>3+x</sub>S<sub>4</sub>), pyrite (FeS<sub>2</sub>), and marcasite (FeS<sub>2</sub>) at favored conditions [3]–[5]. The formation and transformation of iron sulfides is a complex process determined by both thermodynamics and kinetics. There are many mechanistic steps relating to iron sulfide formation and transformation that remain unclear, even unknown. Smith and Wright [50], [58] proposed a conceptual corrosion product diagram shown in Figure 11, used to qualitatively predict iron sulfide products at oilfield conditions. Accordingly, mackinawite, pyrrhotite, and pyrite are predicted to form with increasing H<sub>2</sub>S concentration. The iron sulfide reaction pathways proposed by Smith and Miller [5], as well as Morse [13], in corrosion systems, are frequently used in H<sub>2</sub>S corrosion research. Note that Figure 12 shows mackinawite formed initially, converting to pyrrhotite group, pyrite, marcasite and greigite under appropriate conditions.

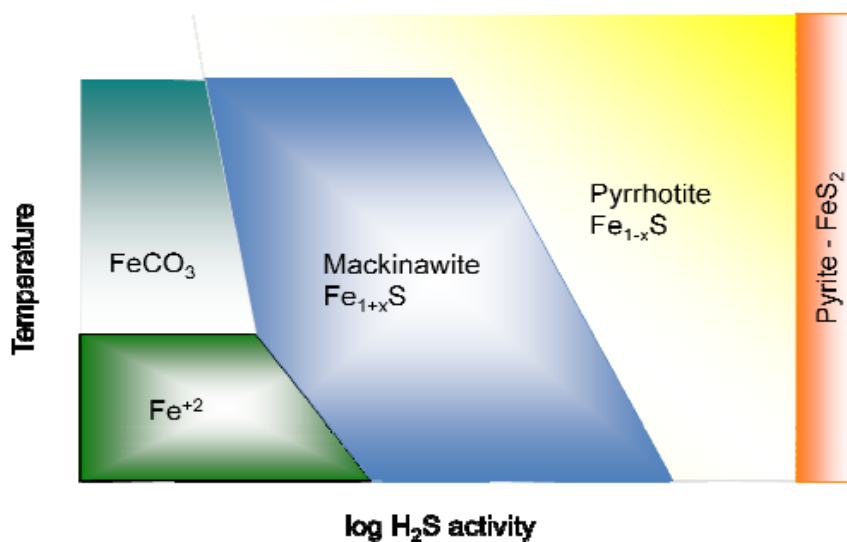


Figure 11. Conceptual corrosion product diagram (reproduced from [58]).

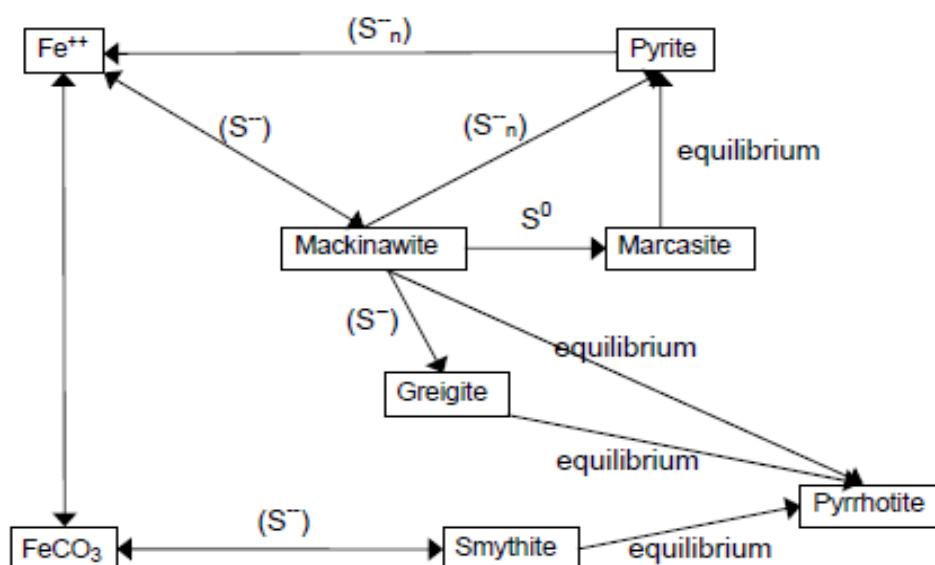


Figure 12. Iron sulfide reaction pathways from Smith and Miller [5], and Morse *et al.*[13].

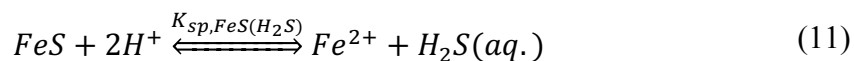
### 3.3.2 The Various Expressions for Solubility Limit of Iron Sulfides

When it comes to even the most basic chemical descriptors of solubility of iron sulfides, there are significant discrepancies between expressions for solubility from

various sources. Moreover, typos, misunderstandings, and mistakes are seen in the open literature. Mackinawite is taken as an example, and the expressions for the solubility limit of mackinawite are reviewed first. In general, the solubility limit of mackinawite can be expressed based on different reaction equilibria [3].

### 3.3.2.1 H<sub>2</sub>S Expression

The reaction for the formation of mackinawite involving aqueous H<sub>2</sub>S is shown in Reaction (11). The corresponding equilibrium constant of this reaction, also known as the solubility limit of mackinawite or solubility product constant (K<sub>sp</sub>), is given by Equation (12). This expression for the solubility limit of mackinawite is called the “H<sub>2</sub>S based expression” or “H<sub>2</sub>S expression”.



$$K_{sp,FeS(H_2S)} = \frac{[Fe^{2+}][H_2S]}{[H^+]^2} \quad (12)$$

### 3.3.2.2 HS<sup>-</sup> Expression

Similarly, the reaction of mackinawite formation involving HS<sup>-</sup> and its associated equilibrium constant expression is shown in Reaction (13) and Equation (14), respectively. The solubility limit of mackinawite expressed in Equation (14) is the so-called “HS<sup>-</sup> expression”.



$$K_{sp,FeS(HS^-)} = \frac{[Fe^{2+}][HS^-]}{[H^+]} \quad (14)$$

### 3.3.2.3 S<sup>2-</sup> Expression

In addition, the formation of mackinawite can also be expressed as shown in Reaction (15), involving S<sup>2-</sup>. The equilibrium constant that corresponds to this reaction is shown in Equation (16). This expression for the solubility limit of mackinawite is called the “S<sup>2-</sup> expression”. However, due to the uncertainty of K<sub>a,2</sub>, its use, should be avoided. The huge uncertainty of K<sub>a,2</sub> (10<sup>-12</sup> to 10<sup>-19</sup> mol/L even at 25°C) makes it hard to compare values for K<sub>sp,FeS(S<sup>2-</sup>)</sub> between various sources if one does not know which K<sub>a,2</sub> value is used.



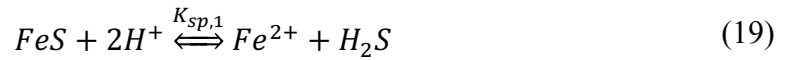
$$K_{sp,FeS(S^{2-})} = [Fe^{2+}][S^{2-}] \quad (16)$$

The expressions for the solubility limit of mackinawite based on different reaction equilibria can be converted into each other by using the H<sub>2</sub>S first dissociation constant K<sub>a,1</sub> shown in Equation (4) and the H<sub>2</sub>S second dissociation constant K<sub>a,2</sub> shown in Equation (6). Accordingly, one can obtain:

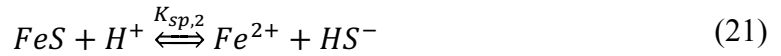
$$K_{sp,FeS(HS^-)} = K_{sp,FeS(H_2S)}K_{a,1} \quad (17)$$

$$K_{sp,FeS(S^{2-})} = K_{sp,FeS(HS^-)}K_{a,2} = K_{sp,FeS(H_2S)}K_{a,1}K_{a,2} \quad (18)$$

In order to simplify the analysis,  $K_{sp,1}$  and  $K_{sp,2}$  were adopted to represent  $K_{sp,FeS(H_2S)}$  and  $K_{sp,FeS(HS^-)}$ , respectively [14]. The reaction equilibria and expressions for defining  $K_{sp,1}$  and  $K_{sp,2}$  are shown below (19) – (22). These two expressions for solubility of iron sulfides ( $K_{sp,1}$  and  $K_{sp,2}$ ) are used in the present work.



$$K_{sp,1} = \frac{[Fe^{2+}][H_2S]}{[H^+]^2} \quad (20)$$



$$K_{sp,2} = \frac{[Fe^{2+}][HS^-]}{[H^+]} \quad (22)$$

One needs to clearly state the specific equilibrium reactions and expressions before using them for calculating of the solubility of mackinawite (i.e.  $H_2S$  expression,  $HS^-$  expression, or  $S^{2-}$  expression). However, in much of the literature, the solubility of mackinawite is described as  $K_{sp}$  or  $K_{sp,FeS}$  without specifying the actual reaction equilibria employed.

### 3.3.3 The Solubility Limit of Iron Sulfides

Mackinawite forms initially as a corrosion product layer on mild steel surfaces during H<sub>2</sub>S corrosion, and then may provide protectiveness to the steel underneath. Therefore, knowing the solubility limit of mackinawite is critical to predicting mackinawite layer formation and the resultant corrosion rate of steel.

Several researchers have proposed solubility limit constants for mackinawite at 25 °C; selected values for  $K_{sp,2}$  from different literature sources are summarized in Table 8. Only Benning [15] proposed an equation relating solubility of mackinawite to temperature as shown in Equation (23). One should be aware that Benning's equation for the solubility of mackinawite is based on the H<sub>2</sub>S expression. Her equation can be converted into the HS<sup>-</sup> expression, that is  $K_{sp,2}$ , as shown in Equation (24).

Table 8  $pK_{sp,2}$  values for mackinawite from literature at 25 °C.

$pK_{sp,2}$ of mackinawite at 25°C	Author
2.95	Berner [16]
3.55	Morse [13]
2.94	Theberge [17]
3.77	Benning [15]
3.5	Rickard [14]

$$K_{sp,1} = 10^{\frac{2848.779}{T_k} - 6.347} \quad (23)$$

$$K_{sp,2} = 10^{\frac{2848.779}{T_k} - 6.347 + \log(K_{a,1})} \quad (24)$$

Variation of the values for the  $pK_{sp,2}$  listed in Table 8 can be observed, though it appears not to be significant. To better appreciate how this kind of variation may affect the prediction of formation of the mackinawite layer, a specific environment was defined (25 °C,  $p_{H_2S} = 0.97$  mbar,  $[Fe^{2+}] = 10$  ppm, pH = 6.0) and saturation values were calculated using Equation (25) and by using the various  $pK_{sp,2}$  values for mackinawite, as shown in Table 8. Calculated saturation values for the given condition are shown in Figure 13.

$$S = \frac{\frac{C_{Fe^{2+}} C_{HS^-}}{C_{H^+}}}{K_{sp,2}} \quad (25)$$

Note the variation of saturation values observed from Figure 13, due to differences in solubility product constants proposed by the various authors. According to Berner [16] and Theberge [17], the solution is close to saturation and the driving force for mackinawite precipitation is small. However, according to Benning [15], mackinawite saturation value is high and precipitation would readily occur. Saturation values based upon  $pK_{sp,2}$  values from Rickard [14] and Morse [13] lie somewhere in between. This indicates that further work is needed to confirm the best expression for  $K_{sp,2}$  of mackinawite.

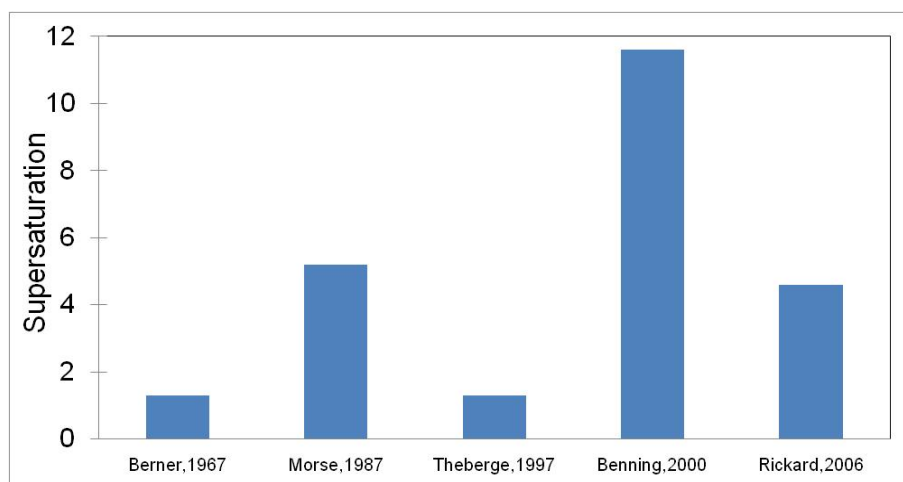


Figure 13. Calculated saturation values using  $pK_{sp,2}$  values in Table 8 for the selected environment ( $25\text{ }^{\circ}\text{C}$ ,  $p_{H_2S} = 0.97\text{ mbar}$ ,  $[\text{Fe}^{2+}] = 10\text{ ppm}$ ,  $\text{pH} = 6.0$ ).

In addition, Davison [51] reviewed and summarized the best estimates of  $pK_{sp,2}$  values at  $25\text{ }^{\circ}\text{C}$  for many types of iron sulfides as shown in Table 9. Amorphous FeS and mackinawite have the smallest  $pK_{sp,2}$  values, suggesting they are the most soluble. Analogously, the largest value for  $pK_{sp,2}$  is pyrite, as shown in Table 9, therefore, the most sparingly soluble iron sulfide is pyrite.

Table 9 Best estimates of  $pK_{sp,2}$  values for polymorphous iron sulfides at  $25\text{ }^{\circ}\text{C}$  [51].

Iron Sulfide	$pK_{sp,2}$
Amorphous (FeS)	$2.95 \pm 0.1$
Mackinawite (FeS)	$3.6 \pm 0.2$
Pyrrhotite ( $\text{Fe}_{1-x}\text{S}$ )	$5.1 \pm 0.15$
Troilite (FeS)	$5.25 \pm 0.2$
Greigite ( $\text{Fe}_3\text{S}_4$ )	$13.2 \pm 0.3$
Pyrite ( $\text{FeS}_2$ )	$16.4 \pm 1.2$

### 3.4 Experimental

The work here initially focused on the solubility limit of mackinawite, as it forms first as a corrosion product and, due to its metastability, can transform into other types of iron sulfide.

#### 3.4.1 Apparatus

The experimental apparatus used in this part of the study is shown in Figure 7. A syringe was used to add a deoxygenated ferrous chloride solution into the glass cell or to take sample solution from the glass cell.

#### 3.4.2 Methodology

A method based on pH variation was used to judge if reaction equilibria were reached during precipitation and dissolution. From the iron sulfide reaction given by Equation (21), the pH value should be stable when this reaction reaches equilibrium. In these experiments, it was considered to be the case when pH values varied by less than 0.01 units over a one hour time period. Dissolved iron concentration was measured spectrophotometrically and the hydrogen ion concentration was determined from the pH value measured at equilibrium. The bisulfide ion concentration was predicted from the previously verified H<sub>2</sub>S-H<sub>2</sub>O thermodynamic prediction model for hydrogen sulfide solubility and dissociation. The  $K_{sp,2}$  value was calculated by Equation (22) at equilibrium.

#### 3.4.3 Procedure

In the experiments, nitrogen was sparged into the 1 wt. % NaCl electrolyte until pH stabilized, and then the H<sub>2</sub>S / N<sub>2</sub> pre-mixed gas was introduced into the glass cell until saturation was achieved. Deoxygenated ferrous chloride solution was then injected into

the glass cell. As no precipitation was typically observed, a deoxygenated 1.0 M sodium hydroxide was injected to increase pH and induce precipitation. The experiment was then left unperturbed and its pH value monitored. A deoxygenated 1.0 M hydrochloric acid (HCl) was then gradually injected into the glass cell to facilitate dissolution of an existing precipitate. This process was repeated to obtain other equilibrium points during precipitation and dissolution of various iron sulfides. Samples of the solution were taken from the glass cell and a 0.45  $\mu\text{m}$  syringe filter was used to separate the precipitate from the solution before measuring ferrous ion concentration spectrophotometrically. The separation process was performed by filtration in an oxygen-free environment using a glove box. Recovered solid precipitate was dried in a nitrogen environment before XRD analysis. The test matrix is shown in Table 10.

Table 10 Test matrix.

Description	Parameter
Temperature	25°C, 60°C
Solution	1 wt. % NaCl brine
Purge gas	H <sub>2</sub> S/balance N <sub>2</sub>
H <sub>2</sub> S concentration	200 ppm, 1000 ppm in gas phase
Stirring speed	400 rpm
Total [Fe]	0.01M

### 3.5 Results and Discussion

#### 3.5.1 Measured $pK_{sp,2}$ Values of Iron Sulfide Formed at 25 °C

Three groups of experiments were conducted to measure  $pK_{sp,2}$  of formed iron sulfide: at 200 ppm H<sub>2</sub>S with adding HCl to facilitate dissolution of precipitate, at 1000 ppm H<sub>2</sub>S with adding HCl and at 200 ppm H<sub>2</sub>S without adding HCl. The results for the

200 ppm with adding HCl are shown in Figure 14. It was observed that measured  $pK_{sp,2}$  values increased during the experiments starting at 2.87, then continued increasing to around 3.5. It was assumed that the  $pK_{sp,2}$  value increased due to iron sulfide type changing. Precipitate filtered from the glass cell when  $pK_{sp,2}$  was 3.48 was sent for X-ray diffraction to confirm this hypothesis.

Mackinawite, sulfur, and lepidocrocite were detected by XRD, as shown in Figure 15. The precipitate ( $pK_{sp,2}$  was 3.48) was totally black when it was filtered and dried, but the surface color turned yellow/brown when it was taken out for analysis. Craig [52] and Bourdoiseau *et al.* [53] found the same: a mackinawite oxidation process, as given by Reaction (26). Mackinawite was readily oxidized to form lepidocrocite and sulfur when it was exposed to an oxygen-containing environment.

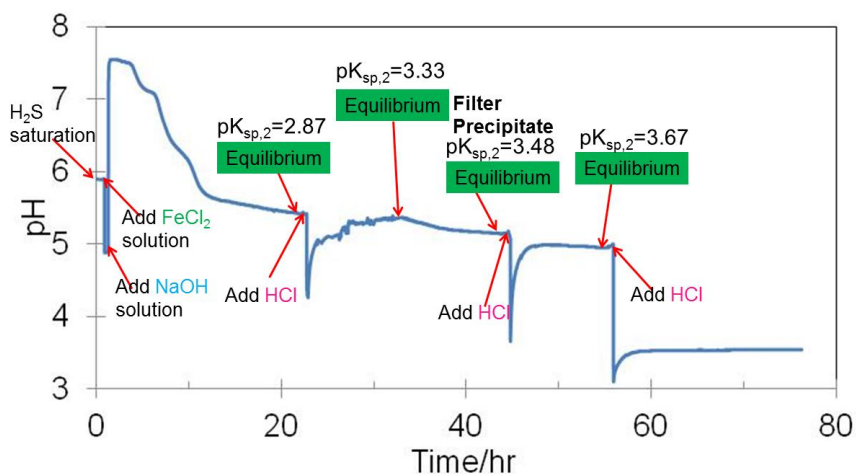


Figure 14. Measured  $pK_{sp,2}$  at 200 ppm  $H_2S$  with adding HCl at 25 °C.

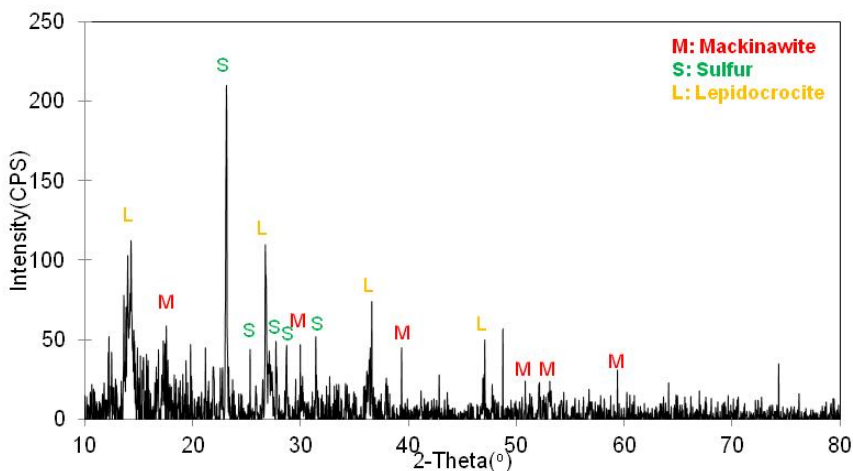


Figure 15. XRD of precipitate ( $pK_{sp,2}$  was 3.48).

The result for the experiment using 1000 ppm  $H_2S$  also indicates that the  $pK_{sp,2}$  value increased during the experiment, from 2.96 initially to 3.41. One more experiment for 200 ppm  $H_2S$  without adding HCl to dissolve the precipitate was performed to check whether the increased  $pK_{sp,2}$  value was related to time of exposure or pH value. The result is shown in Figure 16. The same phenomenon was observed, and  $pK_{sp,2}$  increased during experiments even though no hydrochloric acid was added to adjust the pH. The data from these three experiments were combined and shown in Figure 17. The precipitate when  $pK_{sp,2}$  was 3.48 at 200 ppm  $H_2S$  was confirmed to be mackinawite by XRD. The three experiments shown in Figure 17 were consistent with the review by Davison [51]. Davison [51] reviewed the best estimates of  $pK_{sp,2}$  at  $25^\circ C$  as shown in Table 9, and confirmed that amorphous iron sulfide formed within one to six hours of exposure time. The present results suggest that amorphous iron sulfide was formed initially ( $pK_{sp,2} = 2.95 \pm 0.1$ ), and then converted to mackinawite ( $pK_{sp,2} = 3.6 \pm 0.2$ ).

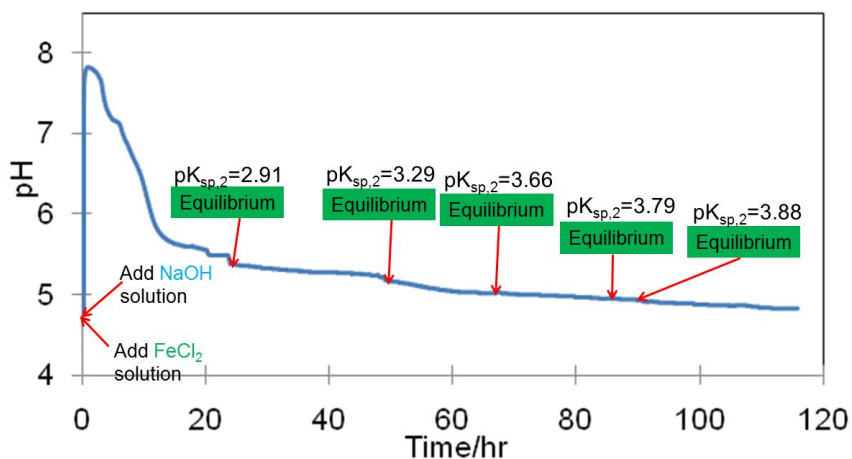


Figure 16. Measured  $pK_{sp,2}$  at 200 ppm  $H_2S$  without adding HCl at 25 °C.

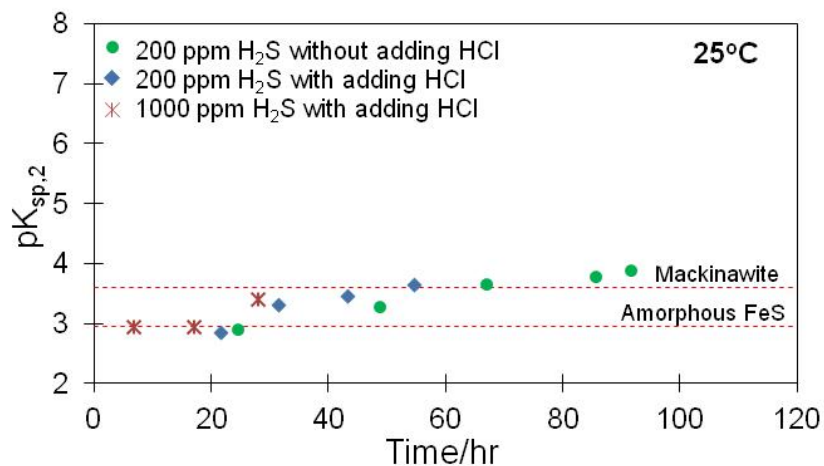


Figure 17. Summary of time dependence of  $pK_{sp,2}$  at 25 °C.

### 3.5.2 Measured $pK_{sp,2}$ Values of Iron Sulfide Formed at 60 °C

Experiments were also conducted at 60 °C with 200 ppm  $H_2S$  and 1000 ppm  $H_2S$ . The result of the 200 ppm  $H_2S$  experiments is shown in Figure 18 and the repeated experiment is shown in Figure 19. It is easy to observe that  $pK_{sp,2}$  values can be divided into two groups: the “3 group” (with values clustered around  $pK_{sp,2} \approx 3$  shown by green highlights) and the “6 group” (with values clustered around  $pK_{sp,2} \approx 6$  and shown by blue highlights in Figure 18 and Figure 19). It was assumed that the  $pK_{sp,2}$  value difference

was due to iron sulfide type changing, but whether this change was truly related to the pH value or an artifact of the experimental duration and sequence was unclear. Deoxygenated sodium hydroxide solution was added to adjust pH values from 3.3 to 5.0 and  $pK_{sp,2}$  value decreased from 6.92 to 3.88 at the last point in Figure 19, which confirmed that  $pK_{sp,2}$  value change was due to the pH value. The precipitate filtered from the glass cell when  $pK_{sp,2}$  was measured to be 3.02 and 3.88 in Figure 19 was analyzed by X-ray diffraction. Both greigite and pyrite were detected in these two samples, as shown in Figure 20 and Figure 21, with greigite being dominant.

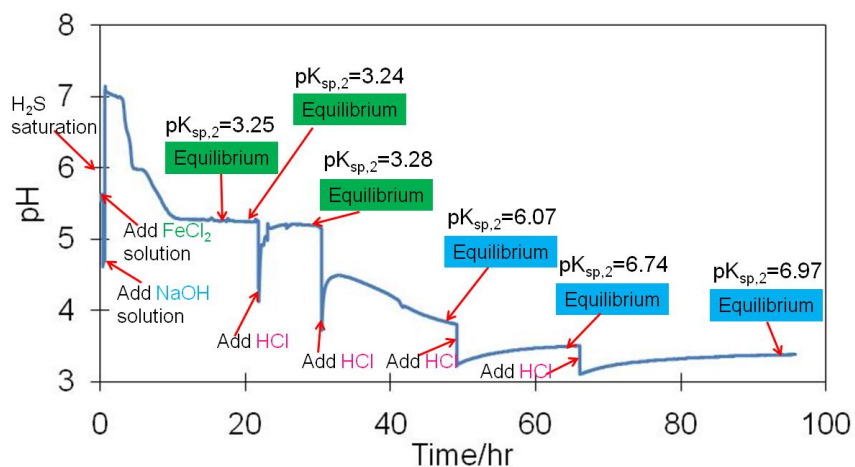


Figure 18. Measured  $pK_{sp,2}$  at 200 ppm  $H_2S$  with adding HCl at 60 °C.

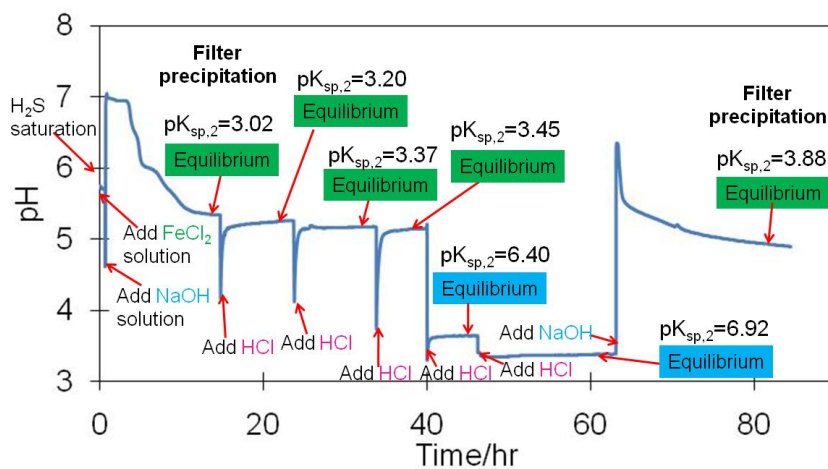


Figure 19. Measured  $pK_{sp,2}$  at 200 ppm  $H_2S$  with adding HCl/NaOH at 60 °C.

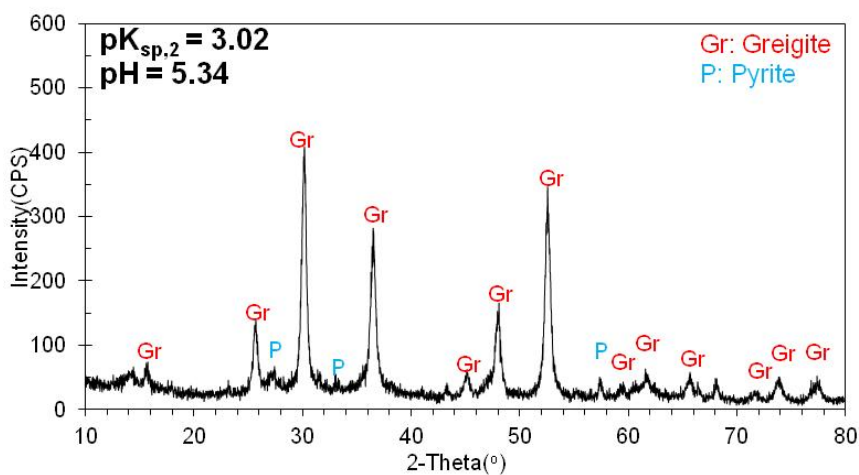


Figure 20. XRD of precipitate ( $pK_{sp,2}$  was 3.02).

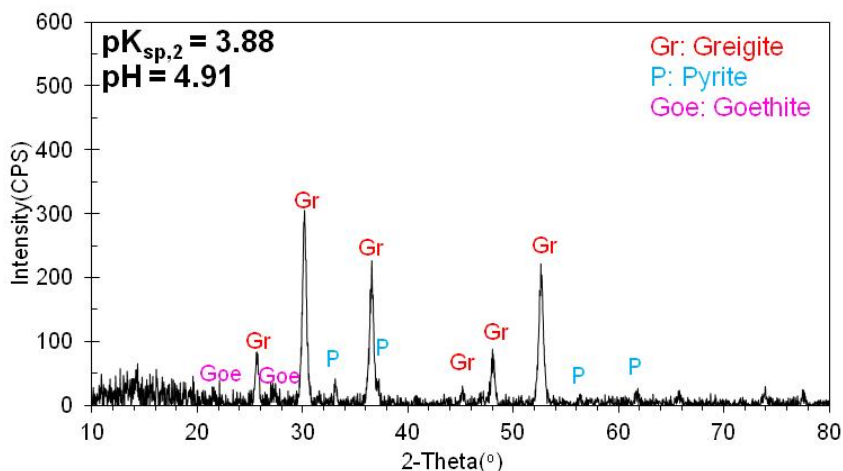


Figure 21. XRD of precipitate ( $pK_{sp,2}$  was 3.88).

The results for 1000 ppm  $H_2S$  are shown in Figure 22 and the repeated experiment is shown in Figure 23. It was also observed that the  $pK_{sp,2}$  values differed between the “3 group” shown with green highlights and the “6 group” shown with blue highlights in Figure 22 and Figure 23. The precipitate was filtered for analysis, taken when  $pK_{sp,2}$  was 6.45, as shown in Figure 22, and taken when  $pK_{sp,2}$  was 6.30, as shown in Figure 23. The XRDs of the precipitate are shown in Figure 24 and Figure 25, respectively. The XRD data with  $pK_{sp,2}$  values of 6.45 and 6.30 showed that both precipitates were a mixture of greigite and pyrite with the latter being dominant. Therefore, it is postulated that pyrite is dominant for  $pK_{sp,2}$  value “6 group” precipitates.

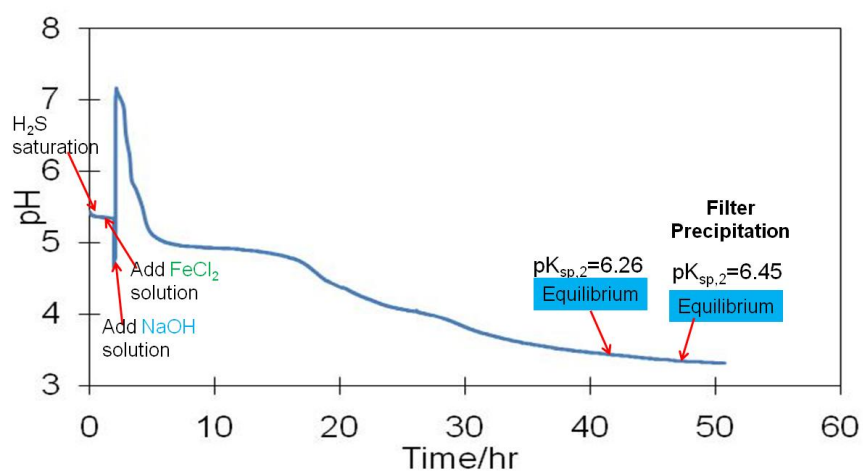


Figure 22. Measured  $pK_{sp,2}$  at 1000 ppm  $H_2S$  without adding HCl at 60 °C.

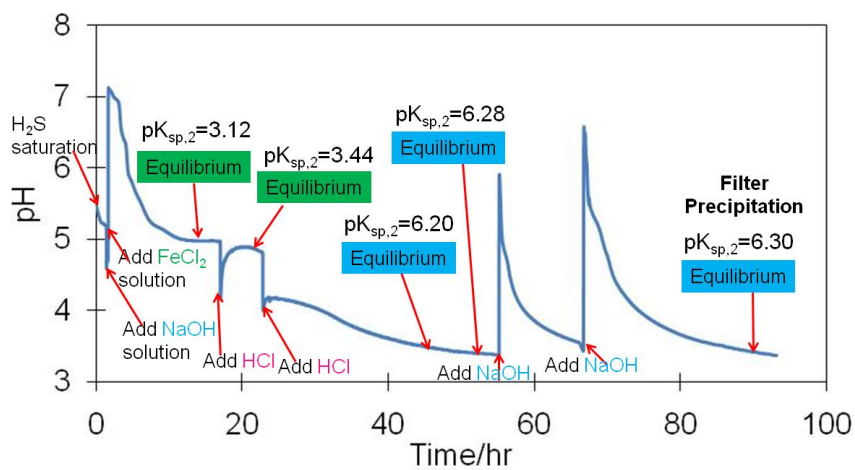


Figure 23. Measured  $pK_{sp,2}$  at 1000 ppm  $H_2S$  with adding HCl/NaOH at 60 °C.

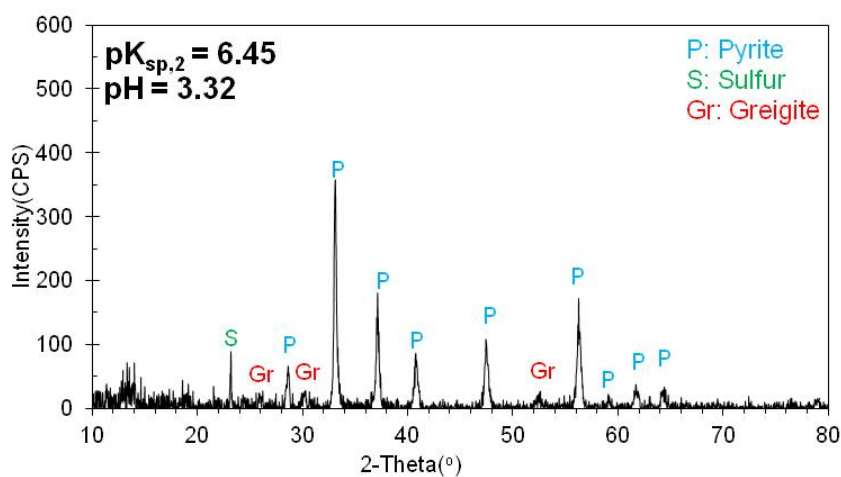


Figure 24. XRD of precipitate ( $pK_{sp,2}$  was 6.45).

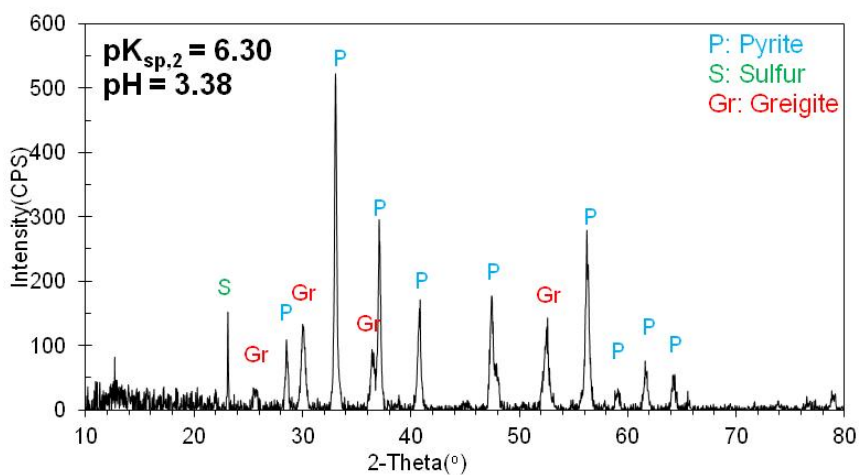
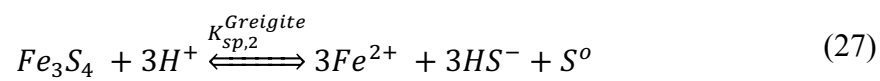


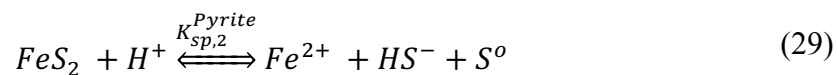
Figure 25. XRD of precipitate ( $pK_{sp,2}$  was 6.30).

### 3.5.3 Recalculation of $pK_{sp,2}$ Values of Greigite and Pyrite

Solubility reactions of greigite ( $Fe_3S_4$ ) and pyrite ( $FeS_2$ ) are written as Reaction (27) and Reaction (29) according to Berner [16], Morse [13], Davison [51], and Rickard [54].



$$K_{sp,2}^{Greigite} = \left( \frac{[Fe^{2+}][HS^{-}]}{[H^{+}]} \right)^3 \quad (28)$$



$$K_{sp,2}^{Pyrite} = \frac{[Fe^{2+}][HS^{-}]}{[H^{+}]} \quad (30)$$

The  $pK_{sp,2}$  values were recalculated as Equation (28) and Equation (30) shown for greigite and pyrite, respectively. The recalculation of  $pK_{sp,2}$  values were plotted with pH value and shown in Figure 26. Two groups can be seen from Figure 26: pyrite formed around pH 3.5 and greigite formed around pH 5.0.

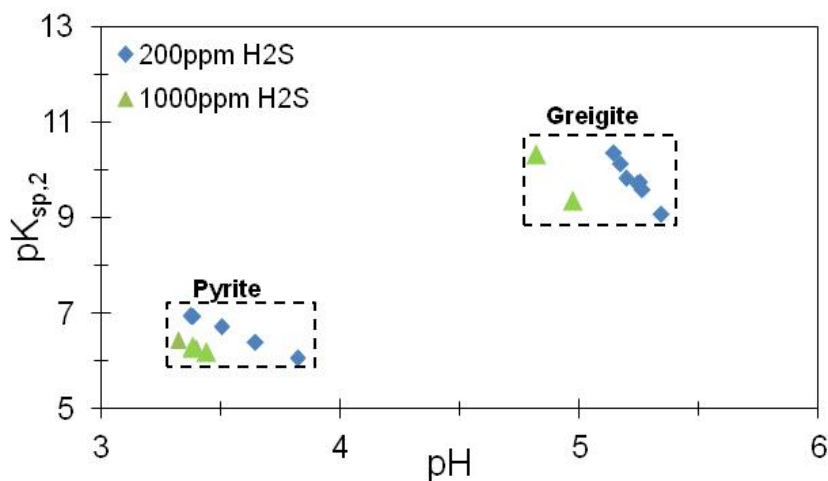


Figure 26. Summary of pH-recalculated  $pK_{sp,2}$  at 60 °C.

### 3.6 Summary

Due to the inconsistencies in existing values for solubility limits of iron sulfides in the literature, the solubility of iron sulfide was measured in experiments. At 25°C, the measured  $K_{sp,2}$  values were observed to increase with time, due to iron sulfide type changing. It is believed that amorphous iron sulfide formed at the beginning, and then converted into mackinawite. Corresponding  $pK_{sp,2}$  of mackinawite at 25°C was measured as  $3.6 \pm 0.2$ . Polymorphs of iron sulfides (pyrite and greigite) were observed in the  $H_2S$ - $H_2O$ - $Fe^{2+}$  system at 60°C. For the investigated condition greigite was dominant around pH 5 with corresponding  $pK_{sp,2}$   $9.8 \pm 0.5$ , while pyrite was dominant around pH 3.5 with  $pK_{sp,2}$   $6.5 \pm 0.5$ .

## CHAPTER 4. ELECTROCHEMICAL THERMODYNAMICS OF THE H<sub>2</sub>S-H<sub>2</sub>O- FE SYSTEM

### 4.1 Introduction

Chemical thermodynamics of the H<sub>2</sub>S-H<sub>2</sub>O system and the H<sub>2</sub>S-H<sub>2</sub>O-Fe<sup>2+</sup> system were described in Chapter 2 and Chapter 3, respectively, and provided a fundamental base for further study of H<sub>2</sub>S corrosion of mild steel in an H<sub>2</sub>S-H<sub>2</sub>O-Fe system. In fact, in H<sub>2</sub>S corrosion of mild steel, polymorphous and related iron sulfides such as amorphous iron sulfide (FeS), mackinawite (FeS), cubic ferrous sulfide (FeS), troilite (FeS), pyrrhotites (Fe<sub>1-x</sub>S), smythite (Fe<sub>3+x</sub>S<sub>4</sub>), greigite (Fe<sub>3</sub>S<sub>4</sub>), pyrite (FeS<sub>2</sub>), and marcasite (FeS<sub>2</sub>) have been found in facilities exposed to H<sub>2</sub>S in the oil and gas industry [58]. These phases have also been detected as corrosion products of mild steel in previously reported small and large scale laboratory tests [8], [59]–[61]. Furthermore, these iron sulfides are reported to either retard [41]–[43] or promote [62], [63] corrosion due to their different physicochemical properties. However, in many of published modeling studies, only the mackinawite layer (the initial corrosion product in sour environments) has been considered, for reasons of simplicity [7], [56]. Therefore, there is a need to investigate the influence of iron sulfide polymorphism on corrosion and incorporate this effect into simulation models.

However, the formation and transformation of the polymorphous iron sulfides is a complex process, which is governed by both thermodynamics and kinetics. A Pourbaix diagram, also known as potential-pH stability diagram, has been frequently used to map the corrosion product stability from a thermodynamic perspective. The Pourbaix diagram is one of the most prominent contributions to corrosion science made by M. Pourbaix

[64], [65]. One can make valuable inferences for practical purposes from a Pourbaix diagram, including developing corrosion mitigation strategies, defining cathodic protection, and designing critical corrosion tests with higher efficiency [66]. In fact, one can find a number of thermodynamic models, in the form of Pourbaix diagrams for sour systems, in both the open literature and derived from the proprietary commercial packages [67]–[70]. However, significant discrepancies among these models have been found, which are attributed to variations in the choice of the underlying thermodynamic data, selection of chemical species and chemical reactions considered, and different assumptions adopted for calculations (for example: open system vs. closed system), making it hard for corrosion engineers to use them. Moreover, the unknown background details pertaining to commercial software packages used for generation of Pourbaix diagrams makes it harder for corrosion engineers to understand and interpret the results they produce. Thus, in the present work, development of the calculations underlying Pourbaix diagrams for mild steel corrosion in  $H_2S$  environments is shown, covering typical conditions seen in the oil and gas industry. The diagrams are based on open literature data and are presented in a simple way, making it easier for corrosion engineers to understand and interpret them.

Considering the relatively narrow corrosion focus in this study, development of Pourbaix diagrams for corrosion of mild steel in aqueous  $H_2S$  solutions is shown below in a stepwise fashion, accompanied by a complete account for all the assumptions, underlying thermodynamic data, and reaction mechanisms.

## 4.2 Classification of Polymorphous Iron Sulfide in H<sub>2</sub>S Corrosion of Mild Steel

As stated above, polymorphous iron sulfides can form including amorphous iron sulfide (FeS), mackinawite (FeS), cubic ferrous sulfide (FeS), troilite (FeS), pyrrhotites (Fe<sub>1-x</sub>S), smythite (Fe<sub>3+x</sub>S<sub>4</sub>), greigite (Fe<sub>3</sub>S<sub>4</sub>), pyrite (FeS<sub>2</sub>), and marcasite (FeS<sub>2</sub>) [3]–[5]. Bouet [67] developed Pourbaix diagrams for the H<sub>2</sub>S-H<sub>2</sub>O-Fe system with iron sulfides FeS, FeS<sub>2</sub>, and Fe<sub>2</sub>S<sub>3</sub>. Ueda [68] generated Pourbaix diagrams for the H<sub>2</sub>O-CO<sub>2</sub>/H<sub>2</sub>S-Fe system with FeS and FeS<sub>2</sub>. Anderko [69], [70] referred to a commercial software package used to calculate and plot Pourbaix diagrams including amorphous iron sulfide, mackinawite, greigite, marcasite, pyrite, and stoichiometric pyrrhotite. Discrepancies between Pourbaix diagrams representing the same species associated with sour corrosion from these authors are due to variations in the sources of thermodynamic data, the different types of iron sulfides considered, and the diversity of reactions considered. Therefore, considering the relatively narrow corrosion focus in this study, the iron sulfides found in sour systems in the oil and gas industry have been classified in order to generate relatively simple Pourbaix diagrams dedicated to internal pipeline corrosion in sour environments.

### 4.2.1 Amorphous Iron Sulfide (FeS)

Amorphous iron sulfide can only be detected by X-ray diffraction as broadened low-intensity peaks, so usually it is assumed that it lacks any sort of significant long-range order (crystallinity). Kornicker [71] found that the physical properties of amorphous iron sulfide changed after drying, which might indicate that amorphous iron sulfide is a hydrate. Wolthers [72] used low angle X-ray powder diffraction (LAXRPD) to determine that “amorphous iron sulfide” is nanocrystalline mackinawite with an

average particle size of  $2.2 \pm 1.7$  nm. Rickard *et al.* [73], [74] concluded that “amorphous FeS” does not exist. They also stated that “amorphous iron sulfide”, which first precipitates from bulk solution, is nanocrystalline mackinawite, and confirmed that it is not hydrated by using nuclear magnetic resonance (NMR) spectroscopy and thermogravimetric analysis (TGA).

#### 4.2.2 Mackinawite (FeS)

Mackinawite is widely considered to be the initial corrosion product in H<sub>2</sub>S corrosion due to its rapid formation kinetics, which then converts into other iron sulfides depending on environmental conditions. The crystal structure of mackinawite consists of 2D layers, as shown in Figure 27 (a). The composition of mackinawite is usually stated as iron rich, Fe<sub>1+x</sub>S (x = 0 to 0.11). Berner [16] reported Fe<sub>0.91</sub>S, Sweeney [75] found Fe<sub>1.09-1.15</sub>S, Ward [76] reported Fe<sub>0.995-1.023</sub>S, and Lennie and Vaughan [77] proposed Fe<sub>0.99±0.02</sub>S. Rickard [54] suggested that the reasons for previous researchers obtaining the composition of mackinawite as iron rich, Fe<sub>1+x</sub>S, are due to an analytical artifact relating to the presence of other metals in mineralogical samples. Rickard [73] measured the composition of mackinawite as stoichiometric FeS.

Field experience [78], [79] and laboratory experiments [8], [18], [41]–[43], [80] show that mackinawite is the dominant corrosion product in most oil and gas pipeline operation conditions up to 90 °C.

#### 4.2.3 Cubic Iron Sulfide (FeS)

The crystal structure of cubic iron sulfide is shown in Figure 27 (b). De Medicis [81] determined that cubic FeS did not form in the presence of oxygen or chlorides. Murowchick [82] also found that it can only crystallize at temperatures < 92 °C and pH 2

~ 6 in 4 to 85 hours, with its formation impeded by the presence of chlorides. Smith [6] concluded that cubic iron sulfide is a transitional product that degrades into mackinawite, troilite, or pyrrhotite over several days and that it is not a major constituent of any long-term corrosion product; it has only been observed in the laboratory, so it is not expected to be found in field conditions.

Cubic FeS has been detected in so-called top-of-the-line corrosion (TLC) [60], where pure condensed water is present. It can be excluded from the current study which primarily focuses on the so-called bottom-of-the-line corrosion, where chlorides are normally present in the produced water.

#### 4.2.4 Pyrrhotite ( $Fe_{1-x}S$ ( $x = 0$ to $0.17$ )) and Troilite ( $FeS$ )

Pyrrhotite is actually a non-stoichiometric group of iron sulfides with formulae corresponding to  $Fe_{1-x}S$  ( $x = 0$  to  $0.17$ ), where troilite is the stoichiometric end member of the pyrrhotite group when  $x = 0$  ( $FeS$ ). The crystal structures of pyrrhotite and troilite are shown in Figure 27 (c) and (d). Pyrrhotite and troilite are thermodynamically stable; they can co-exist below  $150^{\circ}C$  [83]. Troilite and pyrrhotite are differentiated only because the crystals that nucleate seem to initially grow differently at temperatures below  $150^{\circ}C$ . Troilite can be viewed as low temperature and stoichiometric pyrrhotite. A variety of different pyrrhotites have been observed with different values of  $x$  resulting in changes in the unit cells of each. Liu *et al.* [84] studied corrosion products of X52 pipeline steel in a sour environment containing 1.61 MPa  $H_2S$  at  $90^{\circ}C$  with increasing exposure time from 2 hours to 10 days. They found that the corrosion products transformed from initial mackinawite to stoichiometric troilite, and finally to hexagonal pyrrhotite.

Pyrrhotite and troilite are frequently found in pipelines with moderate to high concentrations of hydrogen sulfide, and pyrrhotite is much more often observed [79]. The formation of pyrrhotite in a sour environment simulating typical pipeline conditions usually takes a few days of exposure (*i.e.* 3 to 5 days) [18], [79].

#### 4.2.5 Smythite ( $Fe_{3+x}S_4$ ( $x = 0$ to $0.3$ ))

Smythite is the least studied iron sulfide and has not been reported as a corrosion product [6], so it can be excluded from this study.

#### 4.2.6 Greigite ( $Fe_3S_4$ )

The crystal structure of greigite is shown in Figure 27 (e). Greigite is thermodynamically metastable; Lennie [77] noted that greigite is often present as an intermediary between the initial corrosion product, mackinawite, and the final product, pyrite. Ning *et al.* [80] detected greigite by addition of ferrous ions into an H<sub>2</sub>S saturated aqueous system at 60 °C and by corrosion of pipeline steel API 5L X65 in an H<sub>2</sub>S saturated aqueous system at 80 °C [18]. Bai *et al.* [85] studied transformation of corrosion products of X 52 mild steel in an aqueous sour environment with 1Mpa H<sub>2</sub>S at 50 °C. The transformations of both mackinawite and cubic iron sulfide phases into the greigite phase were observed in their experiments using TEM, leading to their conclusions that the greigite plays an important role as a transitional phase in transformation of iron sulfide phases.

#### 4.2.7 Pyrite ( $FeS_2$ )

Pyrite is the most abundant sulfide mineral in nature, and is also known as "fool's gold". The lattice crystal structure of pyrite is shown in Figure 27 (f). Pyrite and

pyrrhotite are the most stable iron sulfides, and considered to be the corrosion products seen after long exposures.

Ning *et al.* [18] detected corrosion product layers composed of mackinawite, pyrrhotite, and pyrite after four days of exposure with 0.05 bar H<sub>2</sub>S at 80 °C. They also noted that the percentage of pyrite grew from 2 % after four days of exposure to 17 % after seven days using XRD quantitative analysis. This growth is significant, and may suggest rapid kinetics of the growth of pyrite crystals after initial sluggish nucleation. A corrosion product layer consisting of mackinawite, pyrrhotite or troilite, and covered by a thin outer layer of pyrite, is frequently seen in gas fields containing high H<sub>2</sub>S concentrations [78].

#### 4.2.8 Marcasite (FeS<sub>2</sub>)

Marcasite is compositionally identical to pyrite, but structurally different. Benning [15] reported the absence of marcasite under both reducing and oxidizing conditions in corrosion testing. Marcasite is not a typical corrosion product, and the publications related to marcasite are primarily in the geologic literature, such as the work of Schoonen [86] and Murowchick [82]. There is no clear evidence that marcasite appears in corrosion environments, so marcasite is not taken into consideration here to be relevant in corrosion studies.

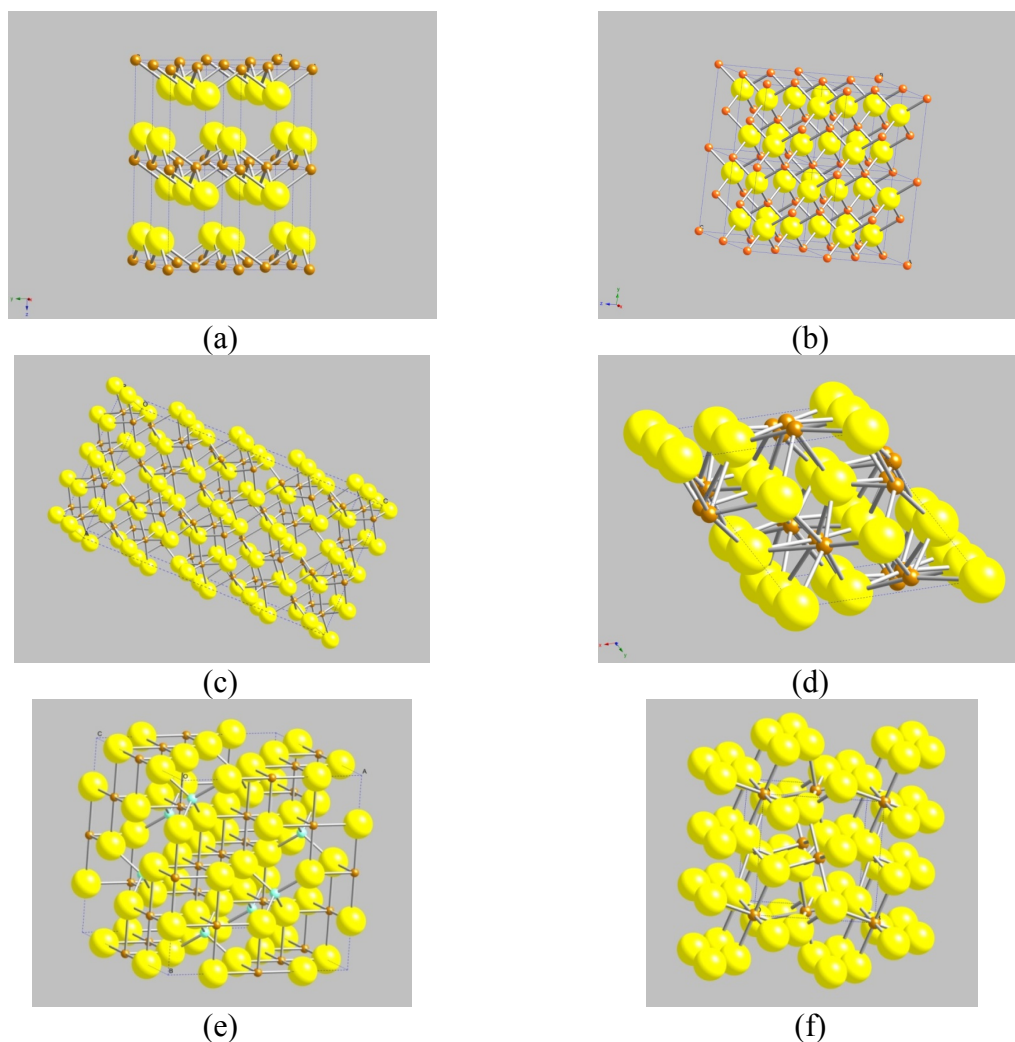


Figure 27. Crystal structures of: (a) Mackinawite; (b) Cubic iron sulfide; (c) Pyrrhotite; (d) Troilite; (e) Greigite; (f) Pyrite generated by CrystalMaker<sup>1</sup>.

#### 4.2.9 Summary

The polymorphous character of iron sulfides have been classified above primarily based on whether they were found in corrosion of mild steel in oil and gas systems. This was done in order to generate relatively simple Pourbaix diagrams dedicated to internal pipeline corrosion environments. In summary: the iron sulfides that have been taken into

---

<sup>1</sup> Trade name.

consideration for generating Pourbaix diagrams below are: mackinawite, pyrrhotite, greigite, and pyrite.

### 4.3 Thermodynamic Background

It is noteworthy that some important assumptions were made here when constructing the Pourbaix diagrams shown below. Only ideal behavior of aqueous solutions was considered in the present work, for reasons of simplicity. Also, only an open system was considered in this study, meaning that the partial pressure of H<sub>2</sub>S is considered to be constant across the whole pH range and potential range (and needs to be given as an input value). This is in contrast to most of the Pourbaix diagrams found in the open literature [69], [70], [87]–[89] for similar conditions, which were constructed for a closed system where the total amount of sulfur species is considered to be constant. This leads to a different water speciation particularly in the high pH range, and consequently a different appearance of the Pourbaix diagram.

#### 4.3.1 Electrochemical Thermodynamics

Corrosion is an electrochemical process that includes reduction and oxidation reactions. From the first and second law of thermodynamics the following reaction can be written:

$$\Delta G + zFE = \Delta \tilde{G} \quad (31)$$

where,  $\Delta G$  represents the Gibbs energy change of a chemical reaction,  $zFE$  represents the electrical energy, and  $\Delta \tilde{G}$  represents the total Gibbs energy change of an

electrochemical reaction. At electrochemical equilibrium,  $\Delta\tilde{G} = 0$ , and Equation (31) becomes,

$$\Delta G = -zFE_{rev} \quad (32)$$

where  $E_{rev}$  represents the reversible potential at equilibrium.

After transformation, the Nernst equation is obtained to calculate  $E_{rev}$  of an electrochemical reaction at equilibrium for any given set of conditions,

$$E_{rev} = E_{rev}^o - \frac{RT}{zF} \sum_{i=1}^k \ln (c_i)^{n_i} \quad (33)$$

where  $E_{rev}^o$  represents the standard reversible potential which is defined at unit concentrations, reference temperature, and reference pressure. It can be computed from,

$$E_{rev}^o = -\frac{\Delta G_r^o}{zF} \quad (34)$$

where  $\Delta G_r^o$  represents the Gibbs energy change of the electrochemical reaction.

For example, the iron deposition/dissolution reaction is an electrochemical reaction shown by Equation (35). The Gibbs energy change of reaction (35) is expressed in Equation (36).



$$\Delta G_r^{\circ} = G_{Fe}^{\circ} - G_{Fe^{2+}}^{\circ} - 2G_{e^{-}}^{\circ} \quad (36)$$

The standard reversible potential of reaction (35),  $E_{rev(Fe^{2+}/Fe)}^{\circ}$ , is calculated by Equation (34), and then it is substituted into Equation (33) to calculate reversible potential of the reaction (35),  $E_{rev(Fe^{2+}/Fe)}$ .

$$E_{rev(Fe^{2+}/Fe)} = E_{rev(Fe^{2+}/Fe)}^{\circ} + \frac{RT}{2F} \ln (c_{Fe^{2+}}) \quad (37)$$

For a pure chemical reaction, where there is no electron exchange in the reaction the equilibrium condition can be written as the Van't Hoff equation:

$$\Delta G_r^{\circ} = -RT \sum_{i=1}^k \ln (c_i)^{n_i} \quad (38)$$

In summary, it is necessary to know the Gibbs energy change of an electrochemical reaction ( $\Delta G_r^{\circ}$ ) in order to obtain the equilibrium line of the reaction in a Pourbaix diagram. Therefore, the Gibbs energy of formation for each species involved in the reaction is needed to construct Pourbaix diagrams. The Gibbs energy of formation for most species at reference temperature, 25 °C, can be found in the open literature.

Since thermodynamic properties are very sensitive to temperature, but relatively insensitive to pressure [66], the effect of increasing pressure on thermodynamic properties is neglected in this study. Therefore, the Gibbs energy of formation for species at elevated temperature,  $G_{T,P}^o$ , is calculated following Equation (39), which is a temperature dependent function of the Gibbs energy of formation at 298.15 K,  $G_{298.15}^o$ , heat capacity,  $C_p$ , and standard molar entropy at 298.15 K,  $S_{298.15}^o$ .

$$G_{T,P}^o = G_{298.15}^o + \int_{298.15}^T C_p dT - T \int_{298.15}^T \frac{C_p}{T} dT - (T - 298.15) \cdot S_{298.15}^o \quad (39)$$

The Gibbs energy of formation and standard molar entropy for most species at reference temperature can be found in the open literature. The heat capacity of various species can be predicted as a function of temperature by using Equation (40):

$$C_p = a + bT + cT^{-2} + dT^2 + eT^{-0.5} \text{ J/mol/K} \quad (40)$$

where  $a, b, c, d, e$  are constants that can be found in the open literature.

It should be noted that the Gibbs energy for the electron is also considered in this work. Since the Gibbs energy of formation for aqueous  $H^+$  is defined as zero at any temperature [90], [91], the Gibbs energy for the electron is considered to be half of Gibbs energy for hydrogen gas, shown by Equation (41) [90], [92]:

$$G(e) = 0.5G(H_2) \quad (41)$$

### 4.3.2 Thermodynamic Data

For most of the species, thermodynamic data such as the standard Gibbs energy at 25 °C,  $G_{298.15}^\circ$ , the standard molar entropy,  $S_{298.15}^\circ$ , and heat capacity,  $C_p$ , are mainly collected from the literature. However, thermodynamic properties for mackinawite and greigite cannot be found in the literature, because these two compounds are not thermodynamically stable, thereby, making experimental measurements hard to perform. Therefore, the heat capacities and entropies for these two species are estimated by following certain principles.

#### 4.3.2.1 Thermodynamic Data Compiled from the Literature

Thermodynamic data for the aqueous, solid, and gaseous species considered here, were compiled from various sources. For some species the thermodynamic data compiled from various sources were consistent. If  $H_2S_{(g)}$  is taken as an example, Figure 28 (a) shows that the data for  $S_{298.15}^\circ$  from various sources [93]–[101] are in good agreement. The average value is  $205.7 \pm 0.1$  J/mol/K. Heat capacity for  $H_2S_{(g)}$  was predicted using five different models [93], [95]–[97], [101], as shown in Figure 28(b). Within the temperature range 298 K - 1800 K, agreement between the different models was exceptionally good. The data for  $S_{298.15}^\circ$  and  $C_p$  for  $H_2S_{(g)}$  from O. Knacke *et al.* [95] were selected for further use in the present study.

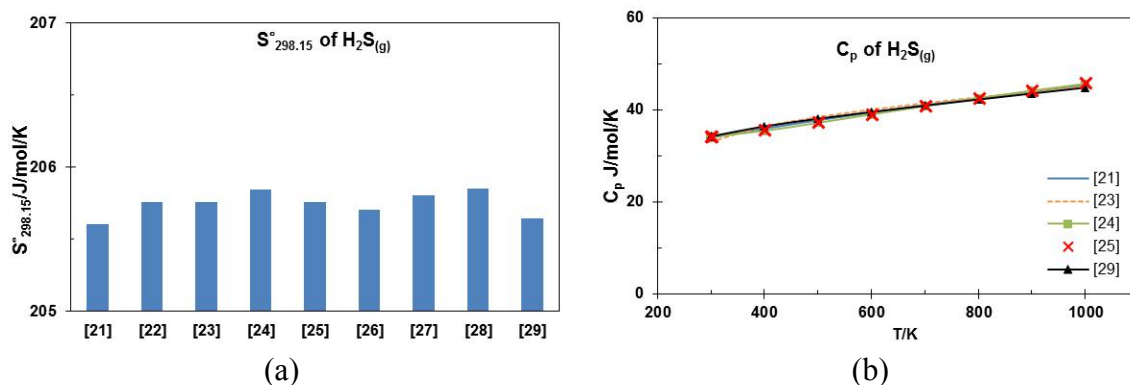


Figure 28. The collection of data for H<sub>2</sub>S(g) from various sources: (a) standard molar entropy at 25 °C,  $S_{298.15}^{\circ}$ ; (b) heat capacity,  $C_p$ .

However, the thermodynamic data for some other species had a significant variation between different sources, for instance  $S_{298.15}^{\circ}$  data for aqueous Fe<sup>2+</sup> and Fe<sup>3+</sup> species, as illustrated in Figure 29. The  $S_{298.15}^{\circ}$  data for these two species calculated by Beverskog *et al.* [102] were adopted for further use in the present study. Moreover, only one source [104], [105] was found for the heat capacity,  $C_p$  for aqueous Fe<sup>2+</sup> and Fe<sup>3+</sup> and was therefore used in the present study even if the valid temperature range was not defined.

In addition, it should be emphasized that both stoichiometric troilite (FeS) and pyrrhotite (Fe<sub>0.877</sub>S) are considered to be part of the pyrrhotite group (Fe<sub>1-x</sub>S, x = 0 to 0.17) in the present work, because of the similarity found for their thermodynamic data. Figure 30 summarizes the heat capacity and the standard molar entropy for both troilite and pyrrhotite. Figure 30 (a) shows that the standard molar entropy for troilite and pyrrhotite are very close, with an average value of  $60.38 \pm 0.21$  J/mol·K. It is acknowledged that phase transitions of troilite and pyrrhotite can affect the heat capacity; hence, different heat capacities were used for each phase in the present study. Figure 30

(b) shows that the heat capacity values for troilite and pyrrhotite phases obtained from various sources agree with each other very well. As a result, the heat capacity and the standard molar entropy for troilite reported by O. Knacke *et al.* [95] were taken for the pyrrhotite group  $\text{Fe}_{1-x}\text{S}$  ( $x = 0$  to  $0.17$ ).

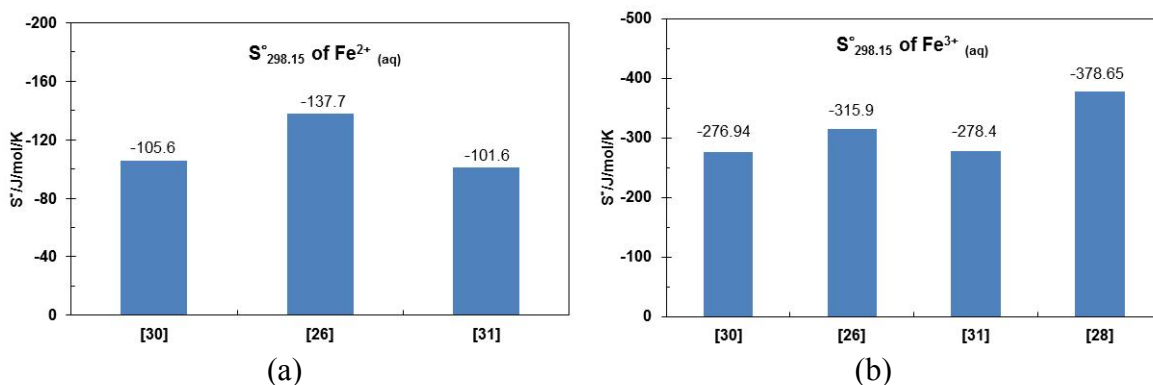


Figure 29. The collection of data of  $S^{\circ}_{298.15}$  for (a)  $\text{Fe}^{2+}_{(\text{aq})}$ ; (b)  $\text{Fe}^{3+}_{(\text{aq})}$  from various sources.

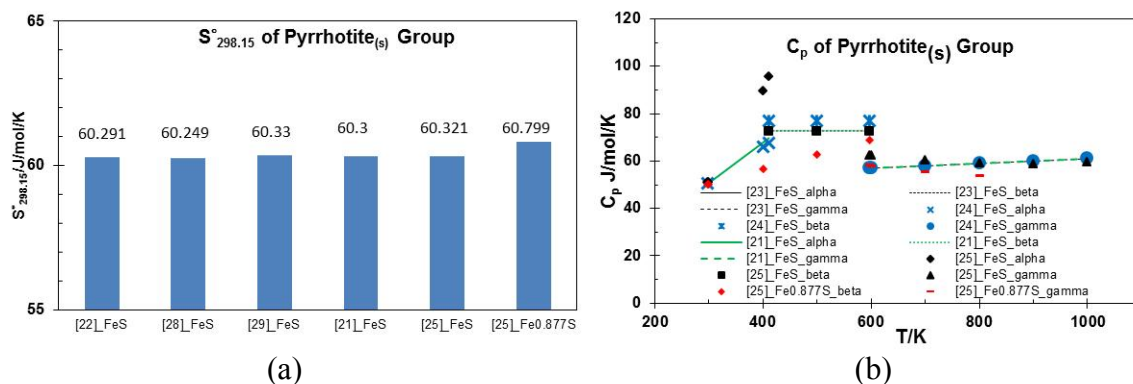


Figure 30. The collection of data for pyrrhotite(s) group from various sources: (a)  $S^{\circ}_{298.15}$ ; (b)  $C_p$ .

The compiled data for  $S^{\circ}_{298.15}$  and  $C_p$  for the following species:  $\text{H}_2\text{O}_{(\text{l})}$ ,  $\text{H}_2_{(\text{g})}$ ,  $\text{O}_2_{(\text{g})}$ ,  $\text{Fe}_{(\text{s})}$ ,  $\text{Fe}^{2+}_{(\text{aq})}$ ,  $\text{Fe}^{3+}_{(\text{aq})}$ ,  $\text{Fe}_2\text{O}_3_{(\text{s})}$ ,  $\text{Fe}_3\text{O}_4_{(\text{s})}$ ,  $\text{Fe}(\text{OH})_2_{(\text{s})}$ ,  $\text{FeS}_{(\text{s})}$  (the pyrrhotite group), and  $\text{FeS}_2_{(\text{s})}$  (pyrite), are summarized in Table 11.

### 4.3.2.2 *Thermodynamic Data by Estimation*

The heat capacity for some species, such as mackinawite and greigite, could not be found in the open literature and had to be estimated. This was done based on data available for other metal sulfides such as those of chromium (Cr), manganese (Mn), cobalt (Co), nickel (Ni), copper (Cu), and ruthenium (Ru), due to the good agreement between data found for their heat capacities, as illustrated in Figure 31 (a), (b), and (c). The heat capacity for NiS was adopted as the heat capacity for mackinawite. Similarly, the heat capacity for  $\text{Co}_3\text{S}_4$  was used for greigite.

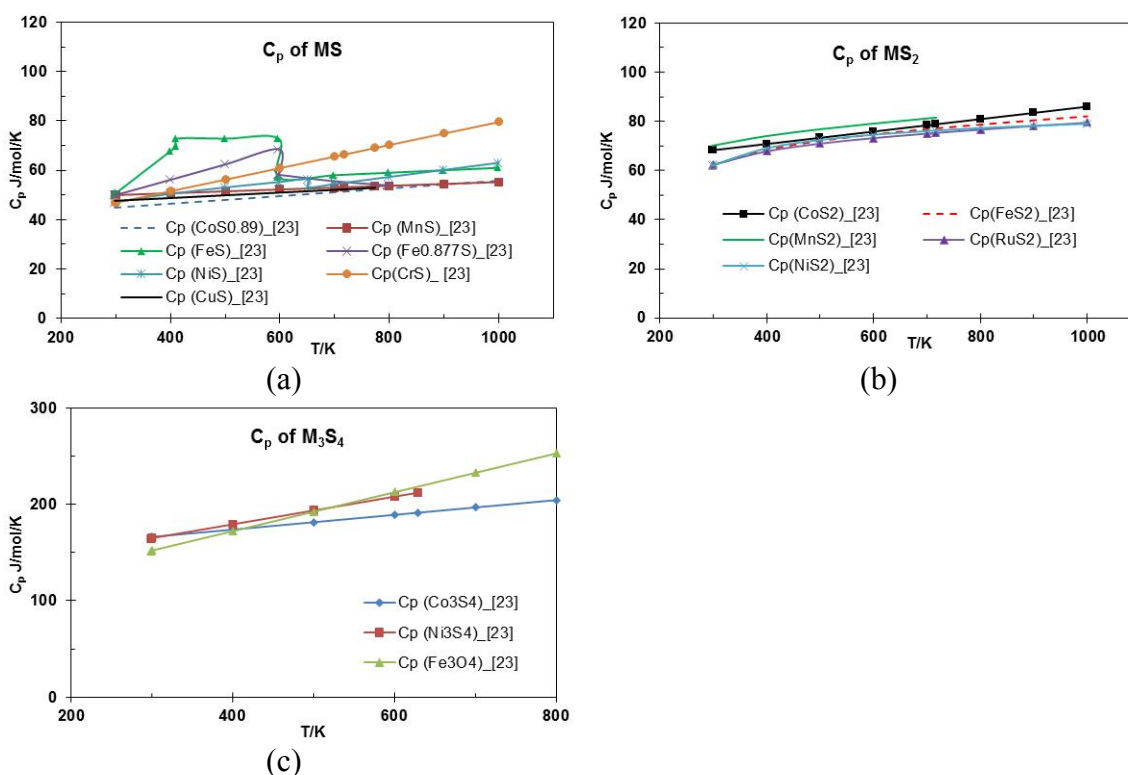


Figure 31. Heat capacity of metal sulfides: (a) MS; (b)  $\text{MS}_2$ ; (c)  $\text{M}_3\text{S}_4$ .

The entropies for mackinawite and greigite were estimated by following two rules. The first one was proposed by F. Gronvold and E. F. Westrum [106], which is to

estimate the entropy of a compound by combining the cationic entropy contribution and anionic entropy contribution. Therefore, the entropies for metal sulfides were calculated as the sum of entropy of chemical elements in accordance with the chemical formula. In light of this estimation rule, the entropies for mackinawite and greigite were estimated to be 56.52 J/mol/K and 182.13 J/mol/K, respectively. Another methodology of estimating entropy [107] was tested in the present work, for verification purposes. The rule is to sum up the average entropies for iron (27.3 J/mol/K) and sulfur (31.92 J/mol/K) according to the chemical formula of a compound. The resultant entropy for mackinawite was estimated to be 59 J/mol/K and for greigite was 208.9 J/mol/K. Overall, similar entropies for mackinawite and greigite were estimated by using these two methodologies, therefore, it was concluded that either can be used with confidence. In the end, the entropies for mackinawite and greigite were estimated by using the first methodology.

Table 11 Thermodynamic data of the species considered for a H<sub>2</sub>S-H<sub>2</sub>O-Fe system.

Species	$G_{298.15}^{\circ}$ (kJ/mol)	$S_{298.15}^{\circ}$ (J/mol/	$C_p = a + bT + cT^{-2} + dT^2$ (J / mol / K)					Ref.
			a	$b \cdot 10^3$	$c \cdot 10^{-6}$	$d \cdot 10^6$	valid tem.(K)	
H <sup>+</sup> <sub>(aq)</sub>	0	0	0	0	0	0	all	[91]
H <sub>2</sub> S <sub>(g)</sub>	-33.329	205.757	34.911	10.686	-0.448	0	298-2000	[95]
H <sub>2</sub> O <sub>(l)</sub>	-237.141	69.948	20.335	109.198	2.033	0	298-500	[95]
H <sub>2</sub> <sub>(g)</sub>	0	130.679	26.882	3.586	0.105	0	298-3000	[95]
O <sub>2</sub> <sub>(g)</sub>	0	205.146	29.154	6.477	-0.184	-1.017	298-3000	[95]
Fe <sub>(s)</sub>	0	27.28	28.18	-7.32	-0.29	25	298-800	[93]
Fe <sup>2+</sup> <sub>(aq)</sub>	-91.5	-105.6	-2	0	0	0	unknown	[102], [105]
Fe <sup>3+</sup> <sub>(aq)</sub>	-17.24	-276.94	-143	0	0	0	unknown	[102], [105]
Fe <sub>2</sub> O <sub>3</sub> <sub>(s)</sub> <sup>a</sup>	-743.523	87.4	-838.61	-2343.4	0	605.19	298-950	[96]
Fe <sub>3</sub> O <sub>4</sub> <sub>(s)</sub> <sup>b</sup>	-1017.438	146.14	2659.1	-2521.53	20.734	1368	298-900	[102]
Fe(OH) <sub>2</sub> <sub>(s)</sub>	-491.969	87.864	116.064	8.648	-2.874	0	298-1358	[95]
FeS <sub>(s)</sub> (mackinawite)	-100.07	56.52	44.685	19.037	-0.289	0		estimated
Fe <sub>3</sub> S <sub>4</sub> <sub>(s)</sub> (greigite)	-311.88	182.13	143.344	76.567	0	0		estimated
FeS <sub>(s)</sub> (pyrrhotite)	-101.95	60.291	-0.502	170.707	0	0	298-411	[95]
			72.802	0	0	0	411-598	
FeS <sub>2</sub> <sub>(s)</sub> (pyrite)	-160.06	52.928	68.952	141	-0.987	0	298-1016	[95]

<sup>a</sup>  $C_{p(Fe_2O_3)} = a + bT + cT^{-2} + dT^2 + fT^{0.5} + gT^{-1}$  (J / mol / K), where  $f = 86.525$  and  $g = 27821$ .

<sup>b</sup>  $C_{p(Fe_3O_4)} = a + bT + cT^{-2} + dT^2 + eT^{-0.5}$  (J / mol / K), where  $e = -36460$ .

#### 4.4 Pourbaix Diagrams

The Pourbaix diagrams for an H<sub>2</sub>S-H<sub>2</sub>O-Fe system were constructed in a stepwise fashion, starting from a simple system moving to a more complicated system, and also starting from standard conditions moving to elevated temperatures.

##### 4.4.1 Construction of Pourbaix Diagrams for a H<sub>2</sub>O-Fe System at Reference Temperature

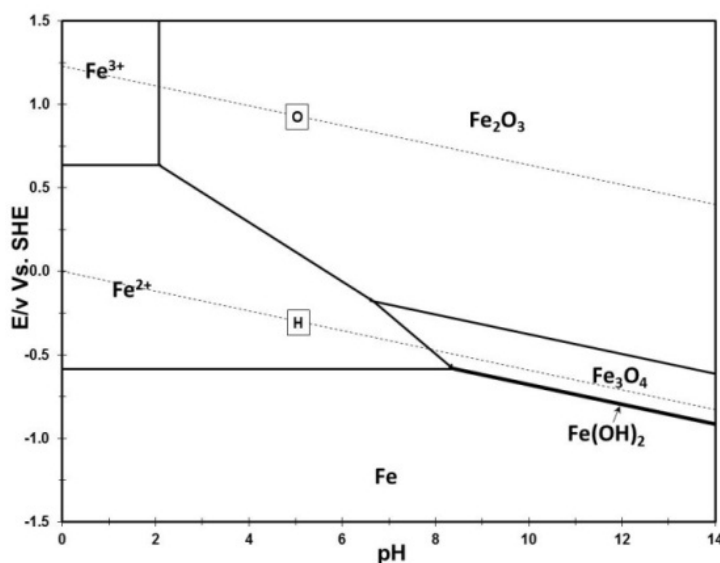
To construct Pourbaix diagrams for an H<sub>2</sub>S-H<sub>2</sub>O-Fe system, the H<sub>2</sub>O-Fe system was used as the starting point. All the equilibria for electrochemical and chemical reactions occurring in the H<sub>2</sub>O-Fe system are listed in the second column of Table 12.

The Nernst equation, Equation (33), is used for electrochemical reactions to calculate the reversible potential at equilibrium, and Equation (38) is used for chemical reactions to compute the equilibrium pH. The expressions for equilibrium potential and pH are shown in the last column in Table 12. Equation (34) is used to calculate the standard reversible potential, using the thermodynamic data in Table 11. The Pourbaix diagram for the H<sub>2</sub>O-Fe system at 25 °C is created for arbitrary conditions similar to the test parameters assumed in this work and is shown in Figure 32.

As a starting point, a well-known Pourbaix diagram for an H<sub>2</sub>O-Fe system generated at a specific condition is shown in Figure 32. The areas of “Fe(OH)<sub>2</sub>”, “Fe<sub>2</sub>O<sub>3</sub>”, and “Fe<sub>3</sub>O<sub>4</sub>” indicate the formation of a certain corrosion product layer, but do not indicate how this layer affects corrosion. The protectiveness of the formed layer depends on its adherence to the steel surface, thickness, porosity, tortuosity, and physicochemical properties, such as crystal structure and defects, which are related to the kinetics of formation [12].

Table 12 Equilibria of electrochemical reactions occurring in the H<sub>2</sub>O-Fe system.

No.	Reaction	Equilibrium Potential or pH
H	$2H^+ + 2e^- \rightleftharpoons H_2$	$E_{rev(H^+/H_2)} = E_{rev(H^+/H_2)}^0 - \frac{RT}{2F} \ln \frac{pH_2}{[H^+]^2}$
O	$O_2 + 4H^+ + 4e^- \rightleftharpoons 2H_2O$	$E_{rev(O_2/H_2O)} = E_{rev(O_2/H_2O)}^0 - \frac{RT}{4F} \ln \frac{1}{pO_2 \cdot [H^+]^4}$
1.	$Fe^{2+} + 2e^- \rightleftharpoons Fe$	$E_{rev(Fe^{2+}/Fe)} = E_{rev(Fe^{2+}/Fe)}^0 - \frac{RT}{2F} \ln \frac{1}{[Fe^{2+}]}$
2.	$Fe^{3+} + e^- \rightleftharpoons Fe^{2+}$	$E_{rev(Fe^{3+}/Fe^{2+})} = E_{rev(Fe^{3+}/Fe^{2+})}^0 - \frac{RT}{F} \ln \frac{[Fe^{2+}]}{[Fe^{3+}]}$
3.	$Fe^{2+} + 2H_2O \rightleftharpoons Fe(OH)_2 + 2H^+$	$pH_{(Fe^{2+}/Fe(OH)_2)} = -0.5 \log(K_{(Fe^{2+}/Fe(OH)_2)} [Fe^{2+}])$
4.	$Fe(OH)_2 + 2H^+ + 2e^- \rightleftharpoons Fe + 2H_2O$	$E_{rev(Fe(OH)_2/Fe)} = E_{rev(Fe^{3+}/Fe^{2+})}^0 - \frac{RT}{2F} \ln \frac{1}{[H^+]^2}$
5.	$Fe_3O_4 + 2H_2O + 2H^+ + 2e^- \rightleftharpoons 3Fe(OH)_2$	$E_{rev(Fe_3O_4/Fe(OH)_2)} = E_{rev(Fe_3O_4/Fe(OH)_2)}^0 - \frac{RT}{2F} \ln \frac{1}{[H^+]^2}$
6.	$6Fe_2O_3 + 4H^+ + 4e^- \rightleftharpoons 4Fe_3O_4 + 2H_2O$	$E_{rev(Fe_2O_3/Fe_3O_4)} = E_{rev(Fe_2O_3/Fe_3O_4)}^0 - \frac{RT}{4F} \ln \frac{1}{[H^+]^4}$
7.	$Fe_3O_4 + 8H^+ + 2e^- \rightleftharpoons 3Fe^{2+} + 4H_2O$	$E_{rev(Fe_3O_4/Fe^{2+})} = E_{rev(Fe_3O_4/Fe^{2+})}^0 - \frac{RT}{2F} \ln \frac{[Fe^{2+}]}{[H^+]^8}$
8.	$2Fe_2O_3 + 12H^+ + 4e^- \rightleftharpoons 4Fe^{2+} + 6H_2O$	$E_{rev(Fe_2O_3/Fe^{2+})} = E_{rev(Fe_2O_3/Fe^{2+})}^0 - \frac{RT}{4F} \ln \frac{[Fe^{2+}]^4}{[H^+]^{12}}$
9.	$2Fe^{3+} + 3H_2O \rightleftharpoons Fe_2O_3 + 6H^+$	$pH_{(Fe^{3+}/Fe_2O_3)} = -\frac{1}{6} \log(K_{(Fe^{3+}/Fe_2O_3)} [Fe^{3+}]^2)$

Figure 32. Pourbaix diagram for H<sub>2</sub>O-Fe system (T = 25 °C, [Fe<sup>2+</sup>] = 10 ppm, [Fe<sup>3+</sup>] = 10<sup>-6</sup> mol/L, pH<sub>2</sub> = pO<sub>2</sub> = 1 bar).

#### 4.4.2 Construction of Pourbaix Diagrams for an $H_2S-H_2O-Fe$ System at Reference Temperature

To construct Pourbaix diagrams for an  $H_2S-H_2O-Fe$  system, the reactions of formation of mackinawite ( $FeS$ ), greigite ( $Fe_3S_4$ ), the pyrrhotite group ( $FeS$ ) and pyrite ( $FeS_2$ ) are incorporated into the Pourbaix diagram for the  $H_2O-Fe$  system shown in Figure 32. Consequently, Pourbaix diagrams for the  $H_2S-H_2O-Fe$  system with addition of mackinawite, greigite, the pyrrhotite group, and pyrite are generated stepwise, as shown below.

##### 4.4.2.1 Pourbaix Diagram with Only Mackinawite in a $H_2S-H_2O-Fe$ System at $25\text{ }^\circ C$

Mackinawite is "added first" into the Pourbaix diagram for the  $H_2O-Fe$  system, as it is the initial corrosion product in the presence of  $H_2S$ . The equilibria of reactions related to the formation of mackinawite (No.10-14) are listed in the second column in Table 13, and the expressions for reversible potential and pH for each reaction are shown in the third column. When added into the  $H_2O-Fe$  system, and the graph, and after "cleaning up", the resulting diagram is shown in Figure 33 (a). Mackinawite and ferric oxide ( $Fe_2O_3$ ) are observed in Figure 33 (a), while ferrous hydroxide ( $Fe(OH)_2$ ) and magnetite ( $Fe_3O_4$ ) have disappeared being less stable than mackinawite.

##### 4.4.2.2 Pourbaix Diagram with Mackinawite and Greigite in a $H_2S-H_2O-Fe$ System at $25\text{ }^\circ C$

The formation of greigite is considered next. The reactions (No.15-19) are taken into consideration, as Table 13 shows, and the correlations between the reversible potential and pH for these reactions are also shown in Table 13. Figure 33 (b) shows the Pourbaix diagram with accounted mackinawite and greigite. Greigite is found in the

higher potential range compared to mackinawite, and is significantly higher than would be typically seen in aqueous H<sub>2</sub>S corrosion of mild steel.

#### 4.4.2.3 Pourbaix Diagram with Mackinawite, Greigite and Pyrrhotite in a H<sub>2</sub>S-H<sub>2</sub>O-Fe System at 25 °C

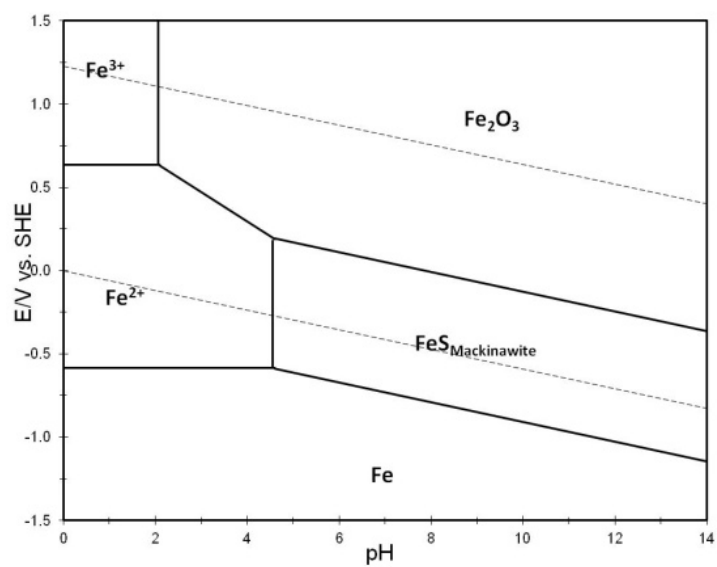
The reactions related to the formation of pyrrhotite were incorporated next; reaction (No. 20-24) details are shown in Table 13. The Pourbaix diagram with pyrrhotite added is shown in Figure 33 (c). Note that mackinawite is no longer present since it is replaced by the more thermodynamically stable product pyrrhotite, which is the species to be expected in longer exposures under these conditions.

#### 4.4.2.4 Pourbaix Diagram with Mackinawite, Greigite, Pyrrhotite and Pyrite for H<sub>2</sub>S-H<sub>2</sub>O-Fe System at 25 °C

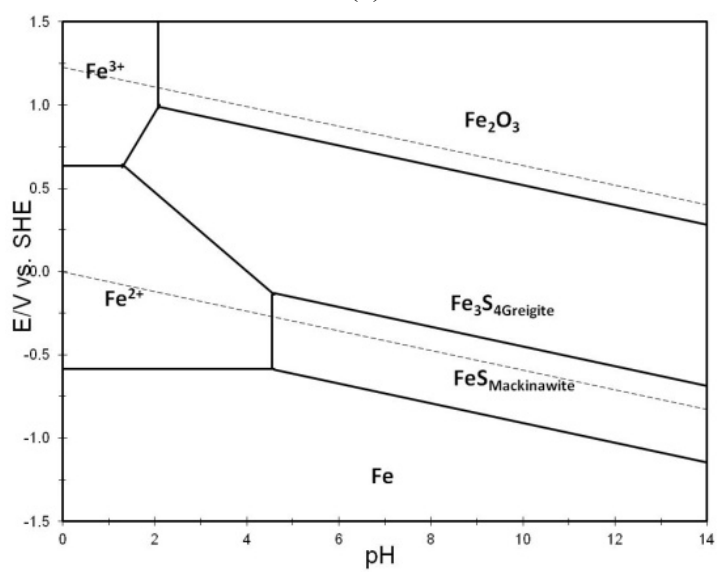
The last of the dominant iron sulfides, pyrite, is added into the previous system. Reactions relating to the formation of pyrite (No. 25-31) are given in Table 13. Figure 33 (d) shows the Pourbaix diagram with all the four dominant iron sulfides considered. Only pyrrhotite and pyrite are present in Figure 33 (d), indicating these two phases are the final and thermodynamically stable iron sulfide corrosion products which are to be expected in long term exposures. Given the typical potential and pH range encountered during internal corrosion of mild steel in aqueous H<sub>2</sub>S solutions, pyrrhotite should be the main species expected in longer term exposures.

Table 13 Equilibria of electrochemical reactions occurring in the H<sub>2</sub>S-H<sub>2</sub>O-Fe system.

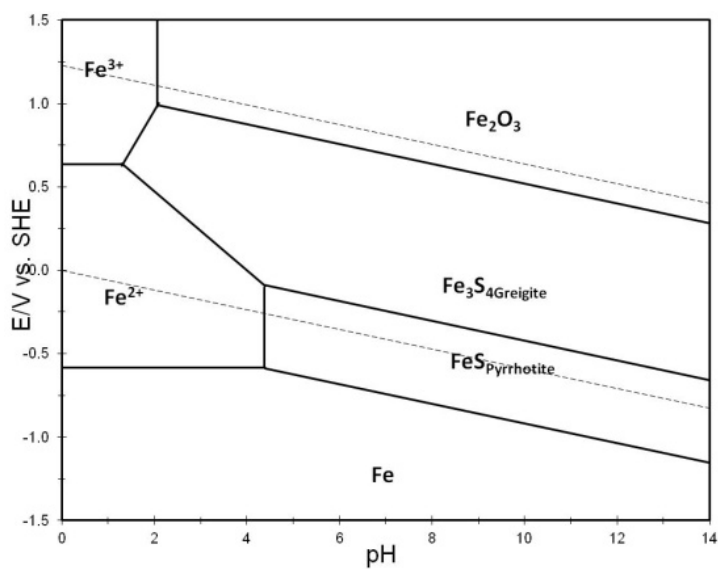
No.	Reaction	Equilibrium Potential or pH
10.	$FeS_m + 2H^+ + 2e^- \rightleftharpoons Fe + H_2S(g)$	$E_{rev(FeS_m/Fe)} = E_{rev(FeS_m/Fe)}^0 - \frac{RT}{2F} \ln \frac{pH_2S}{[H^+]^2}$
11.	$FeS_m + 2H^+ \rightleftharpoons Fe^{2+} + H_2S(g)$	$pH_{(FeS_m/Fe^{2+})} = -0.5 \log \left( \frac{[Fe^{2+}] pH_2S}{K_{(FeS_m/Fe^{2+})}} \right)$
12.	$Fe_2O_3 + 2H_2S(g) + 2H^+ + 2e^- \rightleftharpoons 2FeS_m + 3H_2O$	$E_{rev(Fe_2O_3/FeS_m)} = E_{rev(Fe_2O_3/FeS_m)}^0 - \frac{RT}{2F} \ln \frac{1}{pH_2S^2 \cdot [H^+]^2}$
13.	$Fe_3O_4 + 3H_2S(g) + 2H^+ + 2e^- \rightleftharpoons 3FeS_m + 4H_2O$	$E_{rev(Fe_3O_4/FeS_m)} = E_{rev(Fe_3O_4/FeS_m)}^0 - \frac{RT}{2F} \ln \frac{1}{pH_2S^3 \cdot [H^+]^2}$
14.	$Fe(OH)_2 + H_2S(g) \rightleftharpoons FeS_m + 2H_2O$	$K_{(Fe(OH)_2/FeS_m)} = \frac{1}{pH_2S}$
15.	$Fe_3S_4 + 8H^+ + 8e^- \rightleftharpoons 3Fe + 4H_2S(g)$	$E_{rev(Fe_3S_4/Fe)} = E_{rev(Fe_3S_4/Fe)}^0 - \frac{RT}{8F} \ln \frac{pH_2S^4}{[H^+]^8}$
16.	$Fe_3S_4 + 8H^+ + 2e^- \rightleftharpoons 3Fe^{2+} + 4H_2S(g)$	$E_{rev(Fe_3S_4/Fe^{2+})} = E_{rev(Fe_3S_4/Fe^{2+})}^0 - \frac{RT}{2F} \ln \frac{[Fe^{2+}]^3 pH_2S^4}{[H^+]^8}$
17.	$3Fe^{3+} + 4H_2S(g) + e^- \rightleftharpoons Fe_3S_4 + 8H^+$	$E_{rev(Fe_2O_3/Fe_3S_4)} = E_{rev(Fe_2O_3/Fe_3S_4)}^0 - \frac{RT}{2F} \ln \frac{1}{[H^+]^2 pH_2S^8}$
18.	$3Fe_2O_3 + 8H_2S(g) + 2H^+ + 2e^- \rightleftharpoons 2Fe_3S_4 + 9H_2O$	$E_{rev(Fe_2O_3/Fe_3S_4)} = E_{rev(Fe_2O_3/Fe_3S_4)}^0 - \frac{RT}{2F} \ln \frac{1}{[H^+]^2 pH_2S^8}$
19.	$Fe_3S_4 + 2H^+ + 2e^- \rightleftharpoons 3FeS_m + H_2S(g)$	$E_{rev(Fe_3S_4/FeS_m)} = E_{rev(Fe_3S_4/FeS_m)}^0 - \frac{RT}{2F} \ln \frac{pH_2S}{[H^+]^2}$
20.	$FeS_p + 2H^+ + 2e^- \rightleftharpoons Fe + H_2S(g)$	$E_{rev(FeS_{pyrrhotite}/Fe)} = E_{rev(FeS_{pyrrhotite}/Fe)}^0 - \frac{RT}{2F} \ln \frac{pH_2S}{[H^+]^2}$
21.	$FeS_p + 2H^+ \rightleftharpoons Fe^{2+} + H_2S(g)$	$pH_{(FeS_{pyrrhotite}/Fe^{2+})} = \log \left( \frac{pH_2S \cdot [Fe^{2+}]}{K_{(FeS_{pyrrhotite}/Fe^{2+})}} \right)^{-\frac{1}{2}}$
22.	$Fe_2O_3 + 2H_2S(g) + 2H^+ + 2e^- \rightleftharpoons 2FeS_p + 3H_2O$	$E_{rev(Fe_2O_3/FeS_{pyrrhotite})} = E_{rev(Fe_2O_3/FeS_{pyrrhotite})}^0 - \frac{RT}{2F} \ln \frac{1}{pH_2S^2 \cdot [H^+]^2}$
23.	$Fe_3S_4 + 2H^+ + 2e^- \rightleftharpoons 3FeS_p + H_2S(g)$	$E_{rev(Fe_3S_4/FeS_{pyrrhotite})} = E_{rev(Fe_3S_4/FeS_{pyrrhotite})}^0 - \frac{RT}{2F} \ln \frac{pH_2S}{[H^+]^2}$
24.	$FeS_{Pyrrhotite} \rightleftharpoons FeS_{Mackinawite}$	$K_{(FeS_p/FeS_m)} = 1$
25.	$FeS_2 + 4H^+ + 2e^- \rightleftharpoons Fe^{2+} + 2H_2S(g)$	$E_{rev(FeS_{pyrite}/Fe^{2+})} = E_{rev(FeS_{pyrite}/Fe^{2+})}^0 - \frac{RT}{2F} \ln \frac{[Fe^{2+}] \cdot pH_2S^2}{[H^+]^4}$
26.	$FeS_2 + 4H^+ + 4e^- \rightleftharpoons Fe + 2H_2S(g)$	$E_{rev(FeS_{pyrite}/Fe)} = E_{rev(FeS_{pyrite}/Fe)}^0 - \frac{RT}{4F} \ln \frac{pH_2S^2}{[H^+]^4}$
27.	$2FeS_2 + 3H_2O + 2H^+ + 2e^- \rightleftharpoons Fe_2O_3 + 4H_2S(g)$	$E_{rev(FeS_{pyrite}/Fe_2O_3)} = E_{rev(FeS_{pyrite}/Fe_2O_3)}^0 - \frac{RT}{2F} \ln \frac{pH_2S^4}{[H^+]^2}$
28.	$FeS_2 + 2H^+ + 2e^- \rightleftharpoons FeS_{Mackinawite} + H_2S(g)$	$E_{rev(FeS_{pyrite}/FeS_m)} = E_{rev(FeS_{pyrite}/FeS_m)}^0 - \frac{RT}{2F} \ln \frac{pH_2S}{[H^+]^2}$
29.	$FeS_2 + 2H^+ + 2e^- \rightleftharpoons FeS_{Pyrrhotite} + H_2S(g)$	$E_{rev(FeS_{pyrite}/FeS_{pyrrhotite})} = E_{rev(FeS_{pyrite}/FeS_{pyrrhotite})}^0 - \frac{RT}{2F} \ln \frac{pH_2S}{[H^+]^2}$
30.	$FeS_2 + 4H^+ + e^- \rightleftharpoons Fe^{3+} + 2H_2S(g)$	$E_{rev(FeS_{pyrite}/Fe^{3+})} = E_{rev(FeS_{pyrite}/Fe^{3+})}^0 - \frac{RT}{F} \ln \frac{[Fe^{3+}] \cdot pH_2S^2}{[H^+]^4}$
31.	$3FeS_2 + 4H^+ + 4e^- \rightleftharpoons Fe_3S_4 + 2H_2S(g)$	$E_{rev(FeS_{pyrite}/FeS_{greigite})} = E_{rev(FeS_{pyrite}/FeS_{greigite})}^0 - \frac{RT}{4F} \ln \frac{pH_2S^2}{[H^+]^4}$



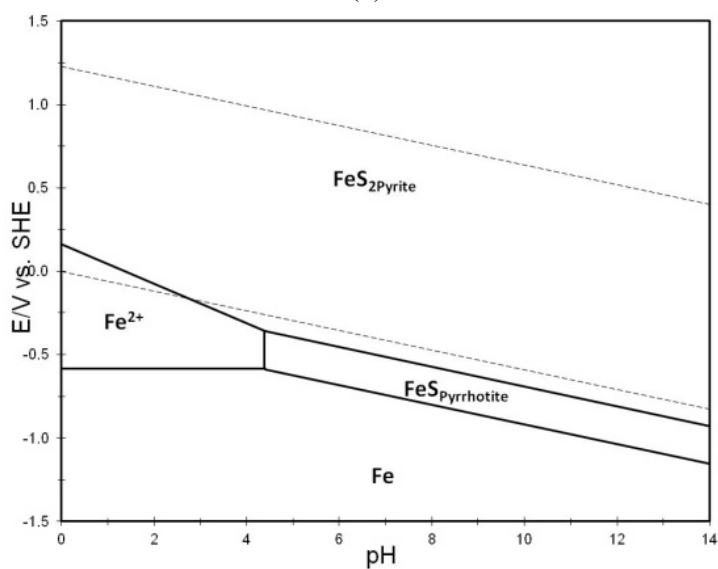
(a)



(b)



(c)



(d)

Figure 33. Pourbaix diagram for  $\text{H}_2\text{S}$ - $\text{H}_2\text{O}$ - $\text{Fe}$  system with (a) Mackinawite; (b) Mackinawite / Greigite; (c) Mackinawite / Greigite / Pyrrhotite; (d) Mackinawite / Greigite / Pyrrhotite / Pyrite ( $T = 25^\circ\text{C}$ ,  $\text{pH}_2\text{S} = 0.1$  bar,  $[\text{Fe}^{2+}] = 10$  ppm,  $[\text{Fe}^{3+}] = 10^{-6}$  mol/L,  $\text{pH}_2 = \text{pO}_2 = 1$  bar).

#### 4.4.3 Construction of Pourbaix Diagrams for H<sub>2</sub>S-H<sub>2</sub>O-Fe System at Elevated Temperature

Pourbaix diagrams for an H<sub>2</sub>S-H<sub>2</sub>O-Fe system at reference temperature (25°C) were constructed and are shown in 4.4.2. To apply this thermodynamic model to a broader range of field operating conditions, Pourbaix diagrams for an H<sub>2</sub>S-H<sub>2</sub>O-Fe system at elevated temperature were generated following the same practice as above. The reactions considered for the formation of those four types of iron sulfides and the expressions for reversible potential and pH for each reaction are the same ones as shown in Table 13. Due to the fact that thermodynamic properties are highly sensitive to temperature, the Gibbs energy of formation for each species at elevated temperature,  $G_{T,P}^{\circ}$ , was calculated following Equation (39) through to Equation (41) and using the thermodynamic data listed in Table 11. Thereby, Pourbaix diagrams for an H<sub>2</sub>S-H<sub>2</sub>O-Fe system at elevated temperature up to 250 °C were generated and are shown in Figure 34.

### 4.5 Parametric Study

The effects of increasing temperature, ferrous ion concentration in solution, and H<sub>2</sub>S partial pressure on features of Pourbaix diagrams for H<sub>2</sub>S-H<sub>2</sub>O-Fe system are described below.

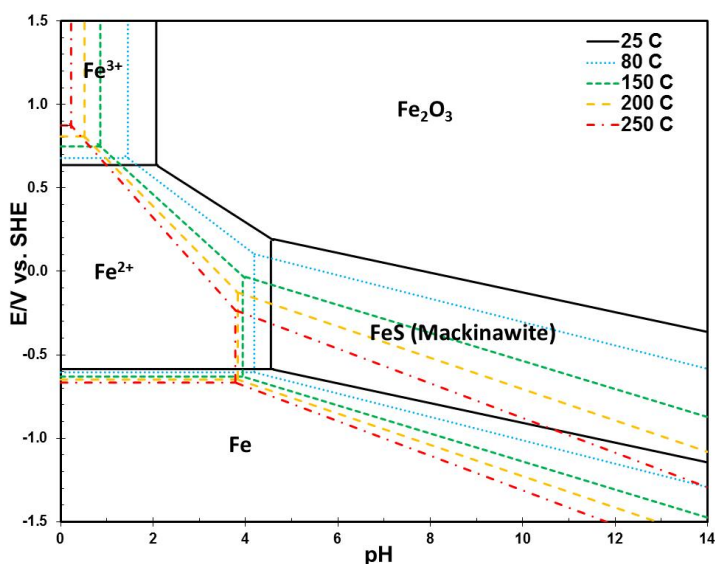
#### 4.5.1 Effect of Temperature

Since thermodynamic properties are highly sensitive to temperature, the Pourbaix diagrams for the H<sub>2</sub>S-H<sub>2</sub>O-Fe system were generated at 25 °C, 80 °C, 150 °C, and 250 °C and are presented in Figure 34 using colored lines. In order to compare Pourbaix diagrams among different temperatures in a reasonable way, the dissolved H<sub>2</sub>S

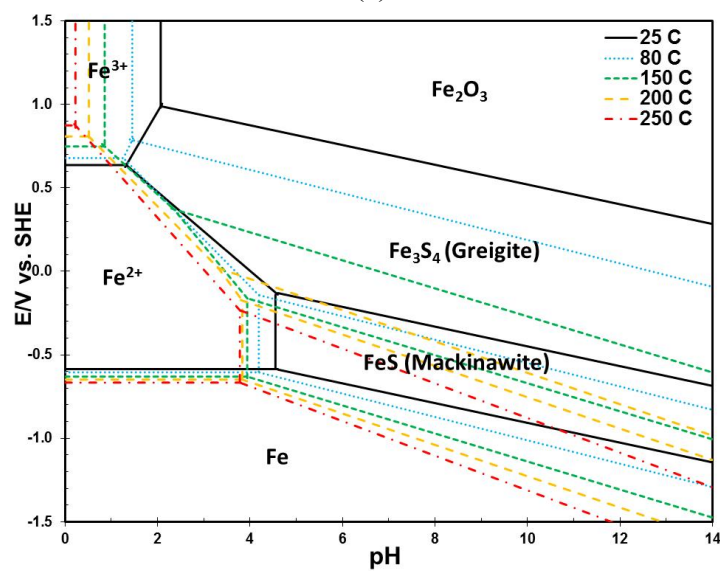
concentration in aqueous solution is maintained at a constant level ( $9.4 \times 10^{-3}$  mol/L) during the construction of this series of Pourbaix diagrams.

A gradual shift of the stability areas for formed solids to lower pH values and to more negative potential with increasing temperature is clear in Figure 34. This indicates that higher temperatures are more thermodynamically favorable for the formation of a corrosion product layer, such as iron sulfides and hematite, possibly retarding corrosion rate of steel underneath. Abayarathna *et al.* [108] conducted steel corrosion tests with a continuous purge of pure  $\text{H}_2\text{S}$  gas into brine at 50 °C, 70 °C, and 90 °C for two days of exposure. The results showed that the final corrosion rate at 90 °C was much lower than at 50 °C due to the formation of a more protective iron sulfide layer.

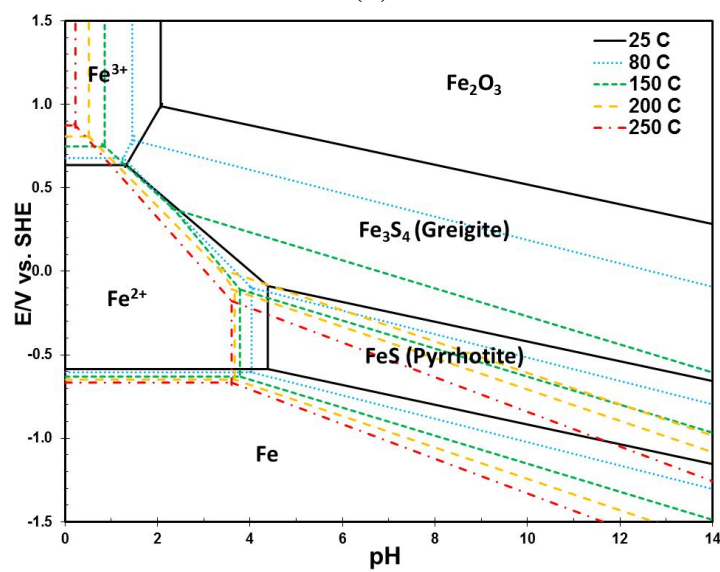
In addition, the type of the corrosion product formed was also affected by changing temperature. In Figure 34 (b) and (c), greigite is predicted to be the main corrosion product at 25°C through 200°C, but not at 250°C. At 250 °C, greigite is completely replaced by hematite since hematite is more stable than greigite at 250°C.



(a)



(b)



(c)

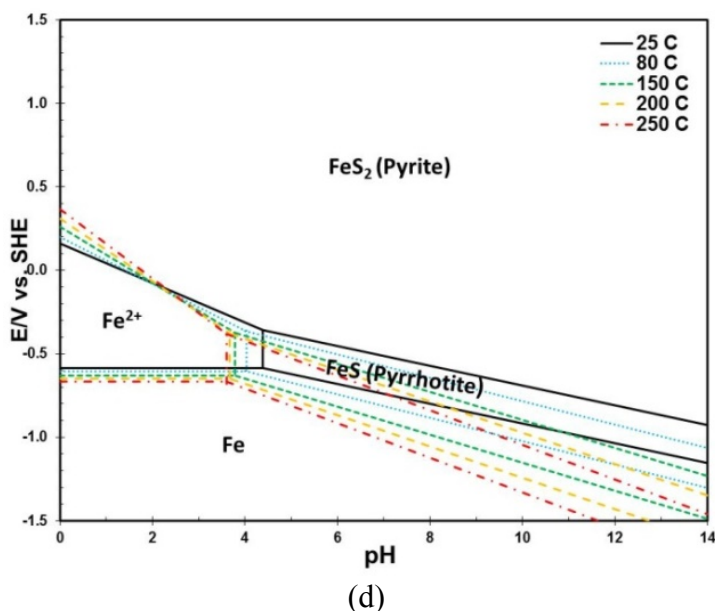


Figure 34. Pourbaix diagrams for H<sub>2</sub>S-H<sub>2</sub>O-Fe system showing step changes in temperature up to 250 °C (T = 25 °C ~ 250 °C, [H<sub>2</sub>S]<sub>aq</sub> = 9.4 × 10<sup>-3</sup> M, [Fe<sup>2+</sup>] = 10 ppm, [Fe<sup>3+</sup>] = 10<sup>-6</sup> M): (a) Mackinawite; (b) Mackinawite / Greigite; (c) Mackinawite / Greigite / Pyrrhotite; (d) Mackinawite / Greigite / Pyrrhotite / Pyrite.

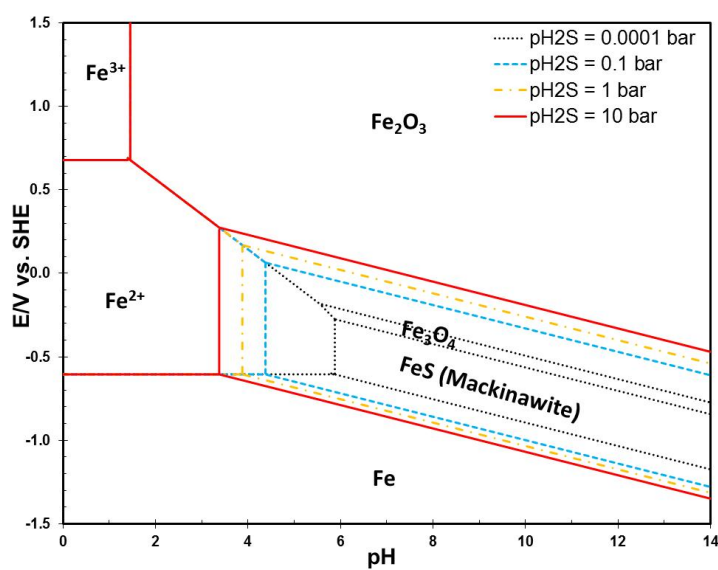
#### 4.5.2 Effect of H<sub>2</sub>S Partial Pressure

Variation of another significant factor, partial pressure of H<sub>2</sub>S, is also considered here. The Pourbaix diagrams are developed for partial pressure of H<sub>2</sub>S at 0.0001 bar (100 ppm at atmospheric pressure), 0.1 bar, 1 bar, and 10 bar and shown in Figure 35.

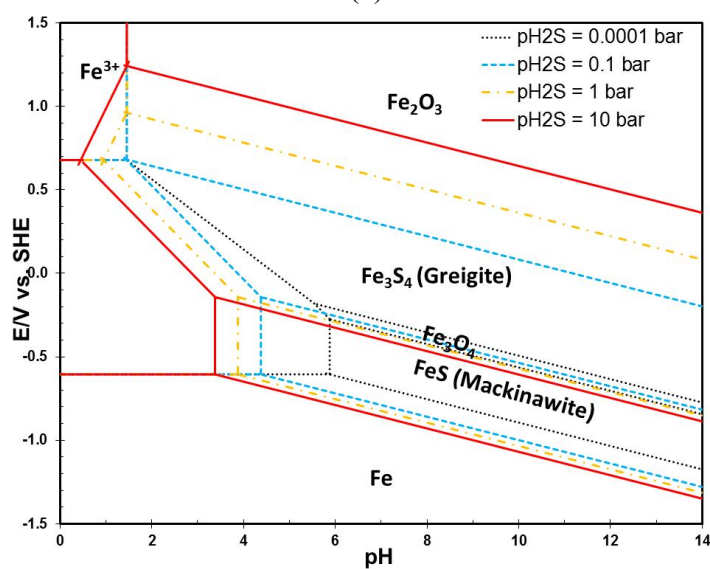
A major effect of increasing partial pressure of H<sub>2</sub>S on the features of Pourbaix diagrams is the expansion of the corrosion product layer stability region, particularly that of iron sulfide. Since mackinawite usually forms as the initial and main corrosion product in H<sub>2</sub>S corrosion and provides some protectiveness, understanding the conditions that lead to establishment of a mackinawite layer is critical to short-term corrosion studies. Figure 35 (a) shows that the increase in H<sub>2</sub>S partial pressure from 0.0001 bar to 10 bar dramatically pushes the boundary of the mackinawite formation region from pH 6.0 to

pH 3.3, revealing the formation of a mackinawite layer is more thermodynamically favored at higher  $H_2S$  partial pressure.

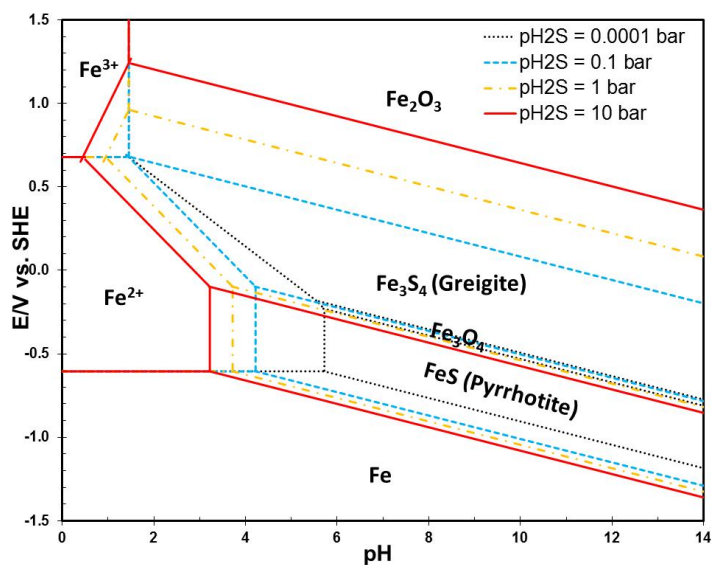
Furthermore,  $Fe_3O_4$  is seen in the presence of trace amounts of  $H_2S$  (0.0001 bar) but is replaced by iron sulfides at higher concentrations of  $H_2S$ , as shown in Figure 35 (a), (b), and (c).



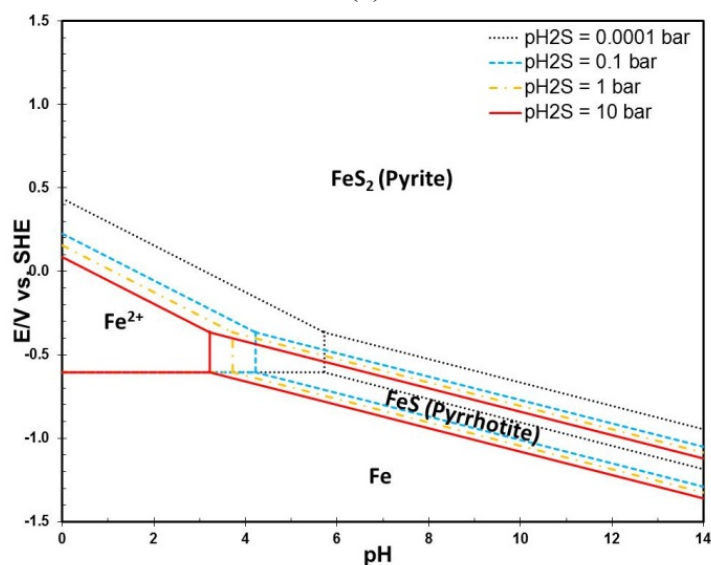
(a)



(b)



(c)



(d)

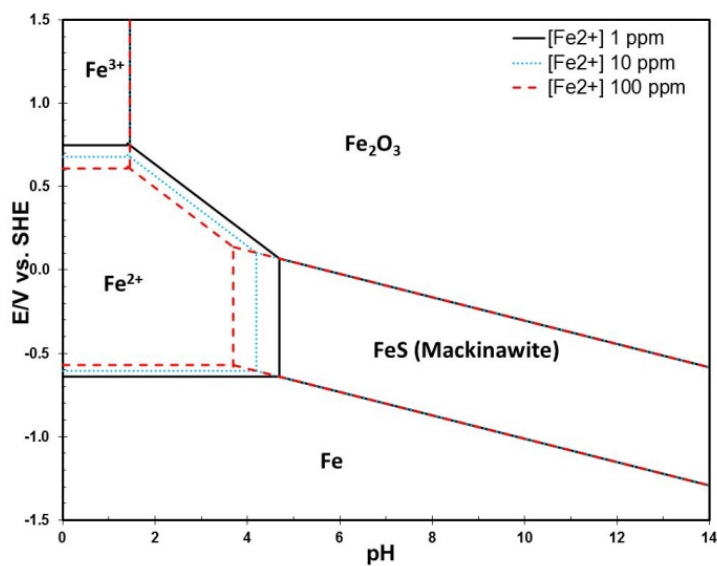
Figure 35. Pourbaix diagrams for  $\text{H}_2\text{S}$ - $\text{H}_2\text{O}$ - $\text{Fe}$  system showing step changes in  $\text{H}_2\text{S}$  partial pressure ( $\text{pH}_2\text{S} = 0.0001 \sim 10$  bar,  $T = 80$  °C,  $[\text{Fe}^{2+}] = 10$  ppm,  $[\text{Fe}^{3+}] = 10^{-6}$  M): (a) Mackinawite; (b) Mackinawite / Greigite; (c) Mackinawite / Greigite / Pyrrhotite; (d) Mackinawite / Greigite / Pyrrhotite / Pyrite.

#### 4.5.3 Effect of Ferrous Ion Concentration

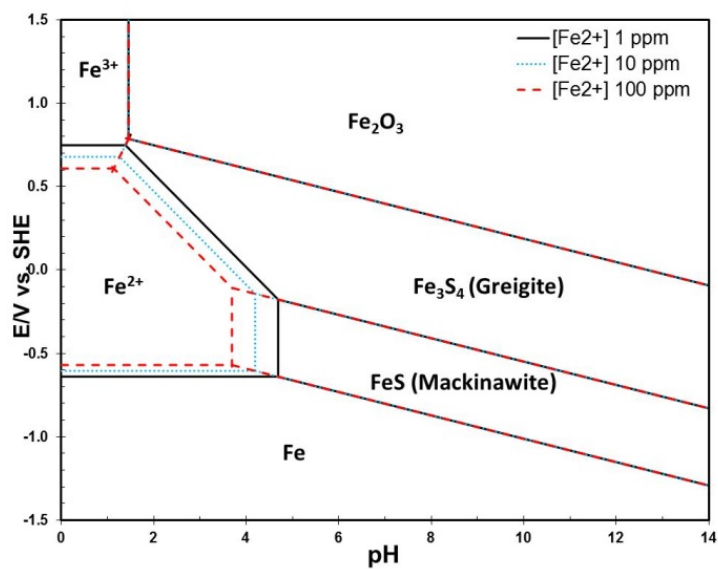
The concentration of ferrous ion in solution directly affects the saturation value for iron sulfide. Sun *et al.* [41] concluded that the effect of ferrous ion concentration on

H<sub>2</sub>S corrosion rate is negligible since the solubility of iron sulfide is so small that supersaturation for iron sulfide can be easily reached.

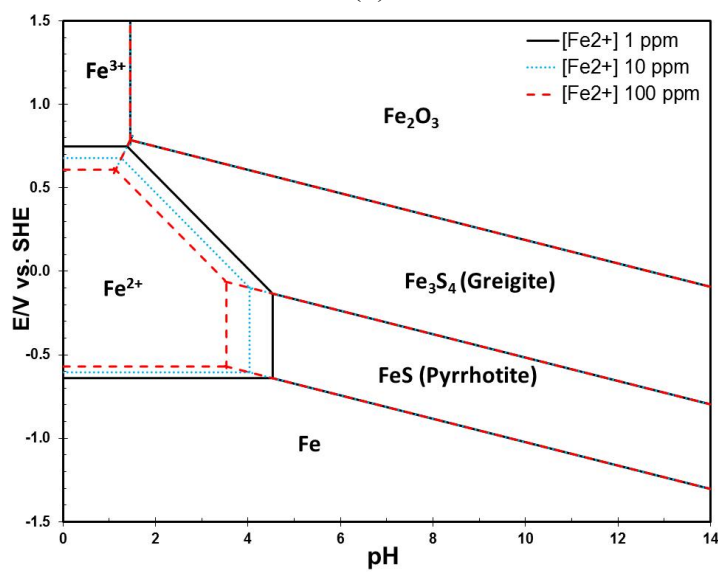
Figure 36 shows a series of Pourbaix diagrams developed with 1 ppm, 10 ppm, and 100 ppm ferrous ion concentration. Notice that the “Fe<sup>2+</sup>” area shrinks with increasing ferrous ion concentration, which is considered to be an indication that bare steel corrosion is less likely. However, the increase in the size of the iron sulfide stability area does not necessarily guarantee better protectiveness of the formed iron sulfide layer, which is more related to kinetics.



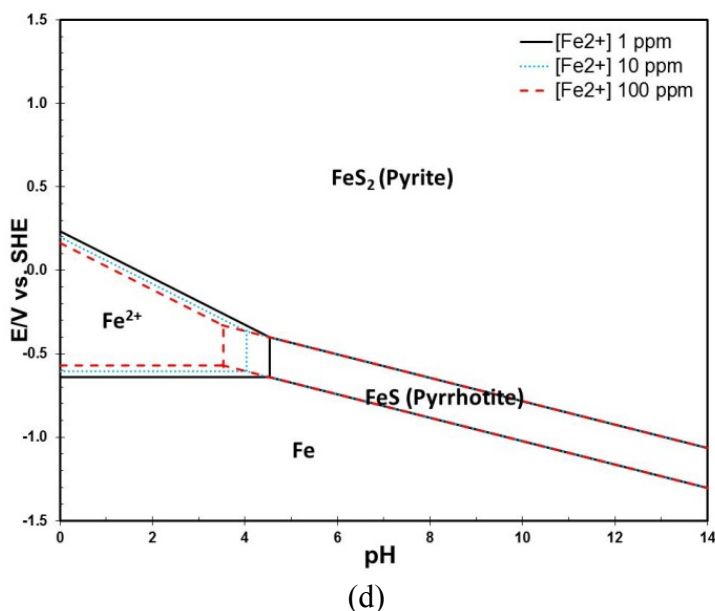
(a)



(b)



(c)



(d)  
Figure 36. Pourbaix diagrams for H<sub>2</sub>S-H<sub>2</sub>O-Fe system showing step changes in ferrous ion concentration ( $[\text{Fe}^{2+}] = 1\sim 100$  ppm,  $T = 80$  °C,  $\text{pH}_{\text{H}_2\text{S}} = 0.24$  bar,  $[\text{Fe}^{3+}] = 10^{-6}$  M): (a) Mackinawite; (b) Mackinawite / Greigite; (c) Mackinawite / Greigite / Pyrrhotite; (d) Mackinawite / Greigite / Pyrrhotite / Pyrite.

#### 4.6 Summary

The polymorphous, and related, iron sulfides were classified based on whether they were found in corrosion of carbon steel in oil and gas systems. The key polymorphous iron sulfides relevant for corrosion of mild steel in oil and gas systems were identified to be: mackinawite (FeS), greigite (Fe<sub>3</sub>S<sub>4</sub>), pyrrhotite (Fe<sub>1-x</sub>S,  $x = 0$  to 0.17), and pyrite (FeS<sub>2</sub>). This was done to generate relatively simple Pourbaix diagrams dedicated to internal pipeline corrosion environments.

A comprehensive thermodynamic model, in the form of Pourbaix diagrams, was developed to predict corrosion products for an H<sub>2</sub>S-H<sub>2</sub>O-Fe system with the focus on the conditions typical for oil and gas applications. The Pourbaix diagrams of the H<sub>2</sub>S-H<sub>2</sub>O-Fe system were constructed indicating that under typical conditions seen during internal corrosion of mild steel in aqueous H<sub>2</sub>S containing solutions (potential and pH range)

mackinawite should be expected in shorter exposures, while pyrrhotite should be the key corrosion product seen in longer exposures. Due to fast kinetics, mackinawite should be the most common species seen in short exposures. Greigite and pyrite are more likely to form at higher pH, higher potentials, and higher temperatures. Moreover, features of those Pourbaix diagrams are sensitive to temperature, ferrous ion concentration, and  $H_2S$  partial pressure.

## CHAPTER 5. VALIDATION OF POURBAIX DIAGRAMS FOR THE H<sub>2</sub>S-H<sub>2</sub>O- FE SYSTEM

### 5.1 Introduction

A comprehensive thermodynamic model for the H<sub>2</sub>S-H<sub>2</sub>O-Fe system, in the form of Pourbaix diagrams, was developed in Chapter 4 with the relatively narrow focus on predicting corrosion products for environments similar to those found in oil and gas fields. The ability to predict the form(s) of iron sulfide formation in sour corrosion is critical to study the subsequent effect on corrosion processes, enabling corrosion prediction and mitigation for pipelines, wells, and facilities in the oil and gas industry.

After the establishment of the theoretical thermodynamic model, verification of these Pourbaix diagrams is required by performing experiments. In fact, it is notoriously difficult to verify Pourbaix diagram due to a variety of theoretical and practical limitations.

First, thermodynamics is a science related to the equilibrium state defined by thermodynamic variables, which are independent on the path and the history (time elapsed) of the system. To be more specific, for given conditions of pH and potential, a specific iron sulfide is predicted to form by the Pourbaix diagram, but how that iron sulfide forms and how long it takes to form are unknown. Considering the stabilities of four different kinds of iron sulfides makes this thermodynamic model more complex and harder to verify. Moreover, in reality, most systems are transient, which means they are not in thermodynamic equilibrium and are gradually changing over time. In the present study, long-term corrosion tests were performed to test corrosion product stability predictions by the Pourbaix diagrams, and especially to compare the equilibrium state

(given by the line) in the Pourbaix diagram with the quasi-equilibrium state attained in long-term experiments.

In addition, there is another experimental challenge and that is to accurately determine pH and ferrous ion concentration at the corroding steel surface, which can be very different from those in the bulk. In the present work, a mesh-capped flat pH probe [109] was used for improved measurement of surface pH values. The measured ferrous ion concentration in the bulk solution in well-mixed conditions was used to approximate the surface ferrous ion concentration.

In this chapter dedicated to validation of Pourbaix diagrams the following was done:

1. Estimation of pH values at the corroding steel surface (described in detail in Appendix B: Surface pH Measurement). pH value at the corroding steel surface was explored by using a mesh-capped flat pH probe. The surface pH values measured in experiments could be very different from those in bulk solution, particularly in stagnant conditions, where the surface pH is up to 3 units higher than the bulk pH. However, an increase in turbulent flow diminished the difference between surface pH and bulk pH due to enhanced mass transfer. Experimental results revealed that surface pH was found to approaching the bulk pH at 400 rpm stirring speed in the experimental glass cell set up.
2. Verification of Pourbaix diagrams by performing long-term experiments at different temperatures, since thermodynamic properties are extremely sensitive to temperature.

3. Verification of predictions of corrosion products made by Pourbaix diagrams by changing solution pH.
4. Validation of predictions made by Pourbaix diagrams by polarizing corrosion potential on the steel (described in detail in Appendix C: Validation of Pourbaix Diagrams by Electrochemical Polarization).

## 5.2 Experimental

### 5.2.1 *Experimental for Verification by Long-term Tests at Different Temperature*

#### 5.2.1.1 Apparatus

The experimental setup is depicted in Figure 37. Experiments were carried out in a 2-liter glass cell filled with 1 wt. % sodium chloride (NaCl) electrolyte at atmospheric pressure. Square samples were suspended in the glass cell. One rotating cylinder electrode (RCE) sample was used as the working electrode to conduct electrochemical measurements, but was not rotated during the experiment. A platinum wire was used as the counter electrode. A saturated silver-silver chloride (Ag/AgCl (sat'd KCl)) electrode connected to the cell externally through a Luggin capillary was used as the reference electrode. The open circuit potential (OCP) of the RCE electrode was monitored using a potentiostat. A magnetic stirring bar (400 rpm) was used to mix the solution during the experiment. A mesh-capped pH probe was used to measure surface pH at the steel mesh surface and a regular pH probe was used to monitor bulk solution pH. The concentration of H<sub>2</sub>S in the mixed H<sub>2</sub>S/N<sub>2</sub> gas was adjusted by using a gas rotameter, and confirmed by a gas sample pump with H<sub>2</sub>S detector tubes. Sodium hydroxide solution and a carbon scrubber were used to remove H<sub>2</sub>S from the gas coming out of the glass cell.

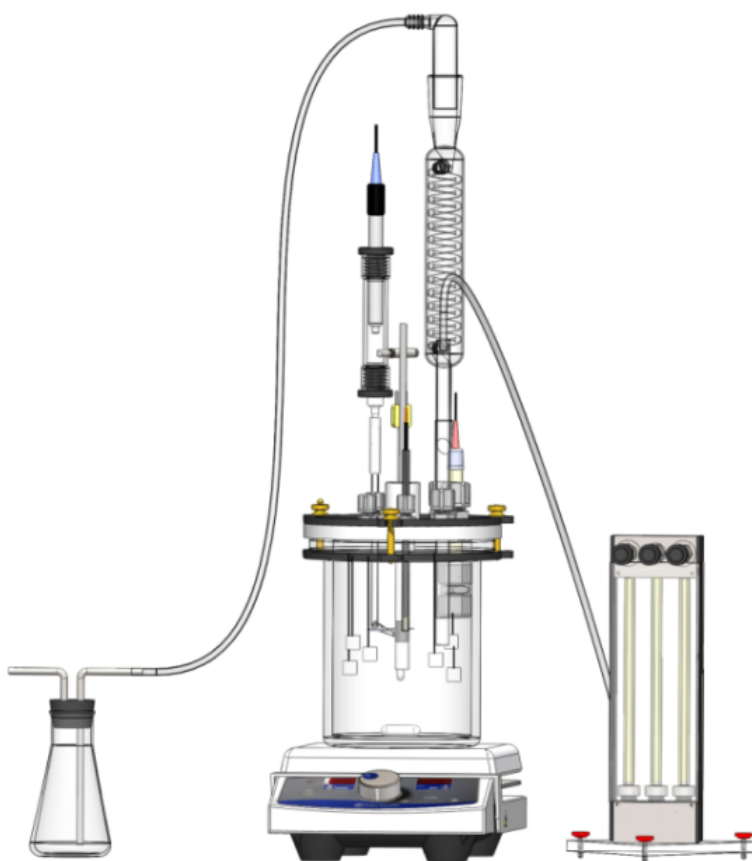


Figure 37. Experimental setup.

### 5.2.1.2 *Material*

The square samples with 1.2 cm x 1.2 cm x 0.2 cm dimension and the RCE sample with an exposed area of 5.4 cm<sup>2</sup> were machined from API<sup>(2)</sup> 5L X65 carbon steel. The chemical composition of this type of carbon steel is presented in Table 14.

Table 14 Chemical composition of 5L X65 carbon steel used in experiment (wt. %).

Cr	Mo	S	V	Si	C	Fe	Ni	Mn	P
0.14	0.16	0.009	0.047	0.26	0.13	Balance	0.36	1.16	0.009

<sup>(2)</sup> American Petroleum Institute(API), 1220 L Street, NW, Washington, DC 20005-4070

### 5.2.1.3 Procedure

The test matrix is shown in Table 15. The experiments were conducted with 10 % H<sub>2</sub>S in the gas phase at 25 °C and 80 °C, corresponding to a H<sub>2</sub>S partial pressure of 0.097 bar at 25 °C and 0.053 bar at 80 °C. Prior to a test, N<sub>2</sub> gas was sparged into the electrolyte until saturation to deoxygenate the solution (typically more than 4 hours). An H<sub>2</sub>S and N<sub>2</sub> pre-mixed gas was then sparged into the solution until the pH stabilized, and was sparged continuously throughout the experiment. Before positioning the steel samples in the glass cell, the solution pH was adjusted to 6.0 using deoxygenated NaOH solution. The RCE sample and square samples were finally polished with 600 grit sandpaper, and rinsed thoroughly with deionized water and isopropanol before immersion in solution. Corroded square samples were taken out for analysis at different points in time, rinsed with deoxygenated DI water and deoxygenated isopropanol, blown dry using N<sub>2</sub>, and stored in desiccator. Scanning electron microscope (SEM) imaging was used to detect the surface morphologies of the square samples. X-ray diffraction (XRD) was applied to determine which iron sulfides formed on the square samples. Both Linear Polarization Resistance (LPR) and weight loss methods were adopted for corrosion rate measurements. Approximately 10 ml of solution was drawn from the glass cell immediately before taking each steel specimen, filtered using a 0.22 μm syringe filter to remove any iron sulfide precipitate from solution, and then taken for the measurement of ferrous ion concentration using a spectrophotometric method (See Appendix A.1).

Table 15 Test matrix.

Description	Parameter
Temperature	25 °C, 80 °C
Electrolyte	1 wt.% NaCl brine
Gas composition	10% H <sub>2</sub> S/balance N <sub>2</sub>
H <sub>2</sub> S partial pressure	0.097 bar (25 °C), 0.053 bar(80 °C)
Speed of stir bar	400 rpm
Material	API 5L X65

### 5.2.2 *Experimental for Verification by Adjusting Solution pH*

#### 5.2.2.1 *Apparatus*

Verification of Pourbaix diagrams was conducted by adjusting pH and investigating the consequent corrosion products after the pH adjustment. The experimental set up was identical to the one used in the above section, as shown in Figure 37. Experiments were performed in a 2 L glass cell filled with 1 wt. % NaCl electrolyte. Ten square samples were hung in the glass cell. One RCE sample was used to conduct electrochemical measurements but was not rotated during experiment. A magnetic stirring bar with 400 rpm stirring speed was used to mix the solution.

#### 5.2.2.2 *Material*

Ten square samples of 1.2 cm x 1.2 cm x 0.2 cm dimension made of API 5L X65 carbon steel were hung in glass cell. One RCE sample made of the same material, 5L X65, was used to conduct electrochemical measurements.

#### 5.2.2.3 *Procedure*

The experiments were conducted according to the experimental design shown in Figure 38, which shows the sample removal times with specific analysis designations for each. The test matrix of this set of experiment is shown in Table 15.

The experiment was conducted at 25 °C following the same procedure for verifying Pourbaix diagrams by conducting long-term tests at different temperatures (5.2.1). However, solution pH was adjusted from 5.5 to 11.5 after seven days of exposure by using deoxygenated 1M NaOH solution. The experiment was carried out for 8 days. Square samples made of 5L X65 pipeline steel were hung in solution from the beginning of the test, and were taken out for analysis on the days indicated in the timeline in Figure 171. The corrosion products formed on square samples after pH adjustment were identified by XRD, and correlated with the predictions made by Pourbaix diagrams.

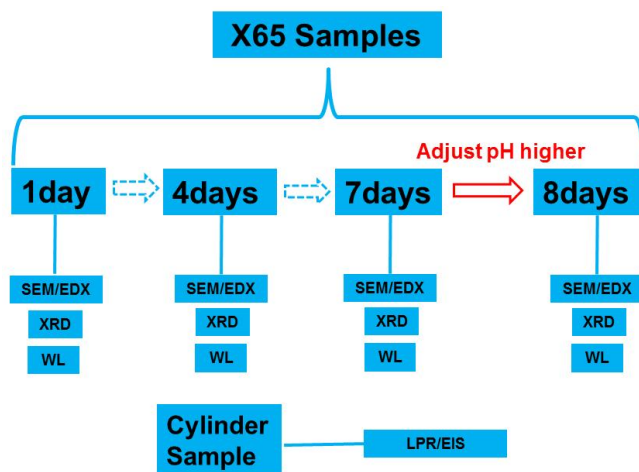


Figure 38. Experimental design for pH adjustment.

### 5.3 Results and Discussion

#### 5.3.1 Validation by Long-term Tests at Different Temperature

##### 5.3.1.1 Verification of Pourbaix Diagram for $H_2S-H_2O-Fe$ System at 25 °C

To verify the basis of this thermodynamic model, the first corrosion test was performed at 25°C. Figure 39 (a) shows the surface pH, bulk pH, and the ferrous ion concentration in the bulk solution changing over time. One can observe that the surface

pH is approximately 0.5 pH unit higher than the bulk pH in the initial three days, which reflects the rapid release of  $\text{Fe}^{2+}$  ions and the consumption of hydrogen ions in the corrosion reaction. After three days, the surface pH was lower than the bulk pH, due to the release of hydrogen ions (acidification) during precipitation of iron sulfide. Figure 39 (b) shows that both the corrosion rate and the OCP had small changes in the first day and were then very stable through the seven days of the experiment.

At the time each square sample was removed from the cell for the determination of corrosion product composition, a set of operational parameters was determined and used to define the “operational point” in the Pourbaix diagram. This includes the values of OCP and surface pH, ferrous ion concentration,  $\text{H}_2\text{S}$  partial pressure, and temperature.

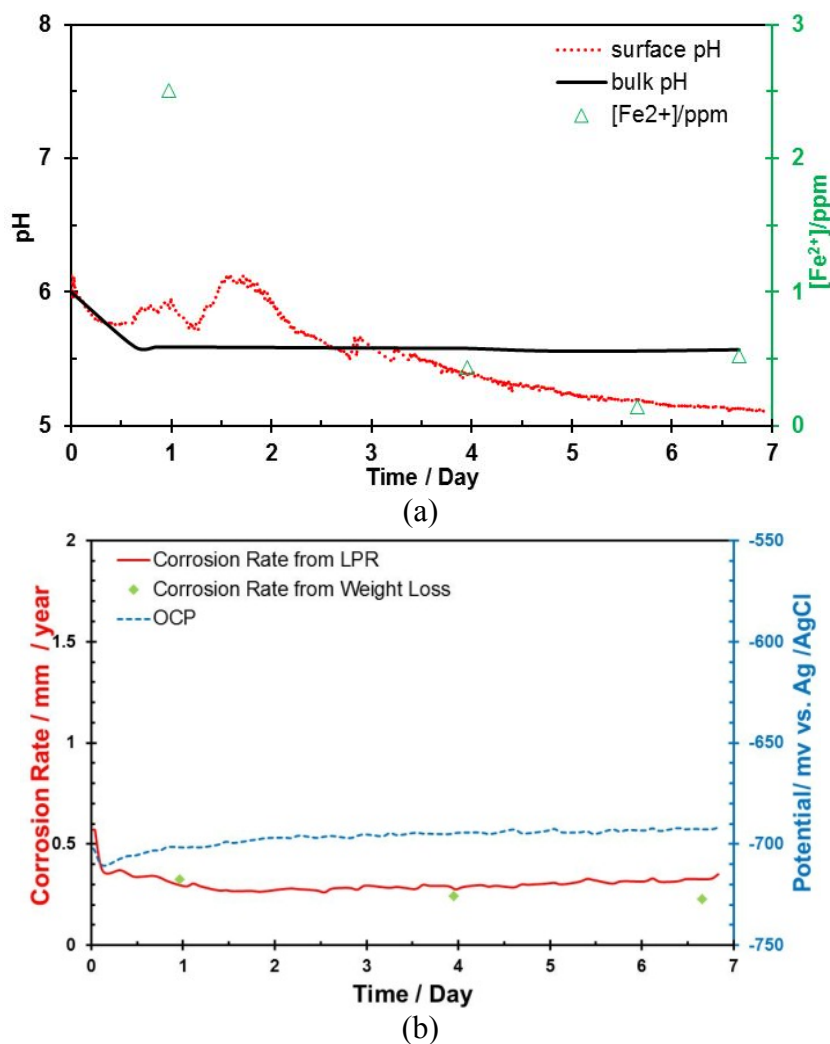


Figure 39. (a) Measured bulk pH, surface pH, and  $[Fe^{2+}]$ ; (b) Corrosion rate and OCP during experiment at 25 °C.

### 5.3.1.2 Verification of Pourbaix Diagram for $H_2S-H_2O-Fe$ System at 25 °C

#### 5.3.1.2.1 *Results after 1 Day of Exposure*

Figure 40 (a), (b) show the surface morphologies of the sample after one day of exposure. A partially covered corrosion product layer was observed on the surface, and was identified to be only mackinawite by XRD, as shown in Figure 40 (c).

Figure 41 shows the Pourbaix diagram constructed at this experimental condition, which considers only mackinawite corrosion product and excludes other polymorphous

or related iron sulfides. According to the intersection of potential and surface pH from the measurement in Figure 41, mackinawite was predicted to form on the steel surface, which was also detected by experiment.

Moreover, the operational point is a little to the right of the equilibrium line between mackinawite and aqueous  $Fe^{2+}$ , which indicates a slight supersaturation for mackinawite (a non-equilibrium state) at this condition. This statement is quantified by calculating the saturation value for mackinawite, using Equation (4), which gives  $S = 20$ . This could be an experimental artifact resulting from the errors made in estimating the surface pH and ferrous ion concentration, but it could also be true – indicating that kinetics of mackinawite formation at 25 °C lag behind the corrosion process. If the latter is true, as time progresses, one would expect the saturation value to decrease and the intersection of potential and surface pH to be closer to the equilibrium line, which is exactly what is seen in the results collected after 4 days and 7 days of exposure (see below).

$$S = \frac{[Fe^{2+}][HS^-]}{K_{sp,2}[H^+]} \quad (42)$$

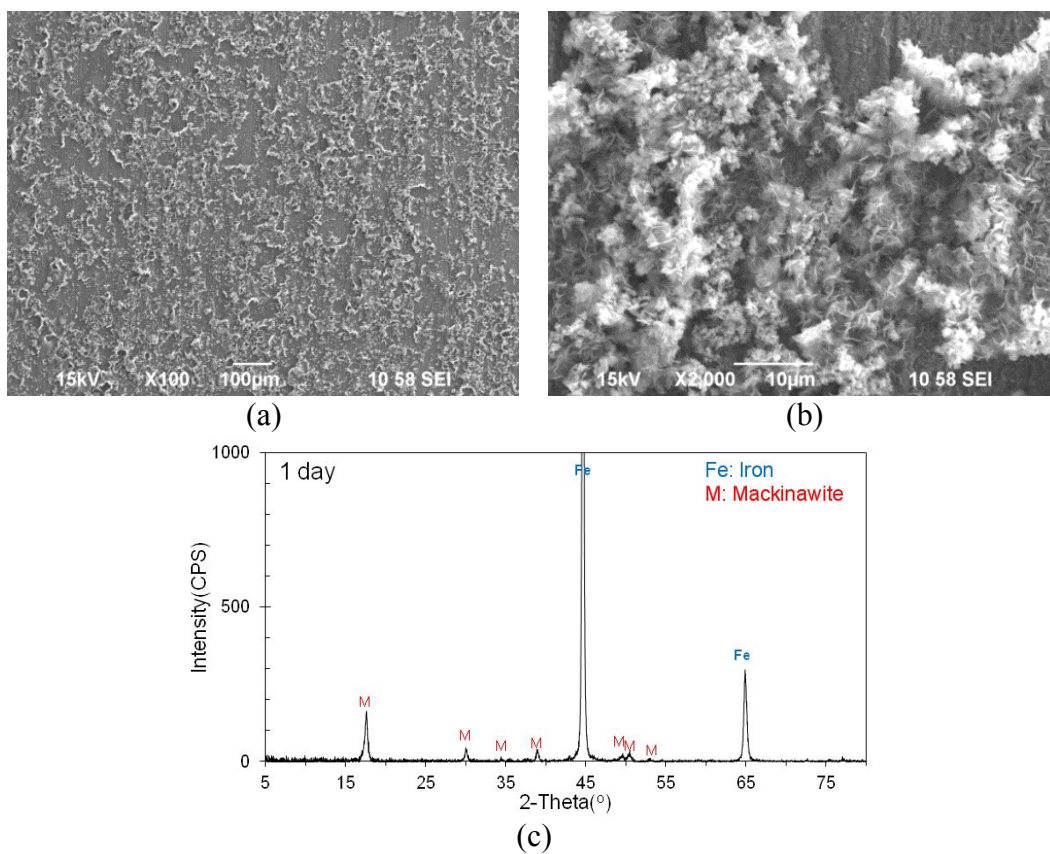


Figure 40. Corrosion product layer after 1 day of exposure at 25 °C: (a) Surface morphology with x100 magnification; (b) Surface morphology with 2,000x magnification; (c) XRD pattern.

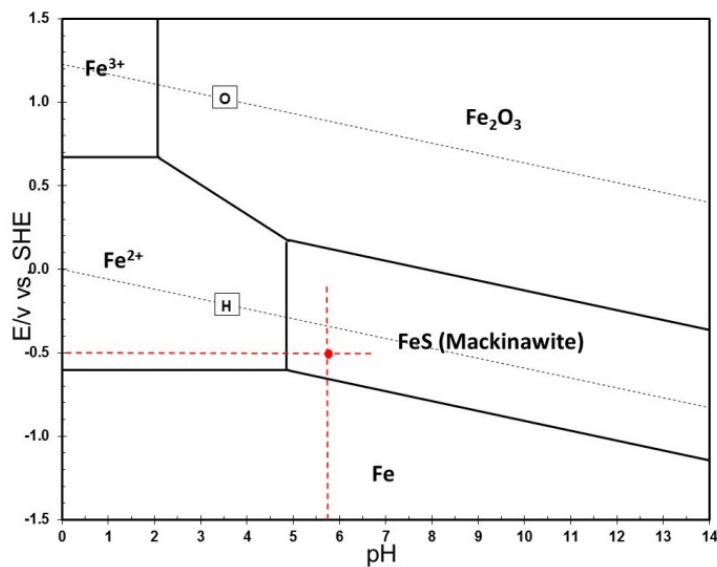


Figure 41. Verification of Pourbaix diagram after 1 day of exposure (Pourbaix diagram was generated at T = 25 °C,  $p_{\text{H}_2\text{S}} = 0.097$  bar,  $[\text{Fe}^{2+}] = 2.5$  ppm,  $[\text{Fe}^{3+}] = 1.0 \times 10^{-6}$  M).

#### 5.3.1.2.2 Results after 4 Days of Exposure

Figure 42 shows the surface morphology and compositional analysis of the corrosion product layer on the steel surface after 4 days of exposure. A steel surface covered with more corrosion product layer was observed in Figure 42 (a). SEM image at higher magnification (Figure 42 (b)) shows this corrosion product to be in the form of “plates” and some slender needle-like clusters. The XRD pattern in Figure 42 (c) suggests the presence of mackinawite with a small amount of pyrrhotite. According to the Pourbaix diagrams constructed at this experimental condition shown in Figure 43, the expected corrosion products are mackinawite and pyrrhotite, which were both detected by XRD. The dominant corrosion product, mackinawite, is a thermodynamically metastable phase which forms first because of its faster kinetics. It will transform to a more thermodynamically stable phase, pyrrhotite or pyrite, over time. However, the time of this transformation cannot be depicted in the Pourbaix diagram, and two different Pourbaix diagrams are shown in Figure 43.

Furthermore, comparing with the previous results collected after one day of exposure, the operational point in Figure 43 (a) is much closer to the equilibrium line for mackinawite, and the saturation value is 2. This implies that the system is approaching the equilibrium for formation of mackinawite. The operational point in the Pourbaix diagram showing pyrrhotite, Figure 43 (b), is further to the right of the equilibrium line, suggesting a slower kinetics of formation.

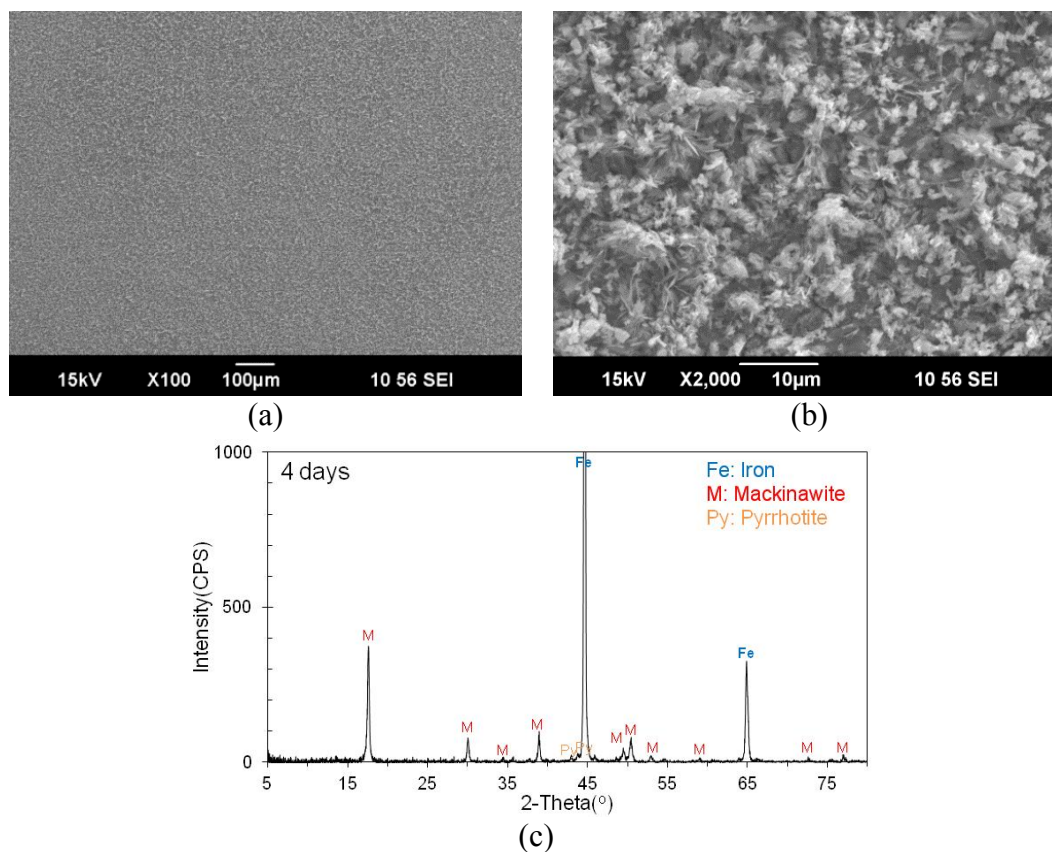


Figure 42. Corrosion product layer after 4 days of exposure at 25 °C: (a) SEM image of surface morphology with 100x magnification; (b) SEM image of surface morphology with 2,000x magnification; (c) XRD pattern.

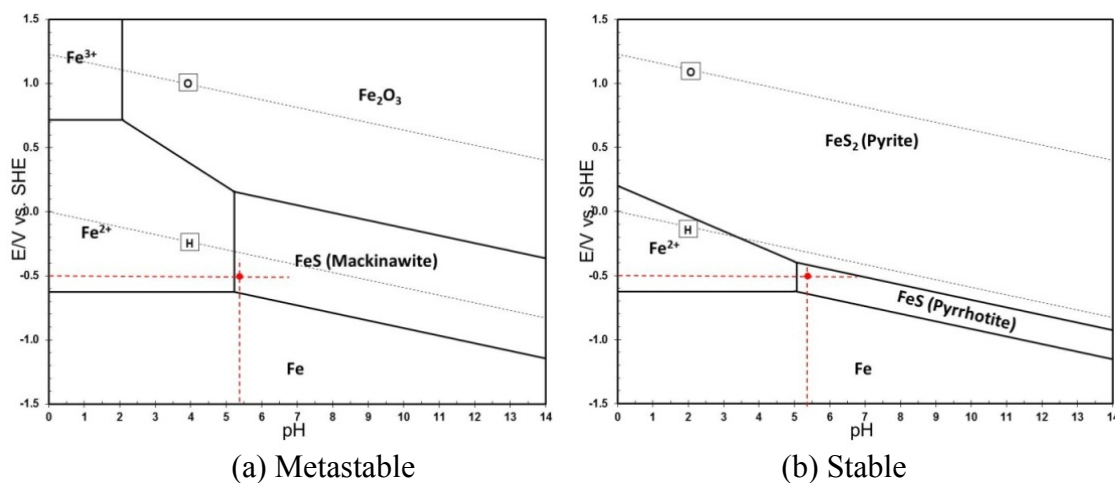


Figure 43. Verification of Pourbaix diagram after 4 days of exposure (Pourbaix diagram was generated at T = 25 °C, p<sub>H<sub>2</sub>S</sub> = 0.097 bar, [Fe<sup>2+</sup>] = 0.44 ppm, [Fe<sup>3+</sup>] = 1.0 × 10<sup>-6</sup> M): (a) Mackinawite; (b) Mackinawite / Greigite / Pyrrhotite / Pyrite.

#### 5.3.1.2.3 Results after 7 Days of Exposure

Figure 44 demonstrates the morphology and composition of the corrosion product layer on the steel surface after corroding for 7 days. The SEM image with x100 magnification shows a fully covered steel surface. The SEM image with higher magnification presents a mixture of flaky crystals and needle-like clusters. Again, mackinawite and pyrrhotite were detected by XRD with mackinawite as the dominant polymorph. Referring to the Pourbaix diagrams generated at this experimental condition (Figure 45), mackinawite and pyrrhotite were predicted as stable, which were also detected in the experiment.

In addition, the operational point is almost on the equilibrium line between mackinawite and ferrous ion in Figure 45 (a), which indicates, that after long-term exposure for 7 days, the system finally reached a state very close to the equilibrium between mackinawite precipitation and dissolution, which is here called quasi-equilibrium. The saturation value for mackinawite after 7 days of test was computed to be 0.7. The operational point in the Pourbaix diagram showing pyrrhotite given in Figure 45 (b) is also closer to the equilibrium line suggesting that the formation of pyrrhotite also approached equilibrium after 7 days of exposure at 25 °C. The consistency of these results presents credible evidence in favor of the accuracy of the current thermodynamic model, at least for 25 °C.

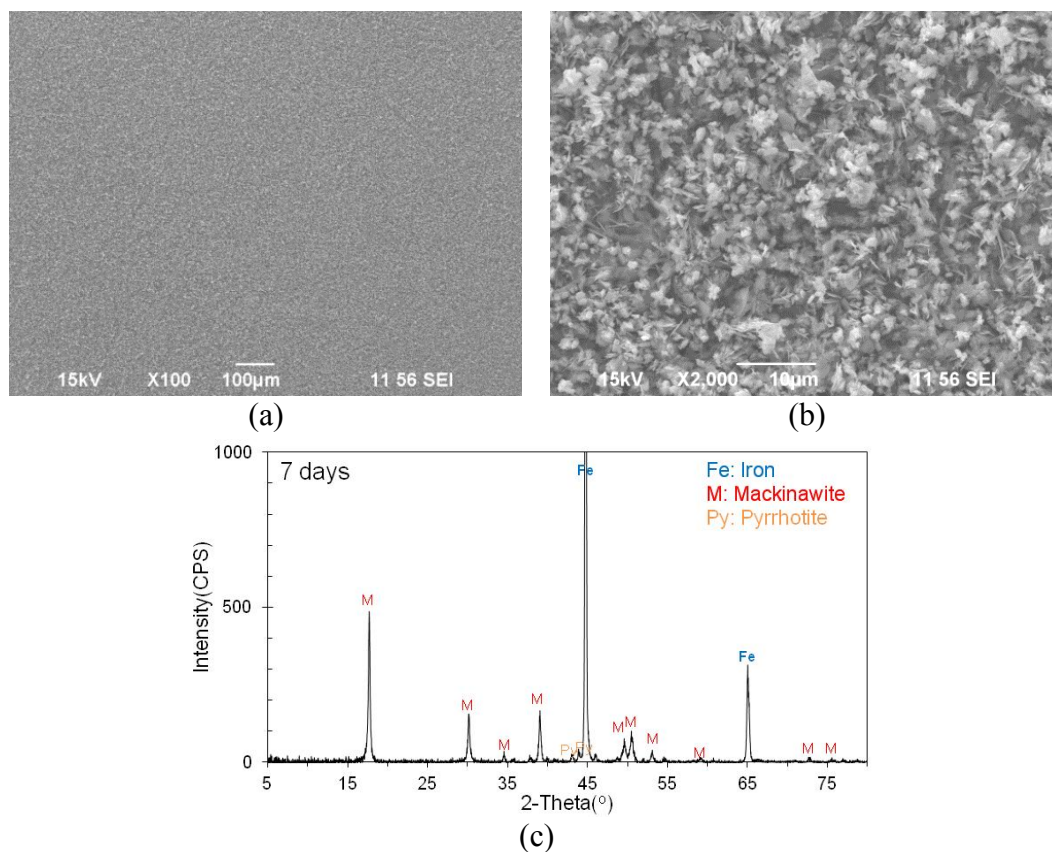


Figure 44. Corrosion product layer after 7 days of exposure at 25 °C: (a) SEM image of surface morphology with 100x magnification; (b) SEM image of surface morphology with 2,000x magnification; (c) XRD pattern.

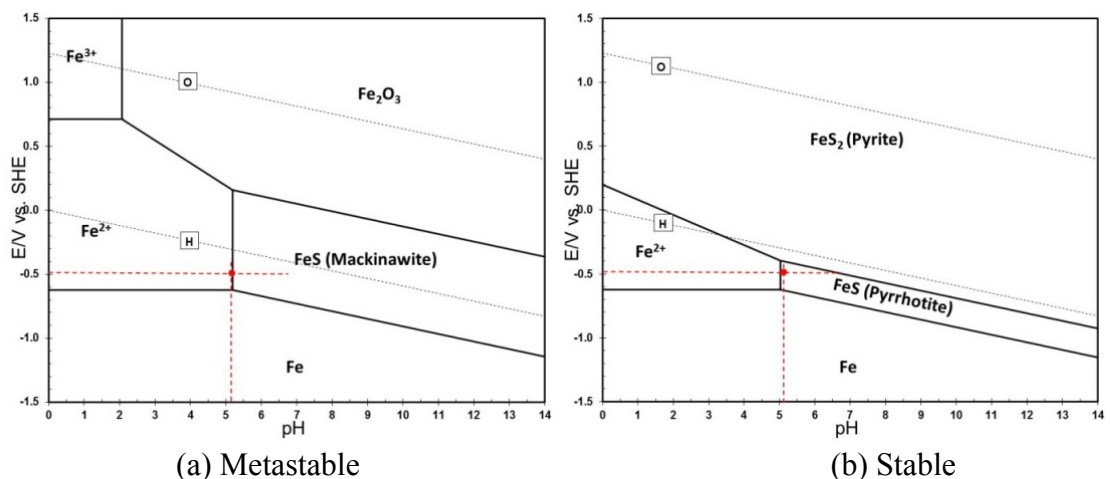


Figure 45. Verification of Pourbaix diagram after 7 days of exposure (Pourbaix diagram was generated at T = 25 °C,  $p\text{H}_2\text{S} = 0.097\text{bar}$ ,  $[\text{Fe}^{2+}] = 0.52\text{ ppm}$ ,  $[\text{Fe}^{3+}] = 1.0 \times 10^{-6}\text{ M}$ ): (a) Mackinawite; (b) Mackinawite / Greigite / Pyrrhotite / Pyrite.

### 5.3.1.3 Verification of Pourbaix Diagram for $H_2S-H_2O-Fe$ System at $80^\circ C$

It is known that increasing temperature facilitates the transformation of the metastable phases, mackinawite or greigite, into more stable phases: pyrrhotite or pyrite. Compared to the low temperature experiments presented above, different phases of iron sulfides should be detected at the higher temperature conditions. Moreover, increasing temperature also expedites the kinetics and the approach of the equilibrium state. Therefore, a second set of experiments at higher temperature,  $80^\circ C$ , were carried out for verification.

Figure 46 (a) shows the bulk pH monitored and  $[Fe^{2+}]$  measured through the experiment. Figure 46 (b) demonstrates the evolution of OCP and corrosion rates during the test. The corrosion rate decreased from 1.1 mm/year to a stable value around 0.07 mm/year in the first four days probably due to the formation of a protective mackinawite layer, but then increased gradually. A significant change in OCP was also observed at the same time. This effect on the corrosion rate is very interesting and could be the effect of other iron sulfide phases forming on the steel surface.

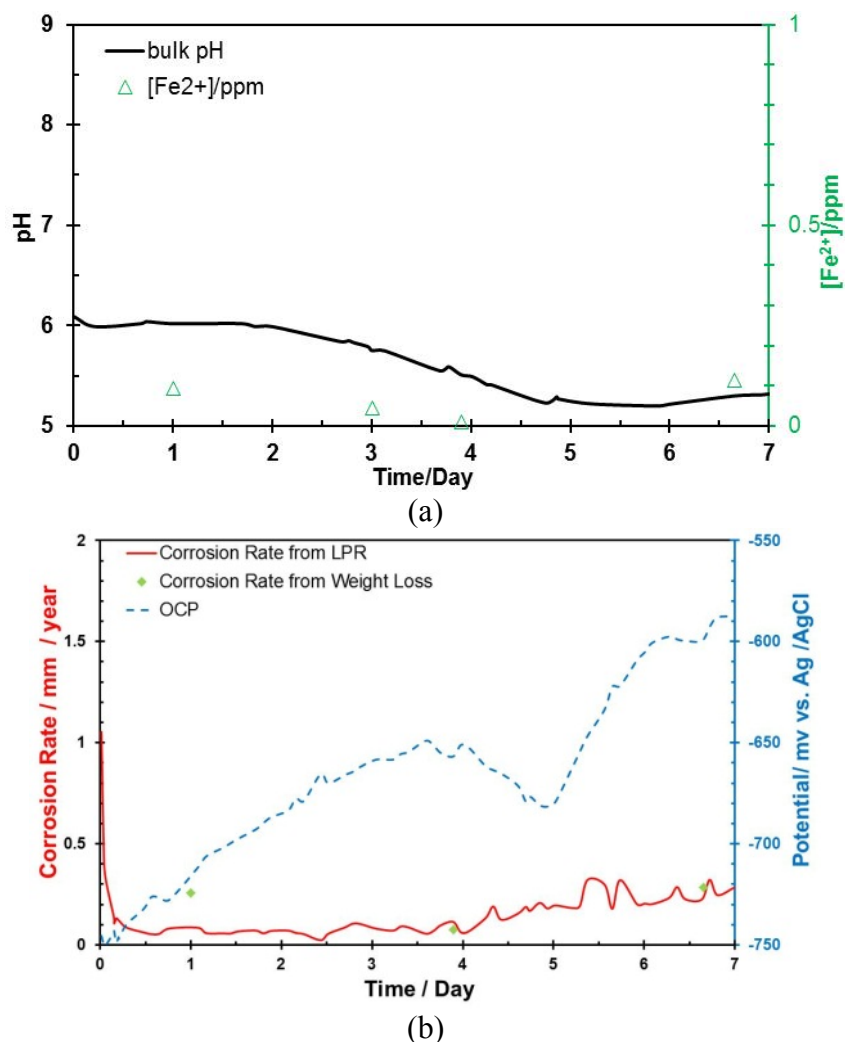


Figure 46. (a) Measured bulk pH and  $[Fe^{2+}]$ ; (b) Corrosion rate and OCP during experiment at 80 °C.

#### 5.3.1.3.1 Results after 1 Day of Exposure

In Figure 47, the SEM images show a uniform corrosion product layer formed on the steel surface after 1 day of exposure, which was characterized to be only mackinawite by XRD. According to the Pourbaix diagram generated at experimental conditions after 1 day in Figure 48, the mackinawite corrosion product was predicted, which matches the experimental results. The operational point is to the right of the equilibrium line, indicating the system is in non-equilibrium state for mackinawite formation after 1 day.

The saturation value for mackinawite was computed to be 78, which suggests the precipitation of mackinawite was not close to an equilibrium state. Even if the precipitation of mackinawite was accelerated at 80 °C, so was the corrosion rate, making it difficult to reach equilibrium after only 1 day of exposure.

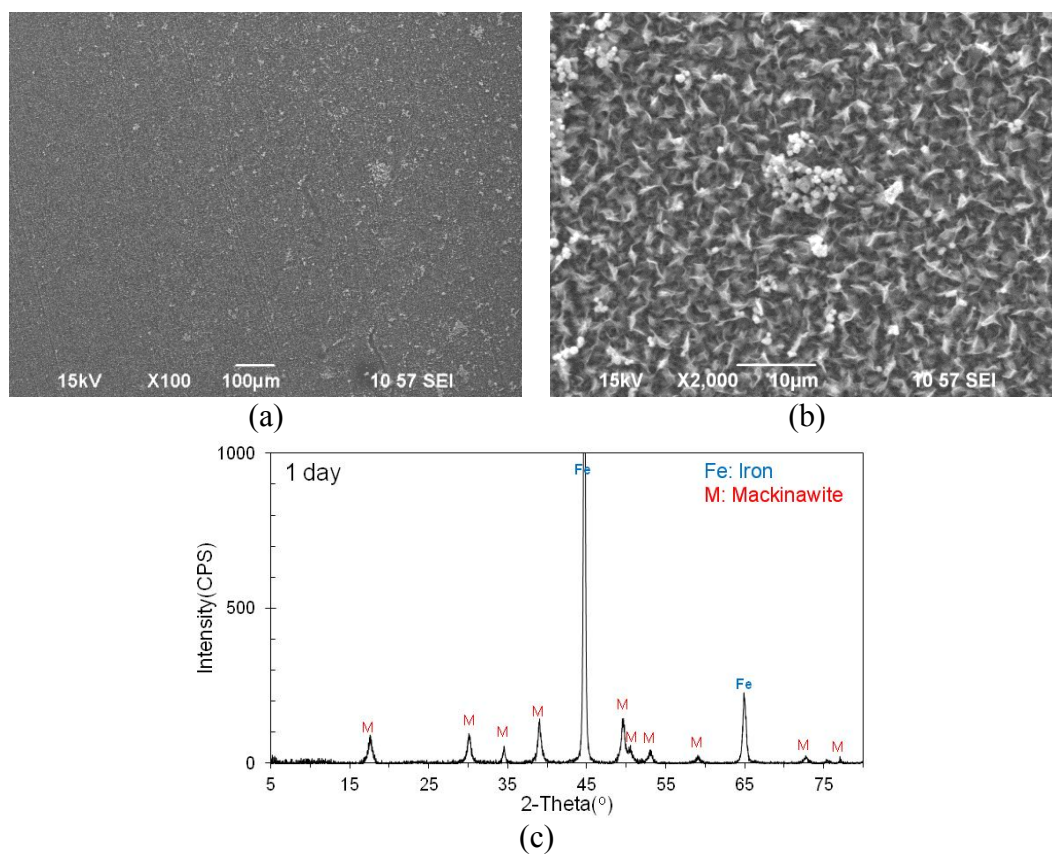


Figure 47. Corrosion product layer after 1 day of exposure at 80 °C: (a) SEM image of surface morphology with 100x magnification; (b) SEM image of surface morphology with 2,000x magnification; (c) XRD pattern.

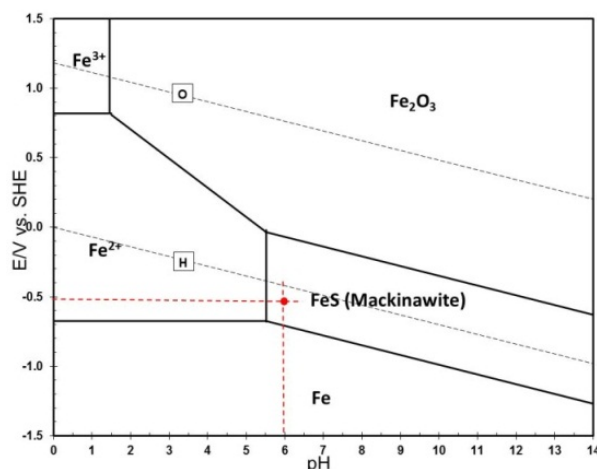


Figure 48. Verification of Pourbaix diagram after 1 day of exposure (Pourbaix diagram was generated at  $T = 80\text{ }^{\circ}\text{C}$ ,  $p\text{H}_2\text{S} = 0.053\text{ bar}$ ,  $[\text{Fe}^{2+}] = 0.1\text{ ppm}$ ,  $[\text{Fe}^{3+}] = 1.0 \times 10^{-6}\text{ M}$ ).

#### 5.3.1.3.2 Results after 4 Days of Exposure

Figure 49 shows the surface morphologies and composition of the corrosion product layer on the sample surface after 4 days of exposure. Figure 49 (b) shows some small cubic crystals on the corrosion product layer, which are suspected to be pyrite. From XRD patterns, besides mackinawite and pyrrhotite, a new iron sulfide phase was detected as pyrite, which never appeared in the previous experiment at  $25\text{ }^{\circ}\text{C}$ . That is because pyrite is a thermodynamically stable phase whose formation was favored by the high temperature in this test. Table 16 gives quantitative analysis of the formed corrosion products by following Reference Intensity Ratio (RIR) methodology (See Appendix A.2). Mackinawite accounts for 76.4 % and pyrite makes up 4.8 % of the total detected layer on the sample surface.

The formation of pyrite was also predicted by the Pourbaix diagram generated according to experimental conditions after 4 days, as shown in Figure 50. From Figure 50 (a), we can see that the operational point is very close to the boundary for mackinawite

formation, which indicates the state of quasi-equilibrium for this phase. The fact that the point is slightly to the left of the line (in the undersaturated region) could indicate that mackinawite gradually converted into pyrite, although the margin is too small to be certain. The same operational point shown in Figure 50 (b) is very close to the boundary for pyrite formation, confirming the XRD findings.

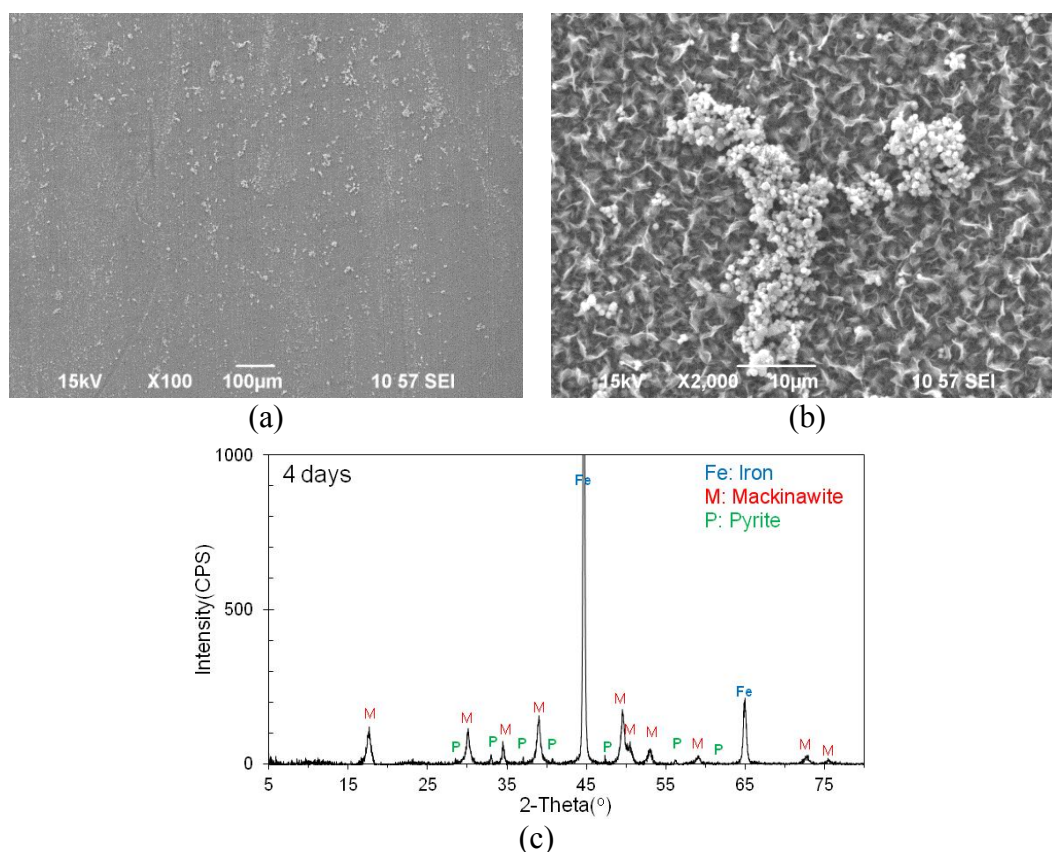


Figure 49. Corrosion product layer after 4 days of exposure at 80 °C: (a) SEM image of surface morphology with 100x magnification; (b) SEM image of surface morphology with 2,000x magnification; (c) XRD pattern.

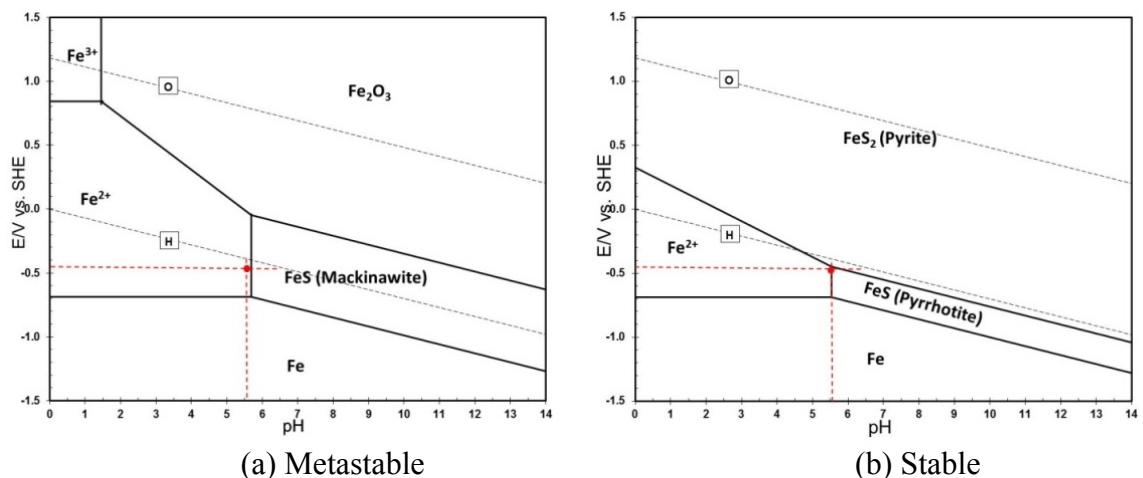


Figure 50. Verification of Pourbaix diagram after 4 days of exposure (Pourbaix diagram was generated at  $T = 80\text{ }^{\circ}\text{C}$ ,  $\text{pH}_2\text{S} = 0.053\text{ bar}$ ,  $[\text{Fe}^{2+}] = 0.045\text{ ppm}$ ,  $[\text{Fe}^{3+}] = 1.0 \times 10^{-6}\text{ M}$ ): (a) Mackinawite; (b) Mackinawite / Greigite / Pyrrhotite / Pyrite.

#### 5.3.1.3.3 Results after 7 Days of Exposure

The surface morphologies and composition of the corrosion product layer on the steel surface after 7 days of exposure are shown in Figure 51. The appearance is similar to the result from 4 days of exposure shown in Figure 49. The major difference is the quantities of the different iron sulfide phases. The SEM images in Figure 51 show more cubic crystals in lighter color on the steel surface compared to the previous 4-day sample, which is probably due to the increase in the amount of the pyrite phase. The growth of the pyrite phase is proven by the quantitative analysis of the corrosion product layer presented in Table 16. Comparing with the sample after 4 days, the percentage of pyrite grew from 4.8 % to 27.8 %. This growth is significant, and may suggest rapid kinetics of the growth of pyrite crystal after the nucleation. In contrast, the pyrrhotite phase is reported to nucleate quickly but grow sluggishly, which was also detected, changing from 5.8 % after 4 days to 14.8 % after 7 days. At the same time, the percentage of mackinawite decreased from 76.4 % to 49.2 %.

The formation of different phases of iron sulfide can be predicted with the Pourbaix diagrams generated at corresponding experimental conditions, shown in Figure 52. The experimental data point in Figure 52 (a) is a little left to the boundary of mackinawite formation, which could again be indicating the transformation of mackinawite into pyrite and pyrrhotite. The experimental data point in Figure 52 (b) is close to the “triple point” where all three phases: mackinawite, pyrite and pyrrhotite are stable matching XRD findings. Generally, it can be concluded that at 80 °C the calculated Pourbaix diagrams are in reasonable agreement with the experimental results, confirming their validity. Furthermore, the Pourbaix diagrams offered complementary information to those obtained by electrochemical and analytical techniques, thereby improving our understanding of the complex evolution of the corrosion process under conditions where different iron sulfide polymorphs and related phases form.

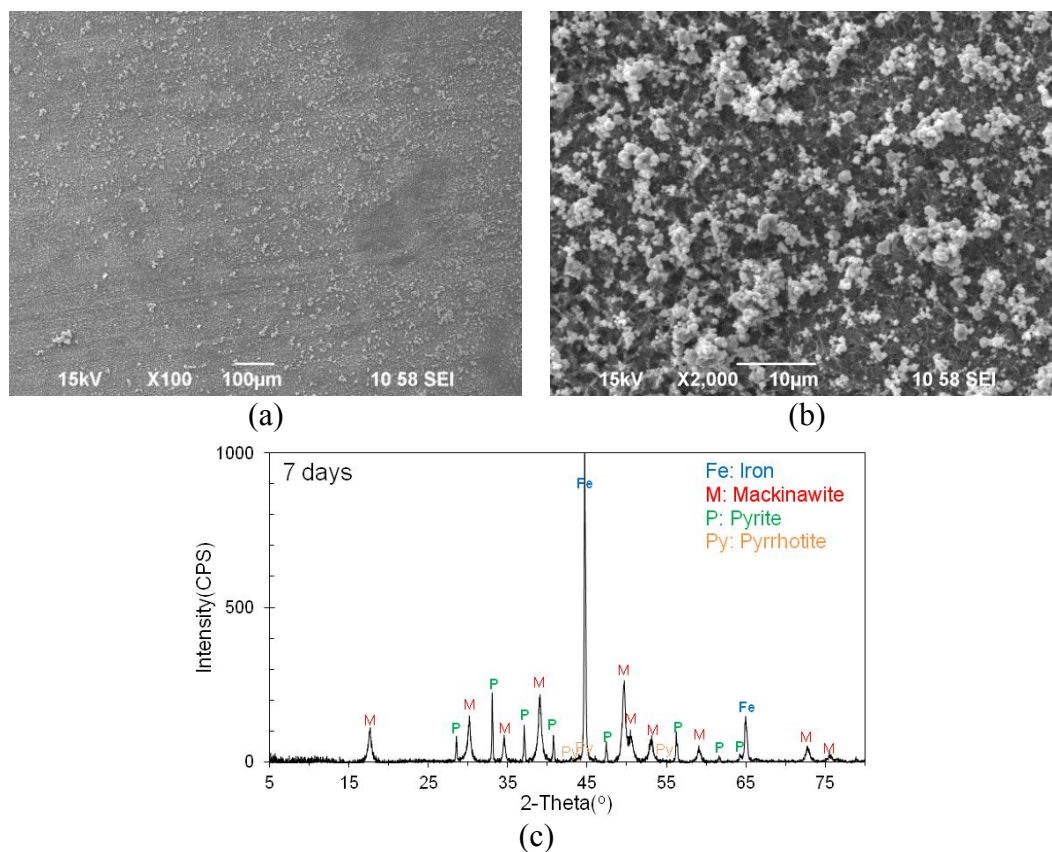


Figure 51. Corrosion product layer after 7 days of exposure at 80 °C: (a) SEM image of surface morphology with 100x magnification; (b) SEM image of surface morphology with 2,000x magnification; (c) XRD pattern.

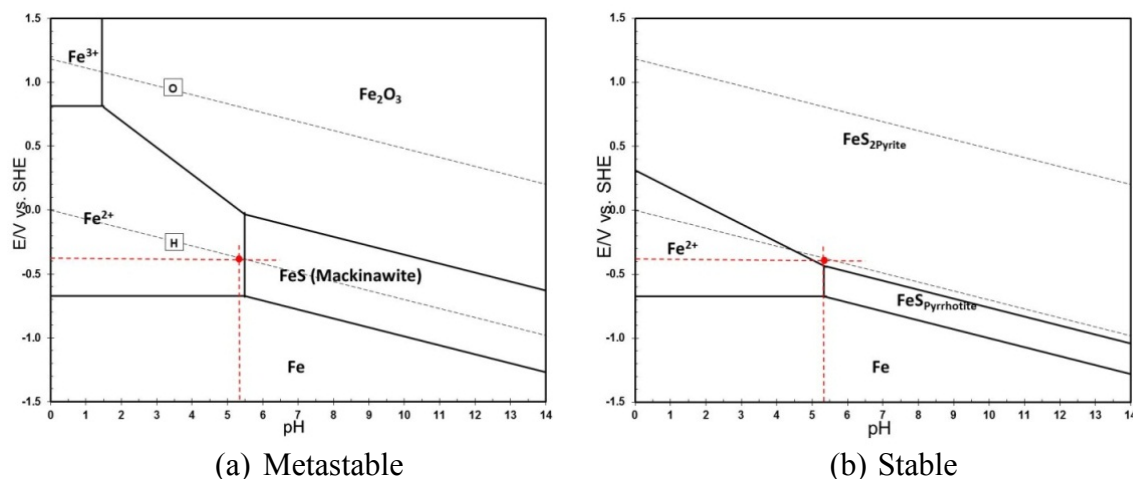


Figure 52. Verification of Pourbaix diagram after 7 days of exposure (Pourbaix diagram was generated at T = 80 °C, p<sub>H<sub>2</sub>S</sub> = 0.053 bar, [Fe<sup>2+</sup>] = 0.115 ppm, [Fe<sup>3+</sup>] = 1.0 x 10<sup>-6</sup> M): (a) Mackinawite; (b) Mackinawite / Greigite / Pyrrhotite / Pyrite.

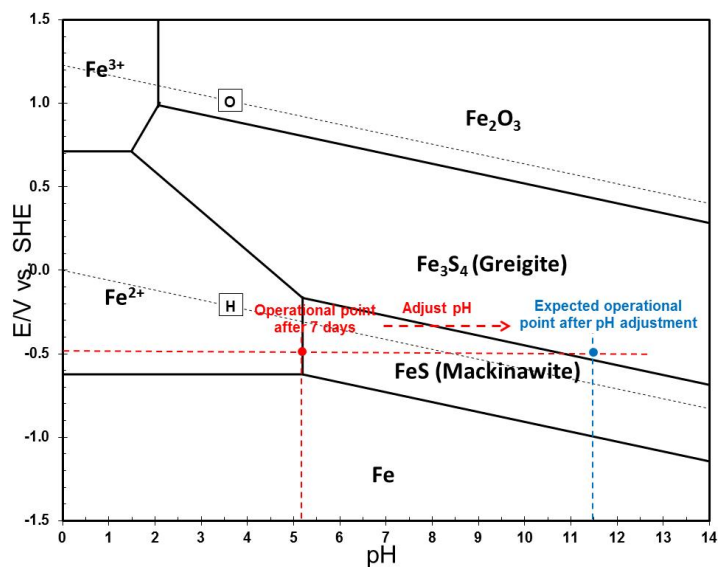
Table 16 XRD quantitative analysis of the formed corrosion products layer at 80 °C (The steel phase was detected by XRD, but was removed from the quantitative analysis).

Phases	Mackinawite	Pyrrhotite	Greigite	Pyrite	Iron
After 4 days	76.4%	5.8%	2.2%	4.8%	10.8%
After 7 days	49.2%	14.8%	3.3%	27.8%	4.9%

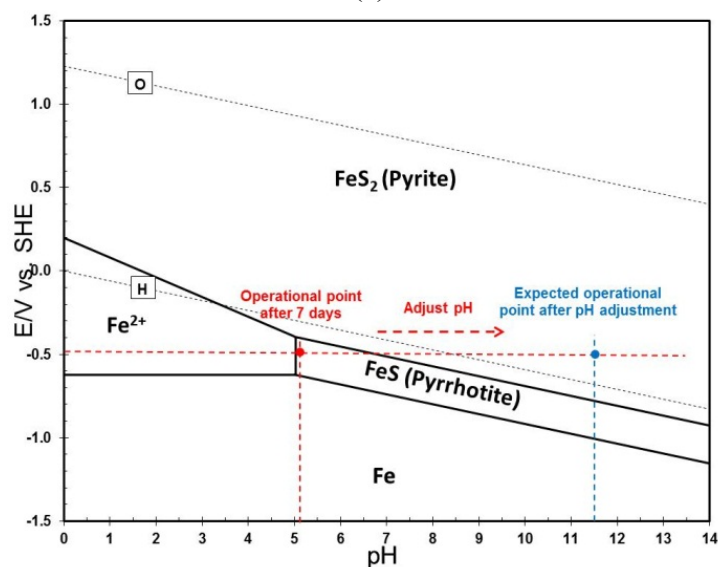
### 5.3.2 Validation by Adjusting Solution pH

#### 5.3.2.1 Hypothesis of Verification of Pourbaix Diagram by Adjusting Solution pH

Pourbaix diagrams were verified by conducting long-term tests at different temperature, 25 °C and 80 °C, respectively, as shown in 5.3.1. Since the Pourbaix diagram is a potential-pH stability diagram, a change in solution pH may lead to different corrosion products. Therefore, the Pourbaix diagrams can also be validated by adjusting solution pH and investigating the resultant corrosion products. The hypothesis of validation of Pourbaix diagram by adjusting solution pH is interpreted in Figure 53. Figure 53 shows the Pourbaix diagrams generated in accordance with the experimental conditions after 7 days in the previous test conducted at 25°C (5.3.1). The red points in Figure 53 represent the operational points after 7 days of exposure. It is known that the mackinawite and pyrrhotite phases were detected as corrosion products after 7 days of exposure at 25°C. One can expect the formation of different phases of iron sulfides if the solution pH is adjusted to a higher value: greigite in Figure 53 (a) or pyrite in Figure 53 (b) (shown as the blue points).



(a)



(b)

Figure 53. Hypothesis of verification of Pourbaix diagram by adjusting pH (Pourbaix diagram was generated at  $T = 25\text{ }^{\circ}\text{C}$ ,  $p\text{H}_2\text{S} = 0.097\text{ bar}$ ,  $[\text{Fe}^{2+}] = 0.52\text{ ppm}$ ,  $[\text{Fe}^{3+}] = 1.0 \times 10^{-6}\text{ M}$ ): (a) Mackinawite / Greigite; (b) Mackinawite / Greigite / Pyrrhotite / Pyrite.

### 5.3.2.2 Verification of Pourbaix Diagram for $\text{H}_2\text{S}$ - $\text{H}_2\text{O}$ - $\text{Fe}$ System by Adjusting pH at $25\text{ }^{\circ}\text{C}$

The results of the initial seven days of the test performed at  $25\text{ }^{\circ}\text{C}$  were presented in the previous section (5.3.1). After seven days of exposure, the solution pH was

adjusted from 5.5 to 11.5 using deoxygenated 1.0 M NaOH solution on the basis of the hypothesis to facilitate the formation of greigite and/or pyrite. The evolution of bulk pH, surface pH, and ferrous ion concentration in solution through the experiment is shown in Figure 54 (a). The bulk pH was adjusted to 11.5, but decreased to 7 quickly due to precipitation from the bulk solution induced by the high pH, as shown in Equation (43). OCP and corrosion rates are presented in Figure 54 (b), where a large increase in both OCP and corrosion rate was observed after adjusting pH. Weight loss was also conducted to confirm LPR measurements. The previous accumulation was subtracted from the last two weight loss results, shown as blue points in Figure 54 (b), for proper comparison with corrosion rate obtained from LPR. The weight loss results agreed well with LPR results, showing a large increase in the corrosion rate after increasing solution pH. This increase in corrosion rate is unexpected but is also of interest, which may be due to the formation of new phases of iron sulfides. A full interpretation of this observation and the detailed mechanism was presented in Chapter 6 and Chapter 7.

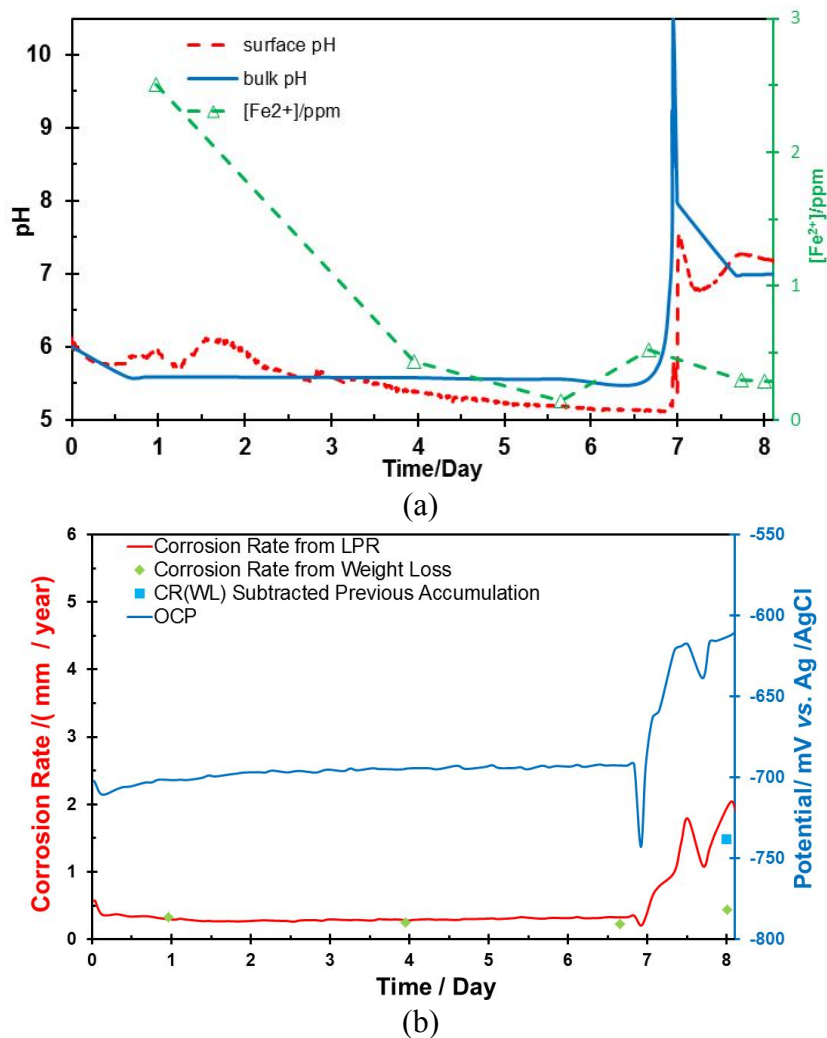


Figure 54. (a) Measured bulk pH, surface pH, and [Fe<sup>2+</sup>]; (b) Corrosion rate and OCP during experiment.

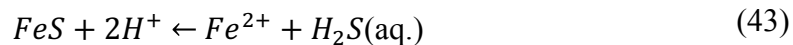


Figure 55 (a) (SEM image with 50x magnification) shows the surface morphology of the steel sample after 8 days, where an exfoliated corrosion product layer on the sample surface was observed. Further, Figure 55 (b) (SEM image with x4,000 magnification) shows some framboidal (raspberry like) clusters consisting of small cubic crystals on the corrosion product layer, which are suspected to be greigite or pyrite (the

Bravais lattices of each are cubic). The iron sulfides formed were defined to be a mixture of dominant mackinawite and greigite by XRD in Figure 55 (c). It is noticed that the greigite phase was detected after adjusting solution pH. Table 17 presents quantitative analysis of the corrosion product layer formed at the steel samples surface. The greigite phase was not seen before the pH adjustment (after 7 days). However, 9.0 % of the greigite phase was detected after the pH adjustment (after 8 days). Hence, the pH adjustment after 7 days induced the formation of greigite, which is a thermodynamically favored phase at high pH condition comparing with mackinawite.

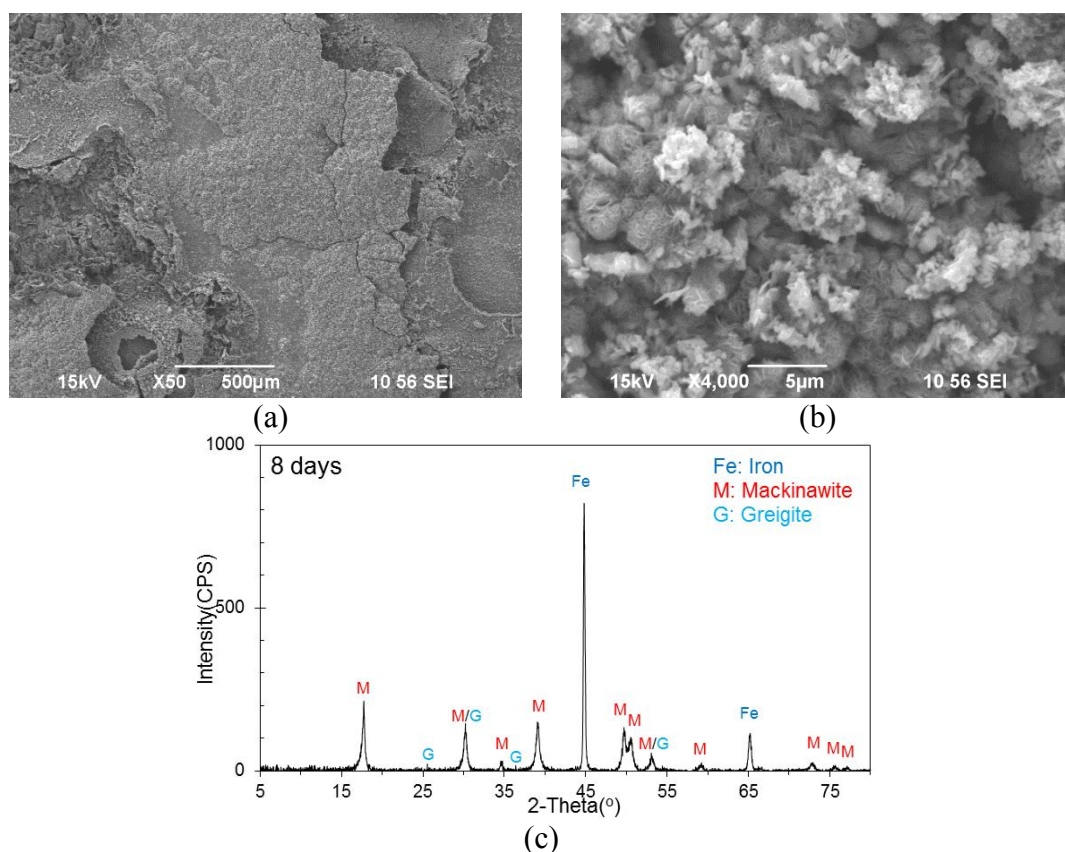


Figure 55. Corrosion product layer after 8 days of exposure at 25 °C: (a) SEM image of surface morphology with 50x magnification; (b) SEM image of surface morphology with 4,000x magnification; (c) XRD pattern.

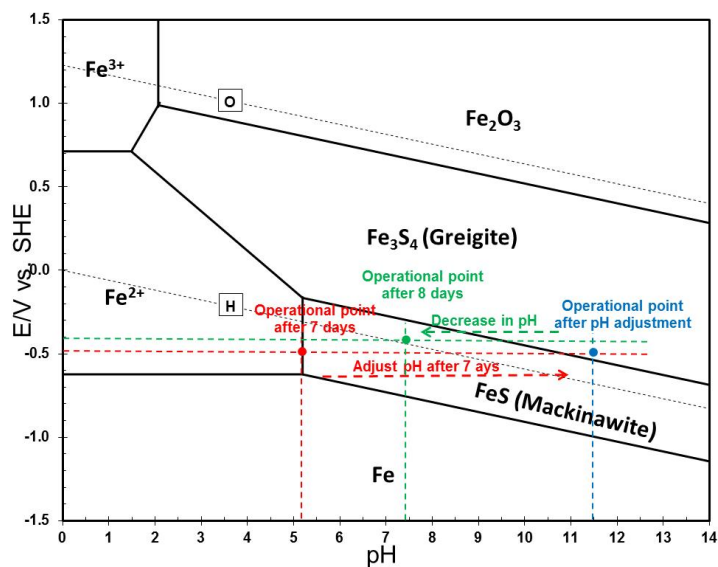
Table 17 XRD quantitative analysis of the formed corrosion products layer with pH adjustment.

Phases	Mackinawite	Pyrrhotite	Greigite	Pyrite	Iron
After 7 days	90.8%	5.2%	0	0	4.0%
After 8 days	90.4%	0.3%	9.0%	0	0.3%

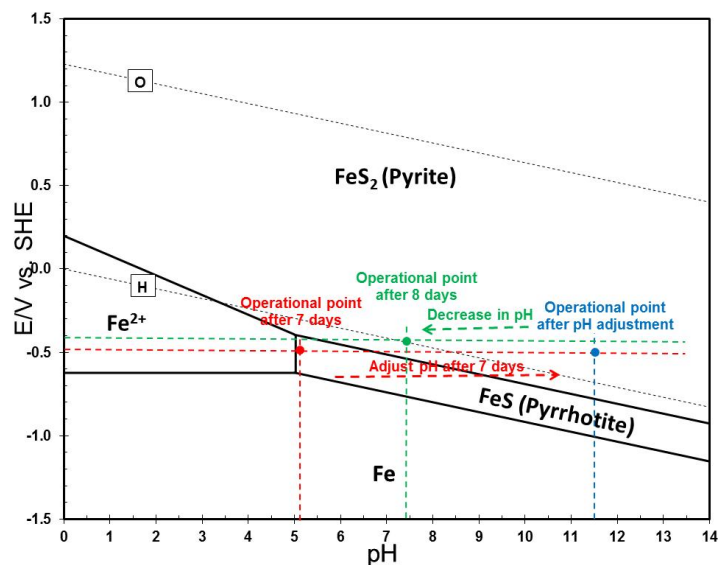
The Pourbaix diagrams generated according to the experimental conditions after 8 days of exposure are shown in Figure 56 for verification. The operational points immediately after adjusting pH (shown as blue points) were brought slightly into the greigite region in Figure 56 (a) and into the pyrite region in Figure 56 (b). However, the operational points after the pH adjustment continuously moved “backward” due to the decrease in solution pH. This is due to hydrogen ions produced from the precipitation of iron sulfides (mainly mackinawite and a few of greigite) after the pH adjustment shown in Equation (43).

However, only greigite was detected as a new iron sulfide phase after the pH adjustment (after 8 days). This is explained by the fact that the high pH would have facilitated the formation of greigite while the kinetics of pyrite nucleation is sluggish. The operational point after 8 days of experiment (shown as green points) in Figure 56 (a) is to the right of the equilibrium line between mackinawite and aqueous  $\text{Fe}^{2+}$ , suggesting supersaturation for the dominant mackinawite phase after 8 days of exposure. On the other hand, the operational point after 8 days in the final thermodynamically stable Pourbaix diagram shown in Figure 56 (b) falls into the pyrite region, revealing that pyrite is also a thermodynamically favored phase under the experimental conditions after 8 days of exposure. Considering the sluggish kinetics of the nucleation of pyrite crystals, no pyrite would have formed after 8 days of experiment. Nevertheless, pyrite was seen in the

previous experiment conducted at a higher temperature, 80 °C (5.3.1), at which the kinetics of formation of pyrite was accelerated by the higher temperature.



(a)



(b)

Figure 56. Verification of Pourbaix diagram after 8 days (Pourbaix diagram was generated at  $T = 25\text{ }^{\circ}\text{C}$ ,  $p\text{H}_2\text{S} = 0.097\text{ bar}$ ,  $[\text{Fe}^{2+}] = 0.52\text{ ppm}$ ,  $[\text{Fe}^{3+}] = 1.0 \times 10^{-6}\text{ M}$ ): (a) Mackinawite / Greigite; (b) Mackinawite / Greigite / Pyrrhotite / Pyrite.

## 5.4 Summary

The comprehensive thermodynamic model, in the form of Pourbaix diagrams, was validated by performing long-term experiments at different temperatures (25°C and 80°C), and by adjusting solution pH. Stable iron sulfide phases, greigite, pyrrhotite, and pyrite, were detected in the high temperature experiment (80°C) compared to the low temperature experiment due to faster kinetics at high temperature. The greigite phase was detected after adjusting solution pH, to higher values. However, pyrite was not detected possibly due to its slow kinetics of nucleation. All these corrosion products formed on the steel surface were captured by the Pourbaix diagrams constructed at the experimental conditions.

## CHAPTER 6. THE ROLE OF IRON SULFIDE POLYMORPHISM IN LOCALIZED CORROSION

### 6.1 Introduction

Corrosion caused by the presence of H<sub>2</sub>S and CO<sub>2</sub> in produced fluids is frequently encountered in pipelines during the production of oil and gas. The two primary classifications of corrosion are general corrosion and localized corrosion. Localized corrosion is more troublesome for corrosion engineers because it is generally considered the main cause for pipeline failures in the oil and gas industry, particularly in sour systems, and it is hard to predict or detect. However, compared to general corrosion [8], [11], [12], localized corrosion is poorly understood and less studied. This makes it difficult to predict and control, thereby, posing a key challenge for integrity management in the oil and gas industry.

In the open literature, H<sub>2</sub>S localized corrosion has been associated with multiple risk factors, such as the presence of elemental sulfur [110]–[114], polysulfides [115]–[117], high salinity [118]–[120], flow velocity [121], a change in local water chemistry at the steel surface [122], and metallurgy. In addition, corrosion and scaling mitigation strategies, such as corrosion inhibitors, alcohol and glycols, and pH stabilization, used in sour systems in the oil and gas industry, can greatly decrease uniform corrosion, while increasing the probability for localized corrosion. Kvarekval *et al.* [123] have showed very strong evidence of this with examples of severe localized corrosion.

Moreover, numerous studies [8], [12], [41]–[43], [124] have revealed that formation of an iron sulfide layer on the steel surface usually can suppress uniform corrosion, which is related to this layer acting as a diffusion barrier and by blockage

effects. In those studies, mackinawite was observed as the dominant iron sulfide phase. In fact, polymorphous iron sulfides have been found as corrosion products in oil and gas fields [58], [78], [79] and in laboratory experiments [8], [59]–[61]. A few studies [63], [125]–[127] have been conducted to explore the impact of different iron sulfide phases on the corrosion process in sour environments. In these studies, severe localized corrosion has been reported in the presence of a mackinawite layer deposit layer [63], [125], [126], but not in the presence of pyrrhotite and troilite [63], [127]. Therefore, in the present study, the focus was on further investigation of localized corrosion seen in a sour environment and the possible link with iron sulfide polymorphism.

## **6.2 Literature Review**

### *6.2.1 The Presence of Elemental Sulfur*

Localized corrosion associated with the presence of elemental sulfur in sour systems has been widely recognized [110]–[114]. This type of localized corrosion is understood to be dominated by an electrochemical reaction between sulfur and iron (iron oxidative dissolution and sulfur reduction) [114].

In order to mitigate localized corrosion caused by the presence of elemental sulfur in sour systems, it is important to understand how elemental sulfur forms in an aqueous sour environment. The possible origins of generating elemental sulfur in sour systems were reviewed to determine their relationship to the localized corrosion mechanisms in the current research.

#### *6.2.1.1 Thermal Decomposition of H<sub>2</sub>S at High Temperature*

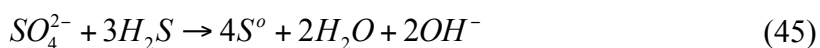
Extensive research has been conducted on thermal decomposition of H<sub>2</sub>S into elemental sulfur [128]–[131]. The decomposition shown in Reaction (44) requires almost

one thousand degrees C. Clearly, this pathway of generating elemental sulfur is not applicable to the current study.



#### 6.2.1.2 Thermochemical Sulfate Reduction

Reaction (45) illustrates thermochemical sulfate reduction, which is a possible route to generate elemental sulfur in sour systems. However, the thermochemical sulfate reduction needs at least 100°C. Hence, it is not the case in the system studied in a glass cell.



#### 6.2.1.3 Oxygen Ingress

Elemental sulfur can also be generated in the presence of oxygen, as shown in Reaction (46). In the present study, all experiments were carried out in a well-controlled 2-liter glass cell with special care taken during experiments to avoid oxygen ingress. Analytical grade N<sub>2</sub> was sparged into solution in the glass cell in advance of each experiment for more than 4 hours to deoxygenate the solution. Analytical H<sub>2</sub>S/N<sub>2</sub> mixed gas was continuously sparged throughout each experiment. Thereby, this pathway of forming elemental sulfur in the presence of oxygen is not likely to occur in the current research.



#### 6.2.1.4 Decomposition of Ionic Polysulfides

The decomposition of ionic polysulfides listed in Reaction (47) through Reaction (50) results in elemental sulfur deposition [115]. However, this route of generating elemental sulfur requires the presence of ionic polysulfides in the aqueous solution to initiate the sequence of reactions.



#### 6.2.2 *Polysulfides*

The presence of polysulfides in aqueous solutions has been widely accepted. Although enhanced corrosion rates have been frequently associated with the presence of polysulfides, no evidence directly supports this hypothesis so far. Their detection, how they are generated, and their role in the corrosion process are unclear. One can find scarce publications regarding polysulfides found in oil and gas fields. It can be said that

the current understanding with respect to polysulfides in sour fields is inconclusive and controversial. Thereby, a rudimentary understanding of polysulfides is necessary to answer the three basic questions listed below:

#### 6.2.2.1 What Are Polysulfides?

Polysulfides are a group of unbranched straight chain molecules, which are usually written as  $H_2S_n$  (typically  $n = 2 \sim 5$ ). Polysulfides are soluble in water and volatile at high temperature. Aqueous polysulfide conjugate acids can dissociate readily into ionic polysulfides, as shown in Reaction (51) and Reaction (52).

Table 18 shows the standard Gibbs free energy and dissociation constants for aqueous  $H_2S$ ,  $H_2S_2$ ,  $H_2S_3$ ,  $H_2S_4$ , and  $H_2S_5$  [116]. Clearly, aqueous polysulfide conjugate acids are relatively stronger acids compared to aqueous  $H_2S$  because of smaller  $pK_a$  values for each polysulfide conjugate acid. However, the concentrations of polysulfide species in aqueous solutions are usually trace amounts in sour systems and only become important at very high pH values [117].



Table 18 Gibbs free energy and dissociation constants of polysulfides.

Aqueous Species	$\Delta G_f^\circ/\text{kJ mol}^{-1}$	$\text{pK}_{a,1}$	Dissociated Species	$\Delta G_f^\circ/\text{kJ mol}^{-1}$
$\text{H}_2\text{S}$	-27.91	7.0	$\text{HS}^-$	11.97
$\text{H}_2\text{S}_2$	-6.46	5.0	$\text{HS}_2^-$	22.07
$\text{H}_2\text{S}_3$	4.88	4.2	$\text{HS}_3^-$	28.84
$\text{H}_2\text{S}_4$	9.79	3.8	$\text{HS}_4^-$	31.47
$\text{H}_2\text{S}_5$	13.56	3.5	$\text{HS}_5^-$	33.53

### 6.2.2.2 *How Are Polysulfides Generated?*

Polysulfide species in sour systems are mainly generated by two pathways, which are illustrated below.

One primary pathway is the oxidation of sulfide species due to oxygen ingress and the presence of metal ions with a highly oxidized state, such as  $\text{Fe}^{3+}$  [117]. The oxidation reaction is given in Reaction (53).



Another pathway of producing polysulfides is a redox reaction involving sulfide species such as  $\text{HS}^-$  and elemental sulfur shown in Reaction (54), which is the backward reaction of Reaction (50). Again, this pathway requires the presence of elemental sulfur in the system.



As illustrated previously, the sour system investigated in the present study is a well-controlled deoxygenated system. Hence, the first pathway to form polysulfides due to oxygen ingress is not likely. The second pathway depends on the existence of elemental sulfur in the system studied.

#### 6.2.2.3 Are Polysulfides Corrosive?

Elevated corrosion rates and occurrence of serious localized corrosion have frequently been associated with the presence of polysulfides in aqueous sour systems, but there is insufficient evidence in favor of the hypothesis that polysulfides are corrosive to carbon steel. Perturbations encountered within the sour systems destabilize ionic polysulfides to finally form elemental sulfur, following the reactions shown as Reaction (47) through Reaction (50) [115]. The last step shown in Reaction (50) generates elemental sulfur, which precipitates from the bulk solution and deposits on the metal surface. Numerous studies and experiences [114] have shown that elemental sulfur in contact with unprotected carbon steel could be very corrosive. Ionic polysulfides, which are present in the fluids carried through oil and gas pipelines, can precipitate elemental sulfur when suitable environmental perturbations are encountered. Thus, ionic polysulfides are corrosive as a consequence of their destabilization and the resultant formation of elemental sulfur.

#### 6.2.3 *High Salinity*

High salinity has been considered to be a significant factor for localized corrosion based on field experience. Severe pitting corrosion has frequently been correlated to field failures of both wells and pipelines when there are very high concentrations of chlorides present [118], [119]. Fang *et al.* [120] studied the effect of salt concentrations on both

sweet corrosion and sour corrosion of carbon steel. Salt concentrations ranging from 3 wt. % to 25 wt. % were used in CO<sub>2</sub> corrosion of carbon steel experiments; however, no initiation of localized corrosion was seen in this series of sweet corrosion tests. Conversely, a decrease in general corrosion rate with the increase in salt concentrations was observed. On the other hand, different salt concentrations were also used in H<sub>2</sub>S corrosion of carbon steel. Again, a marked decrease in both general corrosion rate and penetration rate with increasing salt concentrations was observed in the series of sour corrosion experiments.

Heretofore, there is no clear evidence directly supporting the conjecture that high salinity could initiate localized corrosion of carbon steel. Therefore, more investigation of the influence of high salinity on carbon steel corrosion is needed.

#### *6.2.4 Flow Rate*

Flow rate, is frequently hypothesized to be associated with localized corrosion. However, current explanations of the effect of flow velocity is somewhat contradictory. Some researchers [132], [133] have proposed that a high flow rate may mechanically remove the protective iron sulfide layer and subsequently cause localized corrosion. In contrast, Nesic [121] stated that low flow rates, rather than high flow rates could create more problems. For instance, stratified flow is typical at low liquid volumetric flow rates in the case of oil/water 2-phase flow in pipelines. In the case of stratified flow, the water phase is directly in contact with the steel, which is vulnerable to localized corrosion. In addition, settling of solids at the bottom of pipelines is frequently encountered at low flow rates, leading to under-deposit corrosion and subsequent localized corrosion issue.

### 6.2.5 *A Change in Local Water Chemistry*

From a theoretical standpoint, there is one hypothesis for a mechanism of localized corrosion in sour environments related to a change in local water chemistry at the steel surface. Insufficient and inconclusive experimental results are available in the open literature regarding this effect due to a lack of appropriate testing techniques to measure local water chemistry at the steel surface.

Woollam *et al.* [122] investigated the role of an iron sulfide layer in the corrosion process of carbon steel underneath. A galvanic coupling between a bare carbon steel electrode and an iron sulfide covered carbon steel electrode, and the other galvanic coupling between an iron sulfide covered carbon steel electrode and an iron carbonate covered carbon steel electrode, were studied. The authors found that the iron sulfide covered electrode did not always function as a cathode in the galvanic coupling. Finally, the authors concluded that changes in local environment might have more influence on the initiation and propagation of localized corrosion. However, those experimental results have not directly reflected the role of a change in local water chemistry at the steel surface in a corrosion process.

### 6.2.6 *Metallurgy*

Last, but not least, an effect of metallurgy must be considered as well. The defects or flaws in the microstructures of mild steel are suspected as causes for initiation of localized corrosion.

### 6.2.7 *Effect of Iron Sulfide Polymorphism on Localized Corrosion*

Numerous studies [8], [12], [41]–[43], [124] have revealed that formation of an iron sulfide layer on the steel surface can usually suppress uniform corrosion, which is

related to this layer acting as a diffusion barrier and its surface blockage effect. However, very little understanding has been achieved regarding the effect of iron sulfide polymorphism on the corrosion process of the steel underneath due to different physicochemical properties associated with each phase of iron sulfide. Hence, there is a need to understand the influences of an iron sulfide layer containing polymorphous iron sulfide phases on corrosion processes and incorporate that into corrosion prediction.

From a theoretical standpoint, Wilhelm [62] reviewed understanding of localized corrosion caused by the presence of different types of corrosion product layers due to a galvanic effect mechanism. He stated that an iron sulfide layer on the steel surface functions readily as a cathode, transferring electrons released from steel toward a corrosive aqueous environment for cathodic reactions such as hydrogen reduction, oxygen reduction, and so forth.

To investigate the effect of iron sulfide polymorphism on the corrosion process, a few studies have been done by depositing a certain type of iron sulfide layer on the mild steel sample surface and studying corrosion behavior of the steel underneath. Table 19 summarizes peer research on iron sulfide under-deposit corrosion. Obviously, one can observe that different iron sulfide phase plays its own role in the corrosion process of the steel underneath. It can be said, on the basis of these experimental results [63], [127], the pyrrhotite group (pyrrhotite and troilite), as the final corrosion product formed after long-term exposure, and is considered to be associated with uniform corrosion. However, in the case of a mackinawite deposit layer, either pre-synthesized [63] or *in situ* precipitated [63], [125], [126], all experimental results have manifested that the general corrosion rate was dramatically accelerated, and pitting corrosion was observed. This is contradictory to

the understanding of the role of a mackinawite layer in the corrosion process [8], [11], [12], which is the initial iron sulfide formed on steel surface decreases the initial corrosion rate after its formation. It is hypothesized here that as a thermodynamically metastable phase, the transformation of the mackinawite deposit used in those experiments into more thermodynamically stable iron sulfides is likely to occur during the experiments, consequently causing localized corrosion. Thereby, polymorphous iron sulfides, rather than merely mackinawite, might be present in those experiments. However, corrosion products at the end of all those experiments in the presence of the mackinawite deposit layer were not reported.

Table 19 A summary of peers' work on iron sulfide under deposit corrosion.

Ref.	Experimental Conditions	Test Duration	Deposit Material	General Corrosion Rate	Pitting Occurrence
[125]	pH <sub>2</sub> S = 3550ppm T = 23 °C pH = 4.5	a few hours	in-situ formed suspended mackinawite	accelerated more than 5 times	not report
[126]	pH <sub>2</sub> S = 0.5 bar pCO <sub>2</sub> = 0.5 bar with inhibitor	2 weeks	in-situ precipitated mackinawite	accelerated 4 times	yes
[63]	T = 65 °C, pH <sub>2</sub> S = 71 MPa pCO <sub>2</sub> = 37 MPa	100 hours	pre-synthesized and in-situ precipitated mackinawite	accelerated 40 times	yes
			commercial reagent (pyrrhotite and troilite mixture)	barely changed	no
[127]	T = 37.8 °C pH <sub>2</sub> S = 0.07 MPa pN <sub>2</sub> = 0.07 Mpa pH = 6.08	2 weeks	commercial reagent (64% pyrrhotite and 36% troilite mixture)	did not change much, increased compare to sand deposit	no

### 6.3 Objectives

A thermodynamic model [18], [19] (in the form of Pourbaix diagrams) was used to design experimental conditions leading to formation of different iron sulfides as corrosion products in a sour environment. The subsequent influence of a corrosion product layer containing polymorphous iron sulfides on the corrosion process of steel with a focus on localized corrosion was studied. Three sets of experiments were designed and executed as described below:

Experiment set #1: Experiments with spontaneous formation of polymorphous iron sulfides (mackinawite, pyrrhotite, greigite, and pyrite) were designed and conducted at 80 °C, where formation of polymorphous iron sulfides would be facilitated by a relatively high temperature.

Experiment set #2: Experiments with formation of greigite and pyrite triggered by changing the solution pH were designed and carried out at 25 °C. At those experimental conditions, only mackinawite and pyrrhotite were allowed to form for a week before the solution pH was changed to facilitate formation of greigite and/or pyrite on the basis of predictions made by the Pourbaix diagrams.

Experiment set #3: Experiments similar to those in set #2 except that the change of solution pH was done after 2 days before a significant mackinawite/pyrrhotite layer formed, which is considered to be precursors to the transformation into more thermodynamically stable iron sulfides, such as greigite and pyrite.

## 6.4 Experimental

### 6.4.1 Apparatus

The experimental setup is shown in Figure 37. Experiments were performed in a 2-liter glass cell filled with 1 wt. % sodium chloride (NaCl) electrolyte. Each experiment contained six square shaped steel sample with dimensions of 1.2 cm x 1.2 cm x 0.2 cm, hung in the glass cell using nylon string, and one cylindrical working electrode (WE) sample with dimensions of 1.2 cm diameter x 1.5 cm length, mounted on a stationary rod. The square samples were used for surface analysis and weight loss measurements, while the stationary WE was used for electrochemical measurements. A magnetic stir bar was used to keep the solution fully mixed during the experiments. A typical 3-electrode setup was used to conduct electrochemical measurements. A platinum wire was used as the counter electrode. A saturated silver-silver chloride (Ag / AgCl) electrode connected to the cell externally through a Luggin capillary was used as the reference electrode. The theoretical B value used in linear polarization resistance (LPR) measurements was adjusted using weight loss results, and was found to be 13 mV/decade on average in this study. A mesh capped pH probe [109] was used to measure surface pH at a corroding surface and a glass pH probe was used to monitor bulk solution pH.

### 6.4.2 Material

The WE sample and corrosion test square samples were all made from API 5L X65 carbon steel. The chemical composition of this carbon steel is shown in Table 14.

### 6.4.3 Procedure

The test matrix of this series of experiments is shown in Table 20. In the beginning of each test, N<sub>2</sub> gas was sparged through the electrolyte to deoxygenate the

solution (typically more than 4 hours). An H<sub>2</sub>S and N<sub>2</sub> pre-mixed gas was then sparged into the solution continuously throughout the experiment. The solution pH, decreased due to the addition of H<sub>2</sub>S to the solution, and was adjusted to 6.0 by using deoxygenated 1.0 M NaOH solution. The WE and square samples were polished to a 600 grit sandpaper finish, rinsed thoroughly with deionized water and isopropanol, ultrasonically cleaned in isopropanol, and then dried by an air blower before immersion in electrolyte.

Experiments were conducted following the experimental designs shown in Figure 57, Figure 58, and Figure 59, which indicate the sample removal times with specific analysis designations for each. Solution pH was adjusted to 11.5 after 7 days of exposure in Exp. #2 as indicated in Figure 58 and after 2 days of exposure in Exp. #3 as indicated in Figure 59. In both cases the pH spontaneously decreased to pH 7.0 very quickly. Corroded square samples were taken out for analysis on the days indicated in the timeline, rinsed with deoxygenated DI water and deoxygenated isopropanol, blown dry using N<sub>2</sub>, and stored in a desiccator.

Scanning electron microscope (SEM) imaging was used to detect the surface morphology of the samples, energy dispersive X-ray spectrometry (EDX) and X-ray diffraction (XRD) was applied to determine the nature of the iron sulfide formed on the samples.

Solution was drawn from the glass cell immediately before taking each steel sample, filtered by using a 0.22 μm syringe filter to remove any iron sulfide precipitate from solution, and then measured for ferrous ion concentration using a spectrophotometric method. Bulk pH, surface pH, and open circuit potential (OCP) were

monitored throughout the experiment. Both LPR and weight loss (WL) methods were used to obtain corrosion rate measurements.

Table 20 Test matrix.

Description	Exp. #1	Exp. #2	Exp. #3
Temperature	80 °C	25 °C	25 °C
Electrolyte	1 wt.% NaCl brine		
Gas composition	10 % H <sub>2</sub> S / balance N <sub>2</sub>		
H <sub>2</sub> S partial pressure	0.053 bar	0.097 bar	0.097 bar
Stirring speed	400 rpm		
Material	API 5L X65		
Initial pH	6.0		

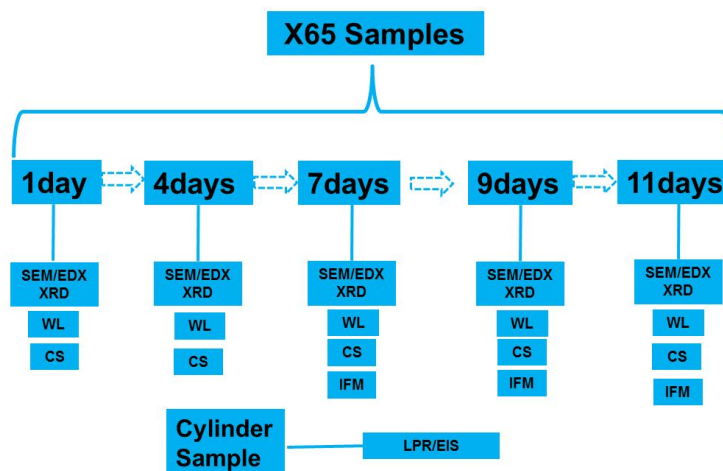


Figure 57. Experimental design for Experiment set #1.

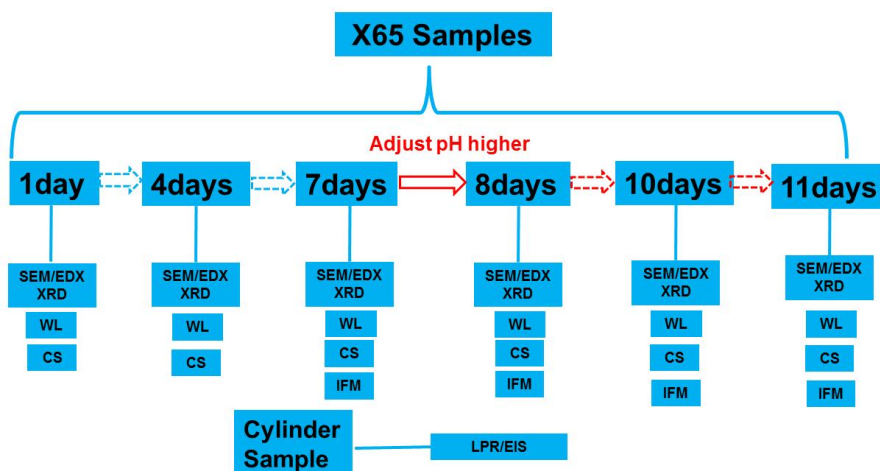


Figure 58. Experimental design for Experiment set #2.

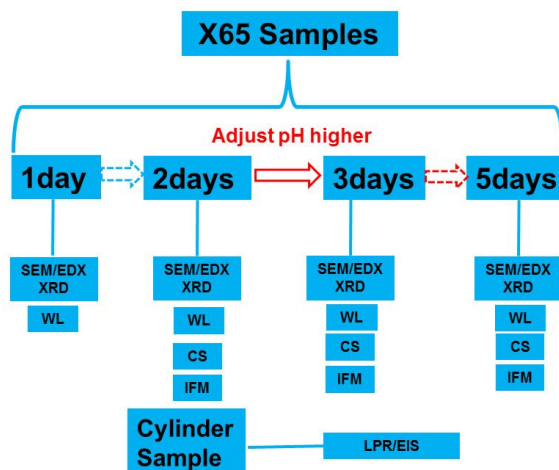


Figure 59. Experimental design for Experiment set #3.

## 6.5 Experimental Results

### 6.5.1 Experiment Set #1: Reproducible Occurrence of Localized Corrosion with Spontaneous Formation of Polymorphous Iron Sulfides

#### 6.5.1.1 Corrosion Behavior

Figure 60 shows the OCP, corrosion rate, solution pH, and ferrous ion concentration evolution monitored during the experiments. Corrosion rates obtained from LPR measurements on the WE were verified by weight loss results from the square

samples. The corrosion rate was 1.1 mm/year initially and then decreased to around 0.07 mm/year in the first four days, due to the formation of a protective iron sulfide layer at the steel sample surface. However, an increase in both OCP and corrosion rate (with the exception of the high initial values) was observed after four days of exposure, which could be explained by an increase in cathodic reaction rate, but the cause of this was yet unknown. It was hypothesized that this increase in cathodic reaction rate was due to either the collapse of the protective corrosion product layer increasing transport of corrosive species required for cathodic reactions or the formation of conductive corrosion products increasing the overall cathodic reaction area.

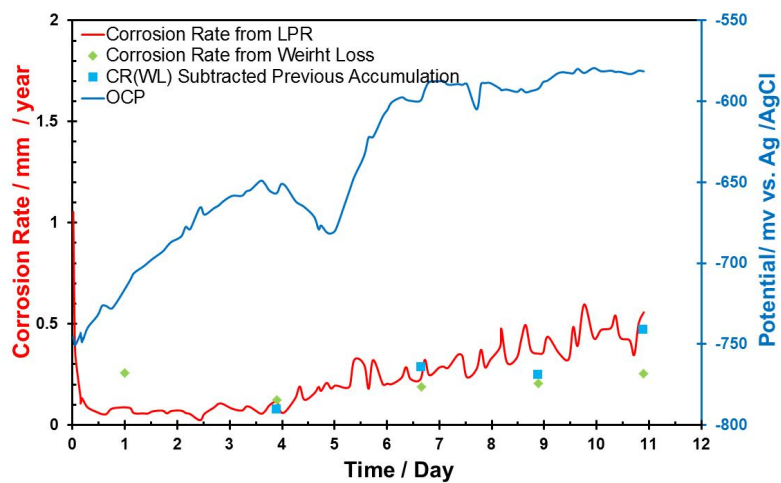


Figure 60. OCP and corrosion rates monitored throughout Experiment #1.

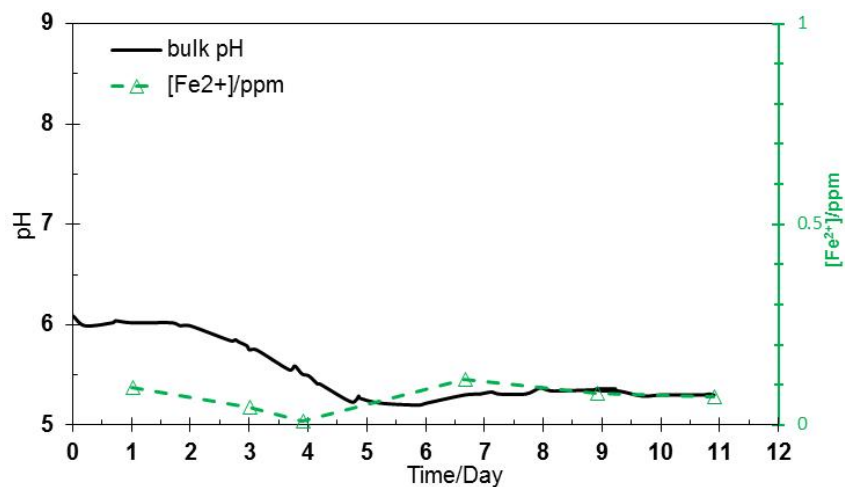


Figure 61. Bulk pH and [Fe<sup>2+</sup>] monitored throughout Experiment #1.

#### 6.5.1.2 Corrosion Products

Figure 62 presents surface morphologies of samples as removed in chronological order. A uniform surface morphology was observed after 1 day and 4 days of exposure, while blistering, cracking, and spalling morphologies were seen after 7 days, 9 days, and 11 days of experiment.

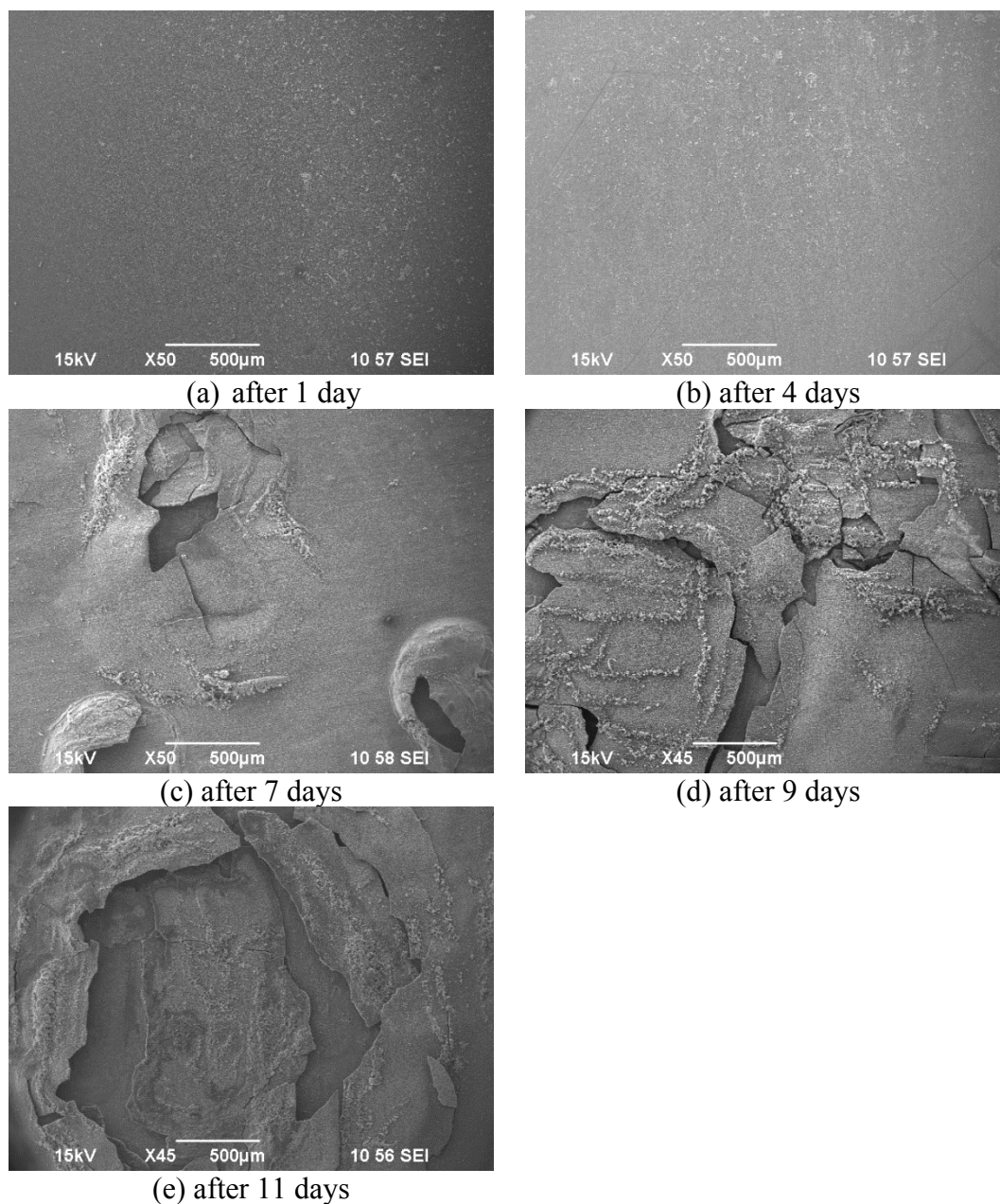
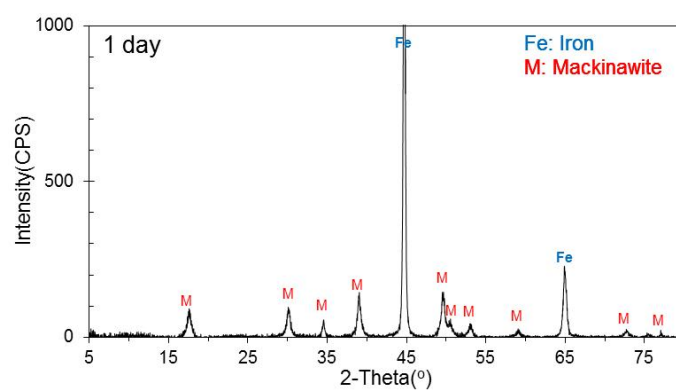


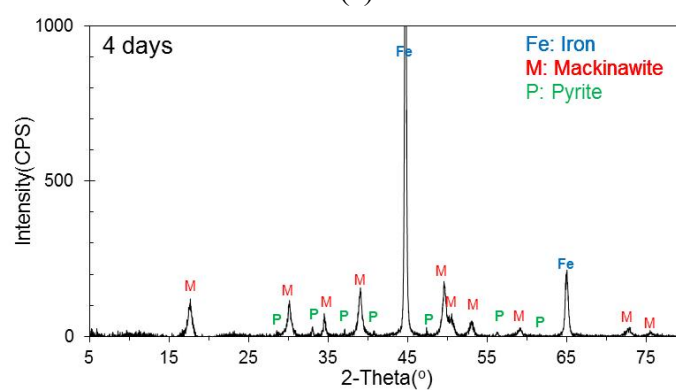
Figure 62. Surface morphologies of samples: (a) after 1 day; (b) after 4 days; (c) after 7 days; (d) after 9 days; (e) after 11 days.

Figure 63 shows XRD patterns of the corrosion product layer formed on the steel sample surface throughout this experiment. In addition, Table 21 summarizes the XRD quantitative analysis of corrosion products determined by the reference intensity ratio (RIR) methodology in order to better understand formation and transformation of

polymorphous iron sulfide phases throughout the experiment. This table clearly shows a transformation of initial thermodynamically metastable mackinawite to the more stable pyrrhotite and pyrite phases. Mackinawite accounts for 90% of corrosion products formed after 1 day of exposure, while decreasing significantly over exposure duration. In contrast, both pyrrhotite and pyrite phases have a steady growth throughout the experiment. In addition, the formation of greigite was indicated as a corrosion product after 1 day through to 9 days of exposure, but was not observed on the last sample from the experiment. That is because greigite is also a metastable phase, developed from the initial mackinawite and then transformed completely to the final thermodynamically stable pyrite after 11 days.



(a)



(b)

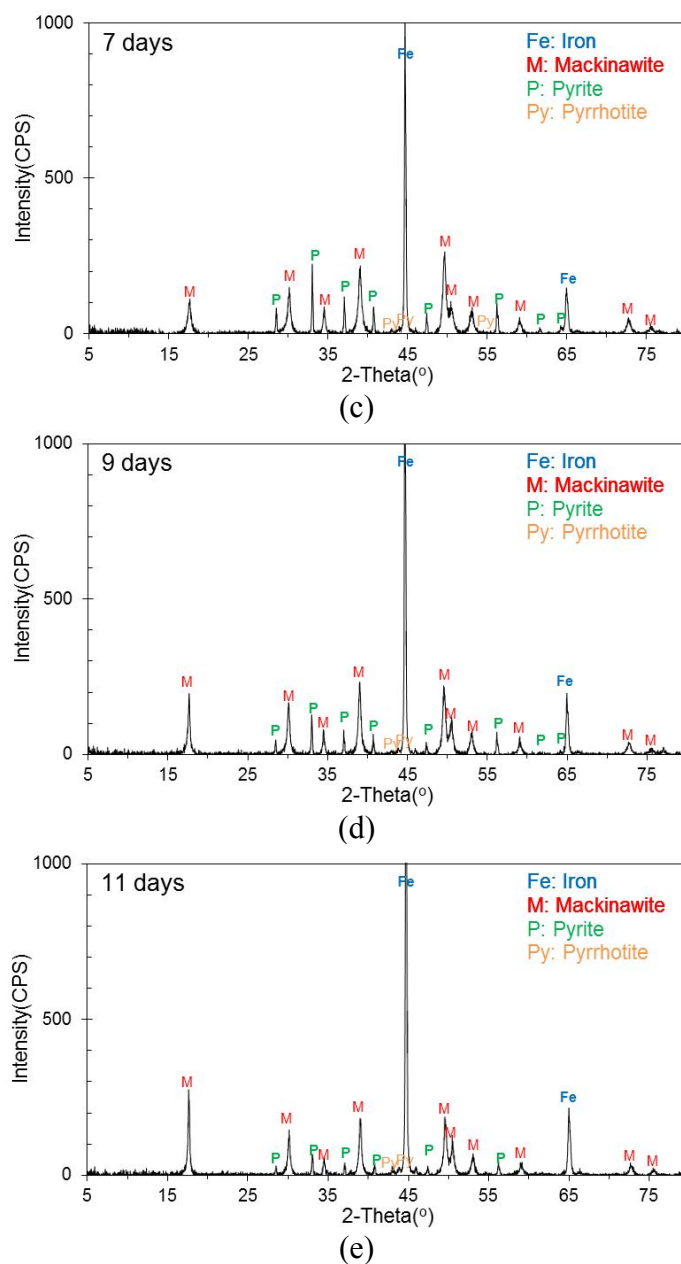


Figure 63. XRD pattern of corrosion product layer formed on samples in Exp. #1: (a) after 1 day; (b) after 4 days; (c) after 7 days; (d) after 9 days; (e) after 11 days.

Table 21 XRD quantitative analysis of corrosion products formed in Exp. #1.

Phases	1 day	4 days	7 days	9 days	11 days
Mackinawite	90.0 %	76.4 %	49.2 %	63.6 %	66.0 %
Pyrrhotite	8.0 %	5.8 %	14.8 %	1.9 %	16.4 %
Greigite	2.0 %	2.2 %	3.3 %	3.3 %	0
Pyrite	0	4.8 %	27.8 %	18.5 %	10.6 %
Iron Carbide	0	10.8 %	4.9 %	12.7 %	7.0 %

Figure 64 shows cross section images of samples after exposure for 1 day, 4 days, 7 days, 9 days, and 11 days, from which a steady increase in thickness of the iron sulfide layer is clearly observed. The corrosion product layer was approximately 2  $\mu\text{m}$  thick on the sample after 1 day of exposure, while a layer of 20  $\mu\text{m}$  thickness was observed on the sample after 11 days of the test.

To have a closer look at the corrosion product layer, surface morphology and cross-section SEM images of samples after 4 days and after 7 days, at a higher magnification, are shown in Figure 65. A lot of small cubic crystals were observed on the mackinawite layer in the surface SEM images of samples shown in (a) and (b), which are believed to be pyrite crystals on the basis of XRD findings. Further, the cross-section images presented in (c) and (d) are backscattered electron composition (BEC) images which show atomic differences by changes of contrast in the image. In general, darker areas that appear in BEC images are atomically lighter while brighter areas are atomically heavier. Accordingly, the crystals with lighter color on top of the grey mackinawite layer are considered to be pyrite as seen on the surface SEM images (a) and (b). Note that there

are many crystals with the lighter color embedded in the darker mackinawite layers of the cross section sample, suggesting that pyrite crystals are also embedded in the mackinawite layer. Furthermore, a steady increase in the thickness of the iron sulfide layer formed on the steel surface throughout experiment was observed. Hence, the first hypothesis proposed for the increase in both OCP and corrosion rate when there was initiation of localized corrosion, a loss of diffusion barrier layer increasing the transport of corrosive species, is proven to be wrong. Therefore, the second hypothesis, the formation of a conductive corrosion product layer increasing overall cathodic reaction area, is taken into consideration.

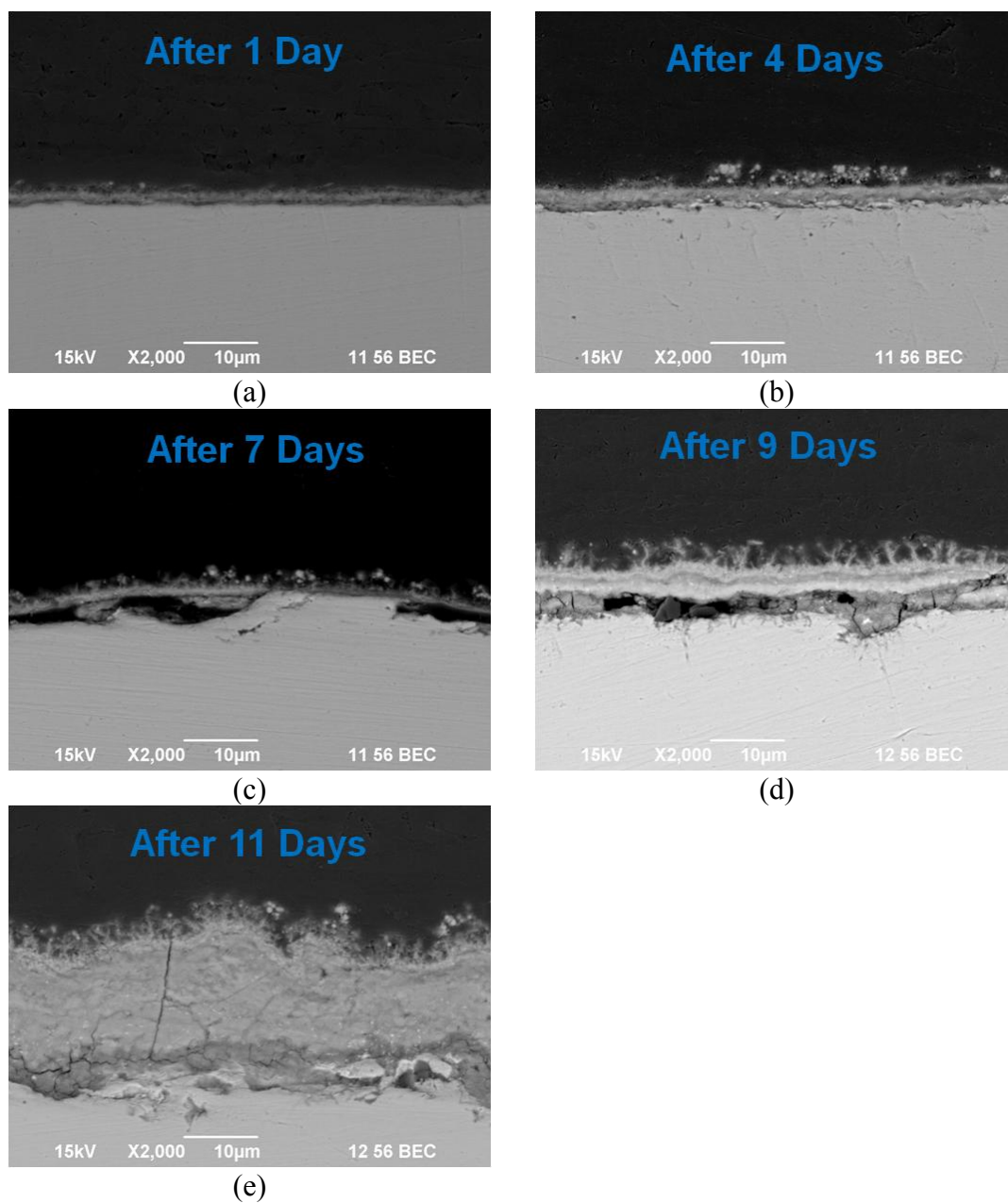


Figure 64. Cross section images of samples: (a) after 1 day; (b) after 4 days; (c) after 7 days; (d) after 9 days; (e) after 11 days.

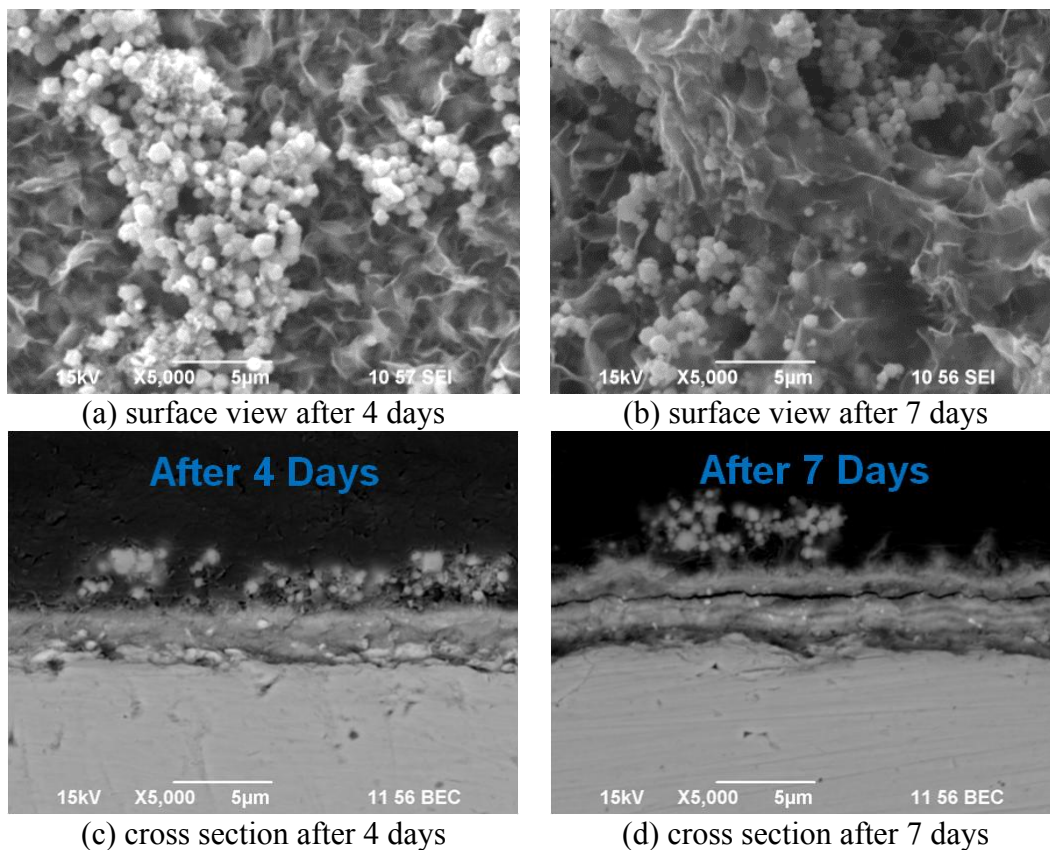
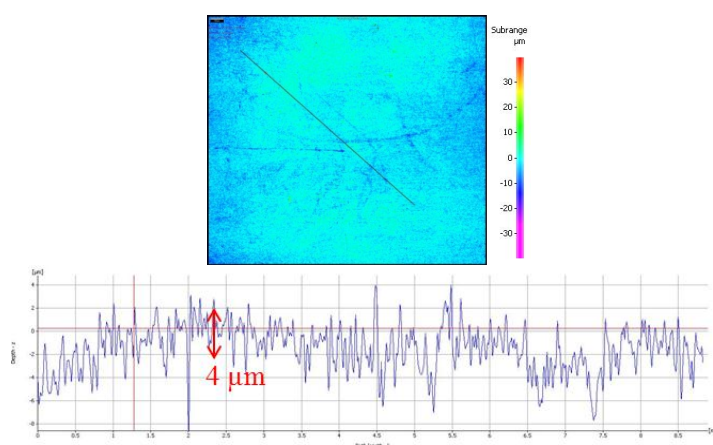


Figure 65. SEM images with 5, 000x magnification: (a) surface view after 4 days; (b) surface view after 7 days; (c) cross section after 4 days; (d) cross section after 7 days.

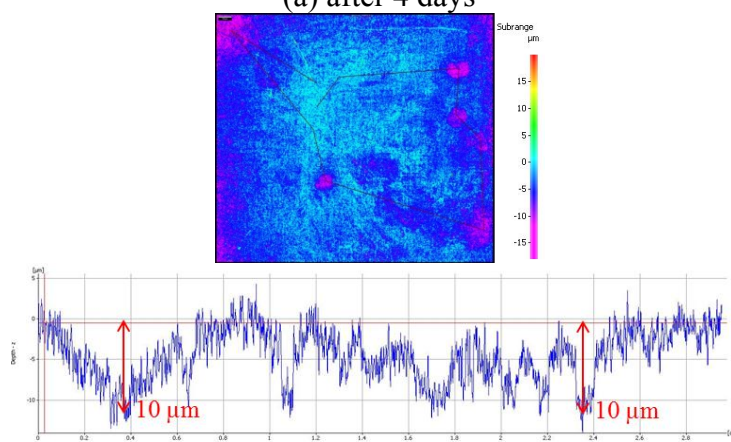
### 6.5.1.3 Surface Profilometry of Samples after Removing Corrosion Product Layer

The corrosion product layer was removed by using a Clarke solution [134] and a cleaning method as outlined in ASTM G1 [135] to observe the corroded steel underneath. A flat surface owing to uniform corrosion after 4 days of test was seen in Figure 66 (a). Then, initiation of localized corrosion was observed as 10  $\mu\text{m}$  deep pits after 7 days in Figure 66 (b). And finally, propagation of localized corrosion can be observed in Figure 66 (c) and (d). At the end of this experiment, after 11 days of exposure, a 40  $\mu\text{m}$  depth of localized corrosion was measured. The penetration rate based on this 40  $\mu\text{m}$  depth was calculated to be 2.1 mm/year. As compared to the general corrosion rate in the initial 4

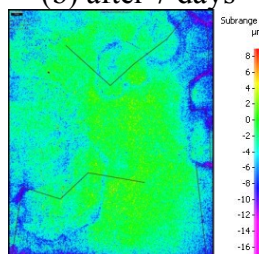
days of 0.07 mm/year, significant localized corrosion occurred. It should be noted that the localized corrosion occurred when quantitative analysis shows higher concentrations of greigite and/or pyrite in the corrosion product, which indicates a probable correlation between localized corrosion and the formation of greigite and/or pyrite. This hypothesis was further verified in the following experiments.



(a) after 4 days



(b) after 7 days



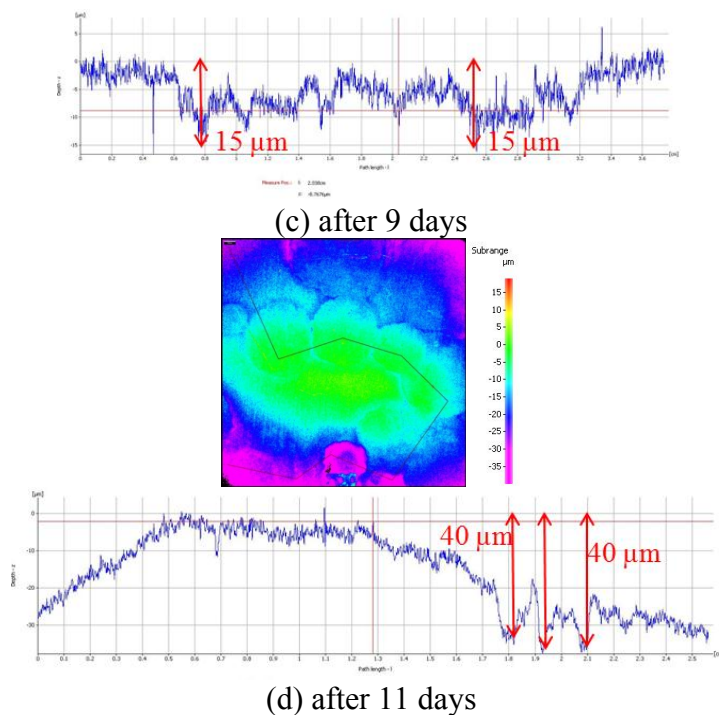


Figure 66. Surface profilometry of samples after removing corrosion product layer: (a) after 4 days; (b) after 7 days; (c) after 9 days; (d) after 11 days.

#### 6.5.1.4 *EIS Measurement*

The EIS data are shown as a Nyquist plot and two Bode plots in Figure 67, Figure 68, and Figure 69, respectively. A decrease in polarization resistance over time was seen in the Nyquist plots, suggesting an increase in corrosion rate over the exposure duration. In Figure 68, one time constant was seen after 2 hours of exposure, which probably indicate that no layer formed on the steel surface initially. Then, two time constants were observed after 1 day, which may indicate formation of a corrosion product layer on the metal surface. In addition, a dramatic decrease in the phase angle over time at low frequencies was also observed in Figure 68, revealing a significant change occurred at the interface between the metal surface and the electrolyte. This is probably due to a change in the properties of the iron sulfide layer formed on the steel surface. The modulus shown

in Figure 69 showed a small increase in solution resistance at high frequencies and a huge decrease in charge transfer resistance at relatively low frequencies over the duration of the experiment. All the EIS data consistently suggests a gradual change at the interface over the exposure duration, resulting in localized corrosion which occurred after the seventh day.

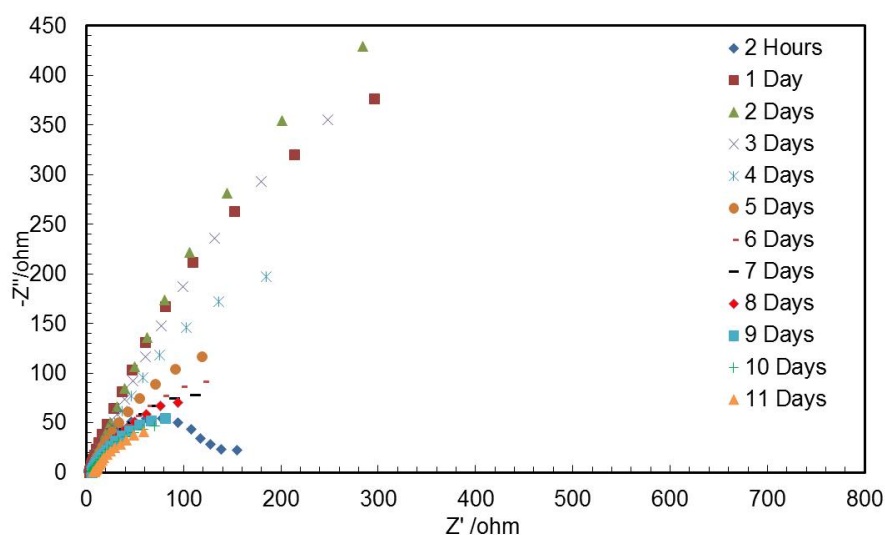


Figure 67. Nyquist plot (5000 ~ 0.003Hz).

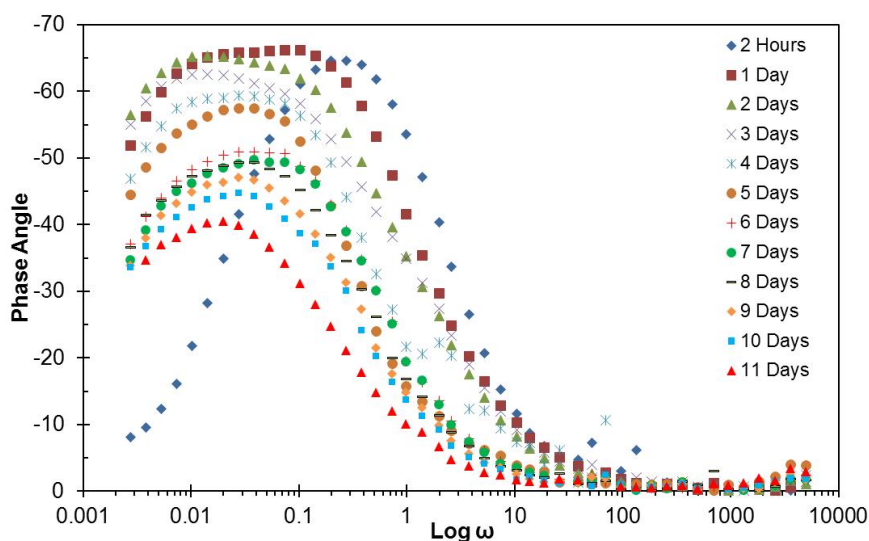


Figure 68. Bode plots (Phase Angle vs.  $\text{Log } \omega$ ) (5000 ~ 0.003Hz).

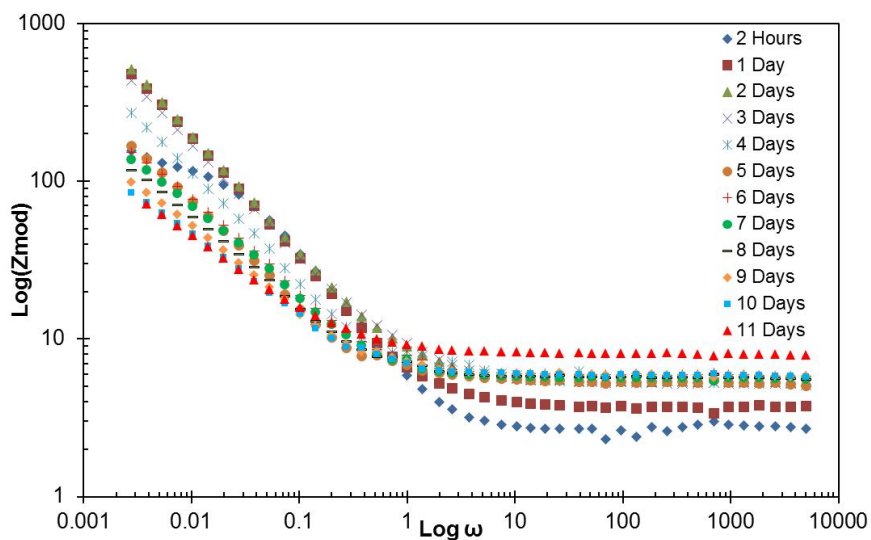


Figure 69. Bode plots ( $\text{Log } Z$  vs.  $\text{Log } \omega$ ) (5000 ~ 0.003Hz).

### 6.5.2 Experiment Set #2: Localized Corrosion Triggered by Facilitating Formation of Greigite/Pyrite at Low Temperature

Experiment set #1 indicated a probable correlation between localized corrosion and the formation of greigite and/or pyrite. To further test this hypothesis, the Experiment set # 2 was designed and carried out at 25 °C by adjusting solution pH after 7 days of exposure to trigger greigite and/or pyrite formation according to Pourbaix diagrams. Figure 53 shows the Pourbaix diagrams generated at experimental conditions after 7 days of exposure, and, accordingly, greigite and/or pyrite are expected to form if the solution pH is adjusted from a low value (around pH 5 after 7 days of test) to a high value (above pH 11).

#### 6.5.2.1 Corrosion Behavior

Figure 70 shows bulk pH and surface pH monitored during this experiment. As mentioned above, solution pH was adjusted from pH 5.5 to 11.5 after 7 days of exposure using deoxygenated NaOH solution, but quickly decreased to approximately pH 7.0.

Figure 71 shows the OCP and corrosion rates throughout the experiment. Both corrosion rates and OCP were very stable throughout the initial seven days of test, but did have a significant increase immediately after adjusting the solution pH and kept slowly increasing until the end of the experiment. In addition, weight loss was also carried out confirming LPR measurements. It is noteworthy that weight loss results were corrected in order to properly compare them with LPR measurements.

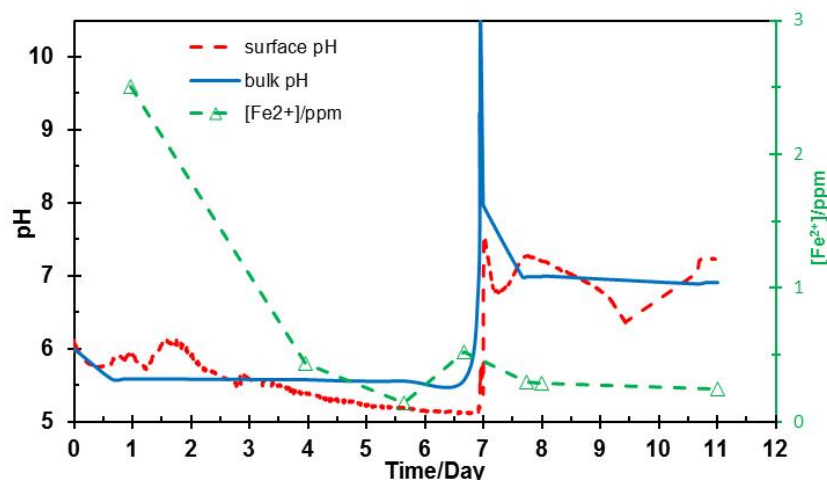


Figure 70. Bulk pH, surface pH, and  $[\text{Fe}^{2+}]$  measured throughout experiment #2.

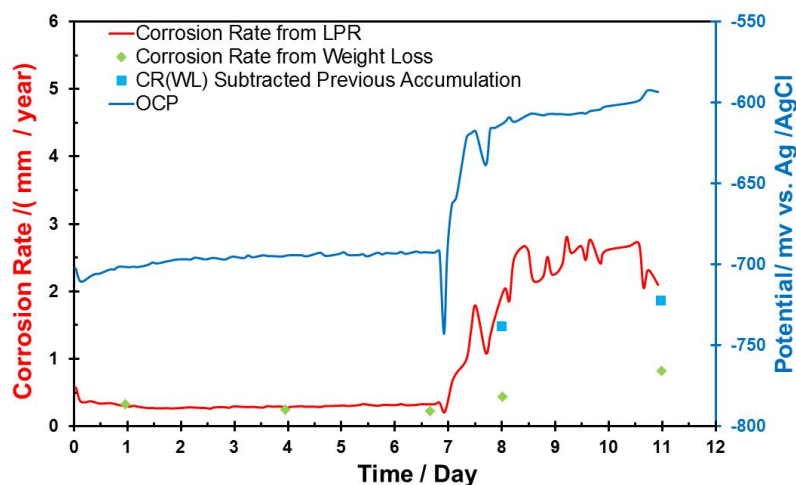
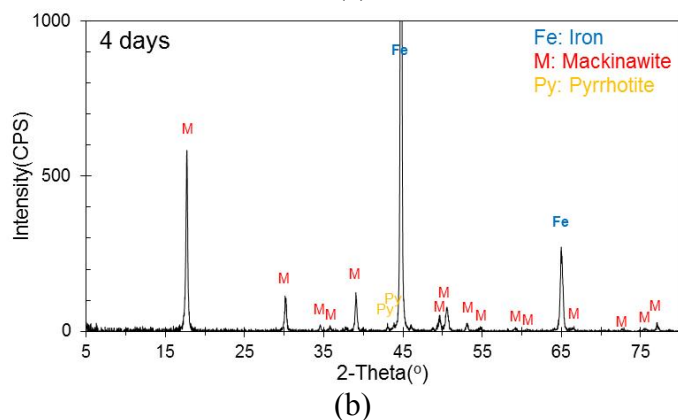
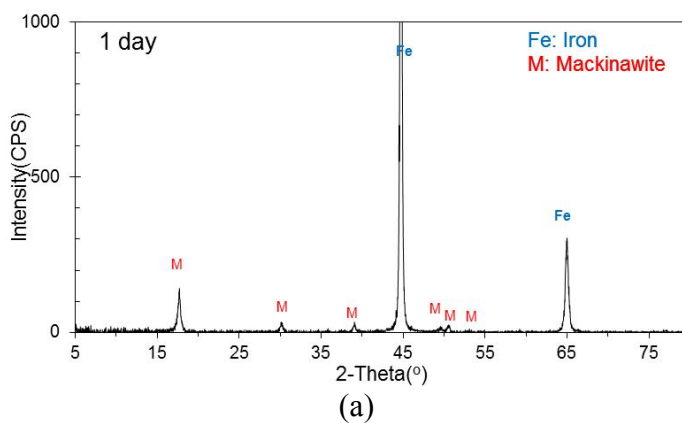


Figure 71. Corrosion rate and OCP monitored during experiment #2.

### 6.5.2.2 *Corrosion Products*

Figure 72 gives the XRD pattern of the corrosion product layer on samples taken out for analysis throughout this experiment. Table 22 shows quantitative analysis of corrosion products formed on samples during this experiment. The formation of greigite after adjustment of solution pH is obvious as the percentage of the greigite phase changed from zero before pH adjustment to 9.0 % after the pH adjustment and to 17.9 % after the 11th day of the experiment. Pyrite was also observed on the last sample. In addition, a decrease in the mackinawite phase can be observed from 90.8 % after 7 days to 78.6 % after 11 days.



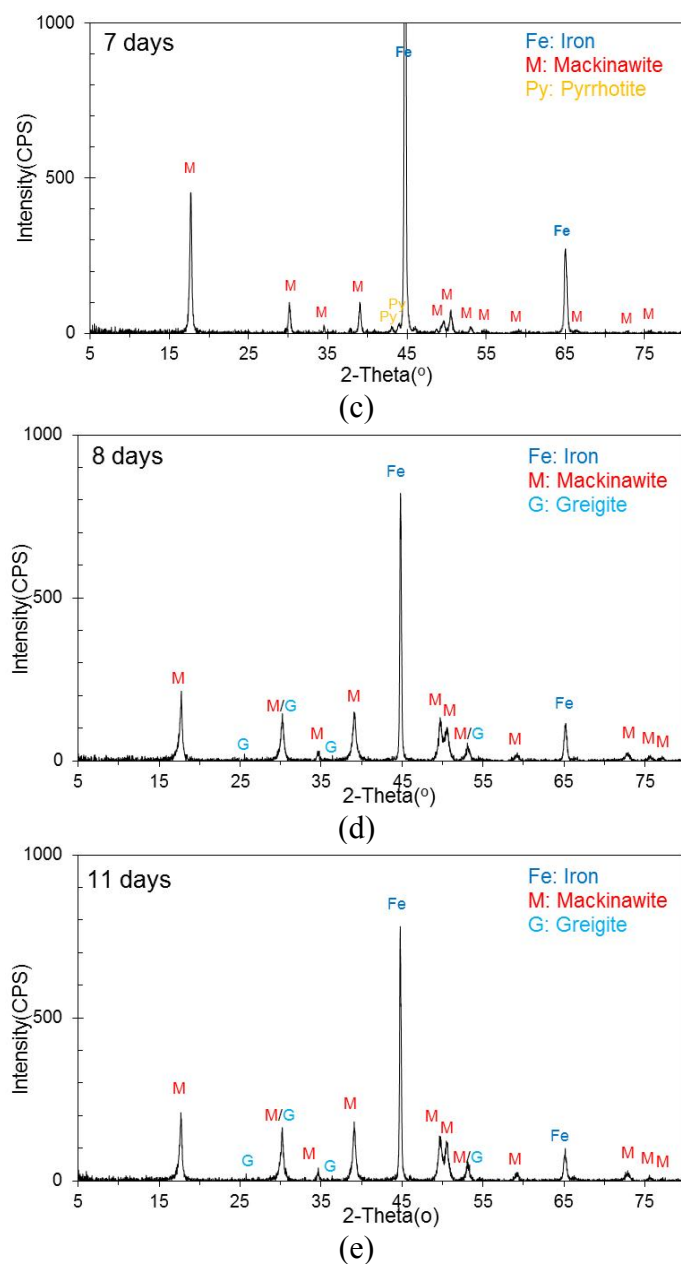


Figure 72. XRD pattern of corrosion product layer formed on samples in Exp. #2: (a) after 1 day; (b) after 4 days; (c) after 7 days; (d) after 8 days; (e) after 11 days.

Table 22. XRD quantitative analysis of corrosion products formed in Exp. #2.

Phases	7 days	8 days	11 days
Mackinawite	90.8 %	90.4 %	78.6 %
Pyrrhotite	5.2 %	0.3 %	0
Greigite	0	9.0 %	17.9 %
Pyrite	0	0	3.2 %
Iron Carbide	4.0 %	0.3 %	0.3 %

Figure 73 presents the comparison of surface morphologies of samples from Experiment #2. A uniform corrosion product layer was observed on samples in advance of the pH adjustment as shown in Figure 73 (a), (b), and (c). However, spalling and exfoliation of a corrosion product layer can be seen on samples after the adjustment of solution pH, as shown in Figure 73 (d), (e), and (f).

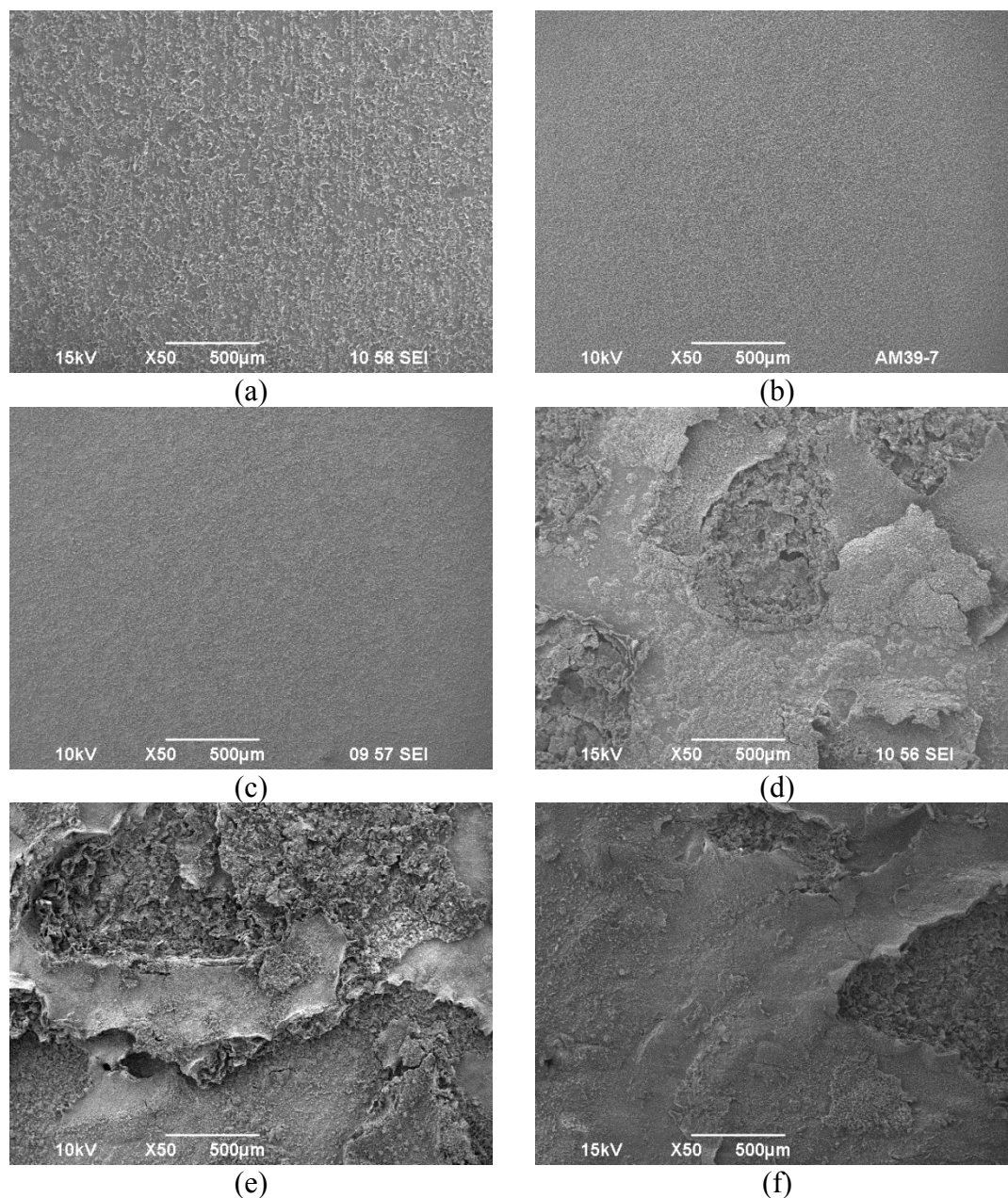


Figure 73. Surface morphologies of samples: (a) after 1 day; (b) after 4 days; (c) after 7 days; (d) after 8 days; (e) after 10 days; (f) after 11 days.

Cross section images of samples after conducting 1 day, 4 days, 7 days, and 8 days of the experiment are shown in Figure 74. A growth of a uniform and porous iron sulfide layers on the steel sample surface was observed in the first three cross section

images, while a possible pit initiation site was seen in the cross section image of the sample after the pH adjustment.

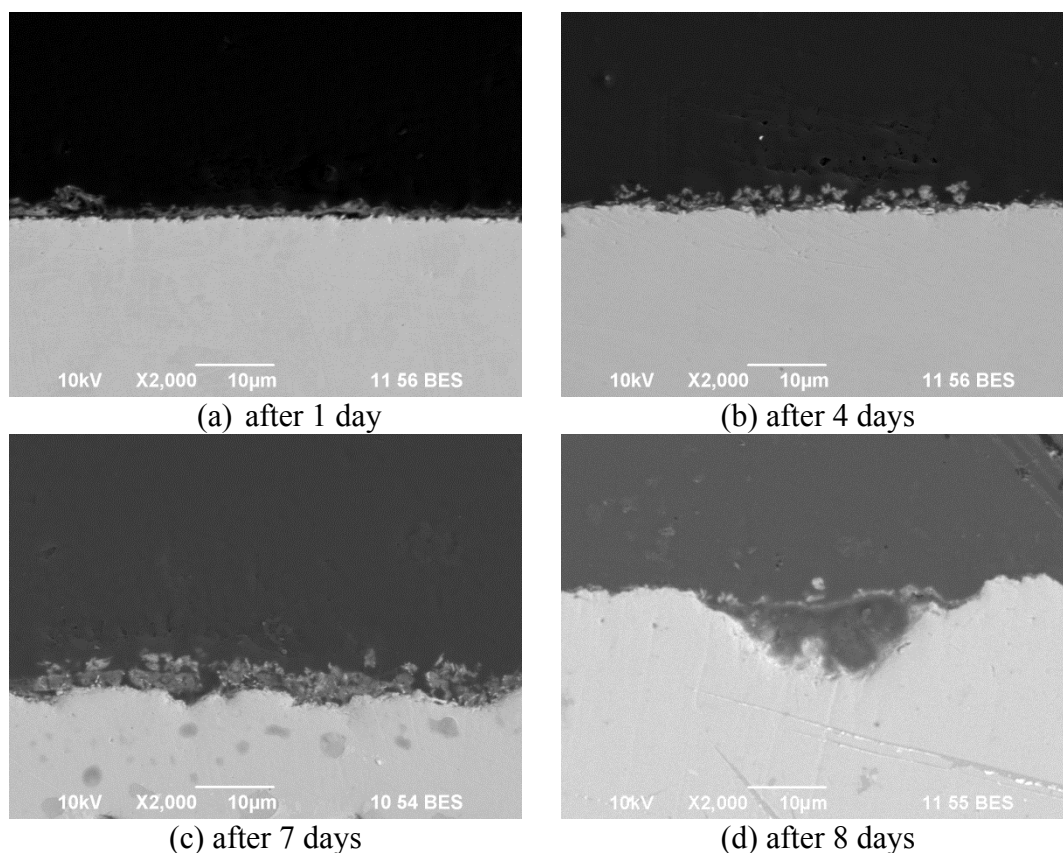


Figure 74. Cross section images of samples: (a) after 1 day; (b) after 4 days; (c) after 7 days; (d) after 8 days.

### 6.5.2.3 Surface Profilometry of Samples after Removing Corrosion Product Layer

Figure 75 shows surface profilometry of samples after removing the iron sulfide layer. The sample before pH adjustment shown in (a) presents a flat surface due to a 0.3 mm/year general corrosion rate; in contrast, the sample after adjusting pH in (b) shows a locally corroded surface with a 14.6 mm/year penetration rate. Again, significant localized corrosion was clearly observed when there was a high content of greigite and/or pyrite phases. In addition, an increase in both OCP and corrosion rate was observed again

when localized corrosion occurred. This experiment was repeated and the experimental results were reproducible. After the pH adjustment, a dramatic increase in both the OCP and the corrosion rate was observed, both greigite and pyrite were detected as new corrosion product phases, and severe localized corrosion occurred with approximately the same magnitude of penetration rate.

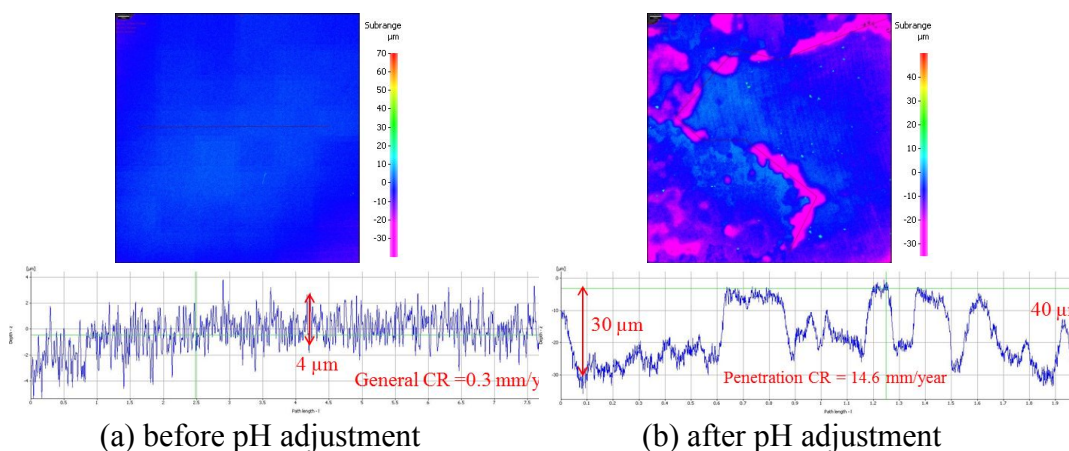


Figure 75. Surface profilometry of samples after removing corrosion product layer: (a) after 4 days; (b) after 7 days; (c) after 9 days; (d) after 11 days.

#### 6.5.2.4 *EIS Measurement*

EIS was conducted to deepen the understanding of this type of localized corrosion. The Nyquist plots are shown in Figure 76, and two Bode plots are shown in Figure 77 and Figure 78. Obviously, these Nyquist plots can be separated into two groups: the first with a larger radius in the first 7 days of experiment before adjusting pH, and the second with a much smaller radius after adjusting pH. The solution resistance was constant throughout the experiment, while a marked decrease in charge transfer resistance was noted after the pH adjustment. The same inference can be drawn from Bode plots shown in Figure 78. Further, a decrease in the phase angle in Figure 77 and a

decrease in the modulus in Figure 78 were observed after adjusting the pH. It is understood that the interface between the metal surface and the electrolyte changed dramatically after adjusting solution pH to a higher value, demonstrated as a significant decrease in charge transfer resistance, which may be attributed to the occurrence of localized corrosion. The huge decrease in charge transfer resistance is considered to be due to the presence of greigite and pyrite, which are more electrically conductive than pure mackinawite and formed after adjusting the solution pH.

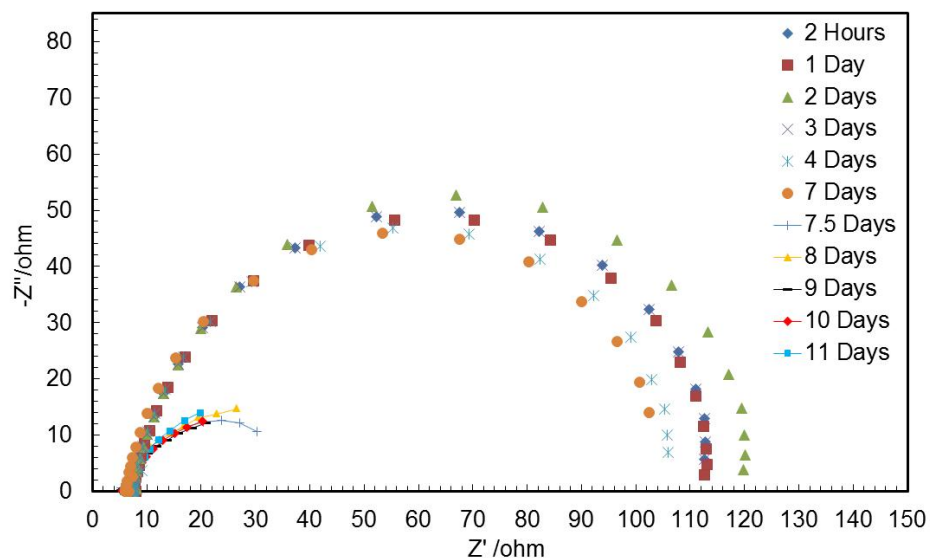


Figure 76. Nyquist plots in Exp. #2.

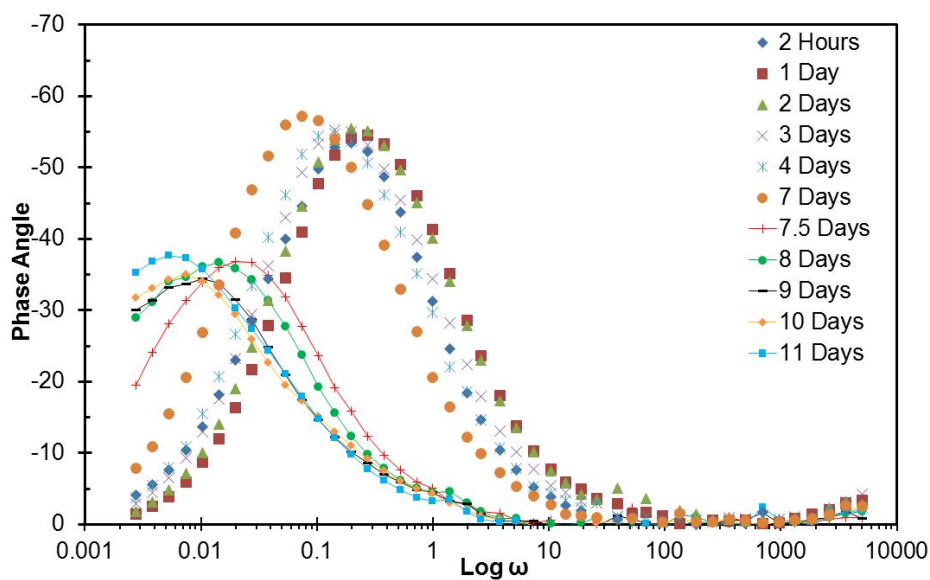


Figure 77. Bode plots (Phase Angle vs.  $\text{Log } \omega$ ) in Exp. #2.

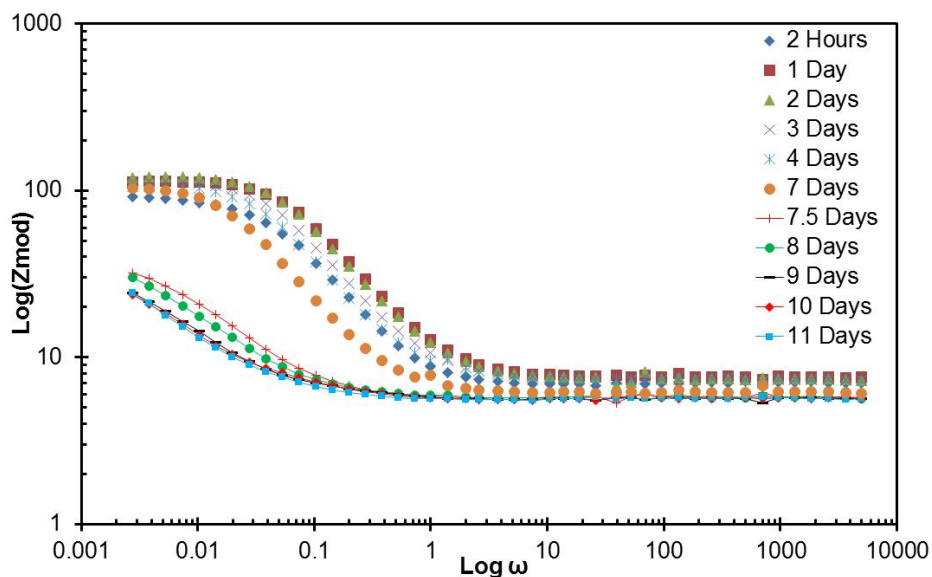


Figure 78. Bode plots ( $\text{Log } Z$  vs.  $\text{Log } \omega$ ) in Exp. #2.

### 6.5.3 Experiment Set #3: Adjusting Solution pH without Formation of Greigite/Pyrite

Experimental set #2 provided strong evidence that there is a correlation between the localized corrosion and the formation of greigite and/or pyrite triggered by adjusting solution pH after 7 days of exposure. However, it was also hypothesized that the

localized corrosion occurred in Exp. #2 was not related to the formation of greigite and/or pyrite but was due to the formation of elemental sulfur and/or polysulfides at high pH condition [114]–[117]. Therefore, one more experiment was designed and executed to better understand the mechanism for this type of localized corrosion in sour environments and confirm that it was indeed due to the formation of greigite and/or pyrite. In the present experiment, the solution pH was adjusted after 2 days rather than 7 days as done in the previous experiment. The idea was that this was insufficient time for the development of a full mackinawite layer, which is a precursor for the transformation into more thermodynamically stable greigite and pyrite. In this experiment, the formation of greigite and/or pyrite after the pH adjustment and the occurrence of localized corrosion were monitored.

#### *6.5.3.1 Corrosion Behavior*

Figure 79 shows the pH values monitored during this experiment. The pH behavior of the present experiment was reproduced exactly the same as in the previous test Exp. #2, but with exception that solution pH was adjusted after 2 days of exposure.

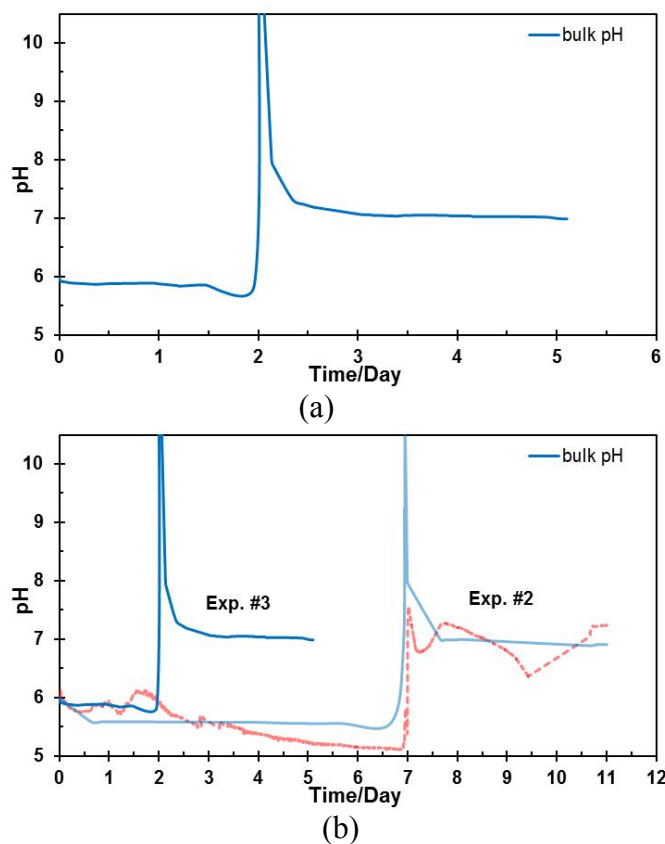


Figure 79. (a) pH values monitored during Exp. #3; (b) comparison of pH values between Exp. #2 and Exp. #3.

Figure 80 shows OCP and corrosion rates monitored during the present experiment. A marked increase in the OCP after adjusting pH was observed, which is similar to Experimental set #2. However, the corrosion rate was stable throughout the experiment, which is different from Experimental set #2 that had an increased corrosion rate immediately after the pH adjustment.

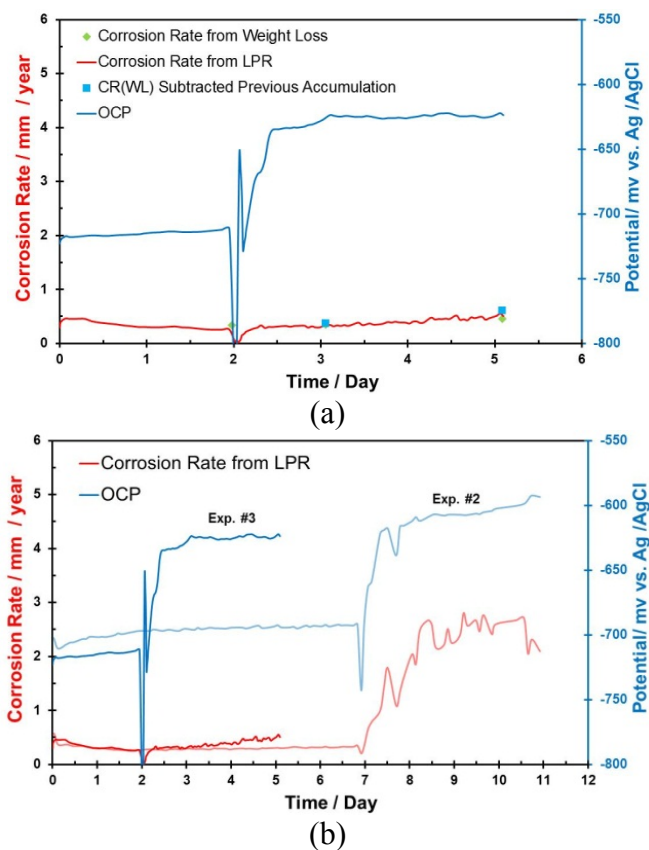


Figure 80. OCP and corrosion rate throughout experiment #3; (b) Comparisons of corrosion rate and OCP between Exp. #2 and Exp. #3.

### 6.5.3.2 Corrosion Products

Figure 81 shows surface morphologies of the samples. Before the pH adjustment (after 1 day and after 2 days of test), a partially covered corrosion product layer was observed on those samples. After the pH adjustment was performed, a uniform and fully covered corrosion product layer with lots of clusters on top of the layer was seen on the samples after 3 days and after 5 days of test, which is believed to be mackinawite precipitated at high pH conditions.

Figure 82 shows the XRD pattern of the corrosion product layer formed on the steel sample surface throughout this experiment. Table 23 presents XRD findings of corrosion products formed on those samples. For the samples before the pH adjustment,

only mackinawite was detected. After the pH adjustment, a mixture of dominant mackinawite and pyrrhotite was observed. Neither greigite nor pyrite was detected after the pH adjustment. This is attributed to the insufficient time for the development of sufficient mackinawite, which is considered to be a precursor for transformation into greigite and pyrite.

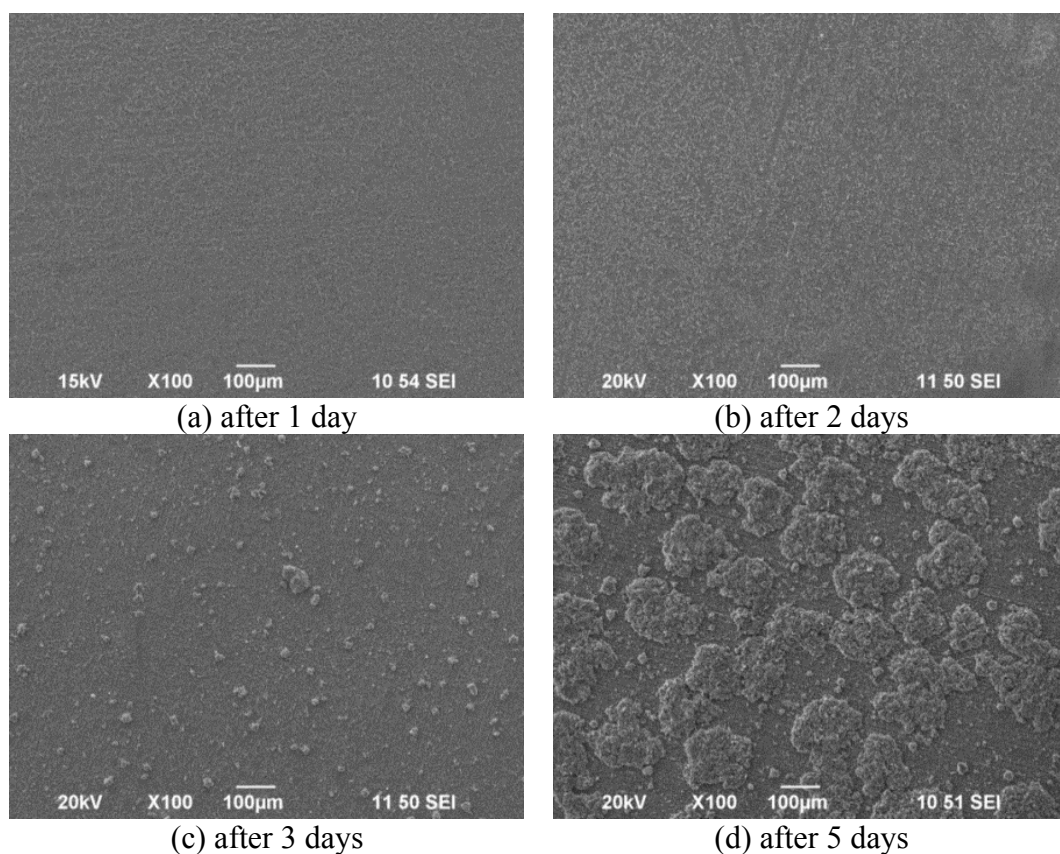
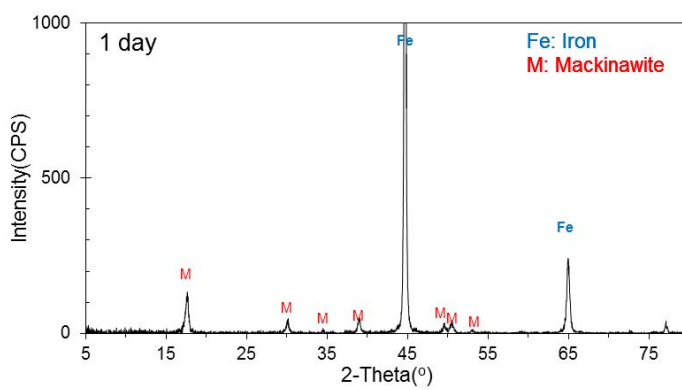
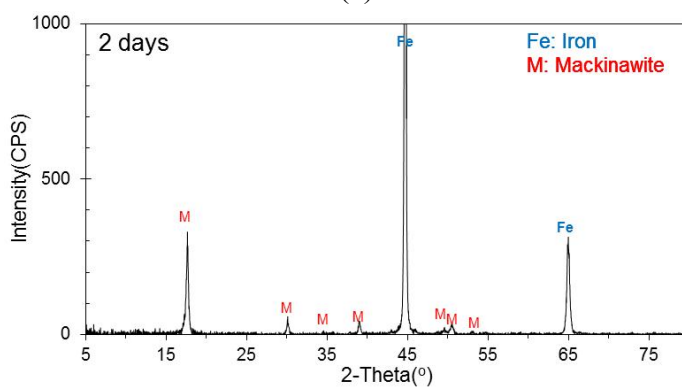


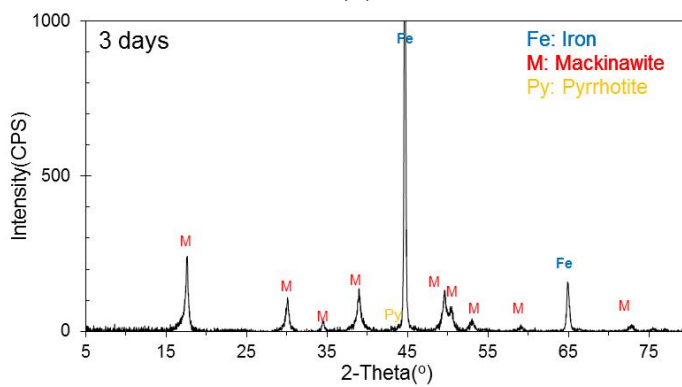
Figure 81. Surface morphologies of samples in chronological order: (a) after 1 day; (b) after 2 days; (c) after 3 days; (d) after 5 days.



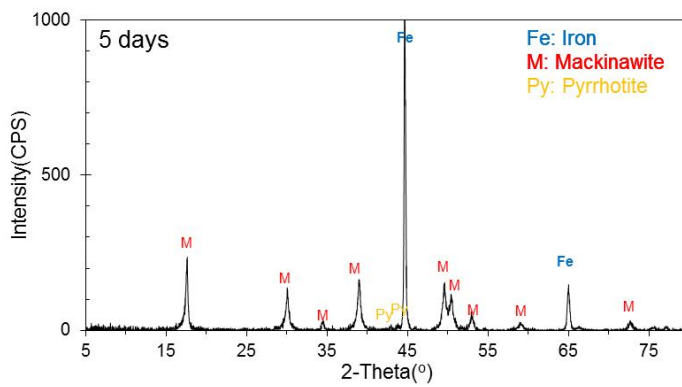
(a)



(b)



(c)



(d)

Figure 82. XRD pattern of corrosion product layer formed on samples in Exp. #3: (a) after 1 day; (b) after 2 days; (c) after 3 days; (d) after 5 days.

Table 23 XRD quantitative analysis of corrosion products formed in Exp. #3.

Phases	2 days	3 days	5 days
Iron	84 %	52 %	45 %
Mackinawite	16 %	45 %	49 %
Pyrrhotite	0	1 %	4 %
Greigite	0	0	0
Pyrite	0	0	0
Iron Carbide	0	2 %	2 %

The cross section images of corrosion product layers formed on samples after exposure for 2 days, 3 days, and 5 days are shown in Figure 83, where an increase in the thickness of the iron sulfide layer from 2 days through to 5 days was observed. A layer of a thickness of 3.3  $\mu\text{m}$  after 2 days of test was seen, while a thickness of 11  $\mu\text{m}$  after 3 days and 21  $\mu\text{m}$  after 5 days were observed. The increase in the thickness of the layer is considered to be due to the precipitation of mackinawite from the bulk solution after the pH adjustment.

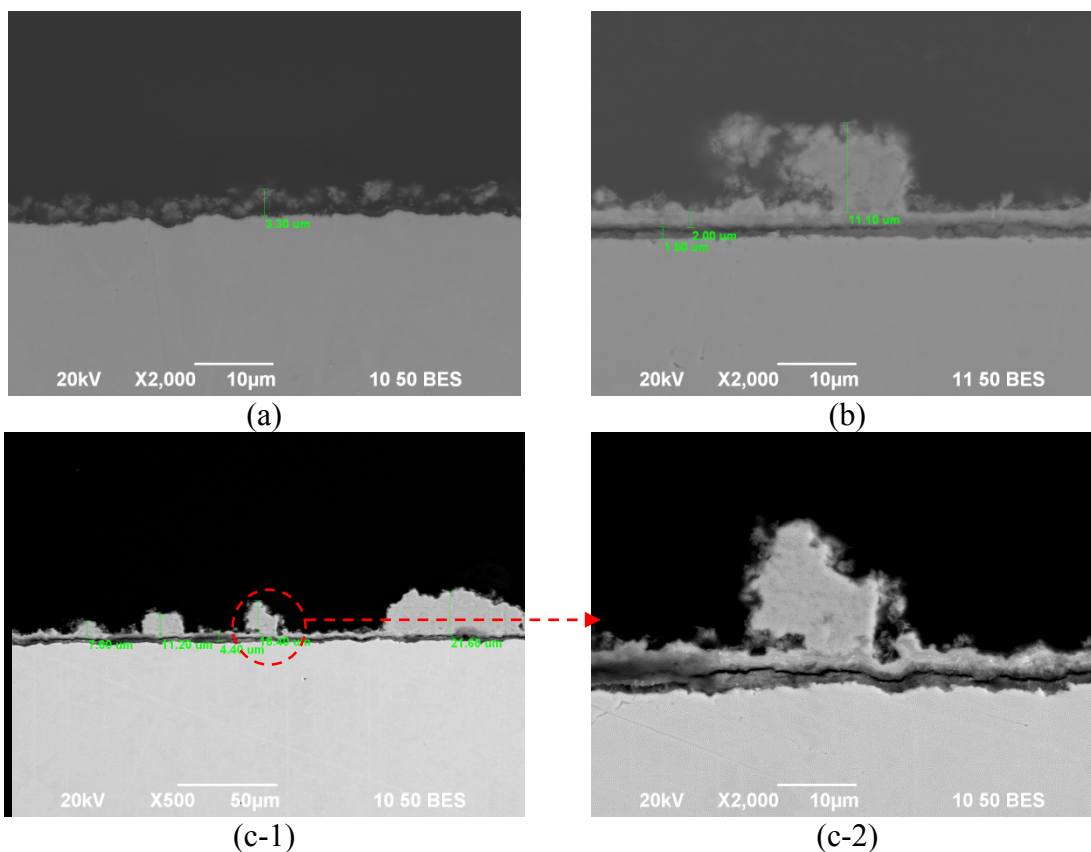


Figure 83. Cross section images of samples in Exp. #3: (a) after 1 day with 2000x magnification;(b) after 3 days with 2000x magnification; (c-1) after 5 days with 500x magnification; (c-2) after 5 days with 2000x magnification.

### 6.5.3.3 Surface Profilometry of Samples after Removing Corrosion Product Layer

The corrosion product layer was removed to check if localized corrosion occurred in the present experiment, particularly after the pH adjustment. A flat surface owing to uniform corrosion before the pH adjustment was seen in Figure 84 (a). After the pH adjustment, a flat surface was observed on the sample after 3 days of exposure in Figure 84 (b) and also on the sample after 5 days of test in Figure 84 (c). Based upon the profilometry of these samples before and after pH adjustment, localized corrosion did not occur in the present experiment. This result confirms the fact that the localized corrosion observed in Exp. Set #2 was not due to elemental sulfur and/or polysulfides formation in

the solution at the high pH conditions. Although high pH conditions were reproduced, it seems that the development of mackinawite was insufficient for transformation into greigite and/or pyrite. Given that neither greigite nor pyrite was detected after the pH adjustment, this is proof of a strong connection between localized corrosion and the formation of greigite and/or pyrite.

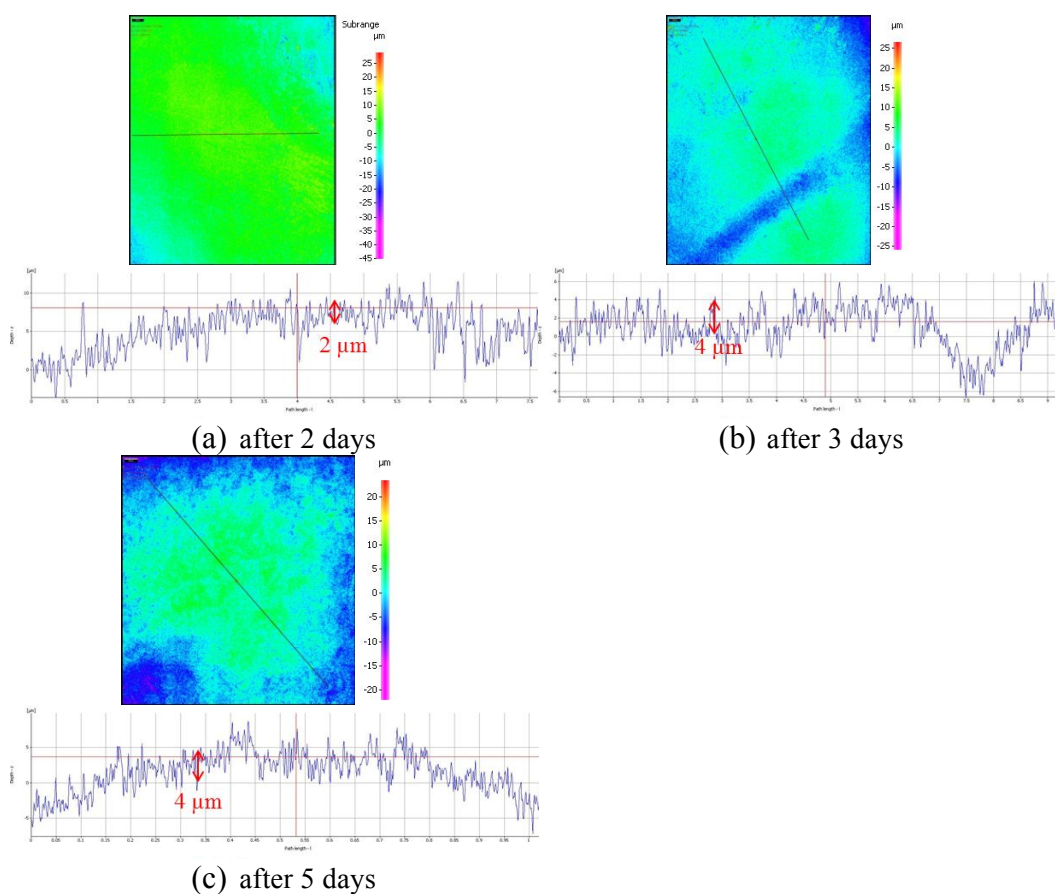


Figure 84. Surface profilometry of samples in Exp. #3: (a) 2 days; (b) 3 days; (c) 5 days.

#### 6.5.3.4 EIS Measurement

The EIS data measured throughout the present experiment is shown as Nyquist plots in Figure 85 and as Bode plots in Figure 86. A typical straight line with a 45° slope at low frequencies immediately after the pH adjustment (after 2.15 days) can be observed

in Figure 85, which is a well-known sign of Warburg diffusion. This suggests that the system was under mass transfer diffused control immediately after the pH adjustment, which is consistent with the experimental findings that considerable mackinawite precipitated from the bulk solution after the change in solution pH. In addition, one time constant was seen before the pH adjustment, but two time constants were observed after the pH adjustment in Figure 86, which may indicate the formation of a protective layer after the pH adjustment.

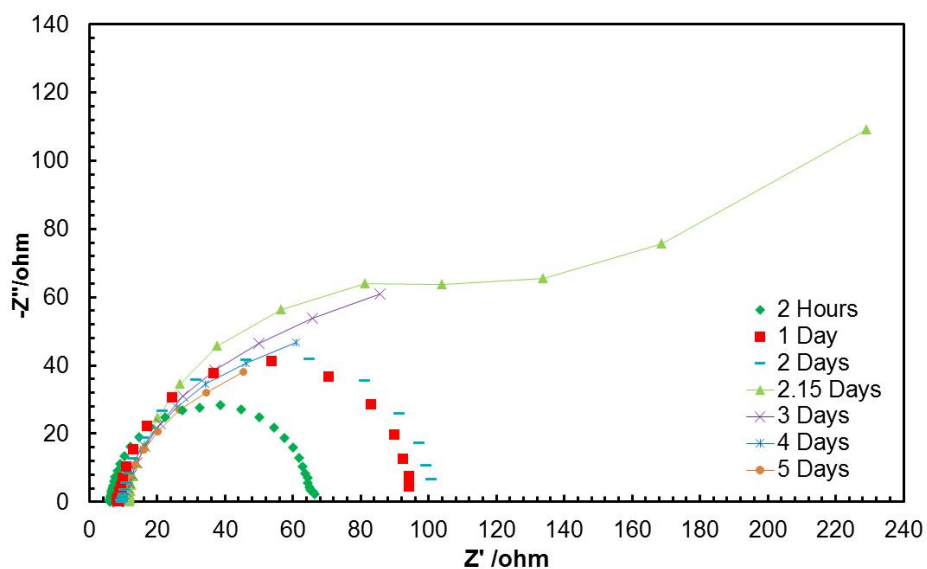


Figure 85. Nyquist plots in Exp. #3.

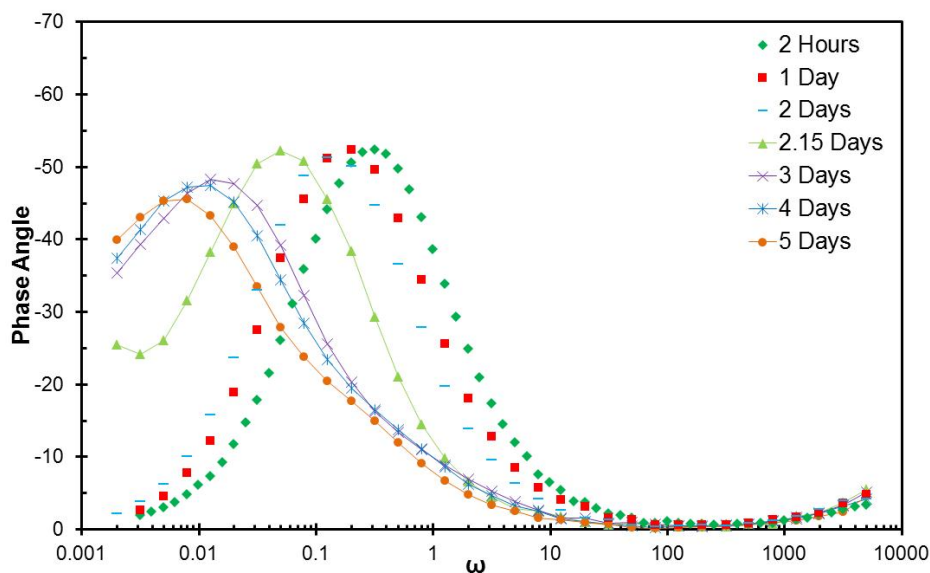


Figure 86. Bode plots (Phase Angle vs. Log  $\omega$ ) in Exp. #3.

## 6.6 Discussion

Based on these three sets of experiments, localized corrosion was observed only in conditions when there was formation of enough greigite and/or pyrite (including both spontaneous formation at high temperature and formation triggered by adjusting solution pH). In addition, localized corrosion was not found when greigite and pyrite did not form. All of these experimental results prove that there is a strong correlation between the localized corrosion and the formation of greigite and/or pyrite. That is, formation of greigite and/or pyrite probably play an important role in the initiation of localized corrosion. However, the mechanism of this type of localization corrosion related to the formation of greigite and/or pyrite is not yet clear.

### 6.6.1 Electrochemical Half Reactions

Although mechanisms of uniform  $H_2S$  corrosion (an electrochemical reaction vs. a direct reaction) have been debated for several decades [8], [136]–[138], more and more

findings [9], [11], [138]–[142] are in favor of the electrochemical mechanism. From the electrochemical perspective, H<sub>2</sub>S corrosion of mild steel is composed of an anodic half reaction, iron dissolution, as shown in Reaction (55), and two cathodic half reactions, hydrogen reduction given in Reaction (56) and H<sub>2</sub>S reduction shown in Reaction (57).



As shown in Figure 60 (Exp. #1) and Figure 71 (Exp. #2), an increase in both corrosion potential and corrosion rate was observed when there was occurrence of localized corrosion. Scenarios of anodic and cathodic half reactions are shown schematically in Figure 87. Both the anodic half reaction and the cathodic half reaction are shown in Figure 87 (a), where corrosion potential and corrosion current density are determined through an intersection point of these two half reactions. One can propose many scenarios simulating experimental findings, which is an increase in both corrosion potential and corrosion current density. Nevertheless, the only one that would explain the experimental results is that the cathodic reaction shifted forward more than the anodic reaction, shown as the dashed lines in Figure 87 (b).

The increase in both the OCP and the corrosion rate may be due to a galvanic effect related to differences in the electrical conductivity associated with polymorphous iron sulfides [143]–[147] or a change in water chemistry at steel surface [122] during the forming process of pyrite and/or greigite. Nevertheless, a comprehensive mechanistic study on this type of localized corrosion is needed and has been performed, as shown in Chapter 7.

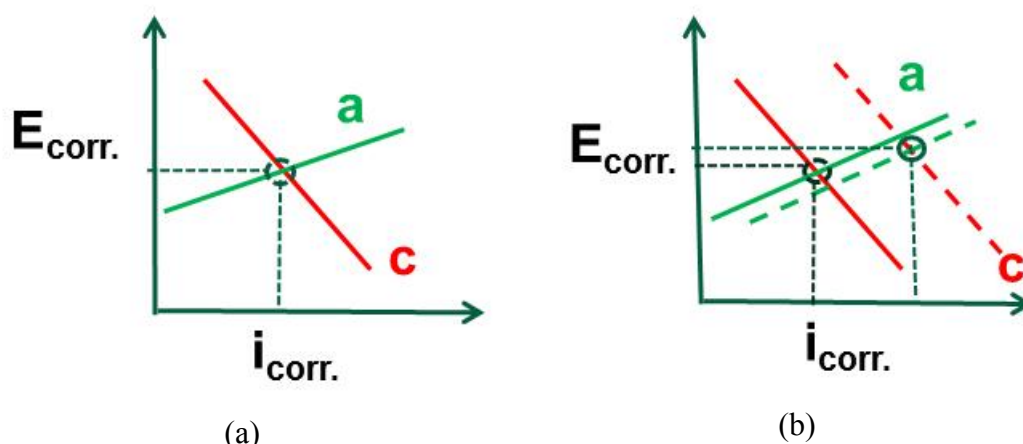


Figure 87. Discussion of electrochemical half reactions.

### 6.6.2 Electrical Conductivity of Polymorphous Iron Sulfides

Mackinawite is composed of 2D layers held together through van der Waals forces shown in Figure 27 (a). Mackinawite is not a thermodynamically stable product, making experimental measurement of its conductivity hard to determine. Therefore, no experimental measurement of mackinawite conductivity could be found in open literature. Devey [143] modeled the structure of mackinawite and surmised that mackinawite is an electronic anisotropy, which means it is a metallic conductor in the single sheet, but acts as an insulator between the sheets.

On the other hand, both greigite (shown in Figure 27 e) and pyrite (shown in Figure 27 f) crystals are composed of compact cubic units. Like mackinawite, greigite is not thermodynamically stable; hence, its conductivity is not addressed by experimental measurement. Nevertheless, greigite is considered to be a semi-conductor by Devey [143], and also referred to be metallic [144]. Based upon the limited available references, greigite is considered to be at least a semiconductor.

Pyrite is a thermodynamically stable iron sulfide, thereby, enabling experimental measurement of its conductivity. Figure 88 shows the resistivity chart of materials. The left side stands for conductors, while the right side represents insulators. In Figure 88, all the experimental data [144]–[147] for the resistivity of pyrite from various sources is adjacent to metals, clearly suggesting that pyrite is a semiconductor with good conductivity based on sufficient experimental data. A specific value is not given because the resistivity data of pyrite from various references varies in wide ranges. This is because of the dependence of the purity of the pyrite mineral and experimental temperature on the measured resistivity.

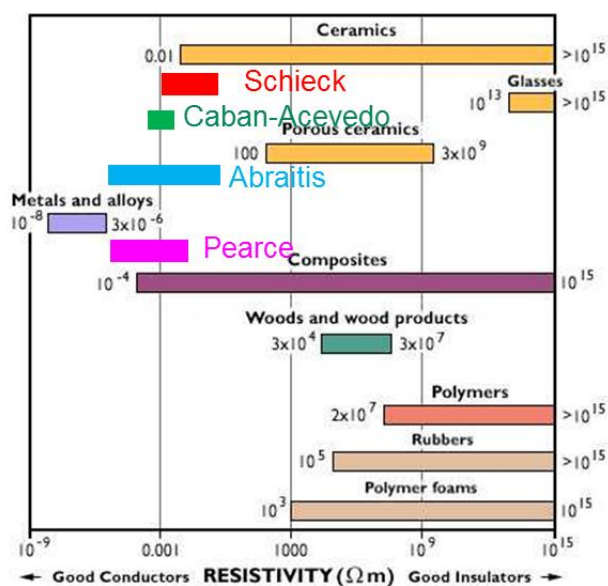


Figure 88. Resistivity data of pyrite from various experimental sources (Schieck [145], Caban-Acevedo [146], Abraitis [147], Pearce [144]) (reproduced from [148]).

## 6.7 Summary

- Experimental conditions leading to reproducible localized corrosion in a sour environment were found.
- In the current experimental conditions, severe localized corrosion was observed in experiments when there was an indication of the formation of greigite and/or pyrite. In addition, localized corrosion was not found when neither greigite nor pyrite formed.
- The formation of greigite and/or pyrite plays an important role in the initiation of the localized corrosion.
- A further comprehensive study is required to investigate the correlation between the localized corrosion and greigite and/or pyrite formation.

## CHAPTER 7. THE ROLE OF PYRITE IN LOCALIZED CORROSION

### 7.1 Introduction

A correlation between localized corrosion and pyrite and/or greigite was seen in Chapter 6. Although experimental results have proven that the formation of greigite and/or pyrite plays an important role in the initiation of the localized corrosion, a comprehensive mechanistic study on this type of localized corrosion is needed. To bypass the complicated transformation step of polymorphous iron sulfides, as a thermodynamically stable iron sulfide, pyrite was directly deposited onto the steel surface and the subsequent corrosion process of the steel was studied. Experiments were designed and conducted to address these questions:

- Does localized corrosion occur when pyrite is deposited on mild steel in an aqueous H<sub>2</sub>S environment?
- If so, is this type of localized corrosion due to a galvanic coupling between the pyrite and steel?

### 7.2 Experimental

#### 7.2.1 Apparatus

The under deposit corrosion (UDC) sample holder used in this study is shown in Figure 89 [149]. The base, shown on the left with three conductive pins, is designed for electrochemical measurement connection. The sample holder in the middle of Figure 89 is for placing the mild steel sample, and the deposit holder shown on the right side of Figure 89 is used to hold and measure the depth of the deposited particles. This UDC setup was exposed to electrolyte in the glass cell depicted in Figure 90. A stirring bar was set underneath the sample holder to fully mix solution during the experiment. In addition,

Figure 90 shows an electrochemical cell consisting of a working electrode (steel sample), reference electrode (vs. Ag/AgCl Sat'd KCl), and counter electrode (a platinum wire).

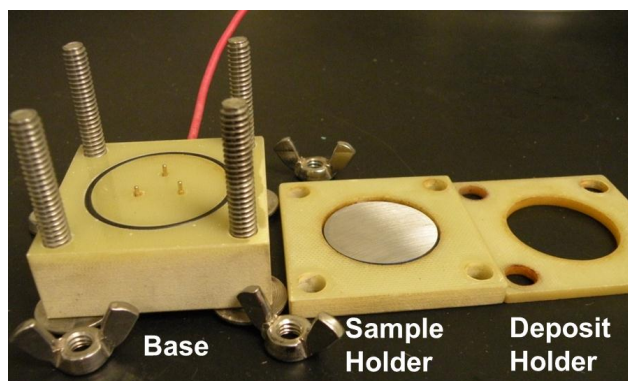


Figure 89. UDC sample holder [149].

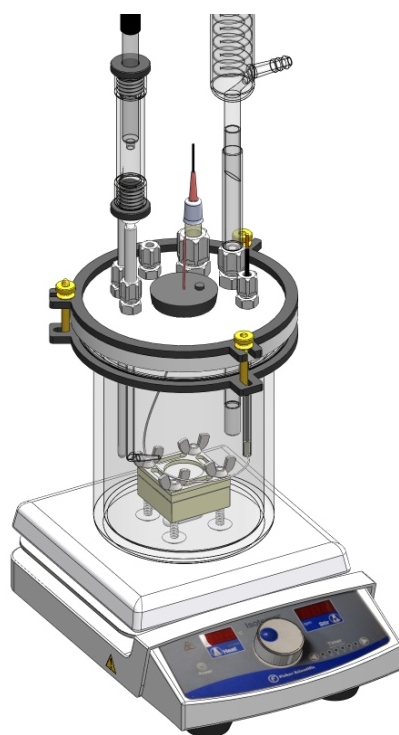


Figure 90. Experimental glass cell setup.

### 7.2.2 *Materials*

Samples with a 7.9 cm<sup>2</sup> exposed area are made from API X65 carbon steel. The chemical composition of this carbon steel is shown in Table 14.

### 7.2.3 *Procedure*

Nitrogen gas (N<sub>2</sub>) was sparged into the glass cell filled with 2-liter of electrolyte until pH stabilized (typically a few hours). In the case of CO<sub>2</sub> corrosion experiments, CO<sub>2</sub> gas was sparged into the electrolyte from the beginning instead of N<sub>2</sub>. Bulk pH of the electrolyte was adjusted to pH 4.0 using 1.0 M deoxygenated HCl or NaOH solutions. Deposits (silica sand and pyrite particles) were washed using acetone, rinsed thoroughly with deionized water, blown dry, and put into a container filled with the same electrolyte. The N<sub>2</sub> or CO<sub>2</sub> gas was also sparged into the container until saturated, and the pH of solution in the container was adjusted to pH 4.0 as well.

An API 5L X65 carbon steel sample with a 7.9 cm<sup>2</sup> exposed area was polished to a 600 grit sand paper, rinsed thoroughly with deionized water and isopropanol, ultrasonically cleaned in isopropanol, dried by an air blower, and mounted into the UDC sample holder as shown in Figure 89. The sample holder was introduced in the glass cell and the steel sample was pre-corroded for one hour. Then, a layer of 2 mm thick silica sand or pyrite particles was deposited onto the steel sample surface. The sample holder images with silica sand and pyrite deposits are shown in Figure 91 (a) and (b), respectively. In the case of using H<sub>2</sub>S gas, an H<sub>2</sub>S and N<sub>2</sub> mixed gas with 10% H<sub>2</sub>S in gas phase was sparged into the glass cell approximately one hour after the deposition of the solid layer. The test was conducted for a week. Electrochemical measurements on the steel sample were conducted to obtain the corrosion rate of the steel sample and the

solution resistance using a Gamry Potentiostat REF-600. After the test, SEM and EDX were used to analyze the surface morphologies of the steel sample. In addition, weight loss of the steel sample was performed to confirm LPR measurements. The surface profilometry of the sample after removing the corrosion product layer was performed confirming the occurrence of localized corrosion.

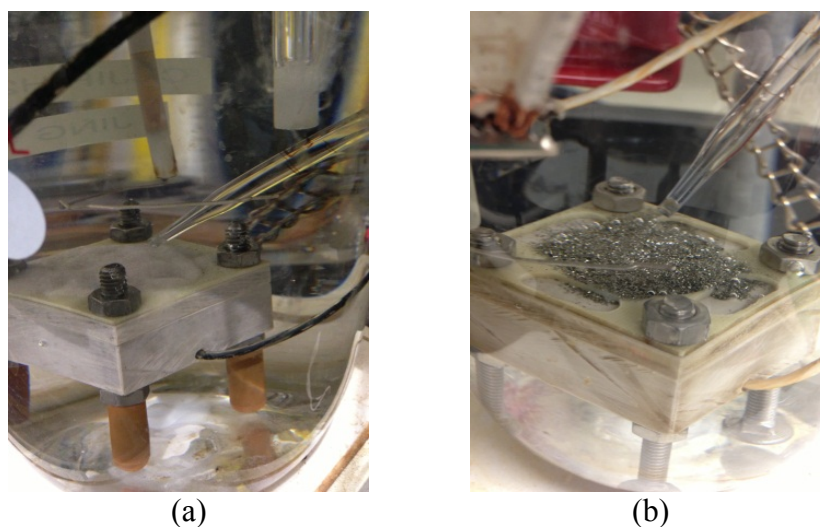


Figure 91. (a) Sample holder with a layer of silica sand deposit; (b) Sample holder with a layer of pyrite particles deposit.

#### 7.2.4 *Characterization of Deposits*

##### 7.2.4.1 *Particle Size*

Figure 92 shows SEM images of the deposits used in experiments. Figure 92 (a) shows the silica sand particles with approximate 150 ~ 400  $\mu\text{m}$  dimensions, (b) shows pyrite particles of the same size, and (c) shows pyrite particles with larger dimensions, 1000 ~ 2000  $\mu\text{m}$ . All deposits were screened using sieves for the desired size.

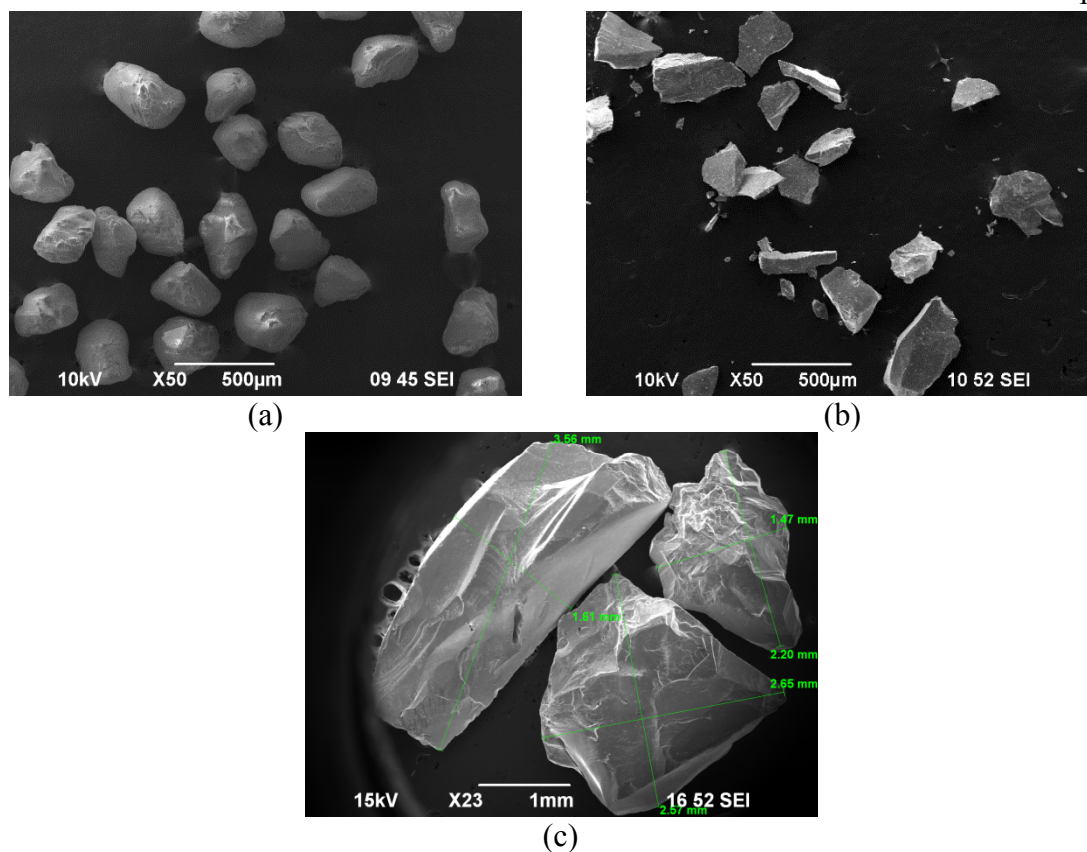


Figure 92. (a) 150 ~ 400  $\mu\text{m}$  silica sand; (b) 150 ~ 400  $\mu\text{m}$  pyrite particles; (c) 1000 ~ 2000  $\mu\text{m}$  pyrite particles.

#### 7.2.4.2 *Purity of Pyrite Particles*

Pyrite particles were ground into powder. Figure 93 shows the XRD pattern of the pyrite powder, and accordingly, only the pyrite phase was detected. Further, quantitative analysis of this powder listed in Table 24 also confirms that pyrite accounts for 99.6% of the pyrite sample used for all experiments.

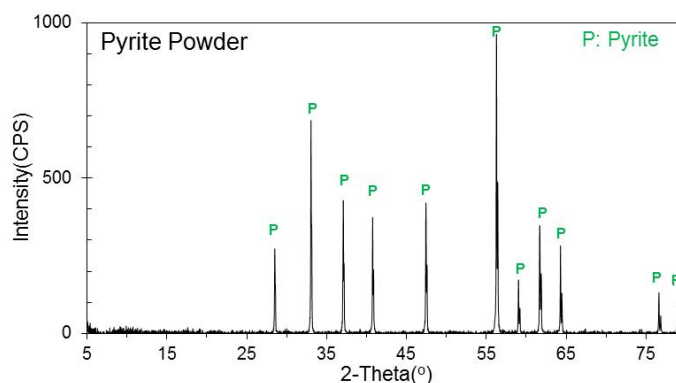


Figure 93. XRD pattern of the pyrite powder.

Table 24 XRD quantitative analysis of the pyrite powder.

Phases	Content (%)
Pyrite	99.6
Iron	0.00
Greigite	0.0
Mackinawite	0.1
Pyrrhotite	0.0
Iron Carbide	0.3
Quartz	0.00

## 7.2.5 Test Matrix

### 7.2.5.1 Test Series #1: Pyrite/Silica Sand UDC Test in an Aqueous H<sub>2</sub>S Environment

The objective of this series of tests was to verify if localized corrosion would occur when pyrite is deposited on mild steel surface in an aqueous H<sub>2</sub>S environment, compared to the blank test in the presence of the silica sand deposit. Table 25 shows the test matrix of this series of tests. Two tests (Test #1 and Test #2) were carried out in a 1 wt. % NaCl solution. Pyrite particles with 150 ~ 400 μm dimensions were used as deposit to study the effect of pyrite on the corrosion process of the steel underneath. In addition, silica sand was also deposited on the steel surface as a blank test.

Table 25 Test matrix for test series #1.

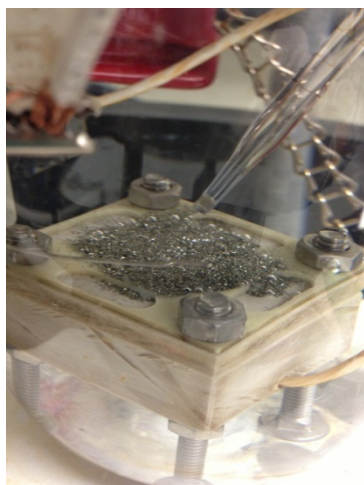
Description	Test #1	Test #2
Deposit	Silica sand	Pyrite particles
Deposit Particle Size	150 ~ 400 $\mu\text{m}$	
Deposit Layer Depth	2 mm	
Temperature	25 °C	
Gas Composition	$\text{pH}_2\text{S}$ (balance with $\text{N}_2$ ) = 0.1 bar	
Stirring Speed	500 rpm	
Electrolyte	1 wt.% NaCl	
Material	API 5L X65	
Test Duration	1 week	
Initial pH	4.0	

#### 7.2.5.2 Test Series #2: The Impact of Pyrite Particle Size on Corrosion

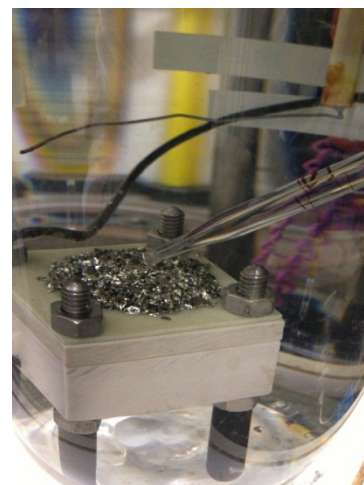
This test series was designed to study the impact of pyrite particle size on the corrosion process, particularly on localized corrosion. A larger pyrite particle size, 1000 ~ 2000  $\mu\text{m}$ , was used in Test #3 comparing with the smaller particle size used in Test #2. The test matrix is shown in Table 26. Figure 94 presents the experimental setup with a layer of the smaller pyrite particles and a layer of the larger pyrite particles, respectively.

Table 26 Test matrix for test series #2.

Description	Test #2	Test #3
Deposit	Pyrite particles	
Deposit Particle Size	150 ~ 400 $\mu\text{m}$	1000 ~ 2000 $\mu\text{m}$
Deposit Layer Depth	2 mm	
Temperature	25 °C	
Gas Composition	$\text{pH}_2\text{S}$ (balance with $\text{N}_2$ ) = 0.1 bar	
Stirring Speed	500 rpm	
Electrolyte	1 wt.% NaCl	
Material	API 5L X65	
Test Duration	1 week	
Initial pH	4.0	



(a)



(b)

Figure 94. Experimental setup with: (a) 150 ~ 400  $\mu\text{m}$  pyrite particles; (b) 1000 ~ 2000  $\mu\text{m}$  pyrite particles.

### 7.2.5.3 *Test Series #3: Investigating Potential Mechanisms for Localized Corrosion*

The objective of this test series was to investigate the mechanism of localized corrosion in the presence of the pyrite deposit by insulating the electrical contact between

pyrite and steel with a Nylon mesh, while maintaining ionic conductivity of the solution. A very thin insulating Nylon mesh was used in this series of experiments. Figure 95 shows a SEM image of this insulating mesh and Table 27 shows the physical properties of the mesh. Figure 96 illustrates the procedure for introducing the mesh in experiments. Two tests were carried out in this series of experiments using the insulating mesh. The test matrix is listed in Table 28. Test #4 was completed using the smaller pyrite particles (150 ~ 400  $\mu\text{m}$ ) and Test #5 was done using the larger pyrite particles (1000 ~ 2000  $\mu\text{m}$ ).

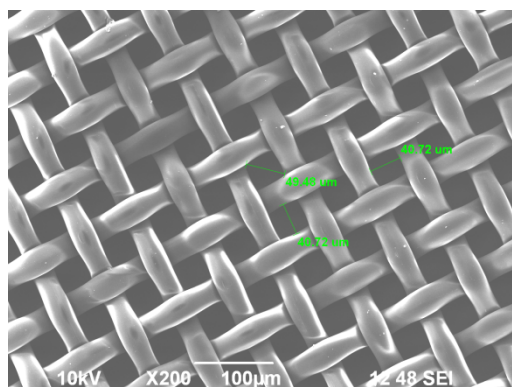


Figure 95. A SEM image of the insulating mesh.

Table 27 Properties of the insulating mesh.

Description	Parameter
Material	Nylon
Opening	41 $\mu\text{m}$
Open area	33 %
Thickness	60 $\mu\text{m}$
Diameter	47 mm
pH Tolerance	3 ~ 10
Thermal Stability	up to 180 $^{\circ}\text{C}$

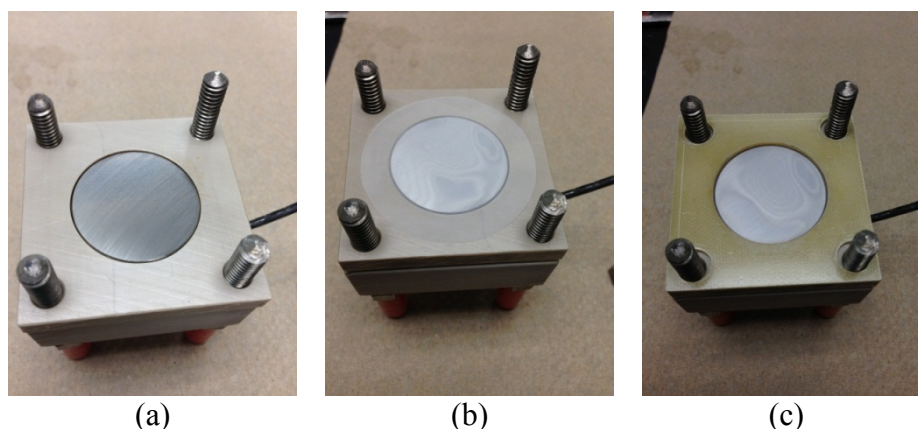


Figure 96. Procedure for introducing the insulating mesh: (a) a steel sample prepared and introduced into the sample holder; (b) a non-conductive mesh used over the sample surface; (c) the deposit holder placed over the mesh.

Table 28 Test matrix for test series #3.

Description	Test #4	Test #5
Deposit Solids	Mesh + Pyrite particles	
Deposit Particle Diameter	150 ~ 400 $\mu\text{m}$	1000 ~ 2000 $\mu\text{m}$
Deposit Layer Depth	2 mm	
Temperature	25 °C	
Gas Composition	$\text{pH}_2\text{S}$ (balance with $\text{N}_2$ ) = 0.1 bar	
Speed of Stir Bar	500 rpm	
Electrolyte	1 wt.% NaCl	
Material	API 5L X65	
Test Duration	6 hours	1 week
Initial pH	4.0	

#### 7.2.5.4 Test Series #4: Pyrite/Silica Sand UDC Test in an Aqueous $\text{CO}_2$ Environment

The objective of this test series was to verify that this type of localized corrosion can occur when  $\text{H}_2\text{S}$  is absent by performing tests in a pure  $\text{CO}_2$  environment, considering  $\text{CO}_2$  gas is ubiquitous in the oil and gas industry. Two tests were completed

by depositing silica sand and pyrite particles onto the mild steel surface in an aqueous CO<sub>2</sub> solution. Table 29 shows the test matrix for these two tests.

Table 29 Test matrix for test series #4.

Description	Test #6	Test #7
Deposit	Silica sand	Pyrite particles
Deposit Particle Diameter	150 ~ 400 μm	
Deposit Layer Depth	2 mm	
Temperature	25 °C	
Gas Composition	pCO <sub>2</sub> = 0.97 bar	
Stirring Speed	500 rpm	
Electrolyte	1 wt.% NaCl	
Material	API 5L X65	
Test Duration	1 week	
Initial pH	4.0	

### 7.3 Results and Discussion

#### 7.3.1 Test Series #1: Pyrite/Silica Sand UDC Test in an Aqueous H<sub>2</sub>S Environment

##### 7.3.1.1 Comparison of Electrochemical Behavior

A silica sand layer was deposited onto the steel sample surface in a blank test. Figure 97 shows the OCP and the corrosion rate in the initial five hours, including the deposition of a silica sand layer and the introduction of H<sub>2</sub>S gas to the solution. A decrease in both OCP and corrosion rate was observed after the deposition of the sand layer, which is considered to be due to the surface coverage and a diffusion barrier effect provided by the sand layer [149]. The addition of H<sub>2</sub>S gas to the solution was done

approximately one hour after depositing the sand layer. It was observed that the corrosion rate gradually increased after the addition of  $H_2S$  gas. This is considered to be due to the introduction of the corrosive aqueous  $H_2S$ . Figure 98 presents the OCP and corrosion rate throughout the test for one week. Weight loss of the steel substrate, shown as a green circular data point in Figure 98, was measured to confirm LPR measurements. A decrease in the corrosion rate after a half-day and the subsequent stability throughout the test was observed, which might be due to the formation of an iron sulfide layer.

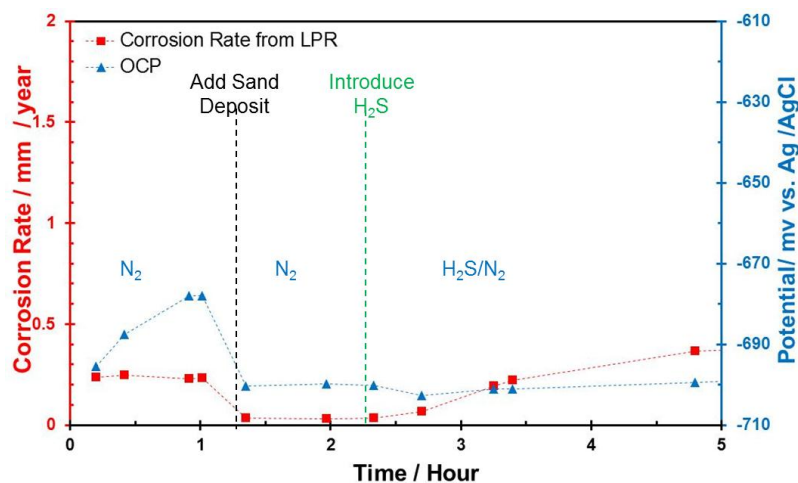


Figure 97. Corrosion rate and OCP using 2 mm thickness of silica sand deposit in the initial hours of Test #1.

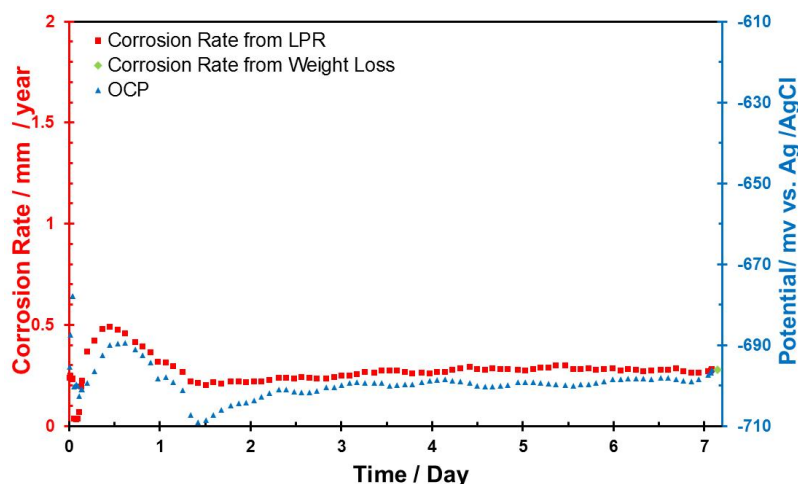


Figure 98. Corrosion rate and OCP using 2 mm thickness of silica sand deposit for a week in Test #1.

In contrast, evolution of OCP and corrosion rate in the initial five hours including the deposition of a pyrite particle layer and the introduction of  $H_2S$  gas are shown in Figure 99. A large increase in both the OCP and corrosion rate was observed after the deposition of the pyrite particle layer. This is understood to be due to a significant increase in cathodic reaction(s). Two hypotheses were proposed for the enhanced cathodic reaction(s). The first is an electrochemical effect providing more cathodic reaction area by electrically contacting pyrite with steel. The second is a chemical effect increasing the concentration of cathodic reaction species during the formation/dissolution process of pyrite, such as  $H^+$ . Both mechanisms are possible for causing the increase in the cathodic reaction(s).

The investigation of this was performed and shown in section 7.3.3. After  $H_2S$  gas was introduced, both OCP and corrosion rate increased dramatically, which is due to the addition of one more cathodic reaction species, aqueous  $H_2S$ . The OCP and corrosion rate throughout the test for a week are shown in Figure 100. The corrosion rate was stable

throughout the test. Weight loss result shown as a green diamond on the right side of Figure 100 agreed well with LPR measurements.

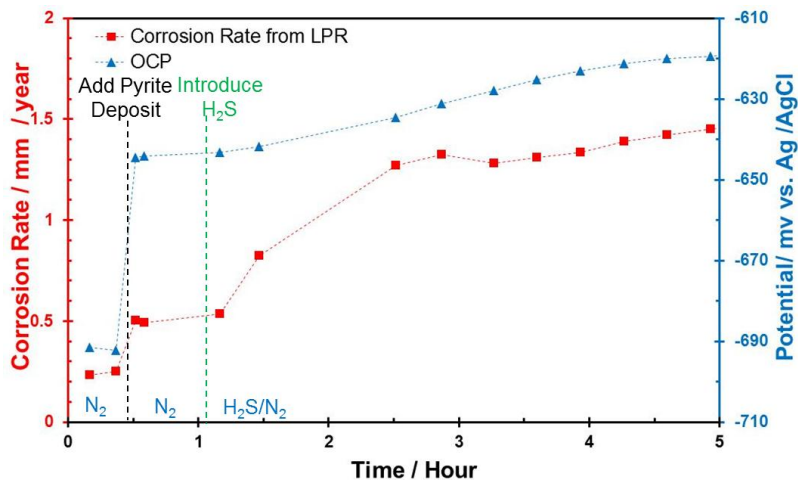


Figure 99. Corrosion rate and OCP using 2 mm thickness of pyrite particle deposit in the initial hours of Test #2.

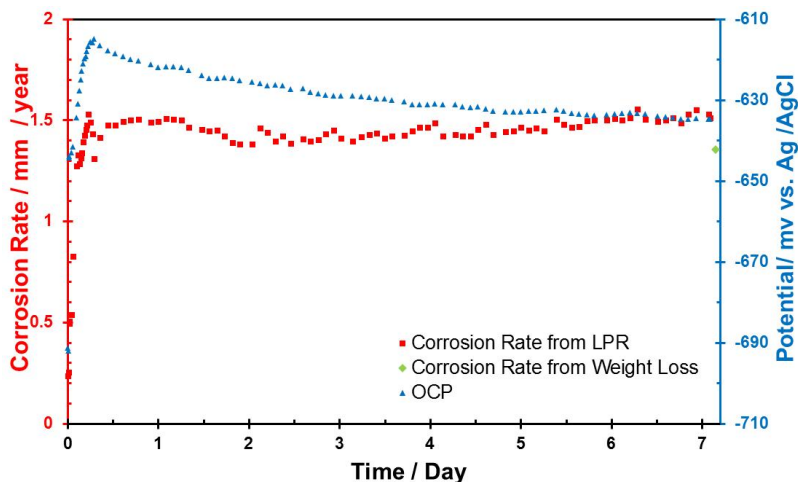


Figure 100. Corrosion rate and OCP using 2 mm thickness of pyrite particle deposit for a week of Test #2.

In addition, EIS was conducted in order to better understand the corrosion mechanisms. EIS data for the Nyquist plots was measured at each step of the experiment and each day during the 7-day experiment for the two tests using silica sand and pyrite

particles and is presented in Figure 101 and Figure 102, respectively. Before the deposition of the sand layer, the corrosion process was under charge transfer control. However, after the deposition of the sand layer, the corrosion process was shifted to diffusion control. This revealed that the sand layer deposited on the steel surface was indeed a diffusion barrier. By contrast, charge transfer control was always dominant in the presence of a pyrite particle layer, as shown in Figure 102. Therefore, the pyrite particle layer deposited on the steel surface did not act primarily as a diffusion barrier.

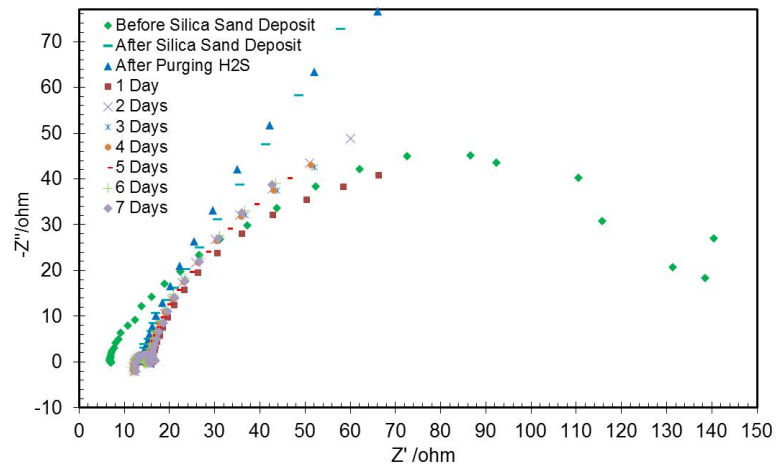


Figure 101. Nyquist plots using 2 mm thickness of silica sand deposit in Test #1.

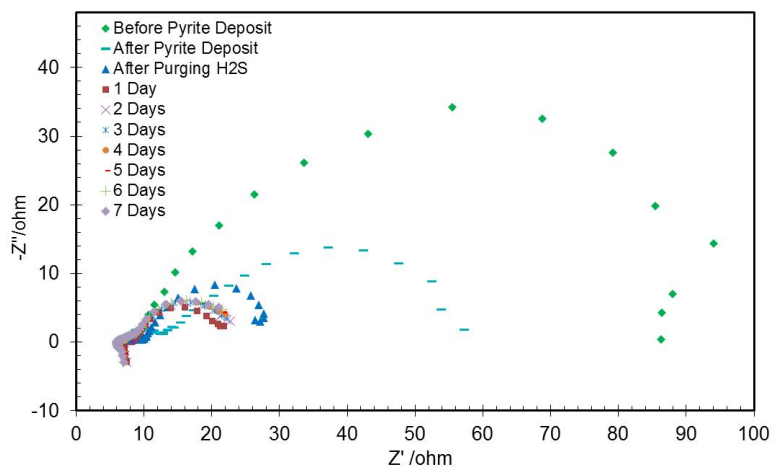


Figure 102. Nyquist plots using 2 mm thickness of pyrite particle deposit in Test #2.

Furthermore, the solution pH and the saturation value for mackinawite ( $S_{\text{mackinawite}}$ ) monitored during the two tests are given in Figure 103. Both pH and  $S_{\text{mackinawite}}$  were stable throughout the test using silica sand deposit due to the low corrosion rate. In the presence of a pyrite deposit layer, an increase in  $S_{\text{mackinawite}}$  values in the initial three days and decrease after three days was observed. This was due to the consumption of  $\text{Fe}^{2+}$  from iron sulfide precipitation and the production of  $\text{Fe}^{2+}$  from corrosion. In the initial days, the corrosion rate was much higher than the precipitation rate of mackinawite. Therefore,  $\text{Fe}^{2+}$  concentration increased, causing an increase in bulk pH as well. This leads to an increase in  $S_{\text{mackinawite}}$  and a subsequent increase in the precipitation of mackinawite. Finally, the equilibrium between the consumption and production of  $\text{Fe}^{2+}$  was reached.

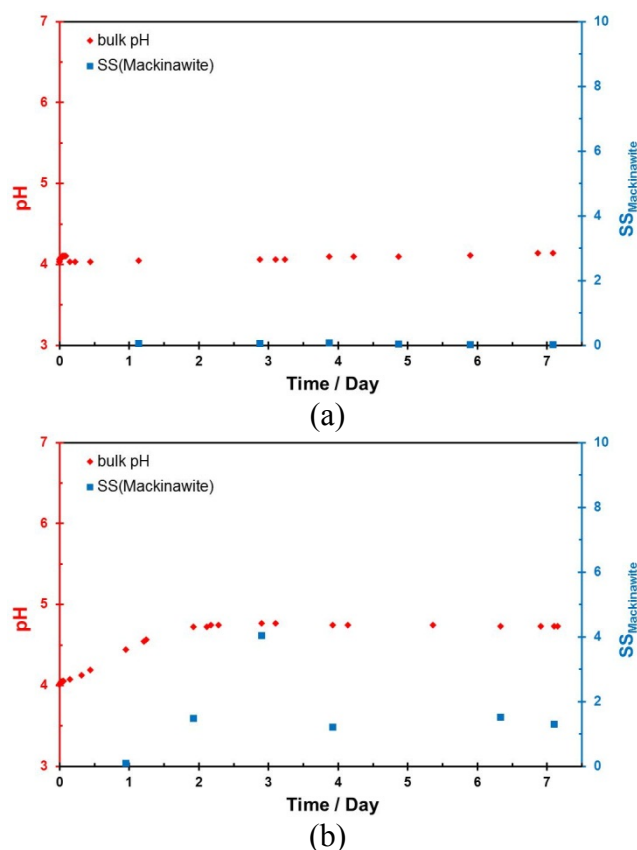


Figure 103. pH and  $S_{\text{mackinawite}}$  with: (a) silica sand deposit in Test #1; (b) pyrite particles deposit in Test #2.

### 7.3.1.2 Comparison of Surface Morphologies

After removal of the silica sand layer, the surface morphologies of the steel sample with the corrosion product layer in place are shown in Figure 104. A uniform surface morphology was observed in Figure 104 (a). A partially covered layer of crystals at a higher magnification was observed in Figure 104 (b). Figure 104 (c) shows EDX analysis, suggesting the chemical composition of the crystal is FeS.

On the other hand, surface morphologies of the steel sample contacted with pyrite particles are shown in Figure 105. After removing those pyrite particles, it was observed that the entire surface was covered by a uniform corrosion product layer. Some locations where damage to this layer occurred can be observed in Figure 105 (a) and are considered

to be related to the pyrite removal procedure after taking the sample out of the glass cell. A SEM image at a high magnification of this damage is shown in Figure 105 (b). Similarly, EDX analysis shown in Figure 105 (c) indicates that the composition of the layer is FeS.

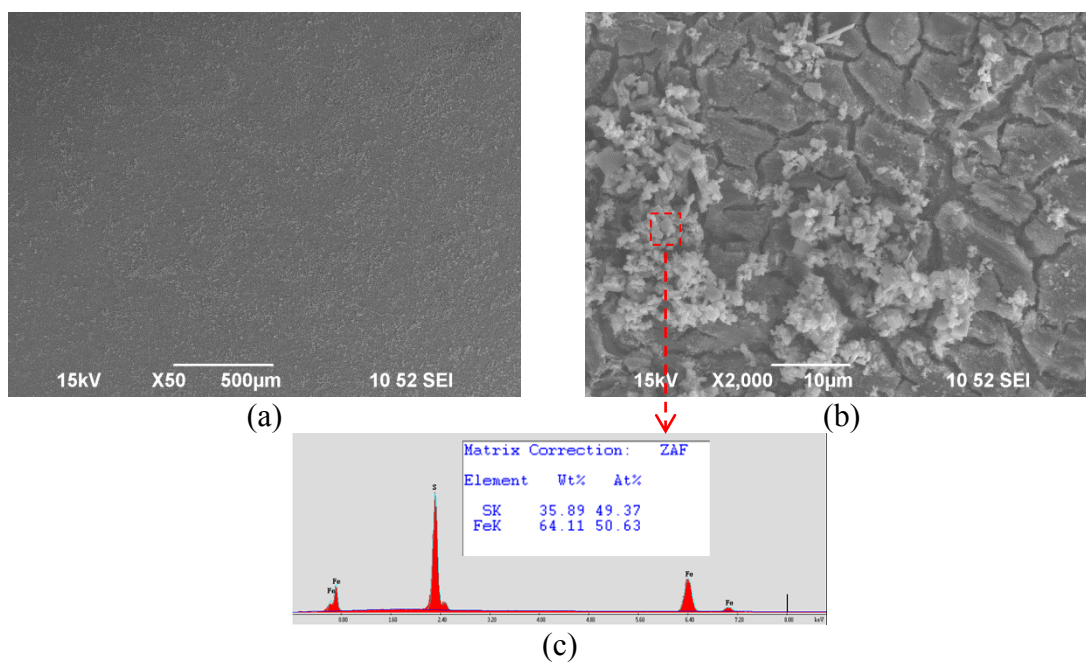


Figure 104. Surface morphologies of the sample with corrosion product layer in place using silica sand deposit in Test #1: (a) 50x SEM image; (b) 2,000x SEM image; (c) EDX analysis of the corrosion product layer.

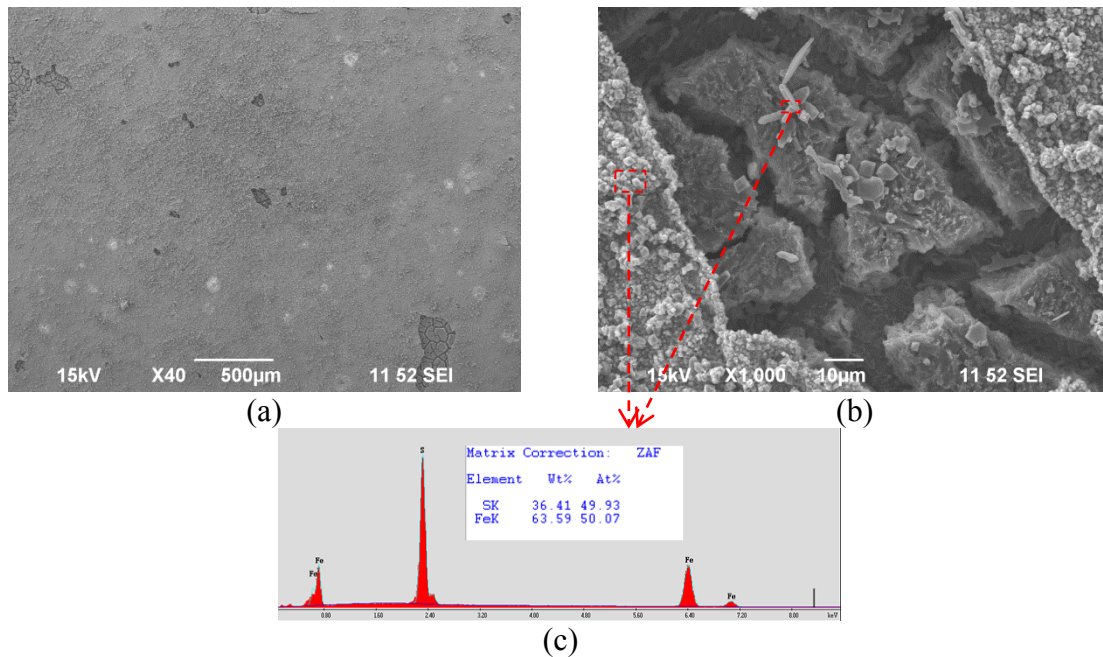


Figure 105. Surface morphologies of the sample with corrosion product layer in place using pyrite particle deposit in Test #2: (a) 50x SEM image; (b) 2,000x SEM image; (c) EDX analysis of the crystals.

Figure 106 shows surface morphologies of the sample after the removal of the silica sand deposit and the corrosion product layer. A steel surface subject to uniform corrosion was observed in Figure 106 (a), although a few inclusions could be found in a high magnification SEM image similar to that shown in Figure 106 (b). In contrast, severe localized corrosion was seen after the removal of the pyrite particle deposit and the associated corrosion product layer in Figure 107. To have a closer look, a collection of locations of pitting corrosion found on the steel sample is shown in Figure 108. The number on the upper left corner of each SEM image in Figure 108 indicates the diameter of the pit.

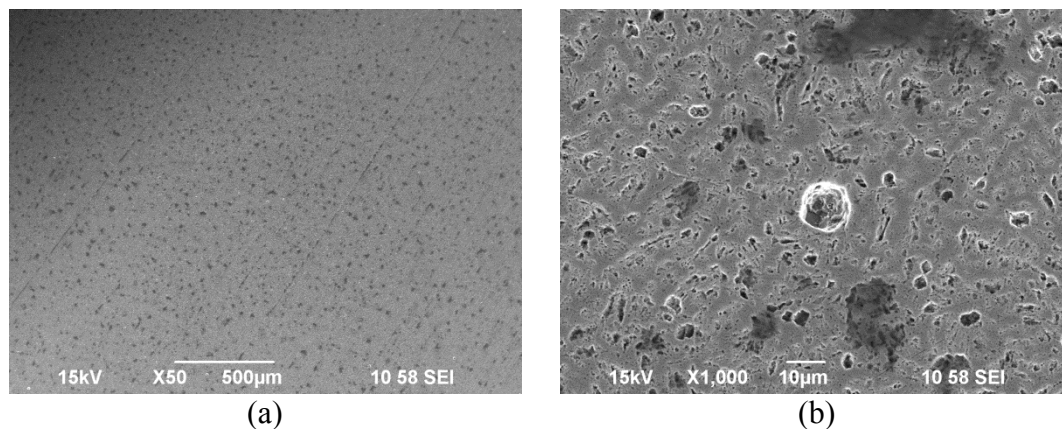


Figure 106. Surface morphologies of the sample after removing the corrosion product layer using silica sand deposit in Test #1: (a) 50x SEM image; (b) 1,000x SEM image.

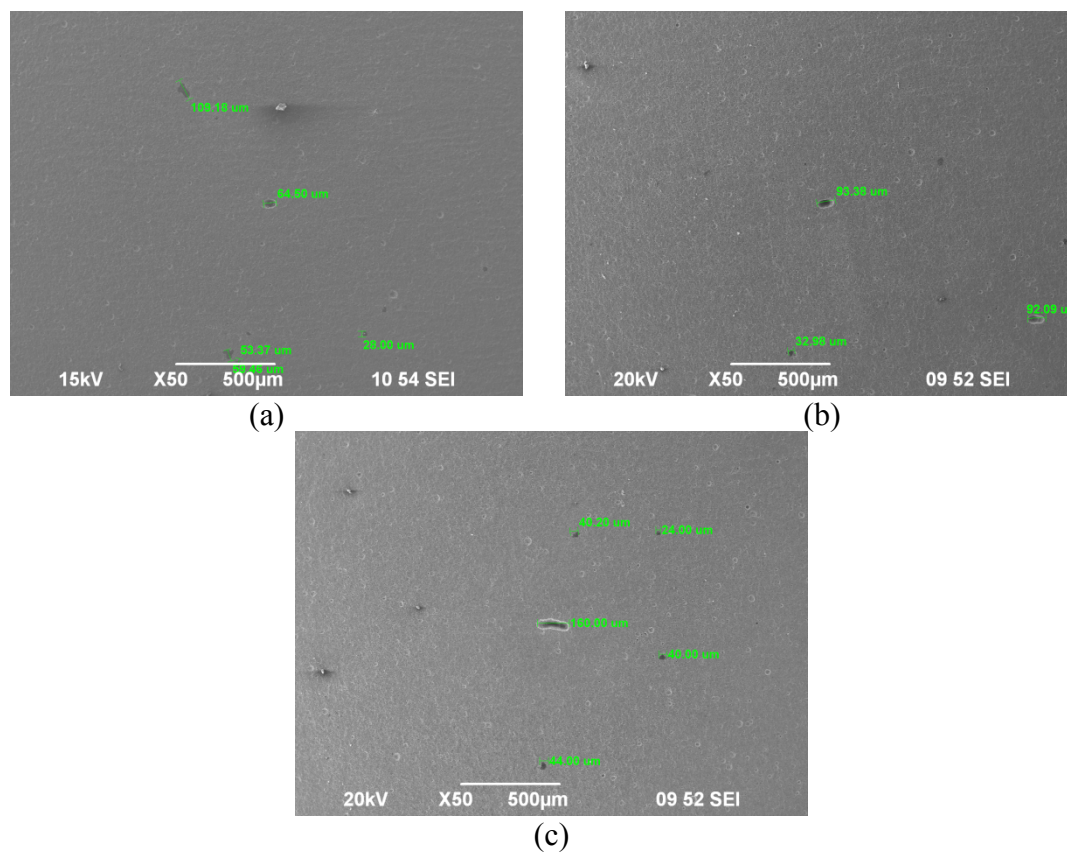


Figure 107. Surface morphologies of the sample after removing the corrosion product layer using pyrite particle deposit in Test #2.

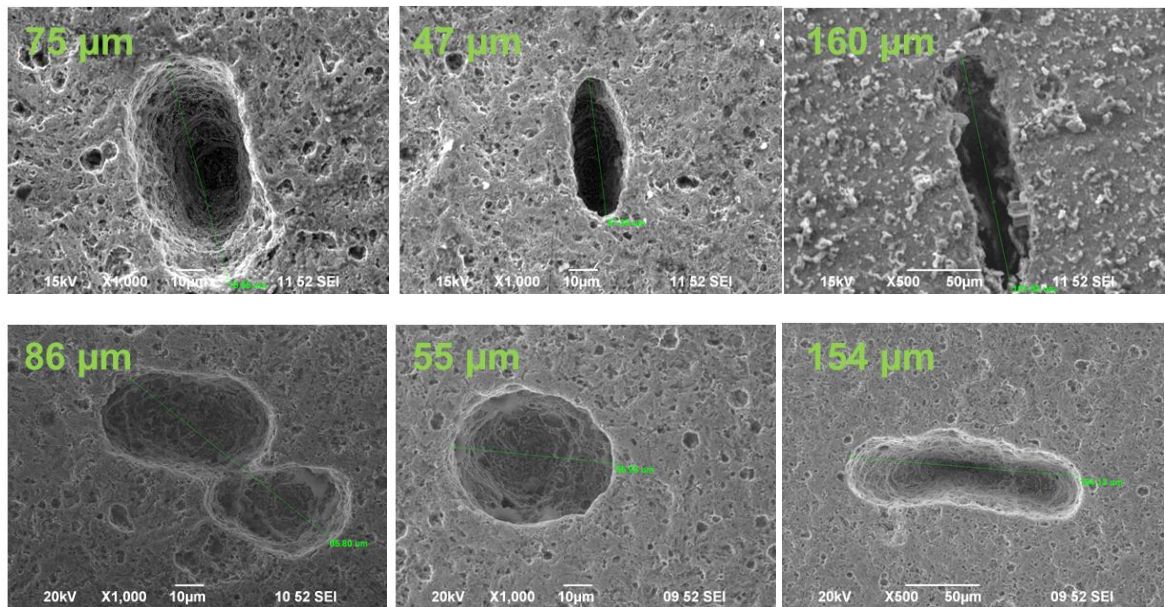


Figure 108. Locations of localized corrosion on the specimen using pyrite particle deposit in Test #2.

Areas on steel samples after removing the corrosion product layer were arbitrarily selected for profilometry analysis to reveal any features across the surface. Profilometry of the sample using the sand deposit is shown in Figure 109 (a) and the maximum pitting depth, 10  $\mu\text{m}$ , found on the sample is shown in Figure 109 (c). In general, uniform corrosion, with a few inclusions, was seen on specimens that had sand deposits. However, many pits with a much greater depth were seen with pyrite, as shown in Figure 109 (b). Figure 109 (d) shows a maximum pitting depth of 135  $\mu\text{m}$  found on the sample.

Figure 110 shows a comparison of corrosion rates between silica sand and pyrite deposits. The general corrosion rate was obtained from weight loss results, and the maximum localized corrosion rate was converted from the maximum pitting depth. Clearly, both general corrosion rate and pit penetration rate were accelerated dramatically in the presence of pyrite particles. The penetration rate was up to 7 mm/year after 7 days of exposure in the presence of pyrite particle layers.

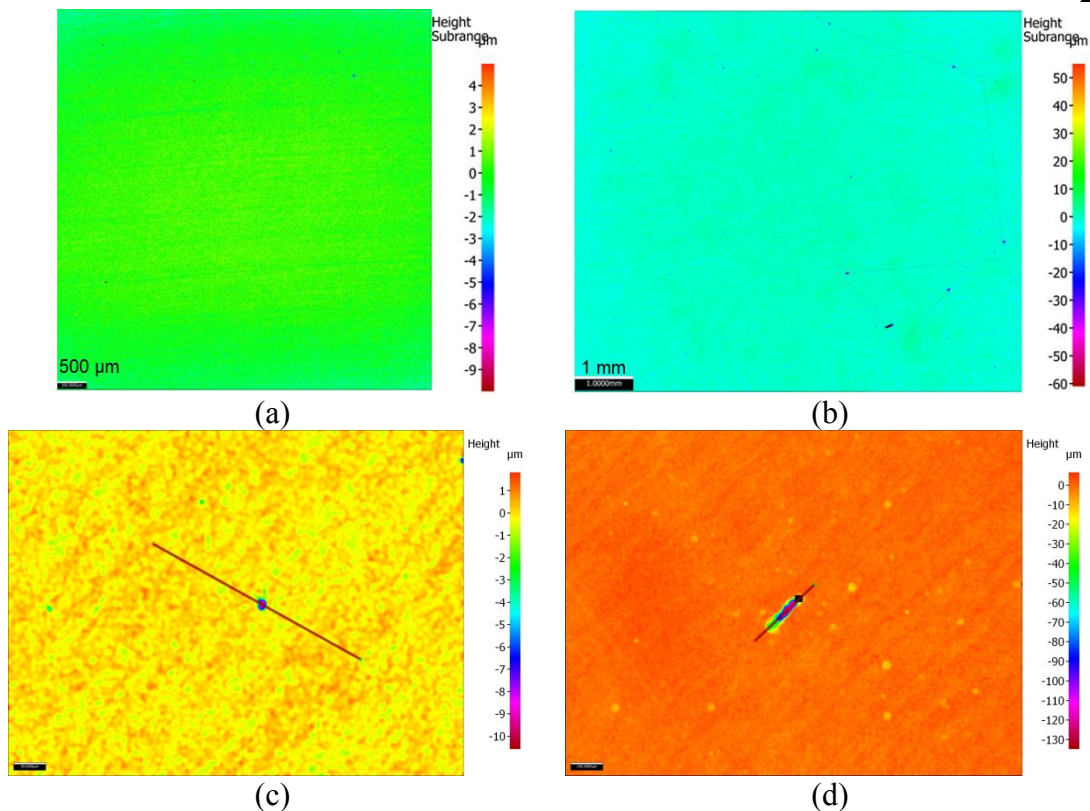


Figure 109. (a) Profilometry feature with sand deposit in Test #1; (b) Profilometry feature with pyrite deposit in Test #2; (c) Maximum pit depth with sand deposit in Test #1; (d) Maximum pit depth with pyrite deposit in Test #2.

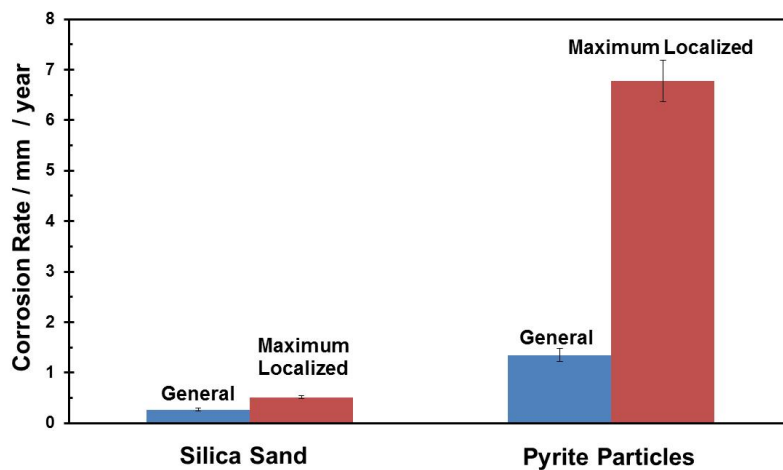


Figure 110. Comparison of corrosion rates between sand deposit and pyrite deposit.

### 7.3.1.3 Summary for Test Series #1

No localized corrosion was observed with the sand deposit. In contrast, serious localized corrosion was seen in the presence of pyrite. The pit penetration rate associated with the pyrite deposit was up to 7 mm/year.

On the other hand, the impact of depositing both sand and pyrite particles on general corrosion of the steel underneath was also observed. General corrosion was retarded after the deposition of sand, which was observed to be 0.3 mm/year. In addition, the Nyquist plots reveal that the corrosion process of the steel sample changed from charge transfer control to diffusion control after the sand deposition. However, in the presence of pyrite particles, general corrosion was accelerated after the deposition of pyrite. The general corrosion rate was 1.4 mm/year. The corrosion process was always dominated by charge transfer control after pyrite was deposited, indicating that the pyrite deposit layer was not primarily acting as a diffusion barrier.

### 7.3.2 *Test Series #2: Impact of Pyrite Particle Size on Corrosion*

#### 7.3.2.1 Comparison of Electrochemical Behavior

Figure 111 presents the OCP and corrosion rate in the presence of the larger pyrite particles in the initial five hours. Again, a large increase in both OCP and corrosion rate was observed after the deposition of the pyrite particles, which is considered to be due to an increase in cathodic reaction(s). H<sub>2</sub>S gas was sparged later and throughout the test, for a week. Figure 112 shows the OCP and corrosion rate throughout the test for a week. Corrosion rate was stable during the test. The weight loss result shown as a green diamond on the right side of Figure 112 confirmed LPR measurements.

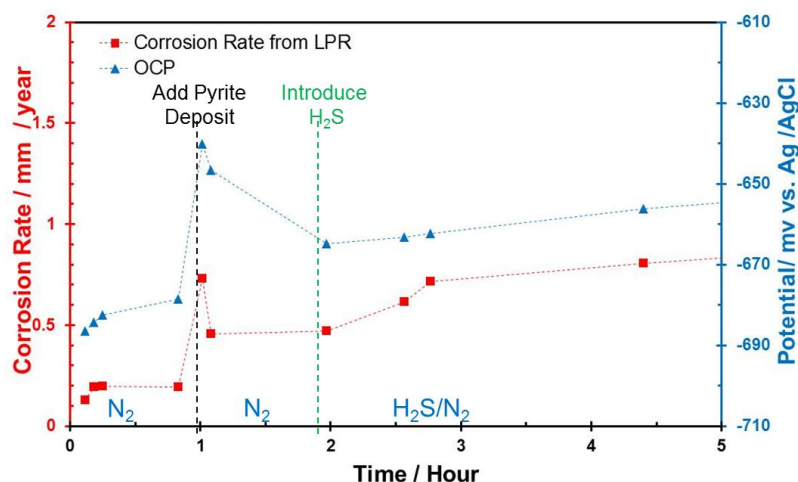


Figure 111. Corrosion rate and OCP using 1000 ~ 2000  $\mu\text{m}$  pyrite particle deposit in the initial five hours of Test #3.

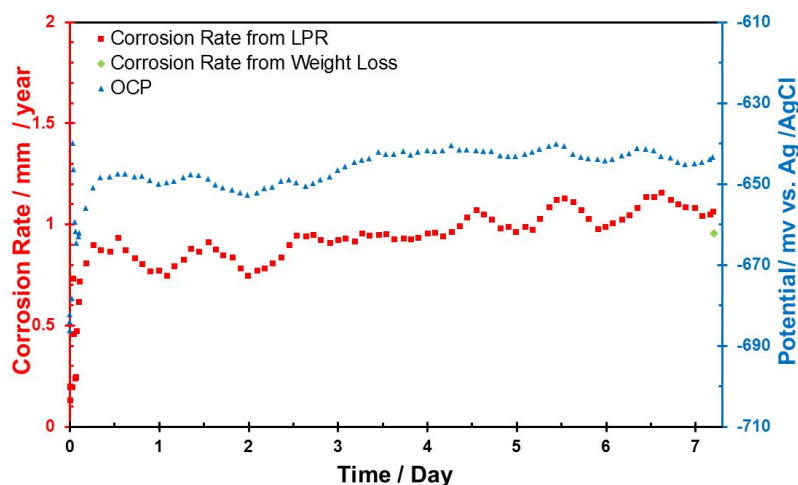


Figure 112. Corrosion rate and OCP during the test of a week using 1000 ~ 2000  $\mu\text{m}$  pyrite particle deposit in Test #3.

The comparison of OCP and corrosion rates between the two different pyrite particle sizes is shown in Figure 113 (a) and (b), respectively. Figure 113 (a) illustrates that OCP was approximately 20 ~ 30 mV lower using the larger particles. In addition, Figure 113 (b) shows that the general corrosion rate was much lower using the larger pyrite particles. In general, much less acceleration of both OCP and general corrosion rate was observed in the presence of larger pyrite particles.

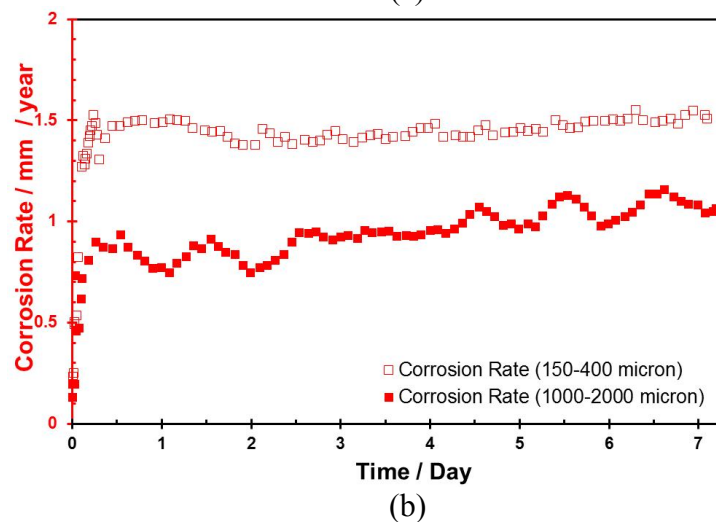
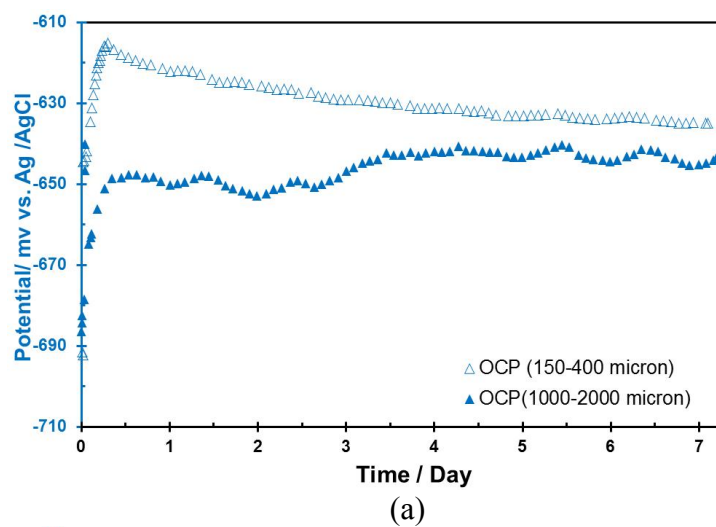


Figure 113. Comparison of (a) OCP and (b) corrosion rates between two different pyrite particle sizes.

Figure 114 shows the Nyquist plots for Test #3. Those Nyquist plots revealed that the corrosion process was always under charge transfer control before and after the deposition of the larger pyrite particles, indicating that this pyrite layer was not primarily acting as a mass transfer barrier. Moreover, Figure 115 shows the solution pH monitored during Test #3, which has the similar trend to Test #1 in the presence of the smaller pyrite particles.

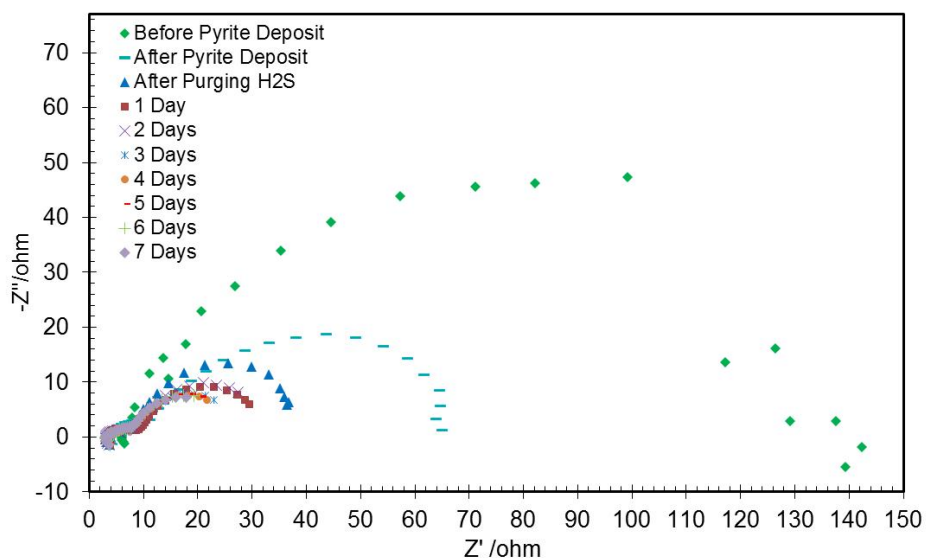


Figure 114. Nyquist plots with 1000 ~ 2000  $\mu\text{m}$  pyrite particle deposit in Test #3.

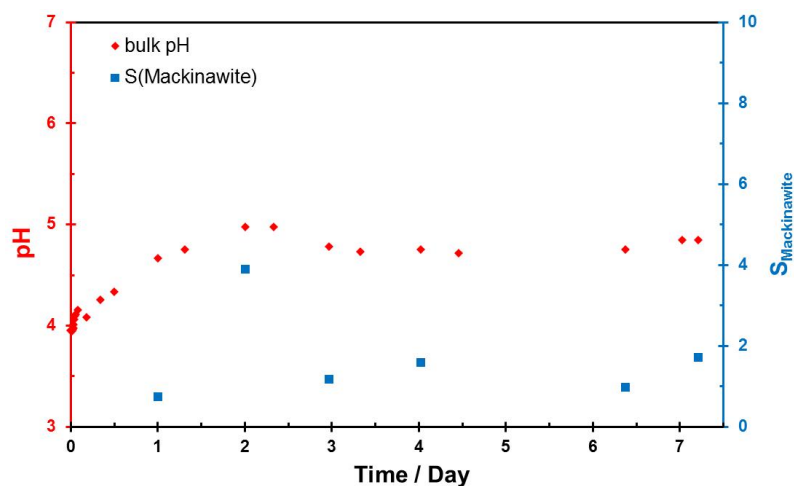


Figure 115. pH and  $S_{\text{mackinawite}}$  during Test #3 using 1000 ~ 2000  $\mu\text{m}$  pyrite particles.

### 7.3.2.2 Comparison of Surface Morphologies

Figure 116 presents surface morphology of the steel sample with the corrosion product layer in place using the larger pyrite particles. A uniform layer was seen in Figure 116 (a), (b), and (c), and EDS analysis on this layer indicated FeS in Figure 116 (d).

The corrosion product layer was removed to present the corroded sample underneath. Figure 117 shows some locations of localized corrosion observed on the sample, it is noteworthy that the pits are consistently elongated. Compared with the localized corrosion associated with the smaller pyrite particles shown in Figure 108, the pits associated with the larger pyrite particles appear to be larger. Moreover, Figure 118 (a) shows the profilometry feature of this sample after removing the corrosion product layer and Figure 118 (b) shows the maximum pitting depth found on the sample. Compared to the profilometry of the sample using the smaller pyrite particles in Figure 109 (b), the pits appeared to be shallower in the presence of the larger pyrite particles.

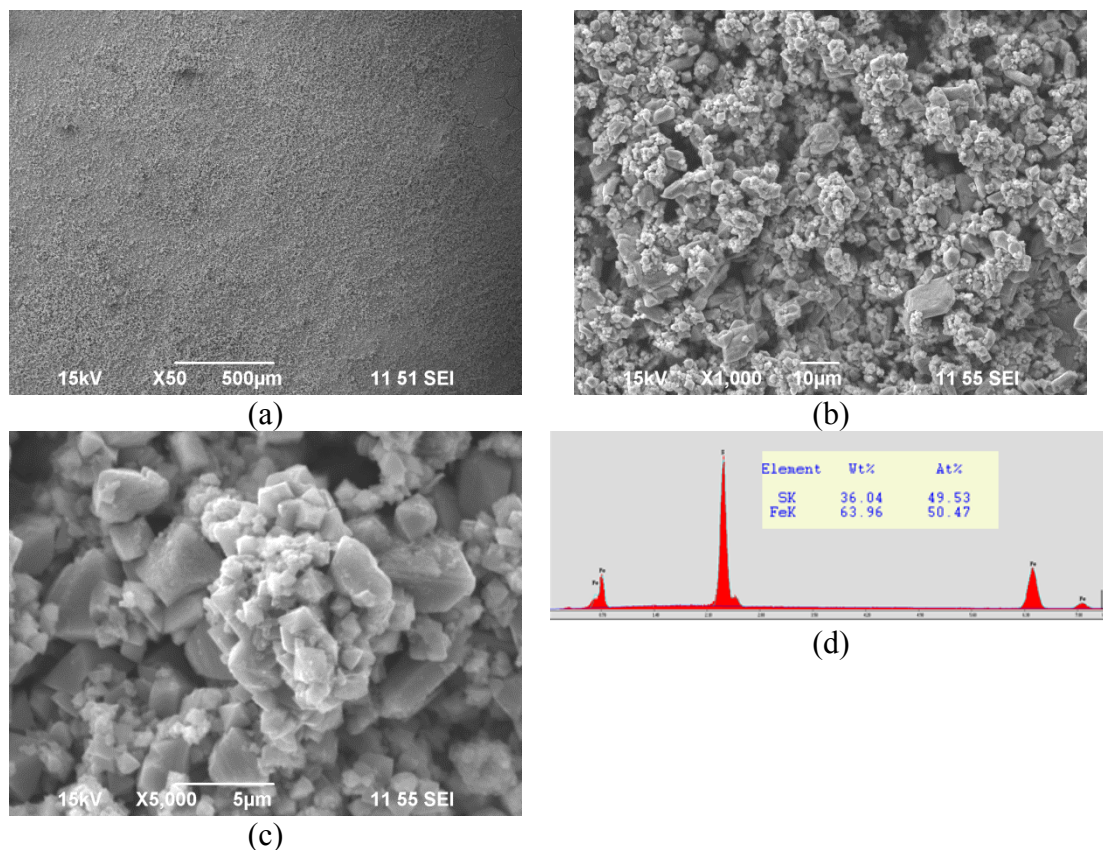


Figure 116. Surface morphologies of the sample with the corrosion product layer in place using 1000 ~ 2000  $\mu\text{m}$  pyrite particle deposit in Test #3: (a) 50x SEM image; (b) 1,000x SEM image; (c) 5,000x SEM image; (d) EDX analysis of crystals.

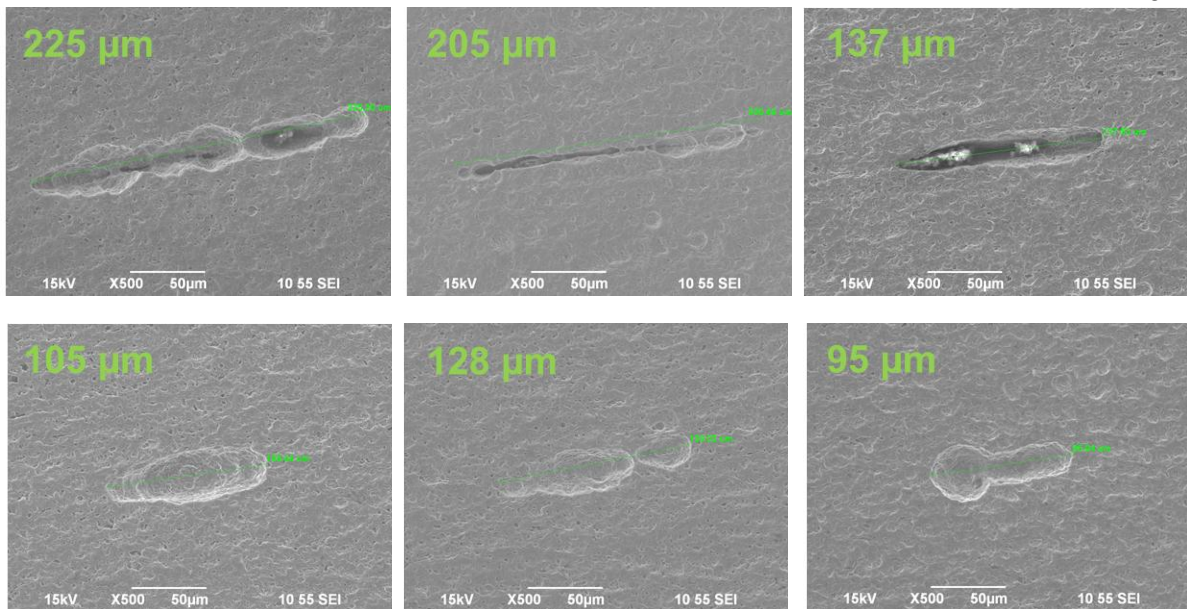


Figure 117. Locations of localized attack on the sample using 1000 ~ 2000  $\mu\text{m}$  pyrite particle deposit in Test #3.

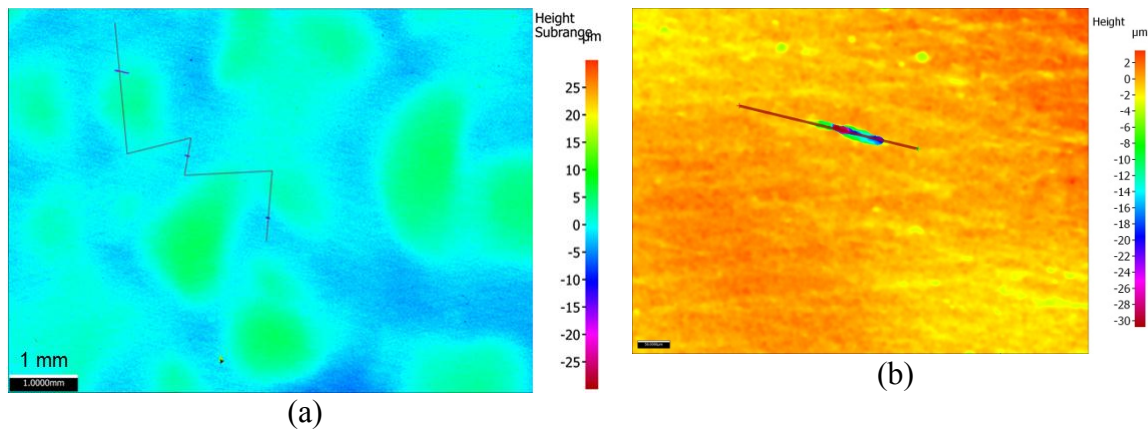


Figure 118. (a) Profilometry feature using 1000 ~ 2000  $\mu\text{m}$  pyrite particle deposit; (b) the maximum pit depth found on sample in Test #3.

Figure 119 shows the comparison of corrosion rates between Test #2 and Test #3 using different pyrite particle sizes. Both general corrosion and localized corrosion was enhanced using the smaller pyrite particle, which is understood to be due to the smaller particles conferring a larger cathodic reaction area.

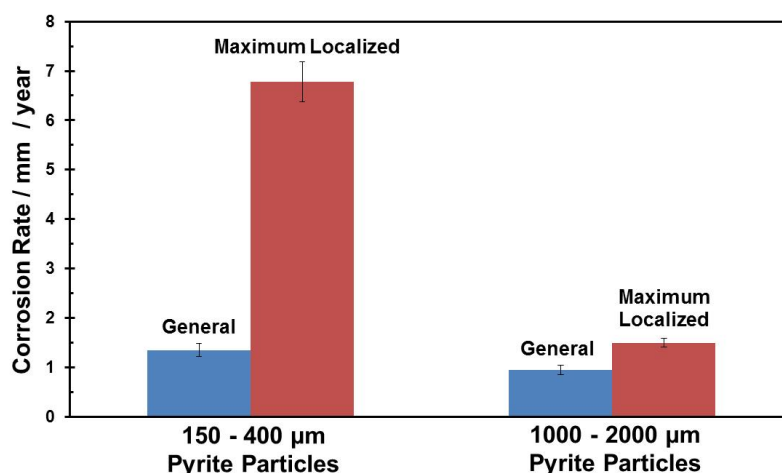


Figure 119. Comparison of corrosion rates between different pyrite particle sizes.

### 7.3.2.3 *Summary for Test Series #2*

Localized (pitting) corrosion was observed in the presence of both smaller (150 ~ 400 µm) and larger (1000 ~ 2000 µm) size pyrite particles. Moreover, the features of the pits are related to the pyrite particle size. Smaller and deeper pits were observed in the presence of smaller pyrite particles. This is due to a larger cathodic area of the small particles, compared to the same amount of larger particles. In addition, more significant acceleration of general corrosion was observed with smaller pyrite particles compared to larger pyrite particles. Again, this is also due to a larger amount of smaller particles conferring a larger cathodic area.

### 7.3.3 *Test Series #3: Investigating Potential Mechanisms for Localized Corrosion*

Serious localized corrosion was observed in the presence of pyrite particles in Test Series #1 and Test Series #2, suggesting that the formation of pyrite as a corrosion product in sour environments may initiate localized corrosion. Therefore, it is important to understand the mechanism of this type of localized corrosion caused by pyrite. Moreover, this understanding of localized corrosion can be incorporated into the

prediction of corrosion rate, particularly the prediction of localized corrosion in sour environments.

As mentioned above, two hypotheses were proposed for this type of localized corrosion: an electrochemical effect and a chemical effect. In the case of the electrochemical effect hypothesis, certain conditions are necessary for the localized corrosion driven by the galvanic coupling. These include the conductive nature of pyrite, a physical contact between pyrite and the steel underneath, and the presence of electrolyte. It is noteworthy that the physical contact between pyrite and steel is one of the preconditions for forming a galvanic coupling, and one which is easy to control. Therefore, a very thin insulating mesh was introduced between the pyrite particles and the steel sample to avoid physical contact, thereby, eliminating the galvanic coupling between the pyrite deposit layer and the steel sample.

#### 7.3.3.1 Test #4: 150 ~ 400 $\mu\text{m}$ Pyrite Particles with Mesh

Figure 120 shows an image of a few pyrite particles with dimensions 150 ~ 400  $\mu\text{m}$  lying on the insulating mesh. It guarantees that physical contact between pyrite particles and the steel sample can be avoided by introducing this insulating mesh; hence the galvanic coupling can be eliminated.

Figure 121 shows the change of OCP and corrosion rate in the presence of the mesh over the initial six hours, including the steps of the deposition of smaller pyrite particles and the sparging of  $\text{H}_2\text{S}$  gas to the solution. A decrease in both OCP and corrosion rate after the deposition of pyrite particles was observed. In contrast, a large increase in both OCP and corrosion rate was seen without using the insulating mesh as shown in Figure 99. Hence, it is concluded that the increase in OCP and corrosion rate

after the deposition of pyrite in the previous test without using mesh was due to the galvanic effect.

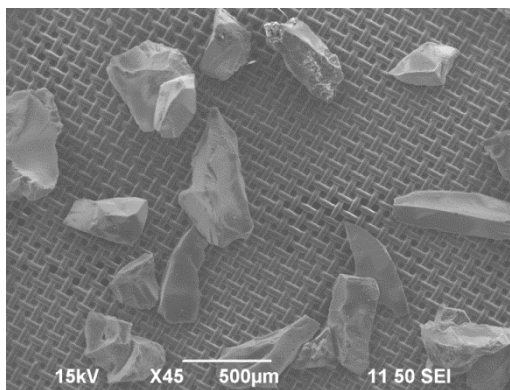


Figure 120. SEM image of 150 ~ 400  $\mu\text{m}$  pyrite particles deposited on the mesh.

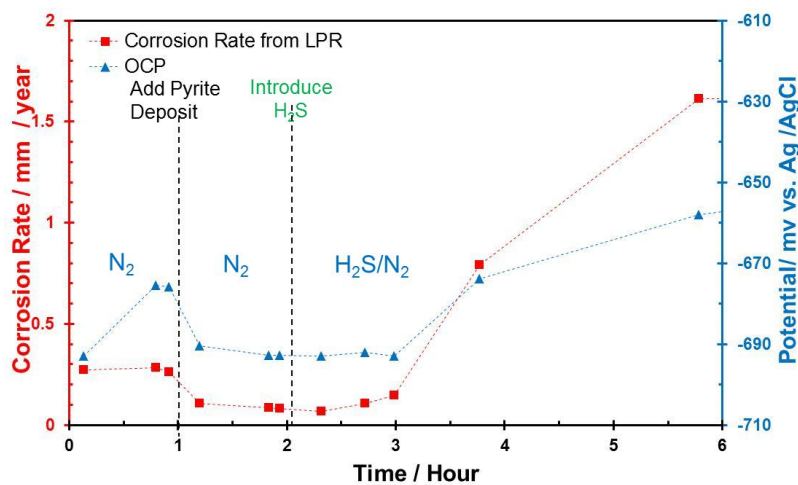


Figure 121. Corrosion rate and OCP with 150 ~ 400  $\mu\text{m}$  pyrite particles deposited on the mesh in the initial hours of Test #4.

### 7.3.3.2 Test #5: 1000 ~ 2000 $\mu\text{m}$ Pyrite Particles with Mesh

Test #5 was carried out in the presence of the mesh and larger pyrite particles following the same procedure. Again, a decrease in corrosion rate was observed after the deposition of pyrite particles in Figure 122. Considering the dramatic increase in both corrosion rate and OCP without using the mesh in Figure 111, this confirms that the

increase in both OCP and corrosion rate after the deposition of pyrite particles was due to the electrochemical effect. This test was conducted for seven days. The OCP and corrosion rate throughout the test of a week are shown in Figure 123.

Figure 124 presents surface morphologies of the steel sample with the corrosion product layer in place. A uniform corrosion product layer was seen as shown in (a), (b), and (c). EDX suggests that the crystals are FeS and the uniform layer underneath is a mixture of FeS and Fe<sub>3</sub>C.

A flat surface was observed in Figure 125 after the removal of the corrosion product layers. Profilometry of the steel sample owing to uniform corrosion is shown in Figure 126, and accordingly, no localized corrosion was observed for this test condition.

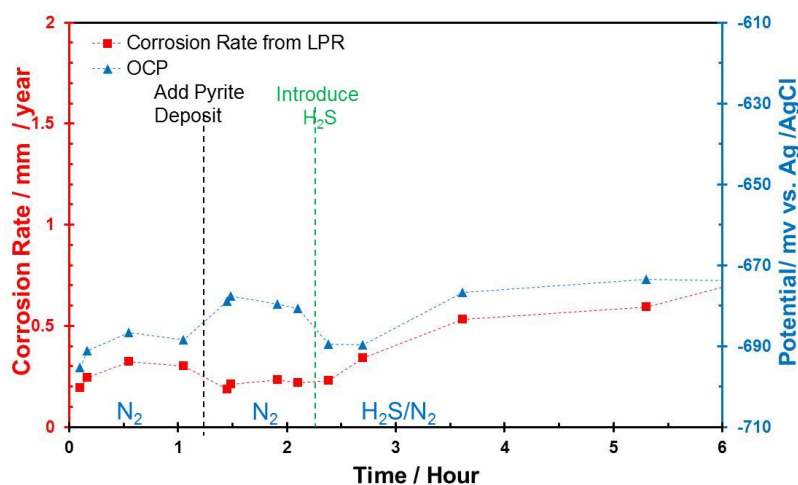


Figure 122. Corrosion rate and OCP using 1000 ~ 2000  $\mu\text{m}$  pyrite particles deposited on the mesh in the initial hours of Test #5.

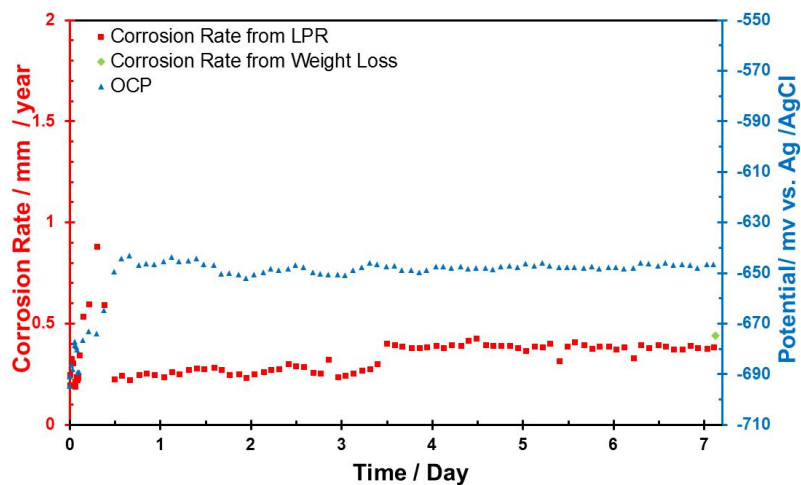


Figure 123. Corrosion rate and OCP using 1000 ~ 2000  $\mu\text{m}$  pyrite particles deposited on the mesh for a week in Test #5.

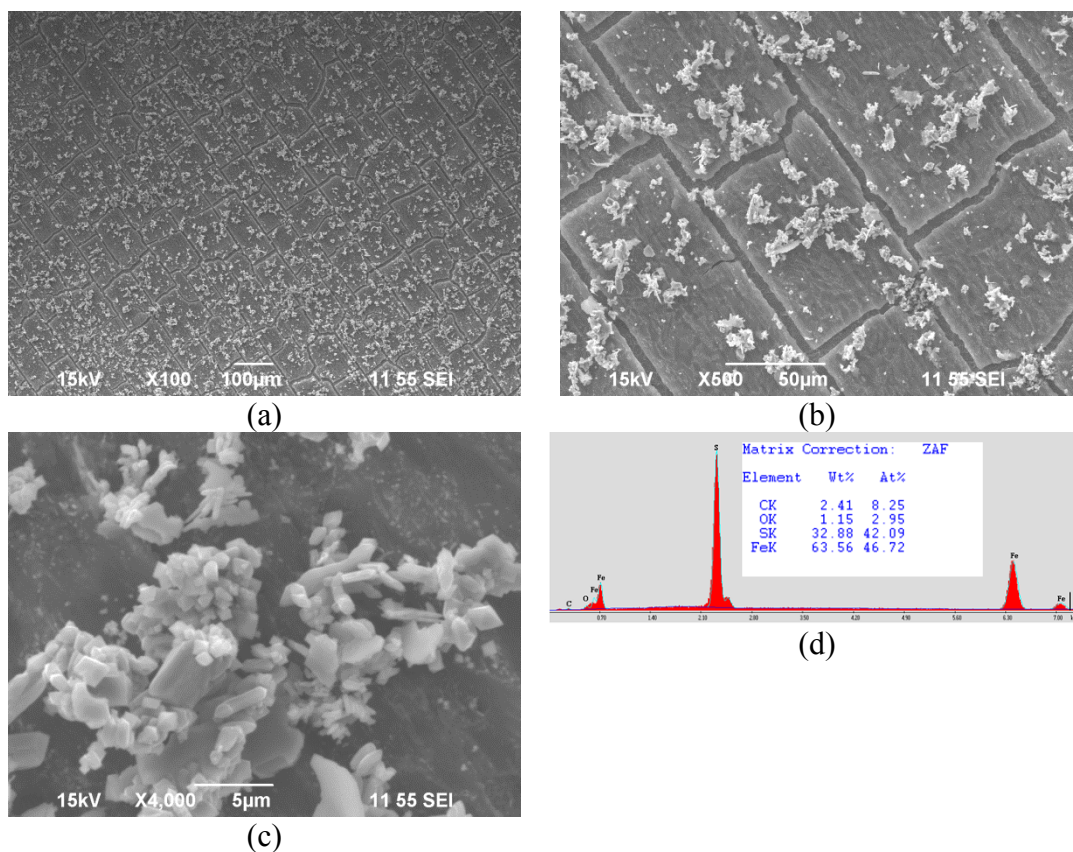


Figure 124. Surface morphologies of the sample with the corrosion product layer in place using 1000 ~ 2000  $\mu\text{m}$  pyrite particles deposited on the mesh in Test #5: (a) 100x SEM image; (b) 500x SEM image; (c) 4,000x SEM image; (d) EDX analysis of crystals.

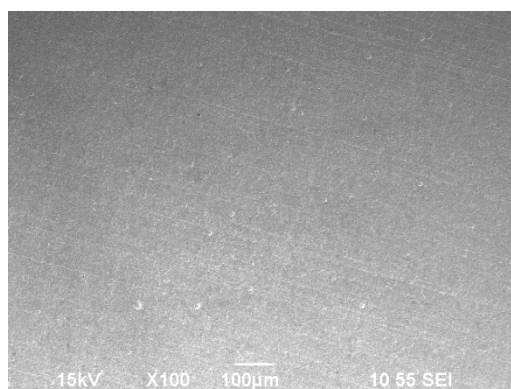


Figure 125. Surface morphologies of the sample after removing corrosion product layer using 1000 ~ 2000 µm pyrite particles deposited on the mesh in Test #5.

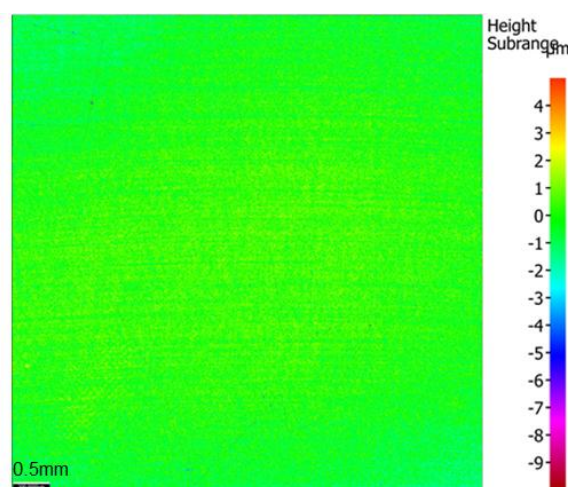


Figure 126. Profilometry feature of the specimen after removing corrosion product layer using 1000 ~ 2000 µm pyrite particles deposited on the mesh in Test #5.

### 7.3.3.3 *Summary for Test Series #3*

When the physical contact between pyrite particles and the steel underneath was eliminated using an insulating mesh, the corrosion rate and OCP did not increase after the deposition of pyrite particles and no localized corrosion was observed. Thus, the electrochemical hypothesis was proven to be the dominant mechanism for this type of localized corrosion.

### 7.3.4 Test Series #4: Pyrite/Silica Sand UDC Test in an Aqueous CO<sub>2</sub> Environment

Since CO<sub>2</sub> gas is ubiquitous in oil and gas production, it is of interest to know if localized corrosion due to pyrite deposits can occur in an aqueous CO<sub>2</sub> dominated environment. The same practice in an aqueous CO<sub>2</sub> environment was conducted to address this question. Test #6 was conducted with a silica sand deposit layer as a blank test. Test #7 was performed in the presence of a pyrite particles deposit layer.

#### 7.3.4.1 Comparison of Electrochemical Behavior

Corrosion rate was retarded after the deposition of the silica sand layer, as shown in Figure 127, and it was then stable through the remainder of the test, as shown in Figure 128. In contrast, a decrease in corrosion rate and an increase in OCP were observed after the deposition of pyrite particles in Figure 129. OCP and corrosion rate throughout Test #7 is shown in Figure 130.

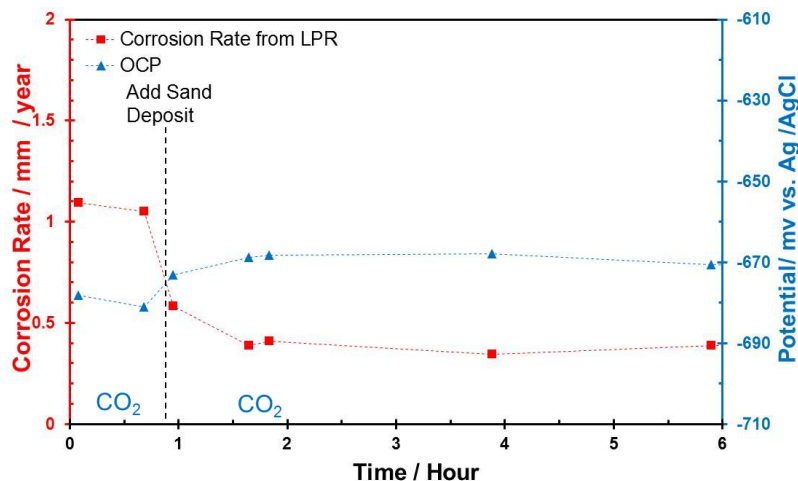


Figure 127. Corrosion rate and OCP using 150 ~ 400  $\mu\text{m}$  silica sand deposit in a solution purged with CO<sub>2</sub> in the initial hours of Test #6.

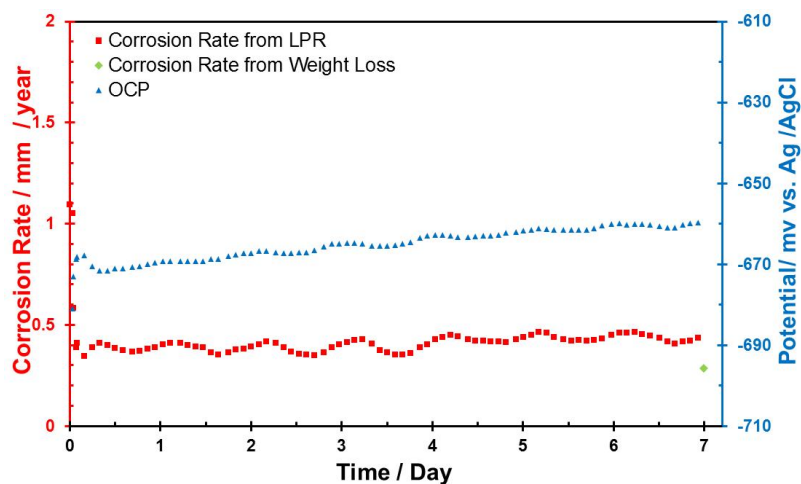


Figure 128. Corrosion rate and OCP using 150 ~ 400  $\mu\text{m}$  silica sand deposit in a solution purged with  $\text{CO}_2$  for a week in Test #6.

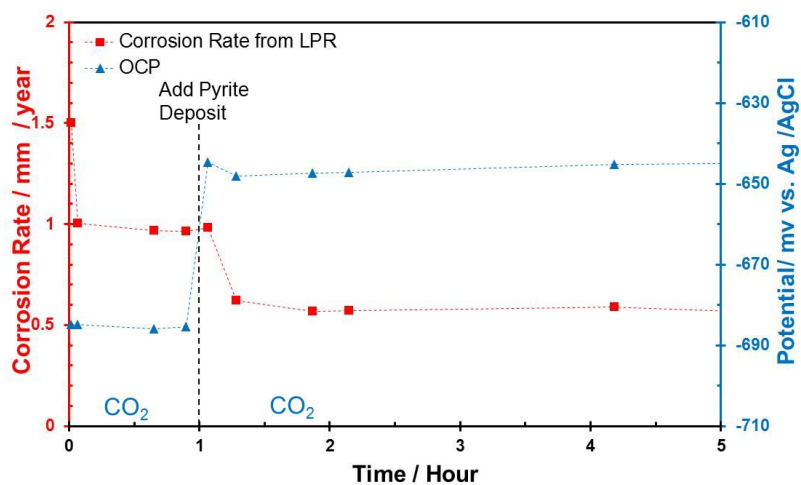


Figure 129. Corrosion rate and OCP using 150 ~ 400  $\mu\text{m}$  pyrite particle deposit in a solution purged with  $\text{CO}_2$  in the initial hours of Test #7.

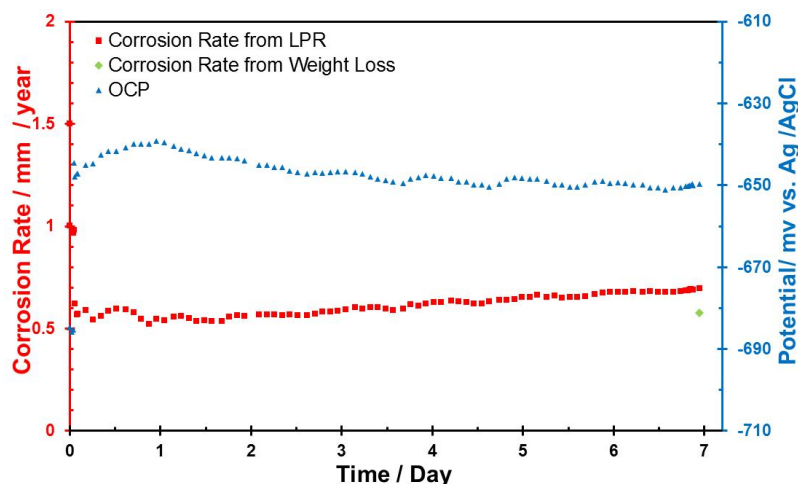


Figure 130. Corrosion rate and OCP using 150 ~ 400  $\mu\text{m}$  pyrite particle deposit in a solution purged with  $\text{CO}_2$  for a week in Test #7.

#### 7.3.4.2 Comparison of Surface Morphologies

Figure 131 shows surface morphologies of the steel sample with the corrosion product layer in place using the silica sand deposit. Polishing marks were observed at locations silica sand occupied. Figure 132 shows surface morphologies with corrosion product layer in place associated with pyrite deposits. Clearly, serious damage to the corrosion product layer was observed in the presence of pyrite particles.

The corrosion product layer on the sample was removed to reveal the corroded steel surface. Figure 133 shows surface morphologies of the sample in Test # 6 in the presence of silica sand. The original steel surface with polishing marks was still seen at a few locations where silica sand occupied in Figure 133. It reveals that the silica sand deposited on the steel surface protected the steel underneath from the corrosive environment due to a blockage effect. Figure 134 shows surface morphologies of the sample in Test #7 with pyrite particles. Severe localized attack was seen on this sample in Test #7. The features of these pits are shown in Figure 135. The profilometry of this steel

sample is shown in Figure 136 (a) and the pit with a maximum depth of 70  $\mu\text{m}$  is shown in Figure 136 (b).

Figure 137 compares corrosion rates between these two tests in an aqueous  $\text{CO}_2$  environment. No localized corrosion was seen in the presence of silica sand. However, localized corrosion with a penetration rate of 4 mm/year was observed for Test # 7 in the presence of pyrite particles in a  $\text{CO}_2$  solution.

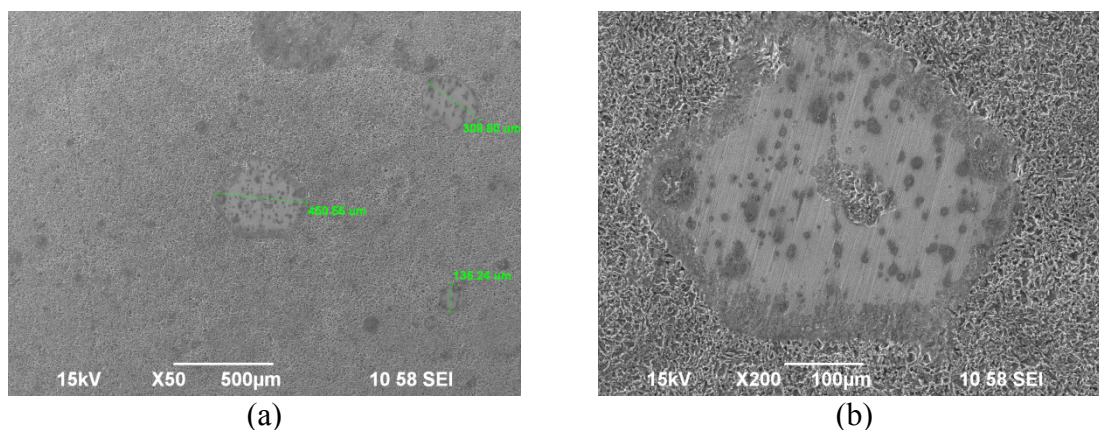


Figure 131. Surface morphologies of the sample with the corrosion product layer in place using 150 ~ 400  $\mu\text{m}$  silica sand deposit in an aqueous  $\text{CO}_2$  solution in Test #6: (a) 50x SEM image; (b) 200x SEM image.

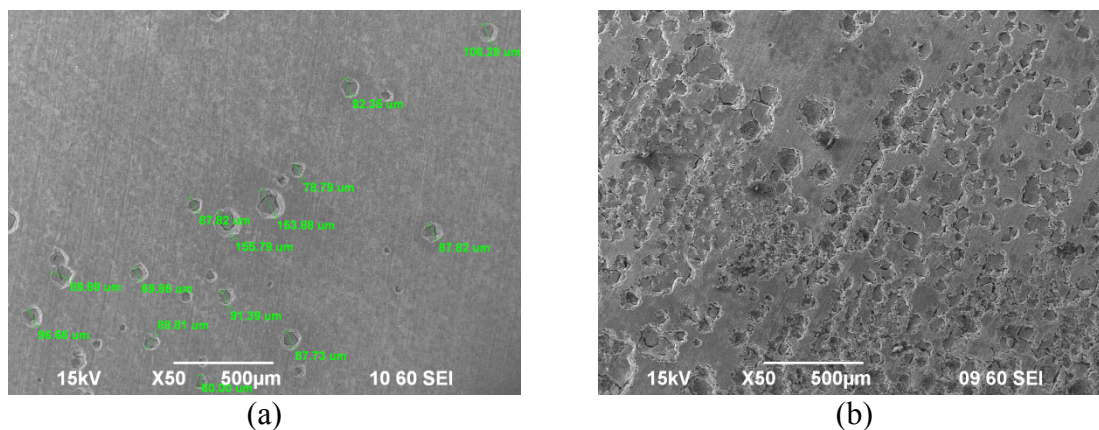


Figure 132. Surface morphologies of the sample with the corrosion product layer in place using 150 ~ 400  $\mu\text{m}$  pyrite particle deposit in an aqueous  $\text{CO}_2$  solution in Test #7: (a) 50x SEM image; (b) 50x SEM image.

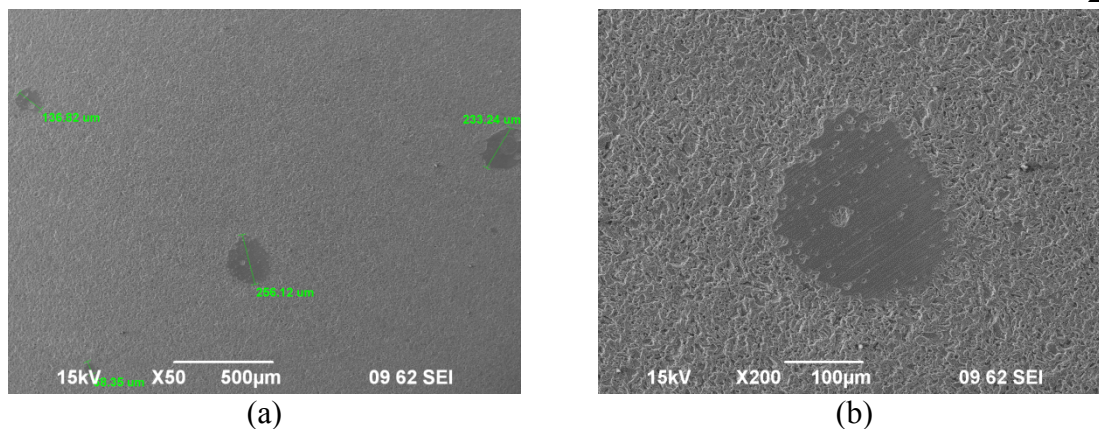


Figure 133. Surface morphologies of the sample after removing the corrosion product layer using 150 ~ 400  $\mu\text{m}$  silica sand deposit in an aqueous  $\text{CO}_2$  solution in Test #7: (a) 50x SEM image; (b) 200x SEM image.

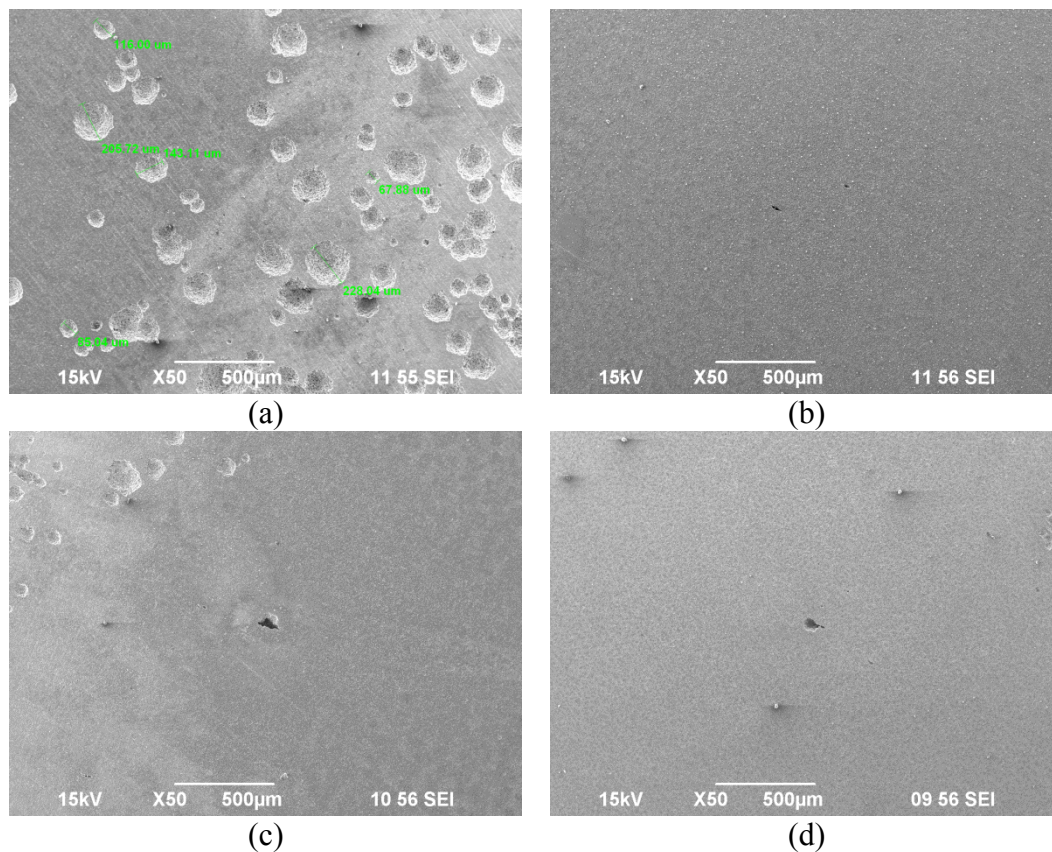


Figure 134. Surface morphologies of the sample after removing the corrosion product layer using 150 ~ 400  $\mu\text{m}$  pyrite particle deposit in an aqueous  $\text{CO}_2$  solution in Test #7.

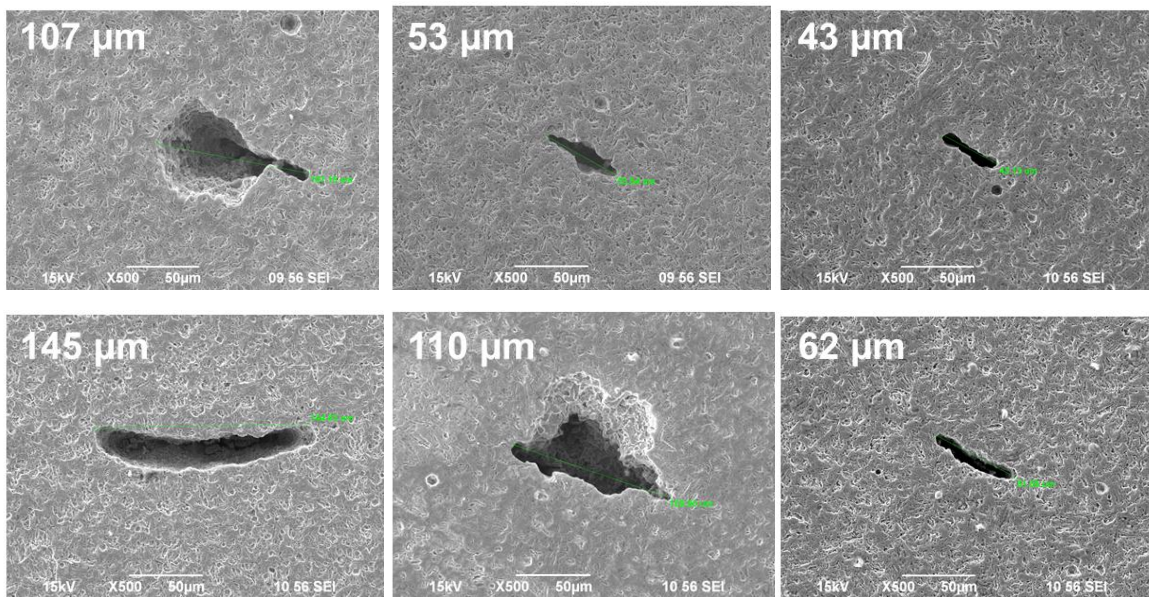


Figure 135. Locations of localized attack on the sample after removing the corrosion product layer using 150 ~ 400  $\mu\text{m}$  pyrite particle deposit in an aqueous  $\text{CO}_2$  solution in Test #7.

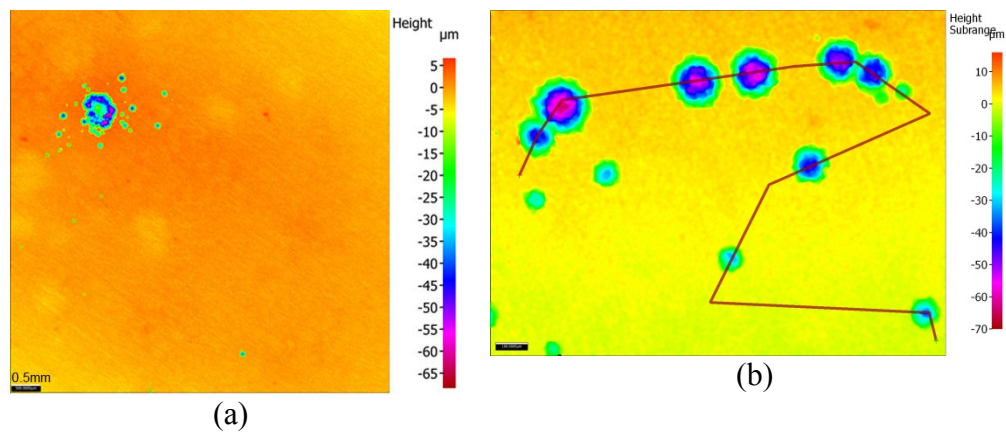


Figure 136. (a) Profilometry feature using 150 ~ 400  $\mu\text{m}$  pyrite particle deposit in an aqueous  $\text{CO}_2$  solution; (b) The maximum pit depth found on the sample in Test #7.

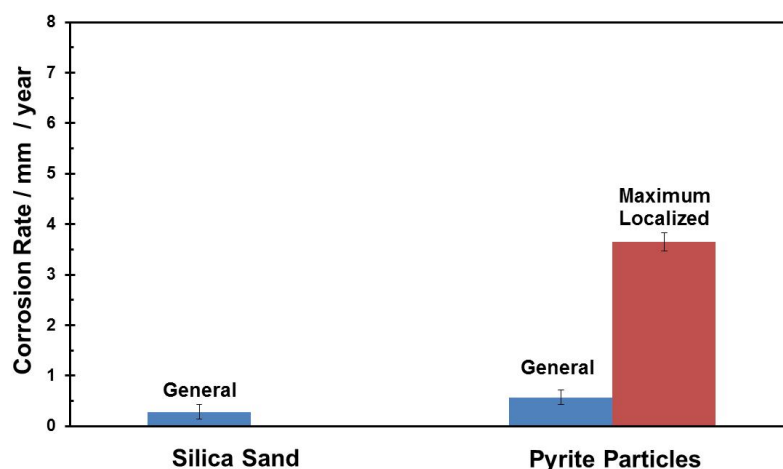


Figure 137. Comparison of corrosion rates between silica sand deposit and pyrite particle deposit in an aqueous CO<sub>2</sub> solution.

#### 7.3.4.3 Summary for Test Series# 4

Severe localized corrosion was also observed in the presence of a pyrite particle deposit layer in an H<sub>2</sub>S free environment, an aqueous CO<sub>2</sub> solution. No localized corrosion was seen in the presence of a sand deposit layer in an aqueous CO<sub>2</sub> solution.

### 7.4 Summary

- Severe localized corrosion was observed and replicated in the presence of pyrite deposit layers in either aqueous H<sub>2</sub>S or CO<sub>2</sub> dominated environments.
- Features of this type of localized corrosion are related to pyrite particle size. The smaller the particle size, the more severe the localized corrosion.
- The galvanic coupling between pyrite particles and steel is the dominant mechanism for localized corrosion.
- General corrosion was accelerated after the deposition of the pyrite in an H<sub>2</sub>S solution due to the overall increase in cathodic area and the magnitude of cathodic reactions.

## CHAPTER 8. A DESCRIPTIVE MODEL FOR LOCALIZED CORROSION IN SOUR ENVIRONMENTS

### 8.1 Introduction

Severe localized corrosion was observed and replicated in the presence of both spontaneously formed pyrite and/or greigite (Chapter 6) and deposited pyrite (Chapter 7), indicating that the formation of pyrite in sour corrosion of mild steel has potential to initiate pitting corrosion. As a thermodynamically stable corrosion product, pyrite has frequently been detected in sour fields in the oil and gas industry [150]. In order to predict and mitigate this type of localized corrosion caused by pyrite, a descriptive model for localized corrosion in a sour environment was built to answer the questions of when, where, and how this type of localized corrosion occurs. In addition, the application of this model to the field is also described in this chapter.

### 8.2 Understanding of Physiochemical Processes of Localized Corrosion Related to Iron Sulfide Polymorphism

A descriptive model for this type of localized corrosion could be easily developed if its physiochemical character is established. The understanding of physiochemical processes of this type of localized corrosion is based on experimental observations and existing knowledge. A few questions must be answered as the foundation of the descriptive model.

#### 8.2.1 *Where are the Pit Locations in Relation to Pyrite?*

The experimental results revealed that pitting corrosion was initiated and propagated by a galvanic coupling between pyrite and steel. In order to outline the

mechanism of this localized corrosion driven by the galvanic coupling, it is critical to know the pitting location in relation to pyrite.

Figure 138 proposes three locations of pit initiation in relation to a pyrite particle, which could be under the pyrite particle, adjacent to the pyrite particle, or far away from the pyrite particle. Experimental results were revisited to verify the location of the pitting corrosion observed in experiments.

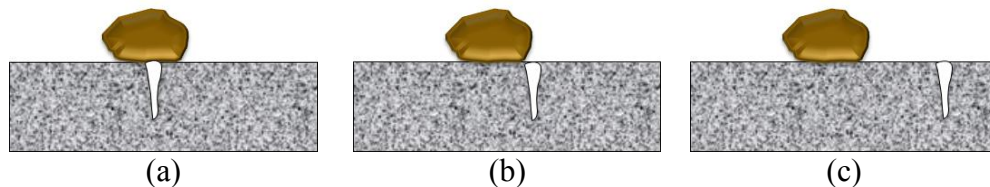


Figure 138. The pit locations in relation to pyrite: (a) pit is underneath the pyrite particle; (b) pit is adjacent to pyrite particle; (c) pit is far away from the pyrite particle.

#### 8.2.1.1 Case 1: 5 mm x 5 mm Pyrite Particles

Experiments [151] carried out by depositing several 5 mm x 5 mm pyrite particles on a steel sample surface were revisited. One was completed at 25 °C and another one was performed at 80 °C in an aqueous CO<sub>2</sub> saturated environment. Figure 139 (a-1) shows a SEM image of the pyrite particles sitting on the sample surface. Figure 139 (a-2) shows the surface profilometry of the sample after removing the corrosion product layer. The green areas in Figure 139 (a-2) are elevated and correspond to the locations of the pyrite particles shown in Figure 139 (a-1), which manifests that the steel immediately underneath the pyrite particles was protected due to a diffusion/surface blockage effect. A similar effect is observed again in the test conducted at 80 °C in Figure 139 (b).

Moreover, a pit (marked by a red oval) was found to be adjacent to the pyrite particle occupied area in Figure 139 (b).

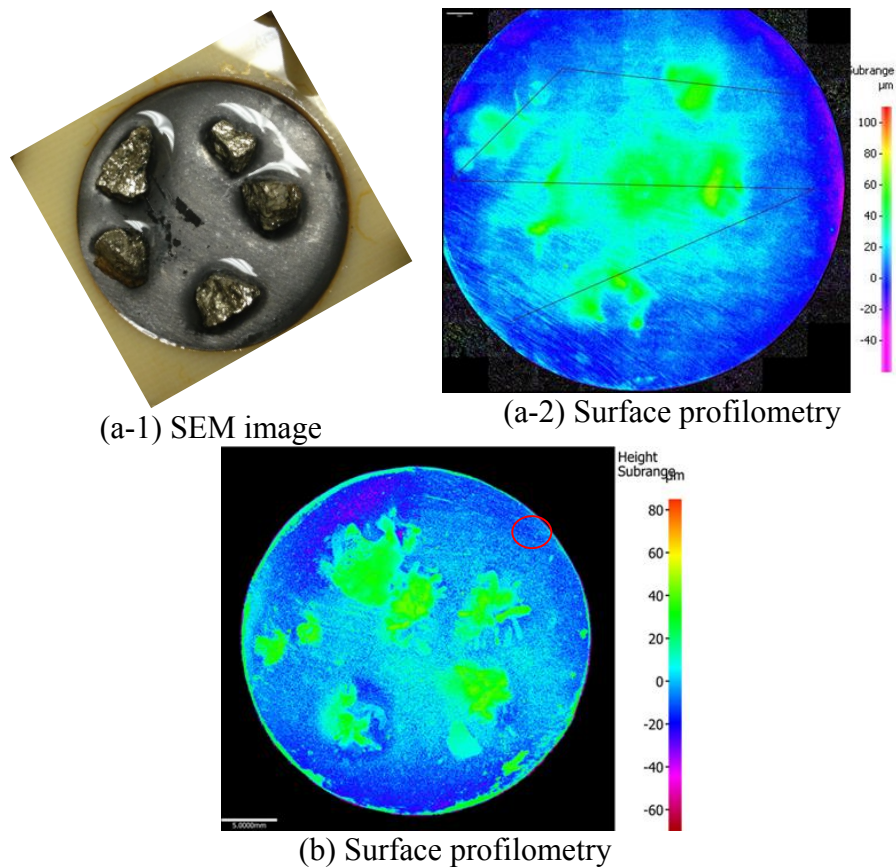


Figure 139. (a-1) A SEM image of 5mm x 5mm pyrite particles deposited on steel surface at  $T = 25\text{ }^{\circ}\text{C}$ ,  $p\text{CO}_2 = 0.97\text{ bar}$ , and initial pH 6.0; (a-2) Surface profilometry of the sample shown in (a-1); (b) Surface profilometry of the sample in the presence of 5mm x 5mm pyrite particles at  $T = 80\text{ }^{\circ}\text{C}$ ,  $p\text{CO}_2 = 0.54\text{ bar}$ , and initial pH 6.0.

#### 8.2.1.2 Case 2: 1000 ~ 2000 $\mu\text{m}$ Pyrite Particles

Another experiment using smaller pyrite particles (1000 ~ 2000  $\mu\text{m}$ ) was taken for comparison. Figure 140 shows the surface profilometry after removing the corrosion product layer. Again, the green portion of the image is where pyrite particles occupied the

metal surface area which was protected. The locations of pits are marked by red ovals in in Figure 140. Most of the pits are observed at locations adjacent to pyrite particles.

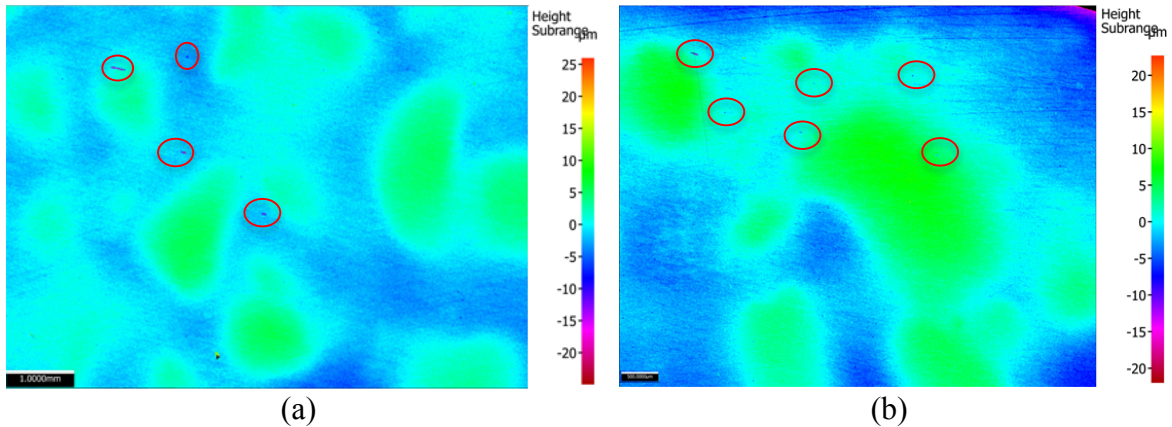


Figure 140. Surface profilometry of different locations of specimen in the presence of 1000 ~ 2000  $\mu\text{m}$  pyrite particles at  $T = 25\text{ }^{\circ}\text{C}$ ,  $p\text{H}_2\text{S} = 0.1\text{ bar}$ , and initial pH 4.0.

### 8.2.1.3 Case 3: 150 ~ 400 $\mu\text{m}$ Pyrite Particles

Similarly, one more case was studied. This test was completed using 150 ~ 400  $\mu\text{m}$  pyrite particles as the deposit. After the experiment, the corrosion product layer was removed to measure the surface topography as shown in Figure 141. Likewise, most of the pits are observed in areas adjacent to pyrite particles.

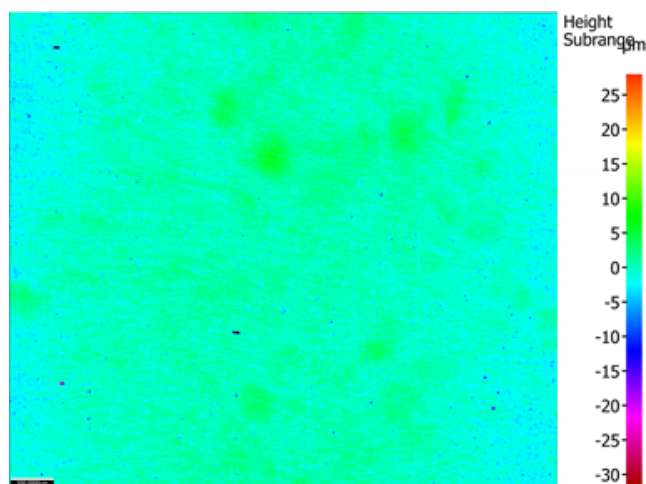


Figure 141. Surface profilometry of specimen in the presence of 150 ~ 400  $\mu\text{m}$  pyrite particles at  $T = 25\text{ }^{\circ}\text{C}$ ,  $p\text{H}_2\text{S} = 0.1\text{ bar}$ , and initial pH 4.0.

In general, according to those three tests conducted at various conditions, the locations of pitting corrosion were observed to be adjacent to pyrite particles.

#### 8.2.2 *When and How Does Localized Corrosion Occur?*

According to experimental observations (Chapter 8), the localized corrosion was due to a galvanic coupling between a pyrite particle (cathode) and the steel adjacent to the pyrite (anode). Therefore, the four precoditions for galvanic localized corrosion must be met. As long as these four elements are present, localized corrosion can be initiated on the steel surface, no the matter whether it is in a  $\text{H}_2\text{S}$  or  $\text{CO}_2$  dominated environment. The four conditions for localized corrosion driven by the galvanic coupling are: dissimilar materials (large potential difference), electrical contact between pyrite and steel, electrolyte (solution conductivity), and large cathodic/anodic area ratio. These conditions were discussed below for a comprehensive understanding of this type of localized corrosion.

### 8.2.2.1 *Dissimilar Materials*

A galvanic coupling refers to an electrical connection between two different materials [152]. One of the two materials is relatively noble and the other is relatively active. As a result of this galvanic coupling, corrosion of the noble material will be retarded and corrosion of the active material will be accelerated. This principle is applied to sacrificial cathodic protection, which is commonly used in oil and gas fields to reduce the corrosion rate of mild steel pipelines by consuming more active metals, such as zinc.

Figure 142 (a) shows the Pourbaix diagram for an Fe-H<sub>2</sub>S-H<sub>2</sub>O system generated at experimental conditions considering iron, mackinawite, greigite, pyrrhotite, and pyrite. Only pyrite, pyrrhotite, and iron are observed in the Pourbaix diagram, which indicates that these phases are thermodynamically stable. The portion of pyrite is above the iron area shown in Figure 142 (a), indicating pyrite is more noble than iron. The potential differences between pyrite and iron are shown in Figure 142 (a), which is at least 400 mV at pH 3 and 250 mV at pH 6.

However, in the experiments, pyrite particles were deposited directly on the steel surface. Hence, other phases of iron sulfides might not be involved in the experiments. Accordingly, Figure 142 (b) shows a Pourbaix diagram that considers only pyrite and iron. The other phases of iron sulfides were excluded from the Pourbaix diagram. Again, pyrite was predicted to be stable in the portion above the iron area in Figure 142 (b), which suggests that pyrite is a material more noble than iron. Likewise, the approximate 400 mV difference in potential between pyrite and iron is seen at pH 3.

It is understood that the higher the potential difference, the more severe the anticipated localized corrosion. One can make inferences from the Pourbaix diagrams

that higher potential difference between those two materials can be attained at lower pH values.

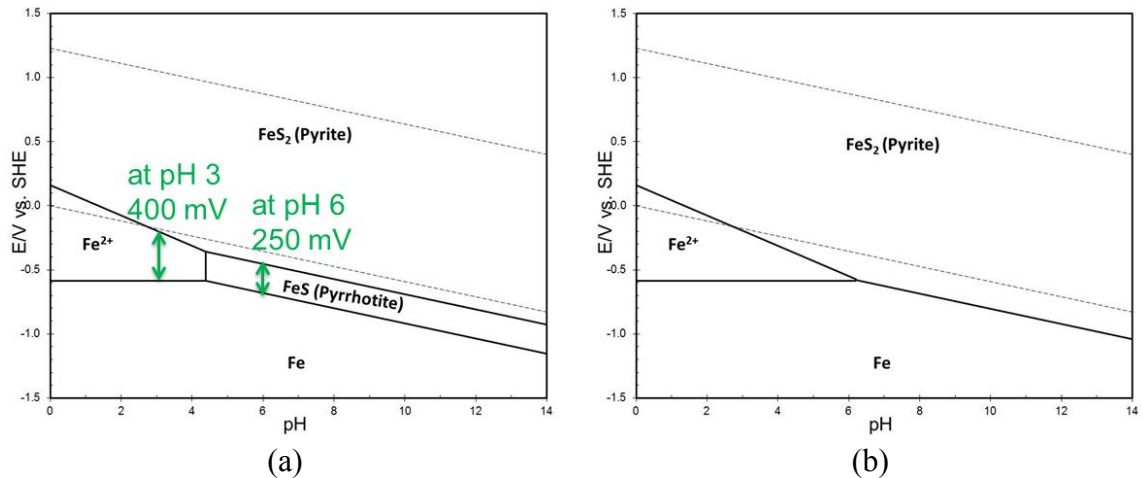


Figure 142. Pourbaix diagram for Fe-H<sub>2</sub>S-H<sub>2</sub>O system (T = 25 °C, p<sub>H<sub>2</sub>S</sub> = 0.1 bar, [Fe<sup>2+</sup>] = 10 ppm, [Fe<sup>3+</sup>] = 10<sup>-6</sup> M) with (a) Fe + Mackinawite + greigite + pyrrhotite + pyrite; (b) Fe + pyrite.

### 8.2.2.2 *Electrical Contact between Pyrite and Steel*

Another important and necessary condition is the electrical conductivity of both materials to make an electrical coupling. It is well-known that steel is electrically conductive. Since pyrite is thermodynamically stable, the conductivity of pyrite has been measured by various researchers [144]–[147] as shown in Figure 88. The left side shows for conductors, while the right side represents insulators. The experimental data for the resistivity of pyrite from various sources strongly suggests that pyrite is a semiconductor with relatively good conductivity based on experimental data.

### 8.2.2.3 *Electrolyte*

When galvanic corrosion occurs, electron flow exists between two sites (from anode to cathode), creating corrosion current in the opposite direction of the electron flow

[152]. In order to avoid accumulation of charge (electrons), an equal ionic current is needed to balance the corrosion current. In reality, the presence of supporting electrolyte (e.g. sodium chloride) is a precondition for an ionic current in a galvanic corrosion system.

Figure 143 [153], [154] shows that solution conductivity increases with the increase in sodium chloride (NaCl) concentration in solution. As localized corrosion was observed in the presence of pyrite in experiments using 1 wt. % NaCl, it is hypothesized that a higher salt concentration may accelerate the localized corrosion. Further study on this matter is needed to establish if this is the case.

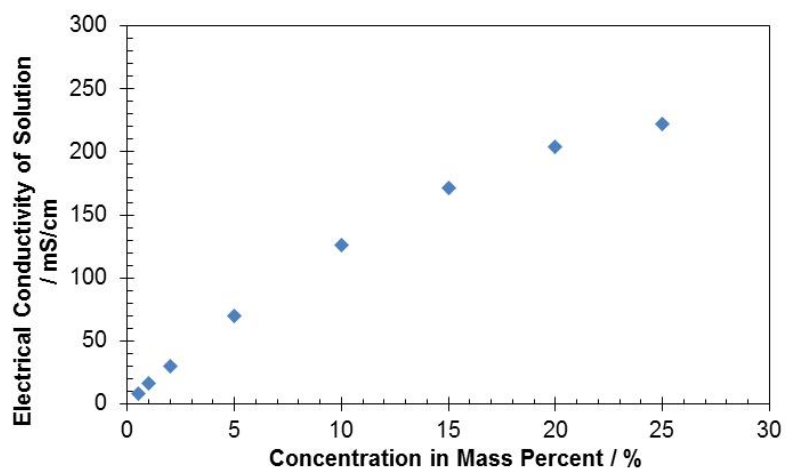


Figure 143. The relationship between solution conductivity and sodium chloride concentration (data reproduced from literature [153], [154])

#### 8.2.2.4 Large Ratio of Cathodic / Anodic Area

Also, the severity of the pitting corrosion is related to pyrite particle size. More severe pitting corrosion was observed using smaller pyrite particles. This is understood to be due to smaller pyrite particles have more surface area for cathodic reactions.

Therefore, a larger cathode /anode (pyrite/steel) area ratio influences galvanic current, and accelerates localized corrosion.

In practical exercises, corrosion current is always calculated by using the surface area of an electrode exposed to electrolyte. For example, steel acts as an anode and pyrite behaves as a cathode in the galvanic coupling between those two materials. One can expect higher anodic corrosion current density, which is a higher corrosion rate of steel, if the surface area of the steel electrode is relatively smaller than the surface area of cathodic pyrite. Therefore, the ratio of cathodic area to anodic area is a driving force of localized corrosion rate. It is understood that a larger ratio of cathodic area to anodic area results in a higher anodic corrosion current density. This effect was observed in experiments, as more severe localized corrosion occurred in the presence of smaller pyrite particles.

### **8.3 A Descriptive Model for Localized Corrosion**

A descriptive model can now easily be established with the fundamental questions answered above, such as where, when and how this type of localized corrosion occurs. Therefore a descriptive model for the scenarios of both pyrite deposit on the steel surface and pyrite spontaneously formed in a sour environment is illustrated below.

#### *8.3.1 Scenario with Pyrite Deposits on the Steel Surface*

A macroscopic scenario of pyrite particles deposited on steel surface is depicted in Figure 144. The red solid line represents the portion where pyrite particles are in contact with steel. Hence, a discontinuous pyrite layer was artificially developed at the steel surface. Accordingly, many micro-galvanic cells are formed between the pyrite covered portion and the adjacent uncovered portion. As a result, pits can be initiated and

propagated by the galvanic coupling between pyrite and the adjacent steel when the aforementioned four conditions are met.

Figure 145 illustrates a microscopic scenario of localized corrosion in the presence of pyrite particles deposited on the steel surface. The electrons are released from dissolution of a portion of steel (anode) adjacent to a pyrite particle (cathode), and then flow to the cathodic pyrite particle, where they are consumed by cathodic reactions ( $H_2S$  reduction and hydrogen reduction). This process occurs continuously and, as a result, localized corrosion is initiated and propagated at a location on the steel surface adjacent to the pyrite particle (anode).

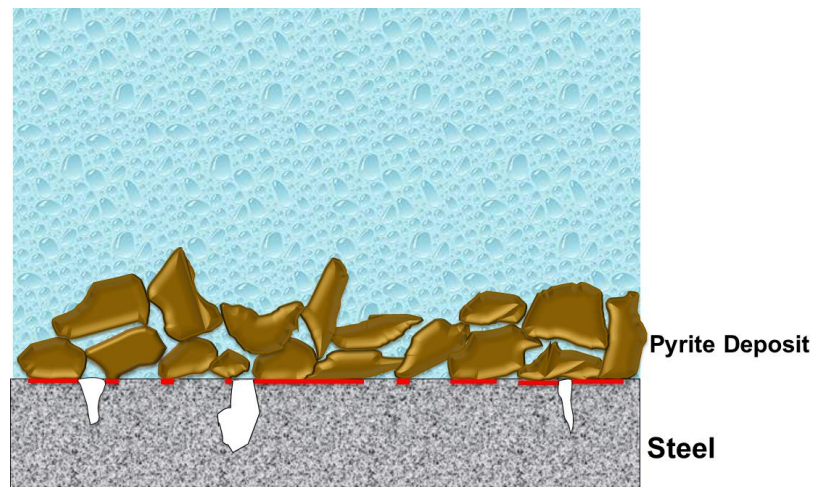


Figure 144. Macroscopic scenario of pyrite particles deposited on steel surface.

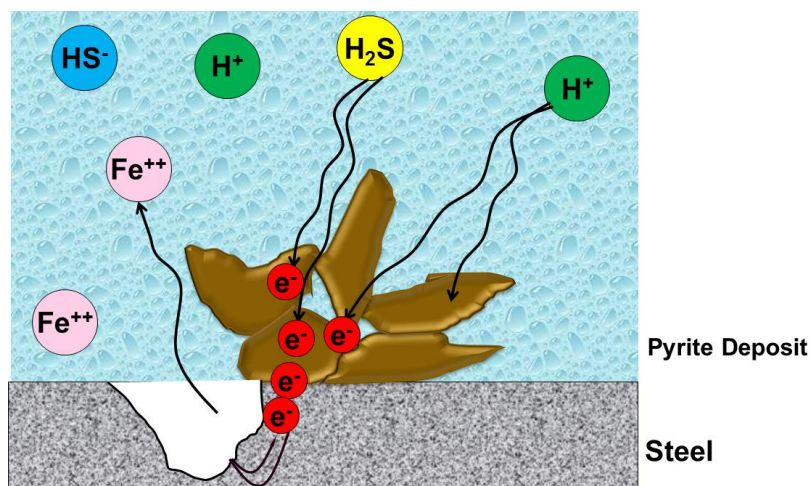
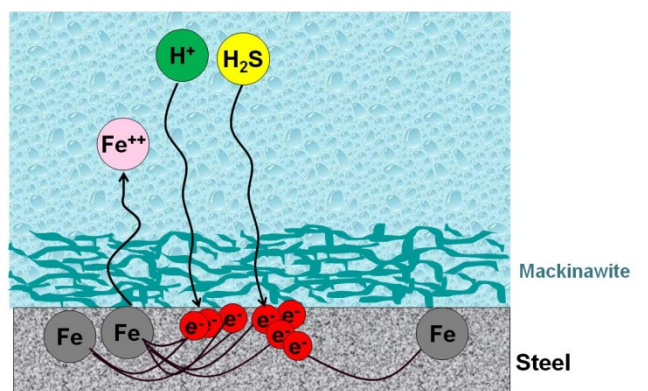


Figure 145. Microscopic scenario of localized corrosion in the presence of pyrite particles deposited on steel surface.

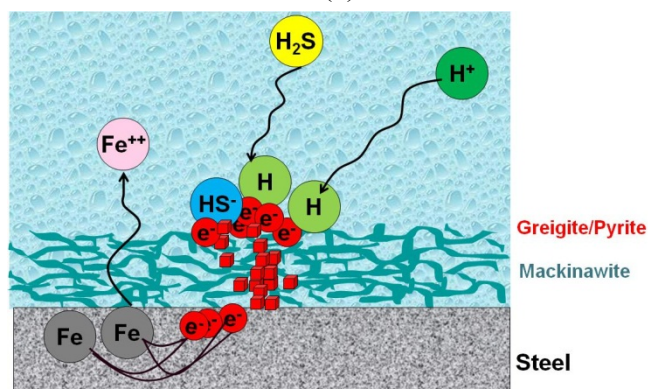
### 8.3.2 Scenario with Pyrite Spontaneously Formed in Sour Systems

Further, the mechanism for localized corrosion in the presence of pyrite spontaneously formed in sour systems was considered as well. The graphical interpretation of the proposed mechanism for localized  $\text{H}_2\text{S}$  corrosion in the presence of pyrite spontaneously formed at favorable conditions is shown as three steps in Figure 146. Step (a) shows formation of a mackinawite layer on the steel surface, where the diffusion of electroactive species are retarded due to the blocking effect of the mackinawite layer, resulting in a drop in the corrosion rate. The anisotropic electronic nature of mackinawite [143] makes it more of an insulator between the sheets of mackinawite on the metal surface, which results in limited pathways to transfer electrons for cathodic reactions. Step (b) shows the formation of pyrite inside the mackinawite layer when the environment is favored for its formation (the formation can be predicted by the Pourbaix diagram). Semiconductive pyrite crystals connect mackinawite sheets together to form less resistive pathway to transfer electrons. Subsequently, the electrons

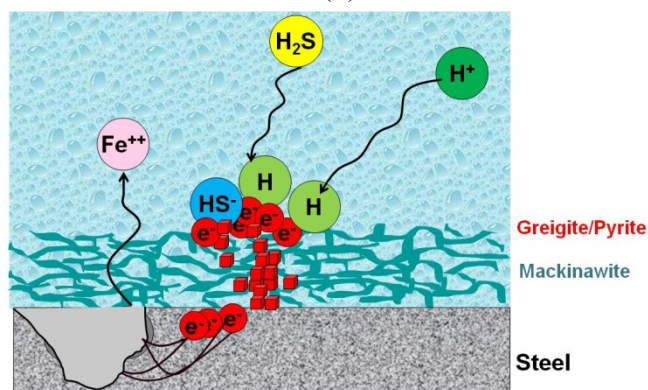
are transferred through the path of the least resistance to the top of the mackinawite layer to be consumed by cathodic reactions on the top of the corrosion product layer. Step (c) illustrates the process of pitting corrosion. The steel next to the pathway continually releases electrons and these electrons are transferred through the pathway, providing more cathodic sites on top of the mackinawite layer, which behaves like a Daniell cell [155]. The anodic part of the cell is the locally corroded area which will become a pit with time.



(a)



(b)



(c)

Figure 146. A descriptive model for localized corrosion in the presence of pyrite formed at favorable conditions: (a) Formation of mackinawite; (b) Formation of pyrite; (c) Localized corrosion.

#### 8.4 An Application of the Model to Field

A descriptive model was developed for localized corrosion in a sour environment when conditions lead to the formation of pyrite. Accordingly, field cases where pyrite is

present are facing the risk of localized corrosion. Therefore, it is critical to know if pyrite will form at specific field conditions.

#### *8.4.1 The Effects of Parameters on Pyrite Formation*

To predict the formation of pyrite at field conditions, it is important to understand the effect of measurable parameters in an upstream oil and gas production pipeline on pyrite formation. Some key parameters were reviewed: temperature, partial pressure of H<sub>2</sub>S, and ferrous ion concentration in solution.

##### *8.4.1.1 Effect of Temperature on Pyrite Formation*

A Pourbaix diagram has frequently been used to predict the formation of pyrite from a perspective of thermodynamics. The Pourbaix diagrams for predicting formation of pyrite at 25 °C, 80 °C, 150 °C, 200 °C, and 250 °C are presented in Figure 34 (d).

A gradual shift of the formed pyrite area to lower pH and to more negative potential with increasing temperature is shown in Figure 34 (d). This indicates that higher temperature conditions are more favorable for the formation of pyrite. Clearly, pyrite formation is sensitive to temperature.

##### *8.4.1.2 Effect of p<sub>H<sub>2</sub>S</sub> on Pyrite Formation*

Partial pressure of H<sub>2</sub>S was also taken into consideration. The Pourbaix diagrams with pyrite formation were developed for partial pressure of H<sub>2</sub>S at 100 ppm, 0.1 bar, 1 bar, 10 bar, and 100 bar and are shown in Figure 35 (d).

A major effect of increasing the partial pressure of H<sub>2</sub>S on the features of Pourbaix diagrams is the extension of the pyrite formation region. The increase in partial pressure of H<sub>2</sub>S from 100 ppm to 100 bar dramatically pushed the pyrite formation zone

from pH 6.0 to pH 2.7 at the conditions used here, suggesting that pyrite formation is very sensitive to partial pressure of H<sub>2</sub>S present in a sour system.

#### *8.4.1.3 Effect of [Fe<sup>2+</sup>] on Pyrite Formation*

The impact of ferrous ion concentration in solution on pyrite formation was considered in the present study as well. Figure 36 (d) shows a series of Pourbaix diagrams developed with 1 ppm, 10 ppm, and 100 ppm ferrous ion concentration. Notice that the pyrite formation is insensitive to the increase in ferrous ion concentration, as shown in Figure 36 (d).

#### *8.4.2 Pyrite Stability T - pH<sub>2</sub>S Map at Different pH*

As discussed above, the formation of pyrite in sour system is particularly sensitive to temperature and pH<sub>2</sub>S, but not to the ferrous ion concentration in solution. Accordingly, these two parameters, temperature and pH<sub>2</sub>S, were taken into consideration for predicting the formation of pyrite at field conditions.

The thermodynamic software ThermoCORP, was built based on the results of the present study by Addis [156]. It was used to rapidly generate the stability diagrams for sour corrosion systems based on temperature and pH<sub>2</sub>S (so-called T-pH<sub>2</sub>S map) at different pH values to predict pyrite formation. These T-pH<sub>2</sub>S maps shown below were generated at a fixed corrosion potential of -0.65 V vs. Ag/AgCl (sat'd KCl), which is a typical corrosion potential measured during laboratory experiments for sour corrosion of mild steel.

##### *8.4.2.1 Pyrite Stability Map at pH 3*

The pyrite stability map (T-pH<sub>2</sub>S map) at pH 3 shown in Figure 147 suggests that only the pyrrhotite group and ferrous ion are the stable corrosion products at the

conditions considered. Thus, there is no concern of pyrite formation at pH 3 at this condition.

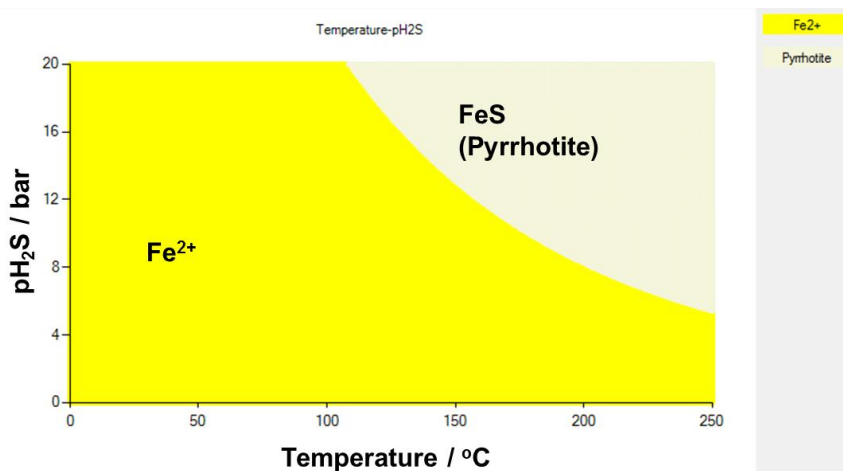


Figure 147. Pyrite stability T-pH<sub>2</sub>S map at pH 3 generated by ThermoCORP (E = -0.65 V vs. Ag/AgCl (sat'd KCl), pH = 3, [Fe<sup>2+</sup>] = 10 ppm, [Fe<sup>3+</sup>] = 1 ppm).

#### 8.4.2.2 *Pyrite Stability Map at pH 4*

Similarly, a pyrite stability map at pH 4 is depicted in Figure 148. Pyrite was predicted to form at this condition shown as the red area, where temperature is higher than 100 °C and pH<sub>2</sub>S is more than 2 bar.

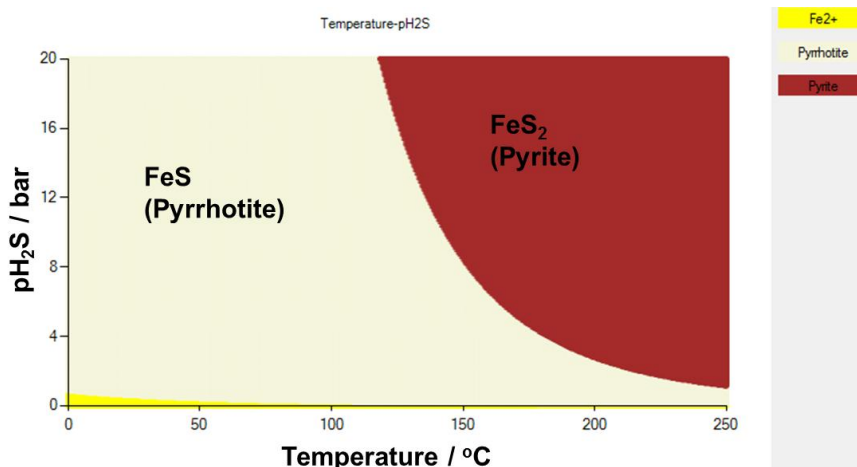


Figure 148. Pyrite stability T- $\text{pH}_2\text{S}$  map at pH 4 generated by ThermoCORP ( $E = -0.65$  V vs. Ag/AgCl (sat'd KCl), pH = 4,  $[\text{Fe}^{2+}] = 10$  ppm,  $[\text{Fe}^{3+}] = 1$  ppm).

#### 8.4.2.3 *Pyrite Stability Map at pH 5*

Likewise, pyrite was also predicted to form at pH 5 in Figure 149. According to the prediction made by this map, pyrite can be formed at conditions of 25 °C and low  $\text{pH}_2\text{S}$ . An extension of the pyrite stability area with increasing pH values from pH 4 to pH 5 was observed, which indicates that higher pH is favorable for pyrite formation.

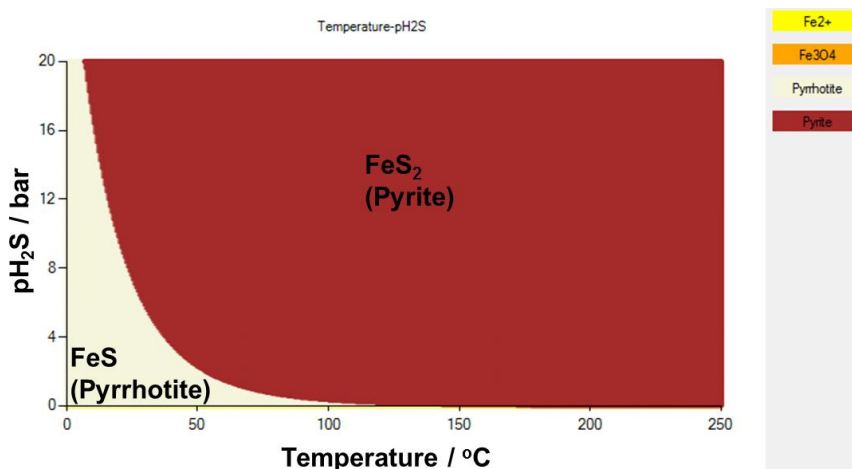


Figure 149. Pyrite stability T- $\text{pH}_2\text{S}$  map at pH 5 generated by ThermoCORP ( $E = -0.65$  V vs. Ag/AgCl (sat'd KCl), pH = 5,  $[\text{Fe}^{2+}] = 10$  ppm,  $[\text{Fe}^{3+}] = 1$  ppm).

#### 8.4.2.4 Pyrite Stability Map at pH 6

Figure 150 shows the pyrite stability map at pH 6. Pyrite is the predominant corrosion product shown in Figure 150 (a). Figure 150 (b) shows the magnification of the lower left corner in Figure 150 (a) to look for other corrosion products. Pyrrhotite was predicted to be a stable corrosion product in the left corner at the bottom of Figure 150 (b). According to the prediction made by the map shown in Figure 150 (b), pyrite can be formed when temperature is higher than 60 °C. Pyrite was detected in the experiment conducted at 80 °C with 0.05 bar  $p\text{H}_2\text{S}$  at pH 6.0 after 4 days of exposure (6.5.1), which agrees with the prediction made by the pyrite stability map. Further, pyrite was not seen in the experiment carried out at 25 °C with 0.1 bar  $p\text{H}_2\text{S}$  at pH 6.0 for 7 days of exposure (6.5.2). Again, the prediction on pyrite formation at this experimental condition made by the pyrite stability map shown in Figure 150 (b) confirmed this experimental observation.

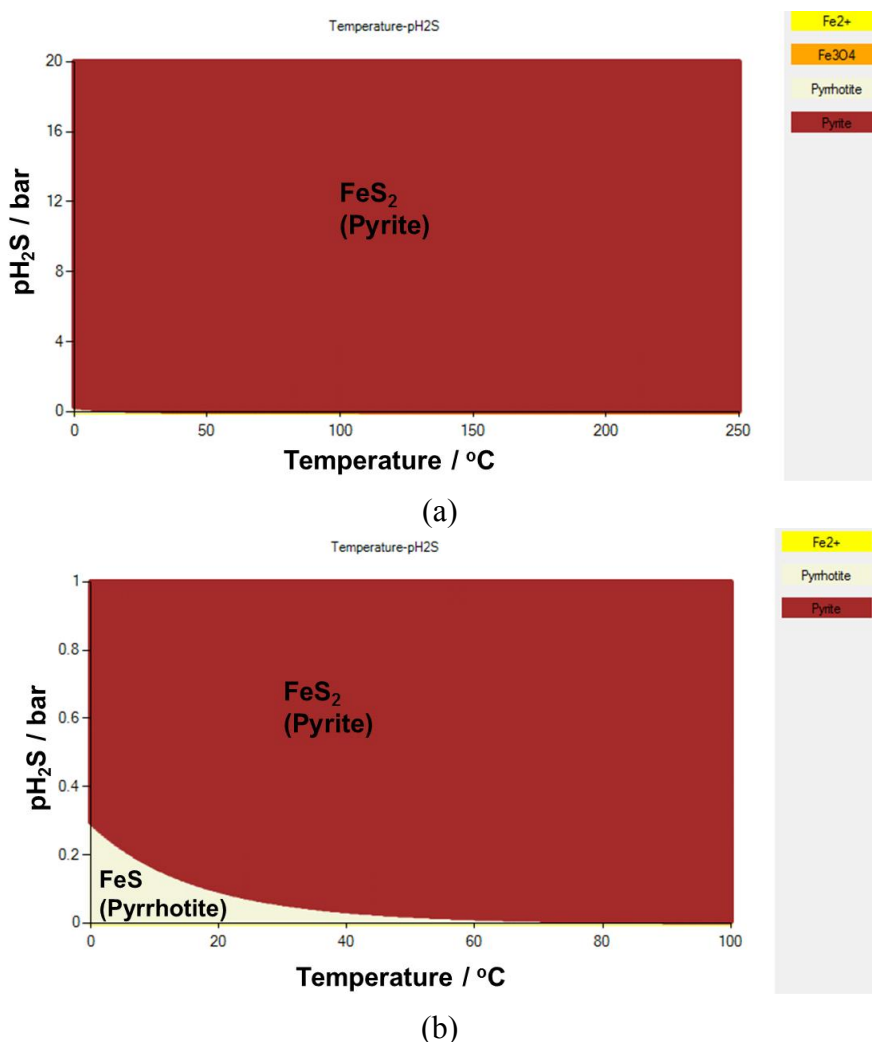


Figure 150. Pyrite stability T- $\text{pH}_2\text{S}$  map at pH 6 generated by ThermoCORP ( $E = -0.65 \text{ V}$  vs.  $\text{Ag}/\text{AgCl}$  (sat'd KCl),  $\text{pH} = 5$ ,  $[\text{Fe}^{2+}] = 10 \text{ ppm}$ ,  $[\text{Fe}^{3+}] = 1 \text{ ppm}$ ): (a)  $T = 0 \sim 250 \text{ }^{\circ}\text{C}$ ,  $\text{pH}_2\text{S} = 0 \sim 20 \text{ bar}$ ; (b)  $T = 0 \sim 100 \text{ }^{\circ}\text{C}$ ,  $\text{pH}_2\text{S} = 0 \sim 1 \text{ bar}$ .

#### 8.4.3 The Impact of Oxygen Ingress on Pyrite Stability Map

Oxygen ingress is often encountered during field operations in the oil and gas industry, from sources such as the injection of chemicals and water or production shutdown. The introduction of oxygen to pipelines and wells is acknowledged as an aggressive corrosion accelerator. In addition, a large increase in corrosion potential is always associated with the presence of oxygen in a corrosion system.

#### 8.4.3.1 How Does Oxygen Ingress Affect Corrosion Potential?

An example of trace amount of oxygen ingress in CO<sub>2</sub> corrosion of mild steel is given here. Figure 151 [157] shows a comparison of OCP between a pure CO<sub>2</sub> environment and 1 ppm O<sub>2</sub> ingress after 2 days of exposure to the CO<sub>2</sub> environment. An increase of approximately 200 mV in OCP was seen immediately after the 1 ppm oxygen ingress, which manifests that the system was dramatically oxidized, even with 1 ppm oxygen. Consequently, the increased OCP can significantly affect the formation of pyrite.

#### 8.4.3.2 The Impact of Oxygen Ingress on Pyrite Stability Map

The impact of an increase in OCP on pyrite formation was studied. Figure 147 shows a pyrite stability map at pH 3 without oxygen ingress at OCP of -0.65 V vs. Ag/AgCl (sat'd KCl). Based on the prediction, pyrite is not a thermodynamically favored corrosion product. However, in the case of oxygen ingress, if OCP is accelerated by 200 mV, the resultant pyrite stability map at pH 3 is shown in Figure 152, where pyrite is predicted to be a predominant corrosion product. The comparison between Figure 147 and Figure 152 clearly reveals that a trace amount of oxygen ingress greatly facilitates the formation of pyrite.

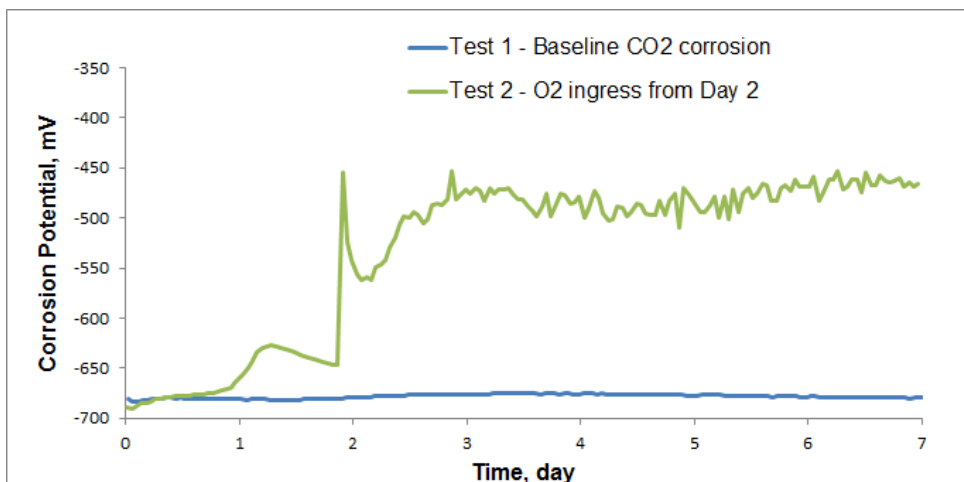


Figure 151. Comparison of corrosion potentials between two tests (80 °C,  $p\text{CO}_2 = 0.5$  bar,  $\text{O}_2$  concentration = 1 ppm in liquid, pH = 6.6, 1 wt.% NaCl) (Reproduced from [157]).

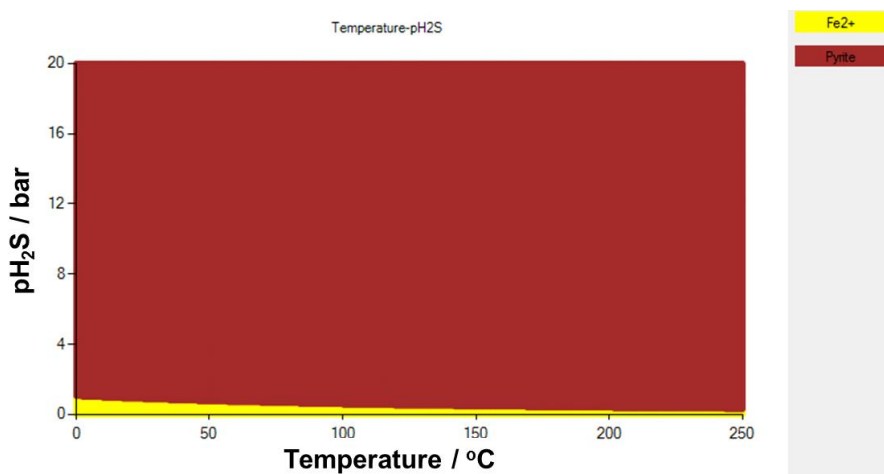


Figure 152. Pyrite stability T- $\text{pH}_2\text{S}$  map with oxygen ingress at pH 6 generated by ThermoCORP ( $E = -0.45$  V vs. Ag/AgCl (sat'd KCl), pH = 3,  $[\text{Fe}^{2+}] = 10$  ppm,  $[\text{Fe}^{3+}] = 1$  ppm).

## 8.5 Summary

A descriptive model for localized corrosion in sour environment was built to answer when, where, and how this type of localized corrosion could occur based on experimental observations and existing knowledge. The initiation of localized corrosion is due to galvanic coupling between a pyrite particle (cathode) and the steel adjacent to

the pyrite particle (anode). Four important preconditions for galvanic coupling are: dissimilar materials, direct electrical contact, electrolyte with certain conductivity, and large cathodic/anodic area ratio. These conditions must be met for the localized corrosion to occur on the steel surface. This model can provide guidance for the mitigation of localized corrosion in field conditions.

## CHAPTER 9. CONCLUSIONS & RECOMMENDATIONS FOR FUTURE WORK

### 9.1 Conclusions

- A comprehensive thermodynamic model, in the form of Pourbaix diagrams, was developed and is able to predict corrosion products for an H<sub>2</sub>S-H<sub>2</sub>O-Fe system with the focus on the conditions typical for oil and gas applications. Pourbaix diagrams generated by the thermodynamic model were experimentally validated at 25 °C and 80 °C.
- For the current experimental conditions, severe localized corrosion was observed in experiments when there was formation of greigite and/or pyrite. Localized corrosion was not found when neither greigite nor pyrite formed.
- Severe localized corrosion was observed and replicated in the presence of pyrite deposit layers in either aqueous H<sub>2</sub>S or CO<sub>2</sub> dominated environments. Experiments were designed and have demonstrated that a galvanic coupling between pyrite particles and steel is the dominant mechanism for this type of localized corrosion.
- A descriptive model for localized corrosion in sour environment was proposed for this type of localized corrosion. In addition, the thermodynamic model can be applied to field conditions to predict formation of pyrite, providing guidance for the mitigation of localized corrosion in field conditions.

### 9.2 Recommendations for Future Work

- Perform more investigation to thoroughly understand the localized corrosion driven by a galvanic coupling mechanism, such as the effect of the salinity of electrolyte on localized corrosion.

- Investigate the conductivity of a corrosion product layer containing greigite and pyrite using state-of-the-art surface examination techniques, such as AFM conductivity mapping.
- Conduct both theoretical and experimental study on the propagation of localized corrosion, such as how pits grow, propagate, and in some cases “die”.
- Explore the impact of other iron sulfide phases on localized corrosion, such as pyrrhotite and mackinawite.

### References

- [1] W. F. Rogers and J. A. J. Rowe, "Corrosion effects of hydrogen sulphide and carbon dioxide in oil production," in *4th World Petroleum Congress*, 1955, pp. 479–499.
- [2] M. R. Bonis, R. R. MacDonald, M. R. Girgis, and K. R. Goerz, "Weight loss corrosion with H<sub>2</sub>S: using past operations for designing future facilities," in *CORROSION/2006*, Houston, TX, 2006, paper no. 06122.
- [3] W. Sun, S. Nesic, D. Young and R. Woolam, "Equilibrium expressions related to the solubility of the sour corrosion product mackinawite," *Ind. Eng. Chem. Res.*, vol. 47, pp. 1738–1742, 2008.
- [4] P. Taylor, "The stereochemistry of iron sulfides-a structural rationale for the crystallization of some metastable phases from aqueous solution." *Am. Mineral.*, vol. 65, pp. 1026–1030, 1980.
- [5] J. S. Smith and J. D. A. Miller, "Nature of sulfides and their corrosive effect on ferrous metals: a review," *Brit. Corros. J.*, vol. 10, pp. 136–143, 1975.
- [6] S. N. Smith and M. Joosten, "Corrosion of carbon steel by H<sub>2</sub>S in CO<sub>2</sub> containing oilfield environments," in *CORROSION/2006*, Houston, TX, 2006, paper no. 06115.
- [7] A. Anderko, P. McKenzie and R. D. Young, "Computation of rates of general corrosion using electrochemical and thermodynamic models," *Corrosion*, vol. 57, pp. 202–213, 2001.

- [8] W. Sun, "Kinetics of iron carbonate and iron sulfide scale formation in carbon dioxide/hydrogen sulfide corrosion," Ph.D. dissertation, Ohio University, Athens, OH, 2006.
- [9] Y. Zheng, B. Brown and S. Nešić, "Electrochemical study and modeling of H<sub>2</sub>S corrosion of mild steel," *Corrosion*, vol. 70, pp. 351–365, 2014.
- [10] Y. Zheng, J. Ning, B. Brown and S. Nešić, "Electrochemical model of mild steel corrosion in a mixed H<sub>2</sub>S/CO<sub>2</sub> aqueous environment in the absence of protective corrosion product layers," *Corrosion*, vol. 71, pp. 259–397, 2015.
- [11] Y. Zheng, "Electrochemical mechanism and model of H<sub>2</sub>S corrosion of carbon steel," Ph.D. dissertation, Ohio University, Athens, OH, 2015.
- [12] B. Brown, "The influence of sulfides on localized corrosion of mild steel," Ph.D. dissertation, Ohio University, Athens, OH, 2013.
- [13] J. W. Morse, F. J. Millero, J. C. Cornwell and D. Rickard, "The chemistry of the hydrogen sulfide and iron sulfide systems in natural waters", *Earth-Sci. Rev.*, vol. 24, pp.1–42, 1987.
- [14] D. Rickard, "The solubility of FeS," *Geochim. Cosmochim. Acta*, vol. 70, pp. 5779–5789, 2006.
- [15] L. G. Benning, R. T. Wilkin and H. L. Barnes, "Reaction pathways in the Fe–S system below 100°C," *Chem. Geol.*, vol. 167, pp. 25–51, 2000.
- [16] R. A. Berner, "Thermodynamic stability of sedimentary iron sulfides," *Am. J. Sci.*, vol. 265, pp. 773–785, 1967.

- [17] S. Theberge and G. W. Luther, "Determination of the electrochemical properties of a soluble aqueous FeS species present in sulfidic solutions," *Aquat. Geochem.*, vol. 3, pp. 191–211, 1997.
- [18] J. Ning, Y. Zheng, D. Young, B. Brown and S. Nešić, "Construction and verification of Pourbaix diagrams for hydrogen sulfide corrosion of mild steel," in *CORROSION/2015*, Houston, TX, 2015, paper no. 5507.
- [19] J. Ning, Y. Zheng, D. Young, B. Brown and S. Nešić, "A thermodynamic model for the prediction of mild steel corrosion products in an aqueous hydrogen sulfide environment," *Corrosion*, vol. 71, pp. 945–960, 2015.
- [20] O. M. Suleimenov and R. E. Krupp, "Solubility of hydrogen sulfide in pure water and in NaCl solutions, from 20 to 320°C and at saturation pressures," *Geochim. Cosmochim. Acta*, vol. 58, pp. 2433–2444, 1994.
- [21] M. Nordsveen, S. Nesic, R. Nyborg and A. Stangeland, "A mechanistic model for carbon dioxide corrosion of mild steel in the presence of protective iron carbonate films—Part 1: theory and verification," *Corrosion*, vol. 59, pp. 443–457, 2003.
- [22] E. Hogfeldt, *Stability Constants of Metal-ion Complexes, Part A: Inorganic Ligands*. Oxford, U. K.: Pergamon Press, 1982.
- [23] R. F. Weiss, "The solubility of nitrogen, oxygen and argon in water and seawater," *Deep-Sea Res.*, vol. 17, pp. 721–735, 1970.
- [24] J. Carroll and A. E. Mather, "The solubility of hydrogen sulphide in water from 0 to 90°C and pressures to 1 MPa," *Geochim. Cosmochim. Acta*, vol. 53, pp. 1163–1170, 1989.

- [25] B. E. Roberts and P. R. Tremaine, "Vapour liquid equilibrium calculations for dilute aqueous solutions of CO<sub>2</sub>, H<sub>2</sub>S, NH<sub>3</sub> and NaOH to 300°C," *Can. J. Chem. Eng.*, vol. 63, pp. 294–300, 1985.
- [26] O. M. Suleimenov and T. M. Seward, "A spectrophotometric study of hydrogen sulphide ionization in aqueous solutions to 350°C," *Geochim. Cosmochim. Acta*, vol. 61, pp. 5187–5198, 1997.
- [27] Y. K. Kharaka, E. H. Perkins, W. D. Counter, J. D. Debral and C. H. Bamford, *Solmineq 88: A Computer Program for Geochemical Modeling of Water Rock Interactions*. Menlo Park, CA: Alberta Research Council, 1988.
- [28] F. J. Millero, "The thermodynamics and kinetics of the hydrogen sulfide system in natural waters," *Mar. Chem.*, vol. 18, pp. 121–147, 1986.
- [29] R. J. Myers, "The new low value for the second dissociation constant of H<sub>2</sub>S: its history, its best value, and its impact on the teaching of sulfide equilibria," *J. Chem. Educ.*, vol. 63, pp. 687–690, 1986.
- [30] A. J. Ellis and W. Giggenbach, "Hydrogen sulfide ionization and sulphur hydrolysis in high temperature solution," *Geochim. Cosmochim. Acta*, vol. 35, pp. 247–260, 1971.
- [31] S. Licht, F. Forouzan and K. Longo, "Differential densometric analysis of equilibria in highly concentrated media: determination of the aqueous second acid dissociation constant of H<sub>2</sub>S," *Anal. Chem.*, vol. 62, pp. 1356–1360, 1990.
- [32] D. A. Skoog and D. M. West, *Fundamentals of Analytical Chemistry*, 4th ed. Philadelphia, PA: W. B. Saunders Co., 1982.

- [33] H. P. Stephens and J. W. Cobble, "Thermodynamic properties of the aqueous sulfide and bisulfide ions and the second ionization constant of hydrogen sulfide over extended temperatures," *Inorg. Chem.*, vol. 10, pp. 619–625, 1971.
- [34] D. Wagman, W. Evans, V. Parker, L. Halow, S. Bailey and R. Schumm, *Selected Values of Chemical Thermodynamic Properties*. Washington, DC: U.S. Government Printing Office, 1968.
- [35] Y. S. Su, K. L. Cheng and Y.C. Jean, "Amplified potentiometric determination of  $pK_{00}$ ,  $pK_0$ ,  $pK_1$ , and  $pK_2$  of hydrogen sulfides with  $Ag_2S$  ISE," *Talanta*, vol. 44, pp. 1757–1763, 1997.
- [36] A. A. Migdisov, A. E. Williams-Jones, L. Z. Lakshtanov and Y. V. Alekhin, "Estimates of the second dissociation constant of  $H_2S$  from the surface sulfidation of crystalline sulfur," *Geochim. Cosmochim. Acta*, vol. 66, pp. 1713–1725, 2002.
- [37] W. Giggenbach, "Optical spectra of highly alkaline sulfide solutions and the second dissociation constant of hydrogen sulfide," *Inorg. Chem.*, vol. 10, pp.1333–1338, 1971.
- [38] B. Meyer, K. Ward, K. Koshlap and L. Peter, "Second dissociation constant of hydrogen sulfide," *Inorg. Chem.*, vol. 22, pp. 2345–2346, 1983.
- [39] S. Licht and J. Manassen, "The second dissociation constant of  $H_2S$ ," *J. Electrochem. Soc.*, vol. 134, pp. 918–921, 1987.
- [40] M. A. A. Schoonen and H. L. Barnes, "An approximation of the second dissociation constant for  $H_2S$ ," *Geochim. Cosmochim. Acta*, vol. 52, pp. 649–654, 1988.

- [41] W. Sun, S. Netic and S. Papavinasam, "Kinetics of corrosion layer formation, Part 2. iron sulfide and mixed iron sulfide/carbonate layers in carbon dioxide/hydrogen sulfide corrosion," *Corrosion*, vol. 64, pp. 586–599, 2008.
- [42] E. Abelev, J. Sellberg, T. A. Ramanarayanan and S. L. Bernasek, "Effect of H<sub>2</sub>S on Fe corrosion in CO<sub>2</sub>-saturated brine," *J. Mater. Sci.*, vol. 44, pp. 6167–6181, 2009.
- [43] S. Kapusta, D. Raghu and J. Richard, "Managing sour gas corrosion: testing, design, implementation and field results," in *CORROSION/2008*, Houston, TX, 2008, paper no. 08641.
- [44] F. H. Meyer, O. L. Riggs, R. L. McGlasson and J. D. Sudbury, "Corrosion products of mild steel in hydrogen sulfide environments," *Corrosion*, vol. 14, pp. 69–75, 1958.
- [45] R. A. Berner, "Tetragonal iron sulfide," *Science*, vol.137, pp. 669–670,1962.
- [46] R. A. Berner, "Iron sulfides formed from aqueous solution at low temperatures and atmospheric pressure," *J. Geol.*, vol. 72, pp. 293–306, 1964.
- [47] H. T. Evans Jr., C. Milton, E. C. T. Chao, I. Adler, C. Mead, B. Ingram and R. A. Berner, "Vallerite and the new iron sulfide, mackinawite," U. S. Geological Survey Professional Paper 475-D, pp.64–69, 1964.
- [48] D. Rickard, "An apparatus for the study of fast precipitation reactions," *Mineral. Mag.*, vol. 53, pp.527–530, 1989.
- [49] D. Rickard, "Experimental concentration-time curves for the iron(II) sulphide precipitation process in aqueous solutions and their interpretation," *Chem. Geol.*, vol. 78, pp. 315–324, 1989.

- [50] S. N. Smith and E. J. Wright, "Prediction of minimum H<sub>2</sub>S levels required for slightly sour corrosion," in *CORROSION/1994*, Houston, TX, 1994, paper no. 11.
- [51] W. Davison, "The solubility of iron sulfides in synthetic and natural waters at ambient temperature," *Aquat. Sci.*, vol. 53, pp. 309–329, 1991.
- [52] D. B. Craig, "The nature of iron sulfides Formed on Steel in an H<sub>2</sub>S-O<sub>2</sub> environment," *Corrosion*, vol. 35, pp. 136–138, 1979.
- [53] J. A. Bourdoiseau, M. Jeannin, R. Sabot, C. Remazeilles and Ph. Refait, "Characterisation of mackinawite by Raman spectroscopy: effects of crystallisation, drying and oxidation," *Corros. Sci.*, vol. 50, pp. 3247–3255, 2008.
- [54] D. Rickard and G. W. Luther, "Chemistry of iron sulfides," *Chem. Rev.*, vol. 107, pp. 514–562, 2007.
- [55] S. Nešić and W. Sun, "Acid gas corrosion," in *Shreir's Corrosion*, 2<sup>nd</sup> ed., vol. 2. T. J. A. Richardson et al. Ed., Elsevier, 2010, pp. 1270–1298.
- [56] W. Sun and S. Nešić, "A mechanistic model of uniform hydrogen sulfide/carbon dioxide corrosion of mild steel," *Corrosion*, vol. 65, pp. 291–307, 2009.
- [57] Y. Zheng, J. Ning, B. Brown and S. Nešić, "Electrochemical model of mild steel corrosion in a mixed H<sub>2</sub>S/CO<sub>2</sub> aqueous environment," in *CORROSION/2014*, Houston, TX, 2014, paper no. 3907.
- [58] S. N. Smith, B. Brown and W. Sun, "Corrosion at higher H<sub>2</sub>S concentrations and moderate temperatures," in *CORROSION/2011*, Houston, TX, 2011, paper no. 11081.
- [59] K. Lee, "A mechanistic modeling of CO<sub>2</sub> corrosion of mild steel in the presence of H<sub>2</sub>S," Ph.D. dissertation, Ohio University, Athens, OH, 2004.

- [60] M. Singer, A. Camacho, B. Brown and S. Nestic, "Sour top of the line corrosion in the presence of acetic acid," in *CORROSION/2010*, Houston, TX, 2010, paper no. 10100.
- [61] M. Singer, S. Nestic and J. N. Al-Khamis, "Corrosion assessment in Karan gas field development," in *CORROSION/2012*, Houston, TX, 2012, paper no. 0001411.
- [62] S. M. Wilhelm and B. R. W. Hinton, "Galvanic corrosion caused by corrosion products," in *Galvanic Corrosion*, H. P. Hack, Ed., Philadelphia, PA: American Society for Testing and Materials, 1988, pp. 23–34.
- [63] C. M. Menendez, V. Jovancicevic, S. Ramachandran, M. Morton, D. Stegmann, "Assessment of corrosion under iron sulfide deposits and CO<sub>2</sub>/H<sub>2</sub>S conditions," *Corrosion*, vol. 69, pp. 145–156, 2013.
- [64] M. Pourbaix, *Atlas of electrochemical equilibria in aqueous solutions*, trans. J. A. Franklin, Houston, TX: NACE, 1974.
- [65] M. Pourbaix, *Lectures on Electrochemical Corrosion*, trans. J.A.S. Green and R.W. Staehle, New York, NY: Plenum Press, 1973.
- [66] E. D. Verink, JR., "Simplified procedure for constructing Pourbaix diagrams," in *Uhlig's Corrosion Handbook*, 3<sup>rd</sup> ed., R. W. Revie, Ed., Hoboken, NJ: John Wiley & Sons Inc., 2011, pp. 93–101.
- [67] J. Bouet and J. P. Brenet, "Potential/pH diagram for iron in sulfide-bearing media," *Corros. Sci.*, vol. 3, pp. 51–63, 1963.
- [68] M. Ueda, "Potential-pH diagram at elevated temperatures for metal-CO<sub>2</sub>/H<sub>2</sub>S-water systems and the application for corrosion of pure iron," *Corros. Eng.*, vol. 44, pp.159–174, 1995.

- [69] A. Anderko and P. J. Shuler, "A computational approach to predicting the formation of iron sulfide species using stability diagrams," *Comput. Geosci.*, vol. 23, pp. 647–658, 1997.
- [70] A. Anderko, S. J. Sanders and R. D. Young, "Real-Solution stability diagrams: a thermodynamic tool for modeling corrosion in wide temperature and concentration ranges," *Corrosion*, vol. 53, pp. 43–53, 1997.
- [71] W. A. Kornicker, "Interactions of divalent cations with pyrite and mackinawite in seawater and NaCl solutions," Ph.D. dissertation, Texas A&M University, College Station, TX, 1988.
- [72] M. Wolthers, S. J. Van der Gaast and D. Rickard, "The structure of disordered mackinawite," *Am. Mineral.*, vol. 88, pp. 2007–2015, 2003.
- [73] D. Rickard, A. Griffith, A. Oldroyd, I. B. Butler, E. Lopez-Capel, D. A. C. Manning and D. C. Apperley, "The composition of nanoparticulate mackinawite, tetragonal iron(II) monosulfide," *Chem. Geol.*, vol. 235, pp. 286–298, 2006.
- [74] J. W. Morse and D. Rickard, "Chemical dynamics of sedimentary acid volatile sulfide," *Environ. Sci. Technol.*, vol. 38, pp. 131–136, 2004.
- [75] R. E. Sweeney and I. R. Kaplan, "Pyrite framboid formation: laboratory synthesis and marine sediments," *Econ. Geol.*, vol. 68, pp. 618–634, 1973.
- [76] J. C. Ward, "The structure and properties of some iron sulfides," *Rev. Pure Appl. Chem.*, vol. 20, pp. 175–206, 1970.
- [77] A. R. Lennie and D. J. Vaughan, *Mineral Spectroscopy: A Tribute to Roger G. Burns*, M. D. Dyar, C. McCammon and M. W. Schaefer, Ed. Houston, TX: The Geochemical Society, 1996, pp. 117–131.

- [78] B. Craig, "Corrosion product analysis-a road map to corrosion in oil and gas production," *Mater. Perform.*, pp. 56–58, Aug. 2002.
- [79] S. N. Smith, "Corrosion product analysis in oil and gas pipelines," *Mater. Perform.*, pp. 44–47, Aug. 2013.
- [80] J. Ning, Y. Zheng, D. Young, B. Brown and S. Nešić, "A thermodynamic study of hydrogen sulfide corrosion of mild steel," *Corrosion*, vol. 70, pp. 375–389, 2014.
- [81] Rinaldo de Médicis, "Cubic FeS, a metastable iron sulfide," *Science*, vol. 170, pp. 1191–1192, 1970.
- [82] B. J. Murowchick and H. L. Barnes, "Formation of cubic FeS," *Am. Mineral.*, vol. 71, pp. 1243–1246, 1986.
- [83] R. G. Arnold, "Pyrrhotite phase relations below 304oC at < 1 atm total pressure," *Econ. Geol.*, vol. 64, pp. 405–419, 1969.
- [84] M. Liu, J. Wang, W. Ke and E. Han, "Corrosion behavior of X52 anti-H<sub>2</sub>S pipeline steel exposed to high H<sub>2</sub>S concentration solutions at 90°C," *J. Mater. Sci. Technol.*, vol. 30, pp. 504–510, 2014.
- [85] P. Bai, S. Zheng, C. Chen and H. Zhao, "Investigation of the iron-sulfide phase transformation in nanoscale," *Cryst. Growth Des.*, vol. 14, pp. 4295–4302, 2014.
- [86] M. Schoonen and H. L. Barnes, "Reactions forming pyrite and marcasite from solution: II. Via FeS precursors below 100°C," *Geochim. Cosmochim. Acta*, vol. 55, pp. 1505–1514, 1991.
- [87] R. J. Biernat and R. G. Robins, "High-temperature potential/pH diagrams for the iron-water and iron-water-sulphur systems," *Electrochim. Acta*, vol. 17, pp. 1261–1283, 1972.

- [88] D. D. Macdonald and B. C. Syrett, "Potential-pH diagrams for iron and nickel in high salinity geothermal brine containing low concentrations of hydrogen sulfide," *Corrosion*, vol. 35, pp. 471–475, 1979.
- [89] C. M. Chen, K. Aral and G. J. Theus, "Computer-Calculated potential pH diagrams to 300°C," Electronic Power Research Institute, Palo Alto, CA, Rep. EPRI NP-3137, 1983.
- [90] T. Tanupabrungsun, D. Young, B. Brown and S. Nešić, "Construction and verification of Pourbaix diagrams for CO<sub>2</sub> corrosion of mild steel valid up to 250°C," in *CORROSION/2012*, Houston, TX, 2012, paper no. 1418.
- [91] E. H. Oelkers, H. C. Helgeson, E. L. Shock, D. A. Sverjensky, J. W. Johnson and V. A. Pokrovskii, "Summary of the apparent standard partial molal gibbs free energies of formation of aqueous species, minerals, and gases at pressures 1 to 5000 bars and temperatures 25 to 1000°C," *J. Phys. Chem. Ref. Data*, vol. 24, pp.1401–1560, 1995.
- [92] M. H. Kaye and W. T. Thompson, "Computation of Pourbaix diagrams at elevated temperature," in *Uhlig's Corrosion Handbook*, 3<sup>rd</sup> ed., R. W. Revie, Ed., Hoboken, New Jersey: John Wiley & Sons Inc., 2011, pp. 111–122.
- [93] O. Kubaschewski, C. B. Alcock and P. J. Spencer, *Material Thermochemistry*, 6th ed., Oxford, New York: Pergamon Press, 1993.
- [94] M. Binnewies and E. Milke, *Thermochemical Data of Elements and Compounds*, 2<sup>nd</sup> revised and extended ed., Weinheim: Wiley-VCH, 2002.
- [95] O. Knacke, O. Kubaschewski and K. Hesselmann, *Thermochemical Properties of Inorganic Substances*, 2<sup>nd</sup> ed., Berlin, New York: Springer-Verlag, 1991.

- [96] R. A. Robie, B. S. Hemingway and J. R. Fisher, "Thermodynamic properties of mineral and related substances at 1 Bar pressure and at higher temperatures," U. S. Geological Survey, Bulletin, Rep. 1452, 1978.
- [97] M. W. Chase, J. R. Downey, *NIST-JANAF Thermochemical Tables*, 4<sup>th</sup> ed., Washington, D.C.: American Chemical Society; Woodbury, N.Y.: American Institute of Physics for the National Institute of Standards and Technology, 1998.
- [98] "Thermodynamic quantities for substances and ions at 25°C," <http://bilbo.chm.uri.edu/CHM112/tables/thermtable.htm>. Accessed 19 Sep. 2016.
- [99] "Standard thermodynamic properties of chemical substances," [http://www.update.uu.se/~jolkkonen/pdf/CRC\\_TD.pdf](http://www.update.uu.se/~jolkkonen/pdf/CRC_TD.pdf). Accessed 19 Sep. 2016.
- [100] H. E. Barner and R. V. Scherman, *Handbook of Thermodynamical Data for Compounds and Aqueous Species*, New York: John Wiley & Sons, 1978.
- [101] K. C. Mills, *Thermodynamic Data for Inorganic Sulfides, Selenides, and Tellurides*, London: Butterworths, 1974.
- [102] B. Beverskog and I. Puigdomenech, "Revised Pourbaix diagrams for iron at 25-300°C," *Corros. Sci.* vol. 38, pp. 2121–2135, 1996.
- [103] V. B. Parker, I. L. Khodakovskii, "Thermodynamic Properties of the aqueous ions (2+ and 3+) of iron and the key compounds of iron," *J. Phys. Chem. Ref. Data* vol. 24, pp. 1699–1745, 1995.
- [104] E. E. Bernarducci, L. R. Morss and A. R. Miksztal, "Partial molal heat capacity of aqueous ferrous chloride from measurements of integral heats of dilution," *J. Solution Chem.* vol. 8, pp. 717–727, 1979.

- [105] E. L. Shock and H. C. Helgeson, "Calculation of the thermodynamic and transport properties of aqueous species at high pressures and temperatures: correlation algorithms for ionic species and equation of state predictions to 5 kb and 1000°C," *Geochim. Cosmochim. Acta* vol. 52, pp. 2009–2036, 1988.
- [106] F. Gronvold and E. F. Westrum, Jr., "Heat capacities and thermodynamic functions of iron disulfide (pyrite), iron diselenide, and nickel diselenide from 5 to 350°K. The estimation of standard entropies of transition metal chalcogenides," *Inorg. Chem.* vol. 1, pp. 36–48, 1962.
- [107] D. J. Vaughan and J. R. Craig, "Sulfide thermochemistry," in *Mineral Chemistry of Metal Sulfides*, W. B. Harland, S. O. Agrell, A. H. Cook and N. F. Hughes, Ed., New York, NY: Cambridge University Press, 1978.
- [108] D. Abayarathna, A. Naraghi and S. Wang, "The effect of surface films on corrosion of carbon steel in a CO<sub>2</sub>-H<sub>2</sub>S-H<sub>2</sub>O system," in *CORROSION/2005*, Houston, TX, 2005, paper no. 05624.
- [109] J. Han, B. Brown, D. Young and S. Nestic, "Mesh-capped probe design for direct pH measurements at an actively corroding metal surface," *J. Appl. Electrochem.*, vol. 40, pp. 683–690, 2010.
- [110] D. W. Davis and R. A. Detro, "Fire and Brimstone The History of Melting Louisiana's Sulphur," Louisiana Geological Survey, Baton Rouge, LA, 1992.
- [111] D. D. Macdonald, B. Roberts and J. B. Hyne, "The corrosion of carbon steel by wet elemental sulphur," *Corros. Sci.* vol. 18, pp. 411–425, 1978.
- [112] N. I. Dowling, P. D. Clark and J. B. Hyne, "Understanding and mitigation corrosion during handling and transportation of elemental sulfur," Alberta Sulfur

Research Center Quarterly Bulletin, Vol. XXXIII, No.1 April-June 1996, pp. 15–28.

- [113] N. I. Dowling, “Corrosion of materials used in storage and handling of solid elemental sulphur,” Proceeding of the International Symposium on Materials Performance: Sulphur and Energy, in *31st Annual Conference of Metallurgists of CIM*, Edmonton, Canada, 1992, pp. 103–115.
- [114] H. Fang, “Investigation of localized corrosion of carbon steel in H<sub>2</sub>S environments,” Ph.D. dissertation, Ohio University, Athens, OH, 2011.
- [115] D. Precoor, “The detection, mitigation and corrosion mechanism of ionic polysulfides in oil & gas systems,” presented at Shell Calgary Sulfur Meeting, Calgary, AB, 2002.
- [116] J. Bojes, J. Lerbscher, W. Wamburi and C. Dilley, “Elemental sulfur in 3-phase sour gas systems-Is condensate really your ally?” in *NACE Northern Area Western Conference*, Calgary, AB, February 2010.
- [117] A. Jr. Kamyshny, A. Goifman, J. Gun, D. Rizkov and O. Lev, “Equilibrium distribution of polysulfide ions in aqueous solutions at 25°C: a new approach for the study of polysulfides’ equilibria,” *Environ. Sci. Technol.* vol. 38, pp. 6633–6644, 2004.
- [118] D. F. Ho-Chung-Qui and A. I. Williamson, “Corrosion experiences and inhibition practices in wet sour gas gathering systems,” in *CORROSION/1987*, Houston, TX, 1987, paper no. 46.
- [119] T. W. Hamby, “Development of high pressure sour gas technology,” *J. Petrol. Technol.*, vol. 33, pp. 792–798, 1981.

- [120] H. Fang, B. Brown and S. Netic, “High salt concentration effects on CO<sub>2</sub> corrosion and H<sub>2</sub>S corrosion,” in *CORROSION/2010*, Houston, TX, 2010, paper no. 10276.
- [121] S. Netic, “Carbon dioxide corrosion of mild steel,” in *Uhlig’s Corrosion Handbook*, 3<sup>rd</sup> ed., R. W. Revie, Ed., Hoboken, NJ: John Wiley & Sons Inc., 2011, pp. 229–245.
- [122] R. C. Woollam, A. Huggins, C. Mendez, J. R. Vera and W. H. Durnie, “Localized corrosion due to galvanic coupling between FeS-covered and uncovered areas: another oilfield myth?” in *CORROSION/2013*, Houston, TX, 2013, paper no. 2715.
- [123] J. Kvarekval, “Morphology of localized corrosion attacks in sour environments,” in *CORROSION/2007*, Houston, TX, 2007, paper no. 07659.
- [124] Y. Zheng, J. Ning, B. Brown, D. Young and S. Nešić, “Mechanistic study of the effect of iron sulfide layers on hydrogen sulfide corrosion of carbon steel,” in *CORROSION/2015*, 2015, Houston, TX, paper no. 5933.
- [125] R. L. Martin and R. R. Annand, “Accelerated corrosion of steel by suspended iron sulfides in brine,” *Corrosion*, vol. 36, pp. 297–301, 1981.
- [126] M. Achour, J. Kolts, P. Humble and R. Hudgins, “Experimental evaluation of corrosion inhibitor performance in presence of iron sulfide in CO<sub>2</sub>/H<sub>2</sub>S environment,” in *CORROSION / 2008*, Houston, TX, 2008, paper no. 08344.
- [127] S. Standlee, K. D. Eford and D. Spiller, “Under deposit corrosion from iron sulfide,” in *CORROSION/2011*, Houston, TX, 2011, paper no. 11266.
- [128] K. Karan, A. K. Mehrotra and L. A. Behie, “On reaction kinetics for the thermal decomposition of hydrogen sulfide,” *AIChE J.*, vol. 45, pp. 383–389, 1999.

- [129] R. B. Slimane, F. S. Lau, R. J. DiHu, M. Khinkis, J. Bingue, A. Saveliev, A. Fridman and L. Kennedy, "Production of hydrogen by superadiabatic decomposition of hydrogen sulfide," in *Proc. of the 2002 U.S. DOE Hydrogen Program Review*, NREL/CP-610-32405, 2002.
- [130] T. Chivers and C. Lau, "The thermal decomposition of hydrogen sulfide over alkali metal sulfides and polysulfides," *Int. J. Hydrogen Energy*, vol. 10, pp. 21–25, 1985.
- [131] T. Chivers, J. B. Hyne and C. Lau, "The thermal decomposition of hydrogen sulfide over transition metal sulfides," *Int. J. Hydrogen Energy*, vol. 5, pp. 499–506, 1980.
- [132] V. Ruzic, M. Veidt and S. Nesic, "Protective iron carbonate films - Part 1: mechanical removal in single-phase aqueous flow," *Corrosion*, vol. 62, pp. 419–432, 2006.
- [133] G. Schmitt, M. Mueller and E. Strobel-Effertz, "Understanding localized CO<sub>2</sub> corrosion of carbon steel from physical properties of iron carbonate scales," in *CORROSION/1999*, Houston, TX, 1999, paper no. 38.
- [134] S. G. Clarke, "The use of inhibitors (with special reference to antimony) in the selective removal of metallic coatings and rust," *Trans. Electrochem. Soc.*, vol. 69, pp. 131–144, 1936.
- [135] *Standard Practice for Preparing, Cleaning, and Evaluating Corrosion Test Specimens*, ASTM G1 - 03, 2011

- [136] J. B. Sardisco and R. E. Pitts, "Corrosion of iron in an H<sub>2</sub>S-CO<sub>2</sub>-H<sub>2</sub>O system: mechanism of sulfide film formation and kinetics of corrosion reaction," *Corrosion*, vol. 21, pp. 245–253, 1965.
- [137] R. H. Hausler, "Contribution to the understanding of H<sub>2</sub>S corrosion," in *CORROSION/2004*, Houston, TX, 2004, paper no. 04732.
- [138] D. W. Shoesmith, P. Taylor, M. G. Bailey and D. G. Owen, "The formation of ferrous monosulfide polymorphs during the corrosion of iron by aqueous hydrogen sulfide at 21°C," *J. Electrochem. Soc.*, vol. 127, pp.1007–1015, 1980.
- [139] Z. A. Iofa, V. V. Batrakov and Cho-Ngok-Ba, "Influence of anion adsorption on the action of inhibitors on the acid corrosion of iron and cobalt," *Electrochim. Acta*, vol. 9, pp.1645–1653, 1964.
- [140] D. R. Morris, L. P. Sampaleanu and D. N. Veysey, "The corrosion of steel by aqueous solutions of hydrogen sulfide," *J. Electrochem. Soc.*, vol. 127, pp. 1228–1235, 1980.
- [141] H. Ma, X. Cheng, G. Li, S. Chen, Z. Quan, S. Zhao and L. Niu, "The influence of hydrogen sulfide on corrosion of iron under different conditions," *Corros. Sci.*, vol. 42, pp. 1669–1683, 2000.
- [142] Y. Zheng, J. Ning, B. Brown and S. Nešić, "Electrochemical model of mild steel corrosion in a mixed H<sub>2</sub>S/CO<sub>2</sub> aqueous environment in the absence of protective corrosion product layers," *Corrosion*, vol. 71, pp. 316–325, 2015.
- [143] A. J. Devey, "Computer modeling studies of mackinawite, greigite and cubic FeS," Ph.D. dissertation, University College London, London, England, 2009.

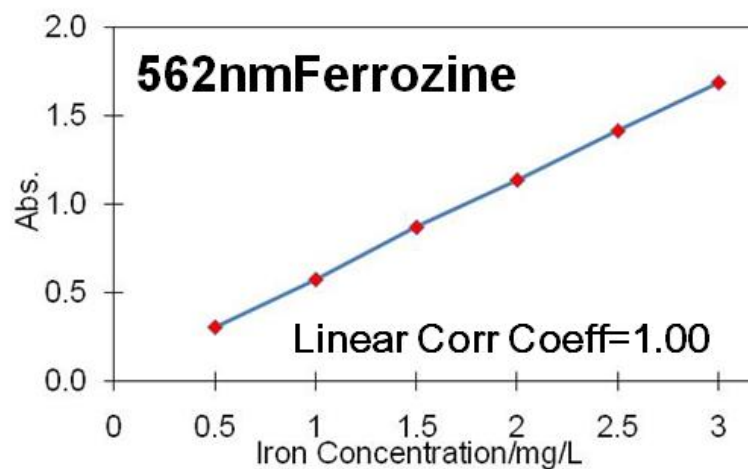
- [144] C. Pearce, R. Patrick and D. Vaughan, "Electrical and magnetic properties of sulfides," *Rev. Mineral. Geochem.*, vol. 61, pp. 127–180, 2006.
- [145] R. Schieck, A. Hartmann, S. Fiechter, R. Konenkamp and H. Wetzel, "Electrical properties of natural and synthetic pyrite ( $\text{FeS}_2$ ) crystals," *J. Mater. Res.*, vol. 5, pp. 1567–1572, 1990.
- [146] M. Caban-Acevedo, M. S. Faber, Y. Tan, R. J. Hamers and S. Jin, "Synthesis and properties of semiconducting iron pyrite ( $\text{FeS}_2$ ) nanowires," *Nano Letters*, vol. 12, pp. 1977–1982, 2012.
- [147] P. K. Abratis, R. A. D. Patrick and D. J. Vaughan, "Variations in the compositional, textural and electrical properties of natural pyrite: a review," *Int. J. Miner Process*, vol. 74, pp. 41–59, 2004.
- [148] "Property Information: Resistivity," <http://www-materials.eng.cam.ac.uk/mpsite/properties/non-IE/resistivity.html>. Accessed 19 Sep. 2016.
- [149] J. Huang, "Mechanistic study of under deposit corrosion of mild steel in aqueous carbon dioxide solution," Ph.D. dissertation, Ohio University, Athens, OH, 2013.
- [150] B. Wilson, "Sour gas corrosion failures (Case Study Examples)," presented at Shell Calgary Sulfur Meeting, Calgary, AB, 2002.
- [151] J. Ning, "Iron sulfide under deposit corrosion in  $\text{CO}_2$  and  $\text{H}_2\text{S}$  environments," presented at Institute for Corrosion and Multiphase Technology CCJIP Advisory Board Meeting, Athens, Ohio, March 2014.
- [152] H. P. Hack, *Corrosion Testing Made Easy: Galvanic Corrosion Test Methods*, Houston, TX: NACE International, 1993.

- [153] *CRC Handbook of Chemistry and Physics*, 70<sup>th</sup> ed., R. C. Weast, Ed., Boca Raton, FL, 1999.
- [154] A. V. Wolf, *Aqueous Solutions and Body Fluids: Their Concentrative Properties and Conversion Tables*, New York: Harper and Row, 1966.
- [155] Wikipedia, "Daniell cell," Internet: [http://en.wikipedia.org/wiki/Daniell\\_cell](http://en.wikipedia.org/wiki/Daniell_cell).
- [156] K. Addis, M. Singer and S. Nestic, "A corrosion model for oil and gas mild steel production tubing," *Corrosion*, vol. 70, pp. 1175-1176, 2014.
- [157] N. R. Rosli, Y. Choi and D. Young, "Impact of oxygen ingress in CO<sub>2</sub> corrosion of mild steel," in *CORROSION/2014*, Houston, TX, 2014, paper no. 4299.
- [158] "FerroVer Method 8008 (Powder Pillows or AccuVac Ampuls)," [www.hach.com/asset-get.download-en.jsa?id=7639983612](http://www.hach.com/asset-get.download-en.jsa?id=7639983612). Accessed 19 Sep. 2016.
- [159] "FerroZine Method 8147," [www.google.com/url?sa=t&rct=j&q=&esrc=s&source=web&cd=2&cad=rja&uact=8&ved=0CCUQFjAB&url=http%3A%2F%2Fwww.hach.com%2Fasset-get.download.jsa%3Fid%3D7639984341&ei=7FOUVJbQINP2yQTa\\_YCoAw&usg=AFQjCNHZLaKqDVoxlai98w2Rn6VjlQNDgQ&sig2=6YNkrDPZXA9pO5y75jUobQ&bvm=bv.82001339,d.ZGU](http://www.google.com/url?sa=t&rct=j&q=&esrc=s&source=web&cd=2&cad=rja&uact=8&ved=0CCUQFjAB&url=http%3A%2F%2Fwww.hach.com%2Fasset-get.download.jsa%3Fid%3D7639984341&ei=7FOUVJbQINP2yQTa_YCoAw&usg=AFQjCNHZLaKqDVoxlai98w2Rn6VjlQNDgQ&sig2=6YNkrDPZXA9pO5y75jUobQ&bvm=bv.82001339,d.ZGU). Accessed 19 Sep. 2016.
- [160] "American mineralogist crystal structure database," <http://rruff.geo.arizona.edu/AMS/amcsd.php>. Accessed 19 Sep. 2016.

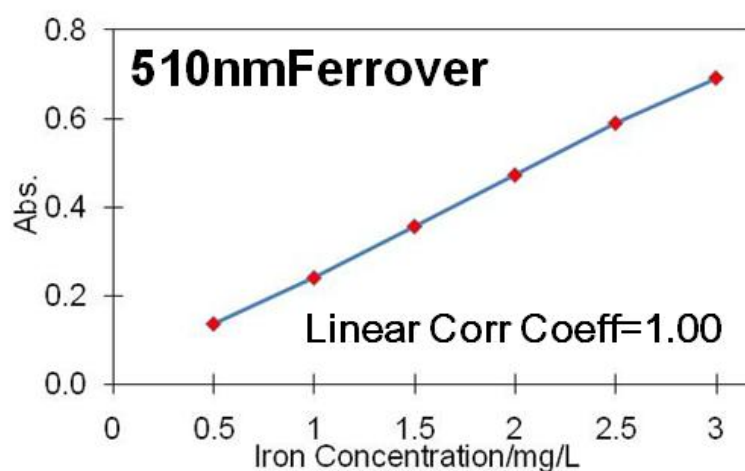
## APPENDIX A: ANALYTICAL TECHNIQUES

### A.1 Measurement of Ferrous Ion Concentration in Solution

Iron concentration in solution was measured using a spectrophotometer. Both FerroZine<sup>®</sup> and FerroVer<sup>®</sup> reagents were used to determine iron concentration in solution. Multipoint standard curves were developed to improve iron concentration measurement accuracy, as shown in Figure 153. It should be noted that measurements using the FerroVer<sup>®</sup> reagent were measured at wavelength of 510 nm, and all measurements using the FerroZine<sup>®</sup> reagent were done at 562 nm. All measurements were conducted using these two standard curves. The procedure for determining iron concentration using FerroVer<sup>®</sup> reagent was developed by referring to Method 8008 [158], provided by the manufacturer. The procedure for using FerroZine<sup>®</sup> reagent was made by referring to Method 8147 [159].



(a)



(b)

Figure 153. Multipoint standard curve plots: (a) for FerroZine<sup>®</sup> reagent; (b) for FerroVer<sup>®</sup> reagent.

### A.1.1 Procedure for Testing Iron Concentration in the Solution Using FerroVer<sup>®</sup> Iron Reagent

1. Turn on and warm up the spectrophotometer for 30 minutes.
2. Prepare samples: Fill each of two sample jars with 10 ml solution. Add one package of FerroVer<sup>®</sup> iron reagent into one of the two jars, swirl the jar for 10 seconds then wait for at least 3 minutes to allow the reagent fully react. The solution will become orange. Fill a cuvette with one-half to three-quarters full of the blank solution. Wipe the cuvette with a

cotton cloth or towel to remove any fingerprints, place the cuvette in the cell holder, and close the lid.

3. Choose a test type. Press Test, and Test types screen appears, highlight Standard Curve and press Enter. The Standards Curve screen appears. If the Standards Curve screen is already there, you can skip the step.

4. Choose a standard curve. Press Stored Tests to display a list of standard curves, choose the standard curve you would like to use and press Enter to load the standard curve. If you use Ferrover as iron reagent, you need to choose 20100927 FERR3ppm as the standard curve. If the Standard Curve Screen with the standard curves you are going to use is already there, you can skip the step.

5. Press Run Test, and then press Measure Blank to measure the blank solution.

6. Take out the blank solution cuvette from cell holder. Fill another cuvette with one-half to three-quarters full of the orange sample solution. Wipe the cuvette with a cotton cloth or towel to remove any fingerprints, place the cuvette in the cell holder, and close the lid.

7. Press Measure Samples to measure the sample iron concentration.

8. After the analysis is completed, turn off the spectrophotometer. Clean the spectrophotometer using a soft tissue.

### **A.1.2 Procedures for Using FerroZine® Iron Reagent**

NOTE: Any contact with FerroZine MUST BE DONE INSIDE THE VENT HOOD.

FerroZine has a health rating of 3 because it is TOXIC if INHALED. It can also be absorbed through the skin or damage your eyes. Extreme care must be taken to avoid ALL possible contact with FerroZine.

1. Turn on spectrophotometer 30 minutes before it is needed for use.
2. You must need to wear safety glasses, latex gloves (or equivalent), and a lab coat for the procedure. You will need two of 50 ml screw top vials with tops, two test tubes with rubber stopper, a pipette and several pipette tips, sodium bicarbonate, pH test paper, and two 100 ml beaker with some cold water in it.
3. Use vials with a screw top lid. Fill 2 vials with 25 ml test solution for testing and 10 ml test solution for reference.
4. In fume hood: Open one package of FerroZine and add into the vial of testing sample, then put the top on the vial immediately. Shake the vial for 10 seconds, and then wait 5 minutes. Fill a tube with testing solution from the vial, and put rubber stopper in the tube immediately. Dissolve some sodium bicarbonate in the extra cold water in one 100 ml beaker to prepare alkali solution with pH value between 6 and 9, then rinse FerroZine container for three times with the alkali solution. Dispose of empty container as normal trash.
5. Fill another tube with reference sample.
6. Take these two tubes for test to spectrophotometer.
7. In fume hood: After testing, fill all the testing sample that mixed with FerroZine into another 100 ml beaker, and dilute to 3 to 5 times the volume with cold water. Adjust to a pH value between 6 and 9 with sodium bicarbonate.
8. Take these two beakers in procedure 4 and 7 to normal sink. Open cold water tap completely, slowly pour the two beakers of reacted solution to the drain. Allow cold water to run for at least 5 minutes to completely flush the reacted solution.

## **A.2 Sample Composition Analysis**

### **A.2.1 X-ray Diffraction on Phase Identification**

After suitable preparation, samples were taken for XRD analysis using Rigaku Ultima IV X-ray diffractometer. The X-ray generator is Cu K $\alpha$  to generate 0.15405 nm X-ray at 40 kV and 44mA conditions. Data was collected ranging from 5° to 80° (2 $\theta$ ) with a scanning rate 1°/min. XRD pattern in terms of intensity (CPS) vs. 2 $\theta$  (°) was plotted after each test and compared with reference cards obtained from RRUFF™ database [160] for phase identification.

### **A.2.2 X-ray Diffraction on Quantitative Analysis**

Polymorphous iron sulfides were frequently detected as corrosion products in this study. A quantitative analysis of those polymorphous iron sulfides is needed to better understand the formation and transformation of iron sulfides during each experiment. The quantitative analysis on each sample was done using XRD data, following a reference intensity ratio (RIR) methodology, and operating in the software PDXL carried by XRD equipment.

## APPENDIX B: SURFACE PH MEASUREMENT

### B.1 Experimental

#### B.1.1 Apparatus

The mesh-capped flat pH probe [109] was developed to improve the estimation of surface pH at a mild steel surface, and is shown in Figure 154.

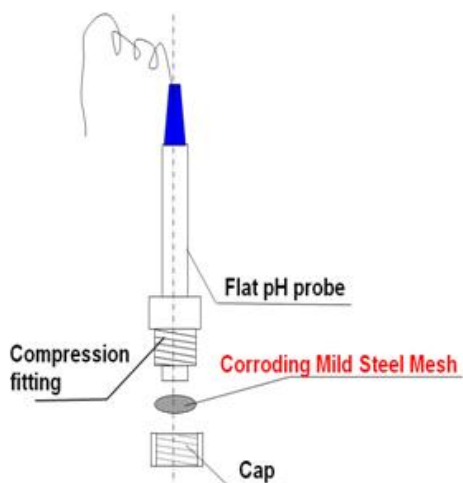


Figure 154. Mesh-capped flat pH probe.

#### B.1.2 Material

A SEM image of the mesh used for measuring surface pH is shown in Figure 155 and the properties of mesh are shown in Table 30.

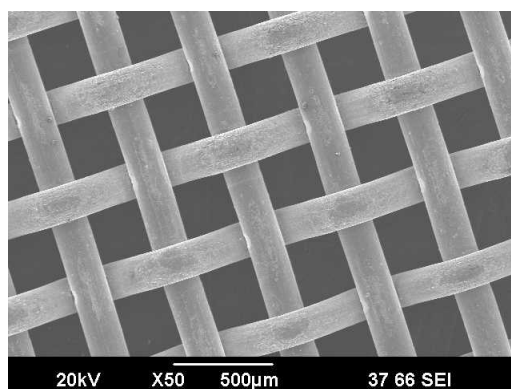


Figure 155. A SEM image of mesh.

Table 30 Properties of the mesh.

Steel Type	Mild Steel
Mesh Size	60 x 60 holes/in <sup>2</sup>
Square Size	0.009 in
Wire Diameter	0.0075 in
Mesh Open Area	30.5 %

### B.1.3 Procedure

Prior to each test, N<sub>2</sub> gas was sparged into the solution in the glasscell for a few hours to deoxygenate the solution until pH stabilization. Then, CO<sub>2</sub> gas or H<sub>2</sub>S/N<sub>2</sub> gas at a desired concentration was sparged into solution until solution pH stabilized. Deoxygenated NaOH or HCl solution was used to adjust solution pH to a desired value. Before each experiment, the mesh was soaked in 0.1 M HCl solution for 10 minutes to remove oxides formed at mesh surface. After cleaning in acid, the mesh was rinsed thoroughly by deoxygenated deionized water and deoxygenated isopropanol, and blown dry using nitrogen gas. The mesh was then mounted into the compression fitting shown in Figure 154 and immersed into solution for measuring surface pH. The pH at the

corroding mesh surface was estimated by using this mesh capped flat pH probe at various conditions. Table 31 shows the test matrix of this series of experiments.

Table 31 Test matrix.

Description	Parameter
Solution	DI water with 1 wt.% NaCl
Temperature	25°C
Total pressure	1.0 bar
Stirring Speed	0, 200, 400 rpm
Purged Gas	CO <sub>2</sub> , N <sub>2</sub> , H <sub>2</sub> S/N <sub>2</sub>
Bulk pH	3.0, 4.0, 5.0

## B.2 Results and Discussion

### *B.2.1 Estimation of Surface pH in an H<sub>2</sub>S-H<sub>2</sub>O-Fe System at Stagnant Condition*

#### 100 ppm H<sub>2</sub>S / N<sub>2</sub>

The surface pH in a 100 ppm H<sub>2</sub>S (in gas phase) saturated solution was measured at different bulk pH values, and is shown in Figure 156, Figure 157, and Figure 158, respectively. The surface pH was measured at about 3 units higher than the bulk pH, which indicates only one of thousands of protons was detected near the corroding steel surface at stagnant conditions.

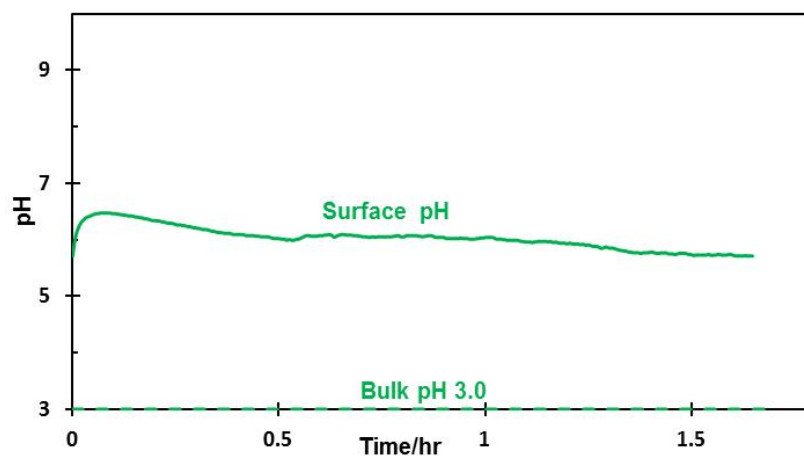


Figure 156. Surface pH with 100 ppm H<sub>2</sub>S / N<sub>2</sub> at bulk pH 3.0.

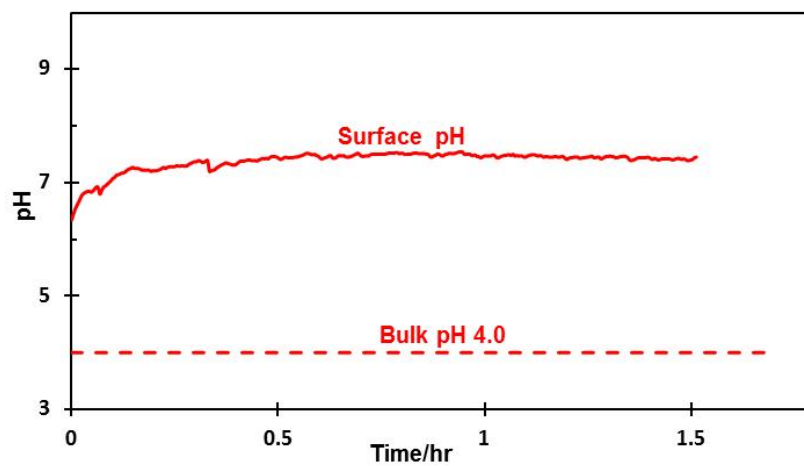


Figure 157. Surface pH with 100 ppm H<sub>2</sub>S / N<sub>2</sub> at bulk pH 4.0.

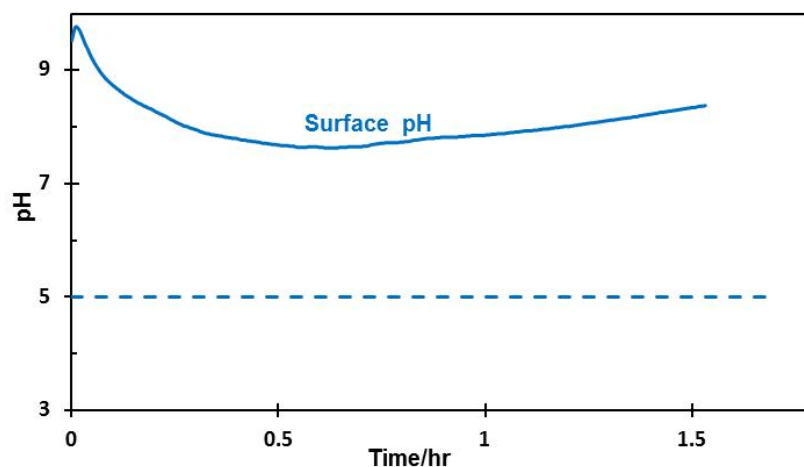


Figure 158. Surface pH with 100 ppm H<sub>2</sub>S / N<sub>2</sub> at bulk pH 5.0.

### 1% H<sub>2</sub>S / N<sub>2</sub>

Similarly, surface pH values measured in a 1% H<sub>2</sub>S / N<sub>2</sub> saturated solution at different bulk pH values are shown in Figure 159, Figure 160, and Figure 161. The measured surface pH was observed to be 2 units higher than bulk pH, suggesting that only one of hundreds protons was detected near the corroding steel surface at stagnant conditions.

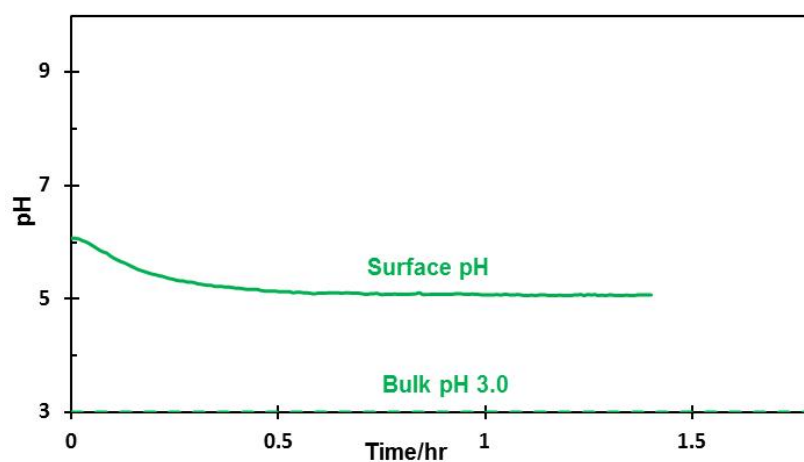


Figure 159. Surface pH with 1% H<sub>2</sub>S / N<sub>2</sub> at bulk pH 3.0.

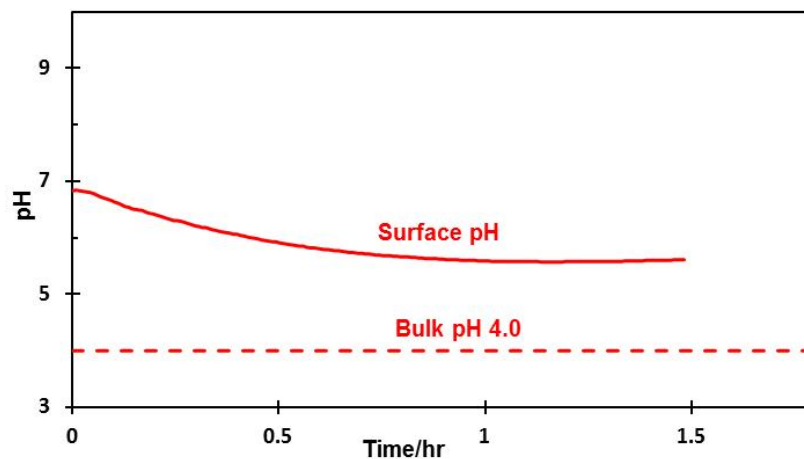


Figure 160. Surface pH with 1% H<sub>2</sub>S / N<sub>2</sub> at bulk pH 4.0.

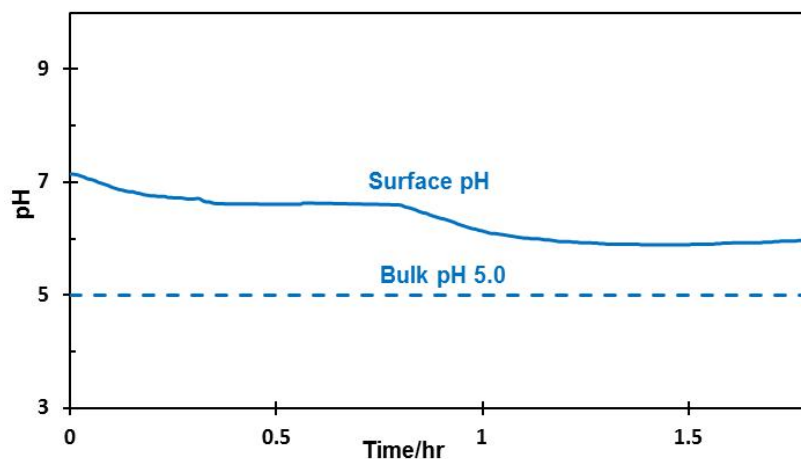


Figure 161. Surface pH with 1% H<sub>2</sub>S / N<sub>2</sub> at bulk pH 5.0.

### 10% H<sub>2</sub>S / N<sub>2</sub>

The surface pH in a 10% H<sub>2</sub>S / N<sub>2</sub> saturated solution was measured at different bulk pH, and is shown in Figure 162, Figure 163, and Figure 164. The measured surface pH was about 1 unit higher than bulk pH, indicating only one of ten protons was detected near the corroding steel surface at stagnant conditions.

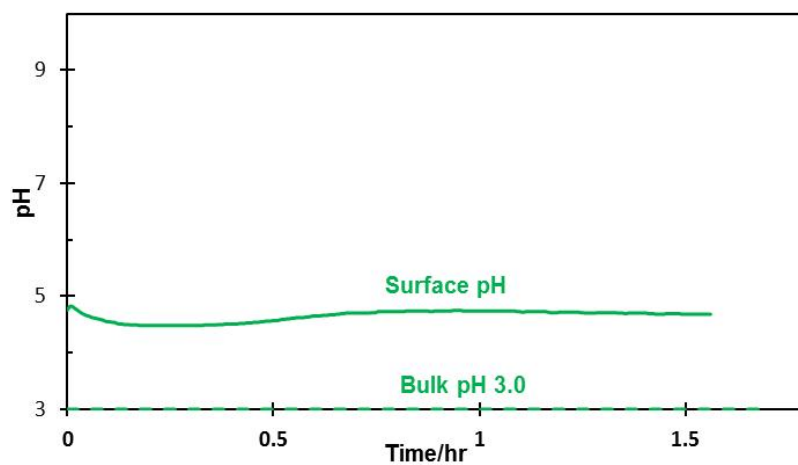


Figure 162. Surface pH with 10% H<sub>2</sub>S / N<sub>2</sub> at bulk pH 3.0.

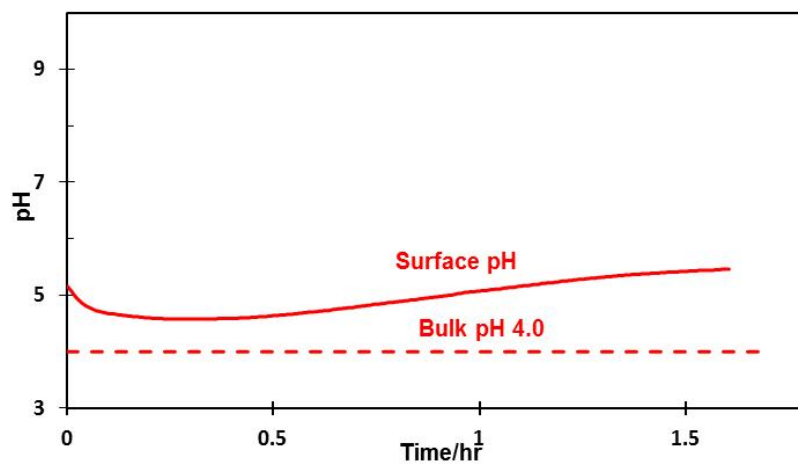


Figure 163. Surface pH with 10% H<sub>2</sub>S / N<sub>2</sub> at bulk pH 4.0.

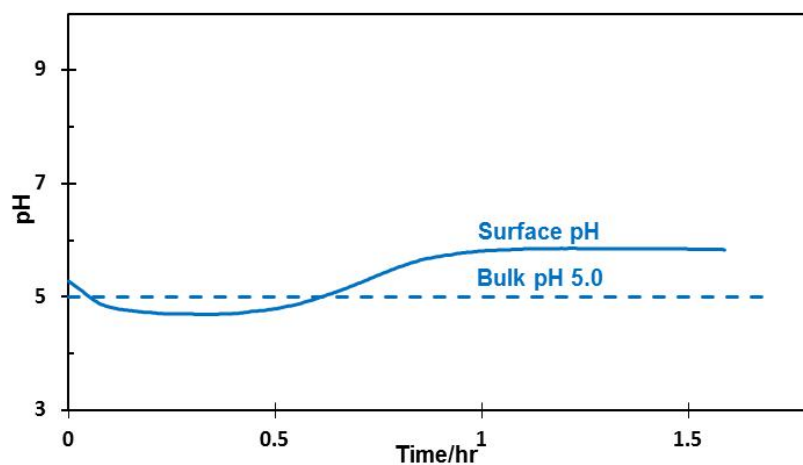


Figure 164. Surface pH with 10% H<sub>2</sub>S / N<sub>2</sub> at bulk pH 5.0.

### Summary

The summary of measured surface pH at different concentrations of H<sub>2</sub>S at bulk pH 4.0 is shown in Figure 165. It is observed that surface pH decreased with the increase in pH<sub>2</sub>S. The increase in pH<sub>2</sub>S leads to an increase in the concentrations of species that contribute protons, as shown in Reactions (1), (3) and (5), hence, more protons could be detected at the corroding steel surface.

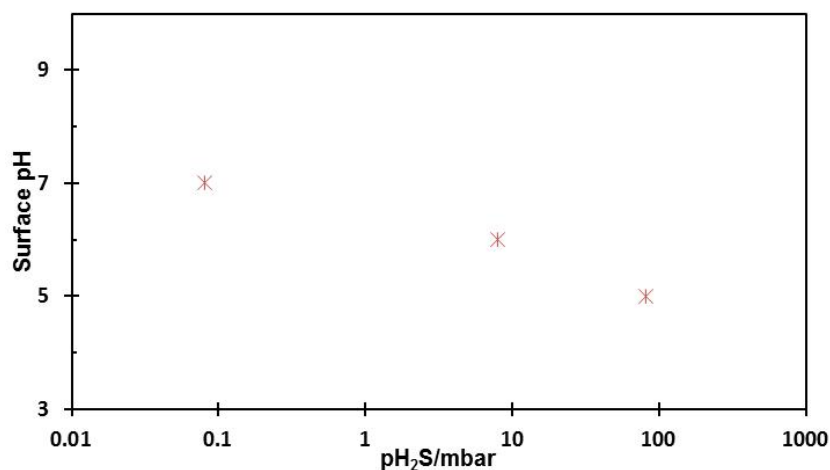


Figure 165. Summary of measured surface pH at bulk pH 4.0.

### B.2.2 Surface pH in an H<sub>2</sub>S-H<sub>2</sub>O-Fe System Affected by Turbulent Flow

A stirring bar with different stirring speeds was used to simulate various flow conditions. The stirring speed was 0 initially, and then changed to 200 rpm, 400 rpm, 200 rpm and 0 during each experiment. Surface pH of various systems (N<sub>2</sub>, CO<sub>2</sub>, 100 ppm H<sub>2</sub>S/N<sub>2</sub>, 1% H<sub>2</sub>S/N<sub>2</sub>, and 10% H<sub>2</sub>S/N<sub>2</sub>) at different stirring speeds were measured and are shown in Figure 166, Figure 167, Figure 168, Figure 169, and Figure 170, respectively. Repeated tests are shown as blue curves in Figure 166, Figure 167, and Figure 168, and show the high reliability of this surface pH measurement technique.

All the results showed that an increase in flow decreased the difference between surface pH and bulk pH due to enhanced mass transfer. Surface pH was found approached the bulk pH with 400 rpm stirring speed, so in turbulent flow conditions, it should be sufficient to measure the bulk pH and assume the near surface pH is the same.

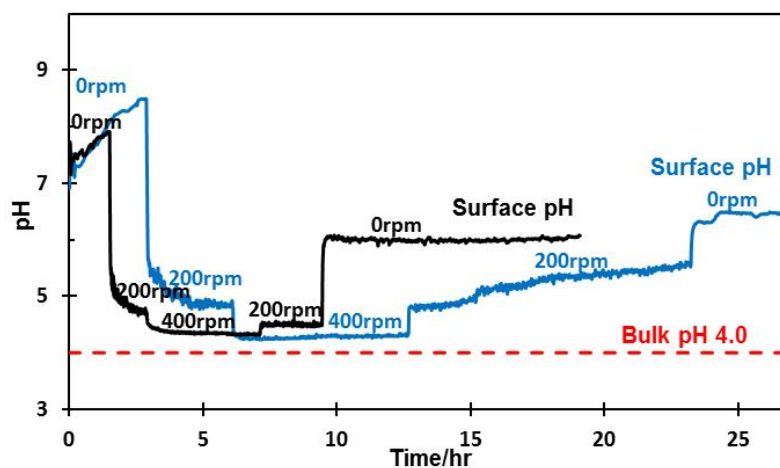


Figure 166. Surface pH affected by flow in N<sub>2</sub> purged solution.

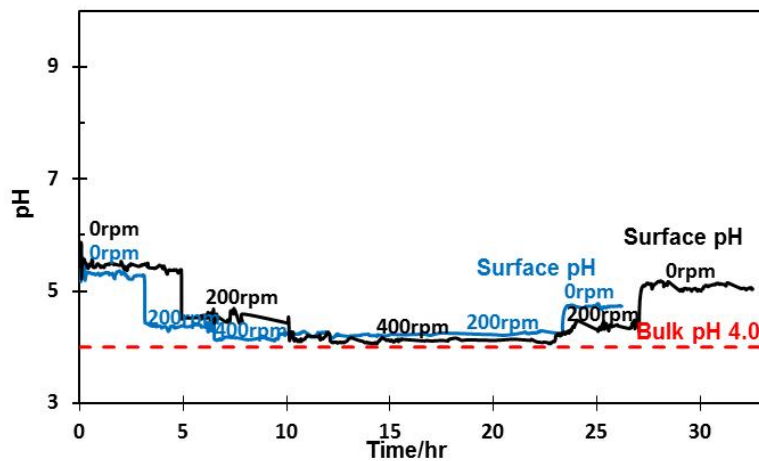


Figure 167. Surface pH affected by flow in CO<sub>2</sub> purged solution.

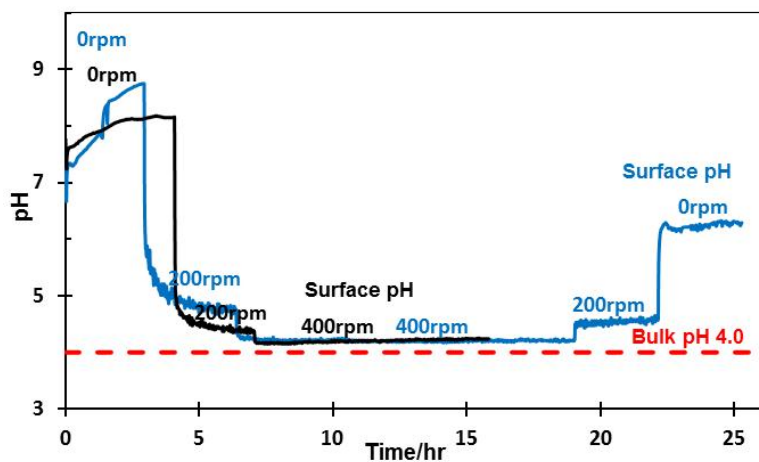


Figure 168. Surface pH affected by flow in 100 ppm H<sub>2</sub>S / N<sub>2</sub> purged solution.

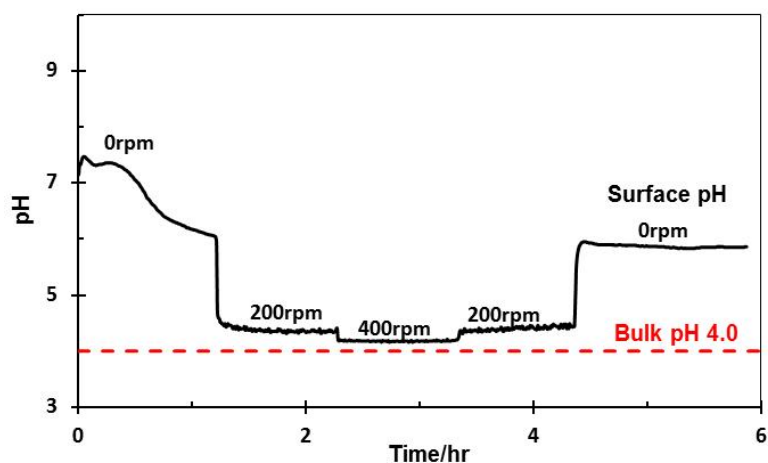


Figure 169. Surface pH affected by flow in 1% H<sub>2</sub>S / N<sub>2</sub> purged solution.

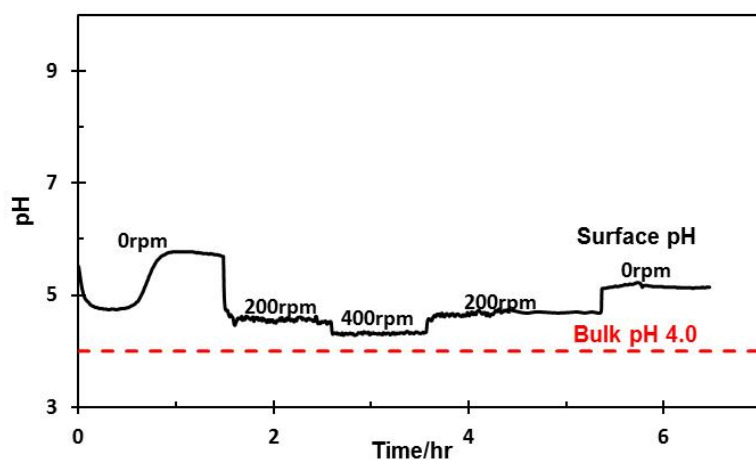


Figure 170. Surface pH affected by flow in 10 % H<sub>2</sub>S / N<sub>2</sub> purged solution.

### B.3 Conclusions

pH value at the corroding steel surface was explored by using a mesh-capped flat pH probe. The surface pH values measured in experiments could be very different from the pH value in bulk solution. Conclusions can be drawn as below.

- Measured surface pH decreased with the increase in pH<sub>2</sub>S.
- Increase in turbulent flow decreased the difference between surface pH and bulk pH due to enhanced mass transfer.

- Surface pH was found approaching the bulk pH with 400rpm stirring speed.
- In turbulent flow conditions, it is sufficient to measure the bulk pH and assume the surface pH is the same.

## APPENDIX C: VALIDATION OF POURBAIX DIAGRAMS BY ELECTROCHEMICAL POLARIZATION

Similar to the verification strategy of an artificial change in solution pH, corrosion potential of a mild steel sample was polarized according to predictions made by the Pourbaix diagrams, and the resultant corrosion products on the sample surface were investigated.

### C.1 Experimental

The schematic of experimental apparatus is shown in Figure 171. An API 5L X65 special sample and a mild steel mesh sample were made in the laboratory, with a Teflon<sup>(3)</sup> coating used to cover the solder joints. Electrochemical polarization was applied to the X65 special sample to study the iron sulfides formed at the steel surface under polarization. The electrochemical polarization was applied to the mild steel mesh as well in order to measure surface pH at the corroding mesh surface under polarization by using a mesh-capped flat pH probe.

The experimental glass cell setup is shown in Figure 172. Experiments were performed in a 2-liter glass cell filled with 1 wt. % NaCl electrolyte at atmospheric pressure. The OCP of the X65 special sample was monitored using a Potentiostat throughout the experiment. The X65 special sample was used as the working electrode. A platinum wire was used as the counter electrode. A saturated silver-silver chloride (Ag / AgCl) electrode connected to the cell externally through a Luggin capillary was used as the reference electrode. A magnetic stirring bar with a 400 rpm stirring speed was used to mix solution during the experiment. A mesh capped pH probe was used to measure

---

<sup>(3)</sup> a trade name

surface pH at steel mesh surface under polarization and a regular pH probe was used to monitor bulk solution pH.

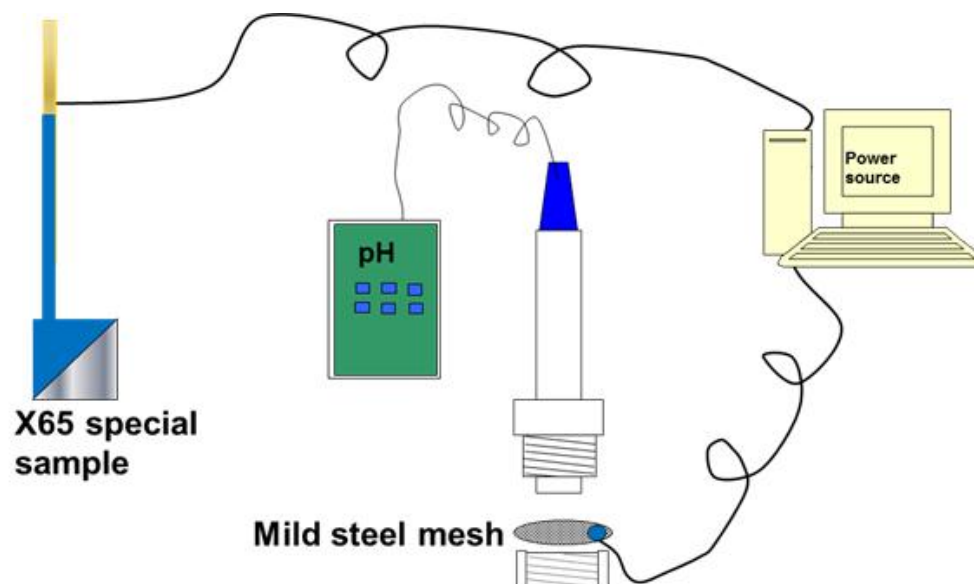


Figure 171. Schematic of experimental apparatus.

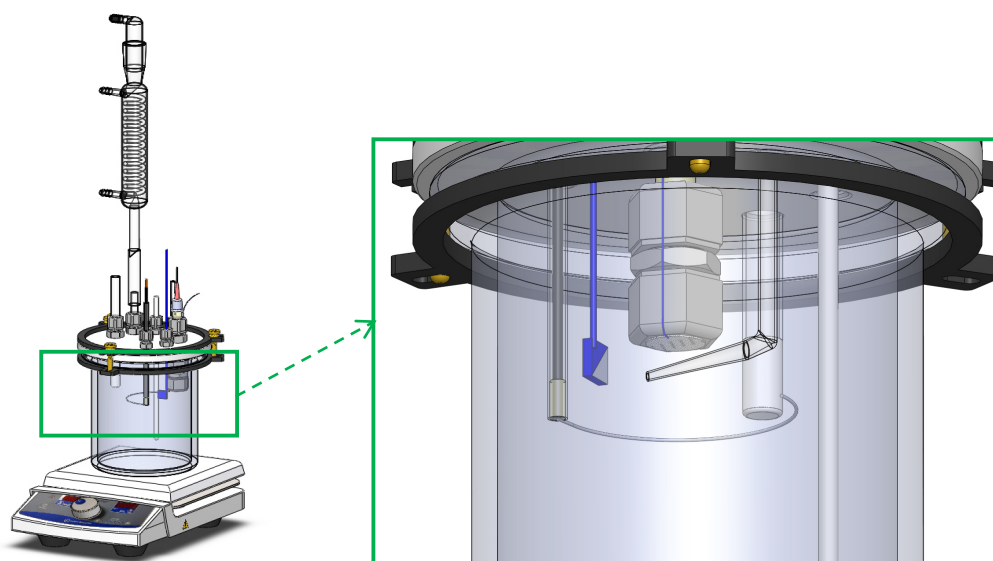
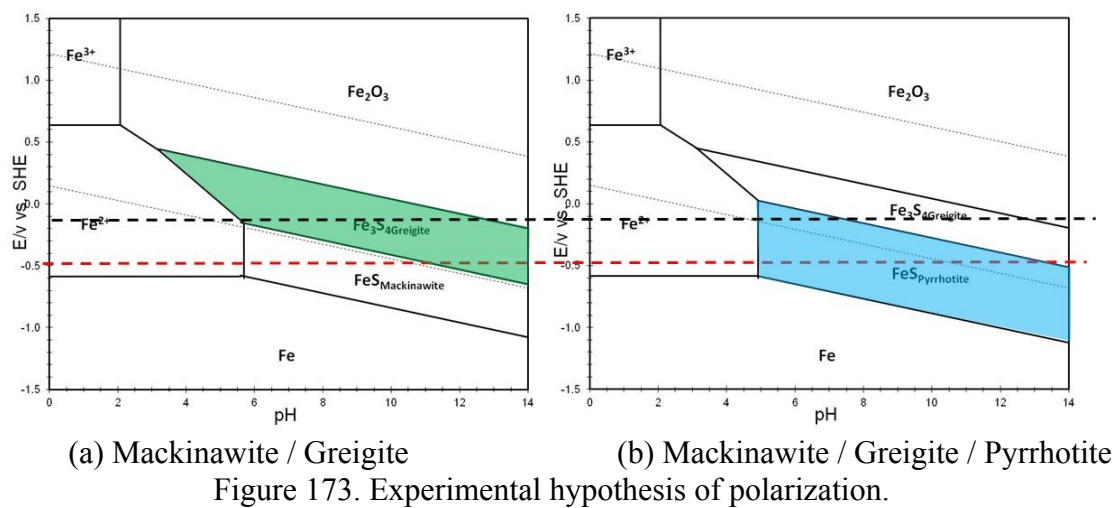


Figure 172. Experimental glass cell setup.

## C.2 Experimental Hypothesis

General corrosion potential of a mild steel sample exposed to a typical sour environment in experiments is shown as a red dashed line in Figure 173. Mackinawite is usually the dominant corrosion product in most of sour corrosion experiments. If the steel sample is polarized to a higher corrosion potential, shown as the black dashed line, a different iron sulfide, such as greigite (green area) or pyrrhotite (blue area) at pH 6.0 probably can form.



## C.3 Results and Discussion

### C.3.1 Electrochemical Polarization on Mesh

Experimental conditions for electrochemical polarization were sought to obtain a stable pH with polarization. Both stable surface pH and bulk pH were observed at the conditions used in Figure 174 ( $p_{\text{H}_2\text{S}} = 0.01$  bar, stirring 400rpm, initial bulk pH 6.0). Figure 174 shows that bulk pH was stable throughout experiment, and surface pH was exactly the same, with the bulk pH at the beginning but lower than bulk pH after two

hours due to precipitation of iron sulfide at the corroding mesh surface. Surface pH was stable at the end of experiment when the precipitation and dissolution of iron sulfides reached equilibrium at the mesh surface.

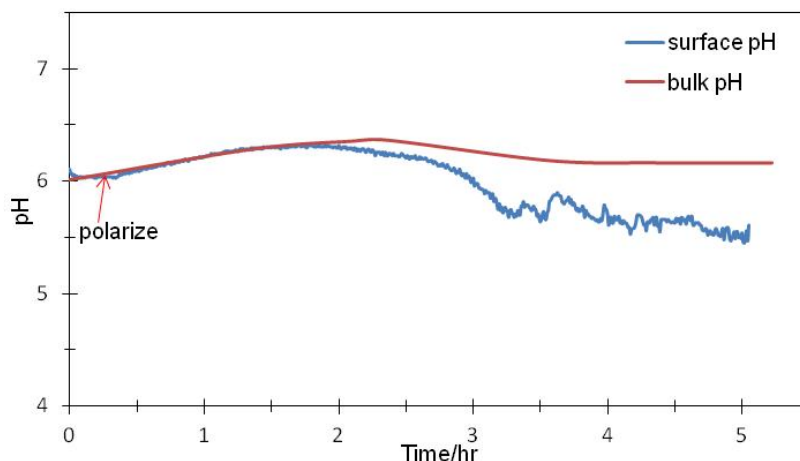


Figure 174. Surface pH with polarization at mesh at  $-0.35$  V vs. Ag/AgCl (Sat'd KCl) (Polarized  $0.36$  V above OCP,  $25$  °C,  $p_{\text{H}_2\text{S}} = 0.01$  bar, stirring  $400$  rpm, initial bulk pH  $6.0$ )

### C.3.2 Electrochemical Polarization on Mesh and Sample

#### Polarize Mesh/Sample Combination to $-0.35$ V vs. Ag/AgCl (Sat'd KCl)

Electrochemical polarization was applied to a mild steel mesh, and was verified with a stable surface pH during the polarization. Therefore, the same experimental conditions were used to apply electrochemical polarization to a mild steel mesh and a mild steel sample together. Bulk pH and surface pH were monitored throughout experiment, as shown in Figure 175. Bulk pH was quite stable. However, surface pH was lower than bulk pH due to precipitation at the mesh surface. Moreover, surface pH was stable after approximately one hour of exposure.

SEM, EDX, and XRD were conducted on the X65 steel sample to analyze the nature of corrosion products formed on the steel surface. Surface morphologies (SEM images) and compositional analysis (EDS) are shown in Figure 176, which shows a very thin corrosion product layer containing iron sulfide. It is understood that the steel sample was undermined significantly due to the electrochemical polarization. Figure 177 shows the XRD pattern of the layer formed on the steel sample. The blue curve indicates an XRD pattern of a blank X65 special steel sample prior to an experiment, and the black curve shows an XRD pattern of the steel sample after the experiment. Pyrrhotite phase was detected on the steel sample surface. Compared to previous experimental findings that pyrrhotite usually takes a couple of days to form, the formation of pyrrhotite was highly accelerated, occurring within hours with polarization. However, mackinawite was not detected, which is explained that mackinawite was transformed to thermodynamically stable pyrrhotite with the electrochemical polarization.

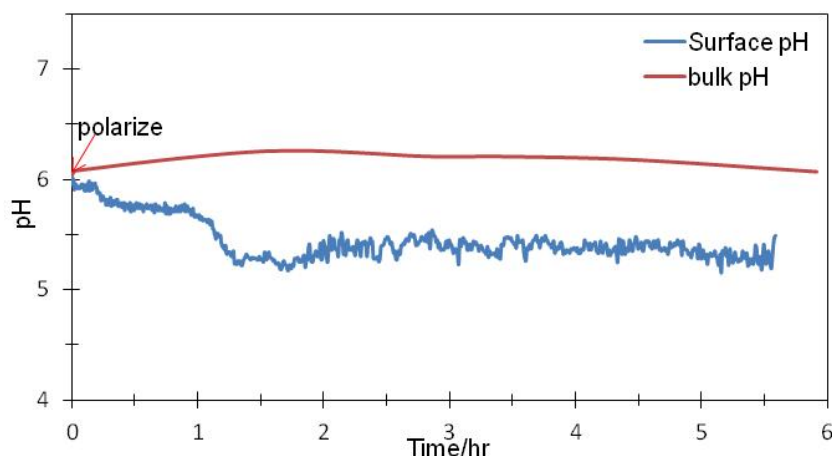


Figure 175. Surface pH with polarization of mesh/sample at  $-0.35$  V vs. Ag/AgCl (Sat'd KCl) (Polarized  $0.36$  V above OCP,  $p\text{H}_2\text{S}=0.01$  bar  $\text{H}_2\text{S}$ , 400 rpm, initial bulk pH 6.0).

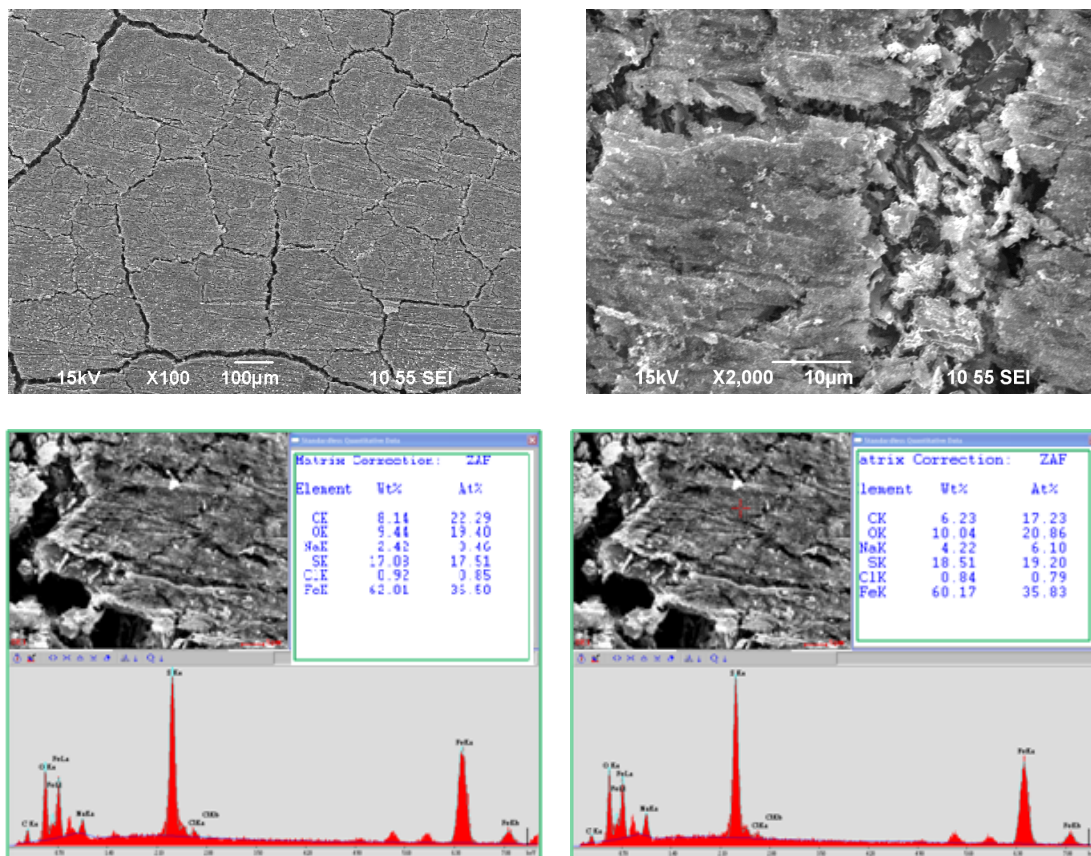


Figure 176. Surface morphology (SEM) and composition analysis (EDX) of steel sample.

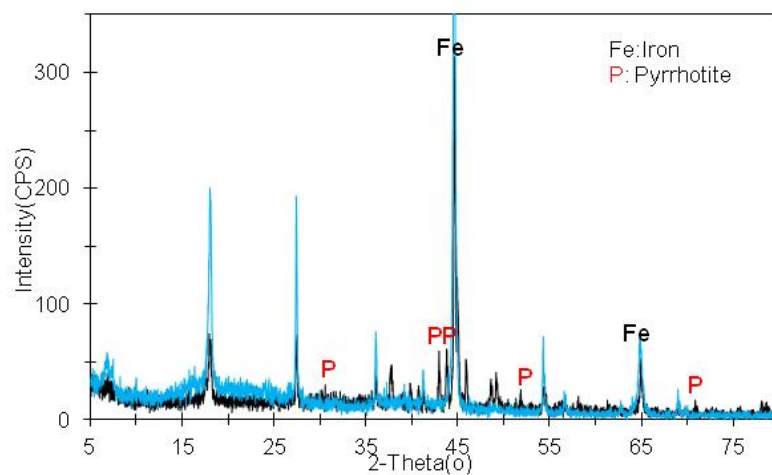


Figure 177. XRD pattern of corrosion product layer formed on steel sample.

Verification of the Pourbaix diagrams is shown in Figure 178 and Figure 179 as related to experimental conditions in the beginning and at the end of the experiment.

Figure 178 shows the verification of the Pourbaix diagrams generated for the beginning of experiment. A lot of ferrous ions were released from the steel surface at the beginning of experiment due to polarization, hence  $[\text{Fe}^{2+}]$  was assumed to be 10 ppm to generate these Pourbaix diagrams. Both the potential applied on the steel sample and the surface pH values measured are shown as the red dashed lines in Figure 178. IR drop is considered because of the presence of solution resistance and high current in this case. The potential after correcting for the IR drop is shown as blue dashed line in Figure 178. The intersection points of the surface pH and the corrected corrosion potential (shown as red dots) are located in the  $\text{Fe}^{2+}$  area in Figure 178 (a) (if only mackinawite and greigite are considered) and in the pyrrhotite area shown in Figure 178 (b) (when pyrrhotite is considered), indicating corrosion products in the beginning are predicted to be  $\text{Fe}^{2+}$  and pyrrhotite by the Pourbaix diagrams. Experimental findings agree well with this prediction made by the Pourbaix diagrams for the beginning of the experiment.

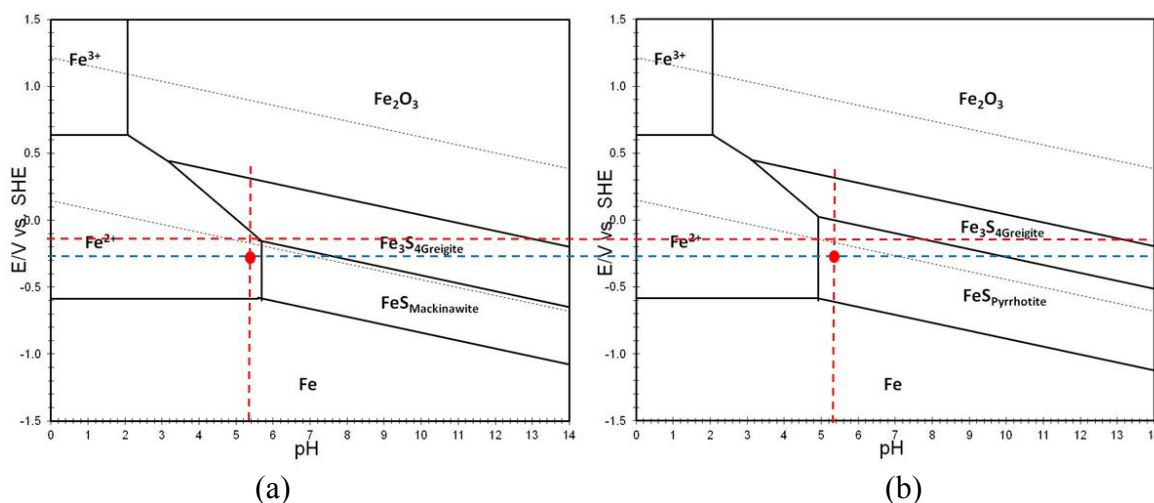


Figure 178. Verification of Pourbaix diagrams generated according to experimental conditions at the beginning of experiment (a) Mackinawite / Greigite; (b) Mackinawite / Greigite / Pyrrhotite (25 °C,  $\text{pH}_2\text{S} = 0.01\text{bar}$ ,  $[\text{Fe}^{3+}] = 10^{-6}\text{M}$ ,  $[\text{Fe}^{2+}] = 10\text{ppm}$ ).

Bulk  $[\text{Fe}^{2+}]$  was measured as 0.8 ppm at the end of experiment. Accordingly, Pourbaix diagrams were generated, and are shown in Figure 179. The intersection point of the surface pH and the corrected corrosion potential is very close to the equilibrium line between ferrous ion and pyrrhotite in Figure 179 (b), indicating the system was at a quasi-equilibrium state at the end of the experiment. In addition, the stable surface pH at the end of experiment in Figure 175 also suggests a state of equilibrium for pyrrhotite at the end of experiment. Therefore, the Pourbaix diagrams generated according to the experimental conditions at the end of experiment were verified by experimental results.

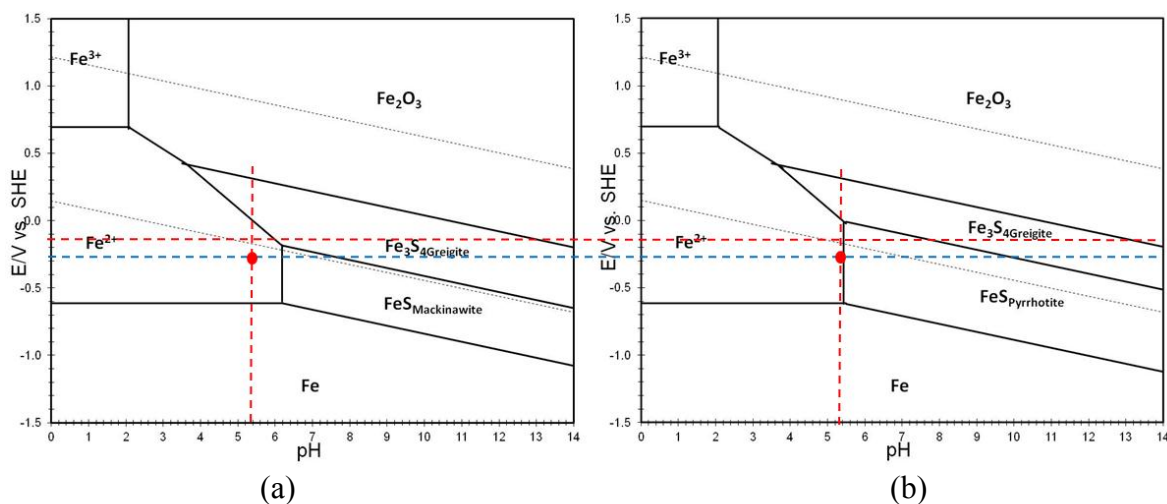


Figure 179. Verification of Pourbaix diagrams generated according to experimental conditions at the end of experiment (a) Mackinawite / Greigite; (b) Mackinawite / Greigite / Pyrrhotite (25 °C,  $\text{pH}_2\text{S} = 0.01\text{bar}$ ,  $[\text{Fe}^{3+}] = 10^{-6}\text{M}$ ,  $[\text{Fe}^{2+}] = 0.8\text{ppm}$ ).

#### Polarize Mesh/Sample Combination to -0.10 V vs. Ag/AgCl (Sat'd KCl)

Electrochemical polarization was applied to a higher value, -0.10 V vs. Ag/AgCl (Sat'd KCl), in order to bring potential into the greigite region according to the Pourbaix diagrams. The surface pH and bulk pH during this experiment is shown in Figure 180. Similarly, bulk pH was stable, and surface pH was lower than bulk pH. However, surface

pH was observed to be stable ( $\text{pH } 5.6 \pm 0.2$ ) after a few hours. Figure 181 shows surface morphologies and composition analysis by using EDX. Pyrrhotite was detected by XRD in Figure 182.

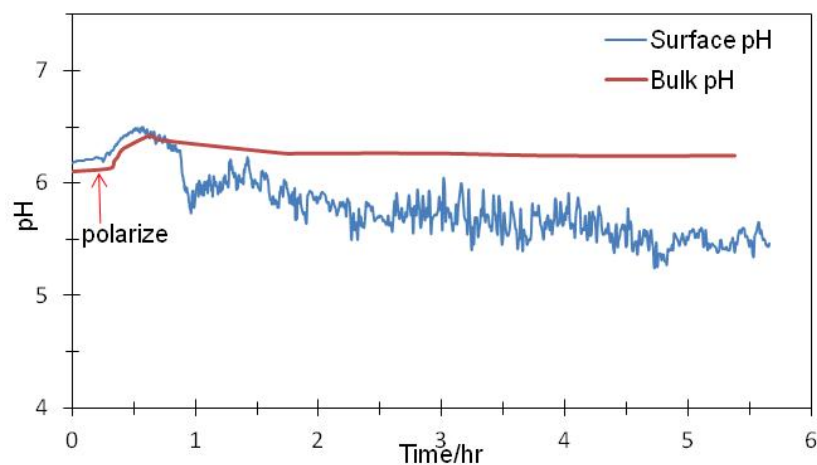
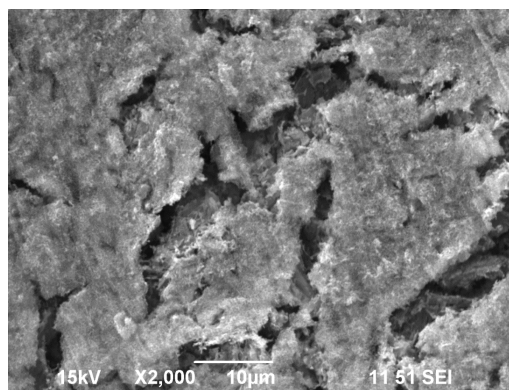
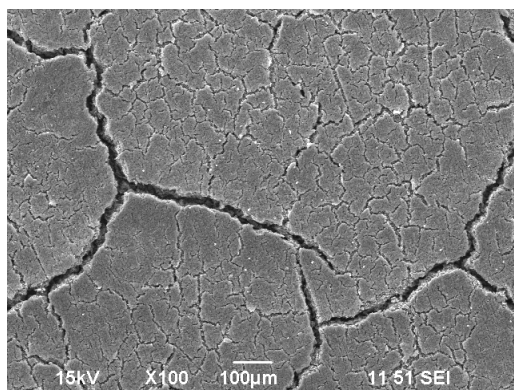


Figure 180. Surface pH with polarization at mesh/sample at  $-0.1 \text{ V vs. Ag/AgCl (Sat'd KCl)}$  (Polarize  $0.61 \text{ V}$  above OCP,  $\text{pH}_{\text{H}_2\text{S}} = 0.01 \text{ bar H}_2\text{S}$ , stirring  $400\text{rpm}$ , initial bulk pH  $6.0$ ).



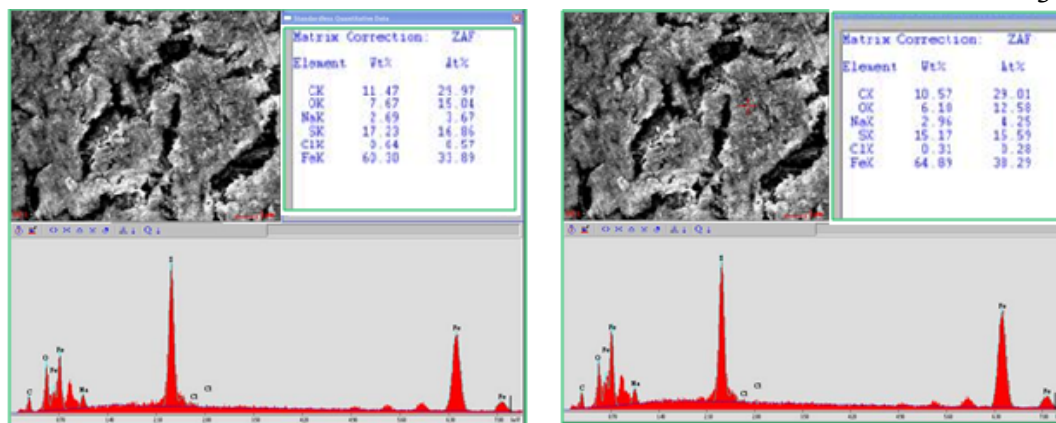


Figure 181. Surface morphologies (SEM images) and composition analysis (EDX) of steel sample after experiment.

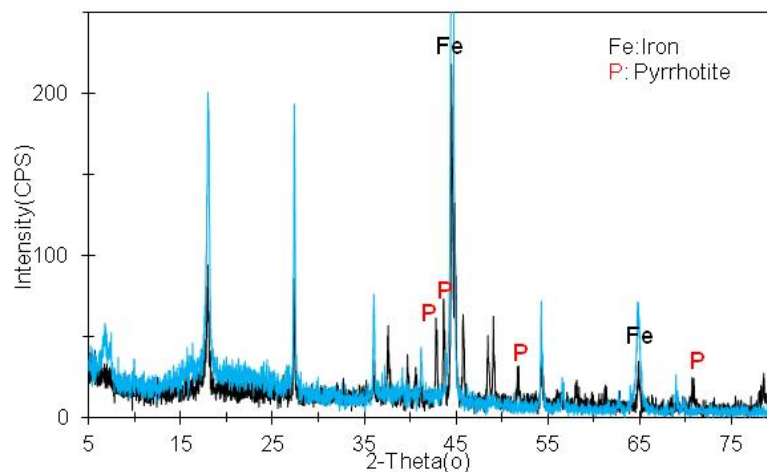


Figure 182. XRD pattern of corrosion product layer formed on sample.

Verification of the Pourbaix diagrams is shown in Figure 183 and Figure 184, respectively, as related to experimental conditions at the beginning and end of the experiment. Pyrrhotite was predicted to form by the Pourbaix diagrams at the beginning of experiment, as shown in Figure 183, which agreed with experimental results. At the end of the experiment,  $[\text{Fe}^{2+}]$  was measured as 1.1 ppm; accordingly Pourbaix diagrams for the end of experiment were generated and shown in Figure 184. The operational point in Figure 184 (b) is very close to the equilibrium line between  $\text{Fe}^{2+}$  and pyrrhotite phase,

which indicates a state of quasi-equilibrium for pyrrhotite at the end of experiment. The experimental findings at the end of experiment also agreed with the predictions made by Pourbaix diagrams.

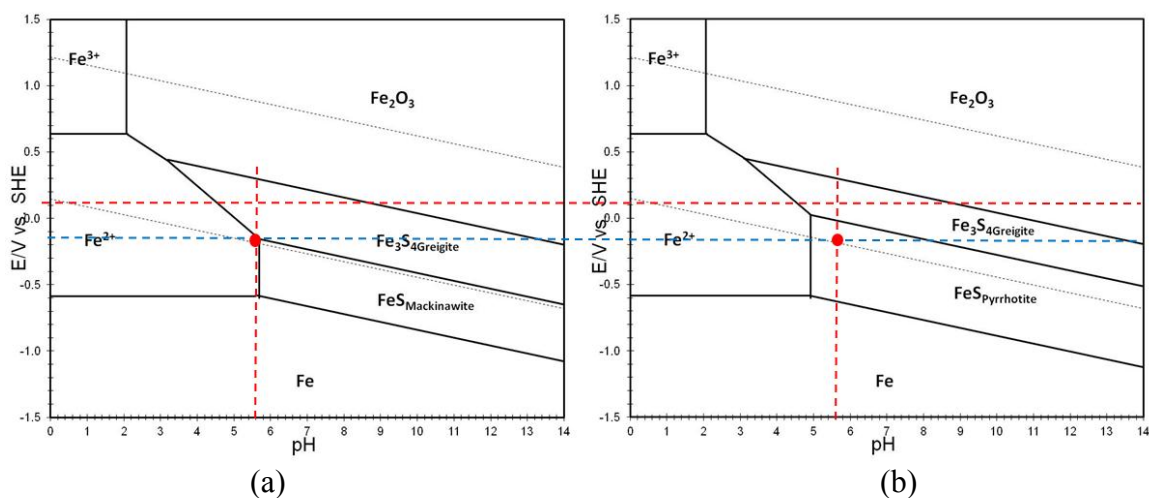


Figure 183. Verification of Pourbaix diagrams generated according to experimental conditions in the begging of experiment (a) Mackinawite / Greigite; (b) Mackinawite / Greigite / Pyrrhotite (25 °C,  $\text{pH}_2\text{S} = 0.01$  bar,  $[\text{Fe}^{3+}] = 10^{-6}$  M,  $[\text{Fe}^{2+}] = 10$  ppm).

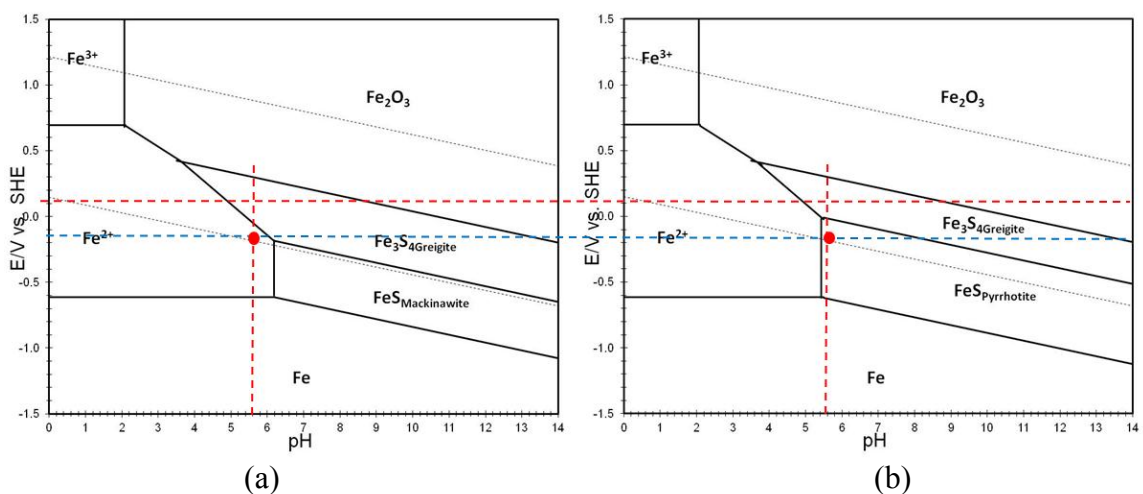


Figure 184. Verification of Pourbaix diagrams generated according to the experimental conditions at the end of experiment (a) Mackinawite / Greigite; (b) Mackinawite / Greigite / Pyrrhotite (25 °C,  $\text{pH}_2\text{S} = 0.01$  bar,  $[\text{Fe}^{3+}] = 10^{-6}$  M,  $[\text{Fe}^{2+}] = 1.1$  ppm).

Polarize Mesh/Sample Combination to +0.20 V vs. Ag/AgCl (Sat'd KCl)

Electrochemical polarization was applied at a higher value, +0.2 V vs. Ag/AgCl (Sat'd KCl), to facilitate the formation of greigite. Figure 185 shows surface pH and bulk pH monitored throughout the experiment. Again, surface pH was lower than bulk pH and became relatively stable ( $\text{pH } 5.0 \pm 0.2$ ) after one hour of exposure.

Figure 186 shows surface morphologies of the steel sample after exposure. Significantly corroded steel surface morphologies were observed. Again, pyrrhotite was identified in Figure 187.

Verification of the Pourbaix diagrams is shown in Figure 188 and Figure 189. Figure 188 shows the Pourbaix diagrams constructed for the beginning of experiment.  $\text{Fe}^{2+}$  and pyrrhotite are the corrosion products in the beginning predicted by those Pourbaix diagrams. XRD findings are consistent with predictions made by Pourbaix diagrams. At the end of experiment,  $[\text{Fe}^{2+}]$  was measured to be 1.3 ppm. The resultant Pourbaix diagrams for the end of the experiment conditions are shown in Figure 189. The operational point in Figure 189 (b) is on the equilibrium line between  $\text{Fe}^{2+}$  and pyrrhotite, indicating the system reached an equilibrium state for pyrrhotite phase at the end of the experiment.

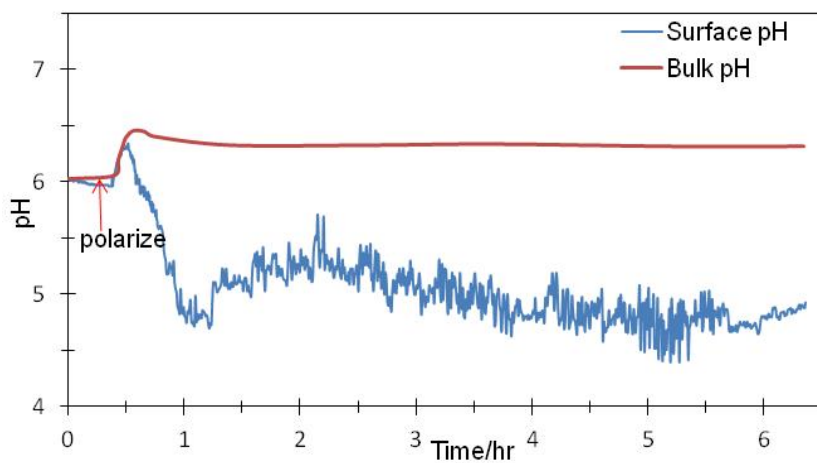


Figure 185. Surface pH with polarization at mesh/sample at +0.2 V vs. Ag/AgCl (Sat'd KCl) (Polarized 0.91 V above OCP,  $p_{H_2S} = 0.01$  bar  $H_2S$ , stirring 400 rpm, initial bulk pH 6.0).

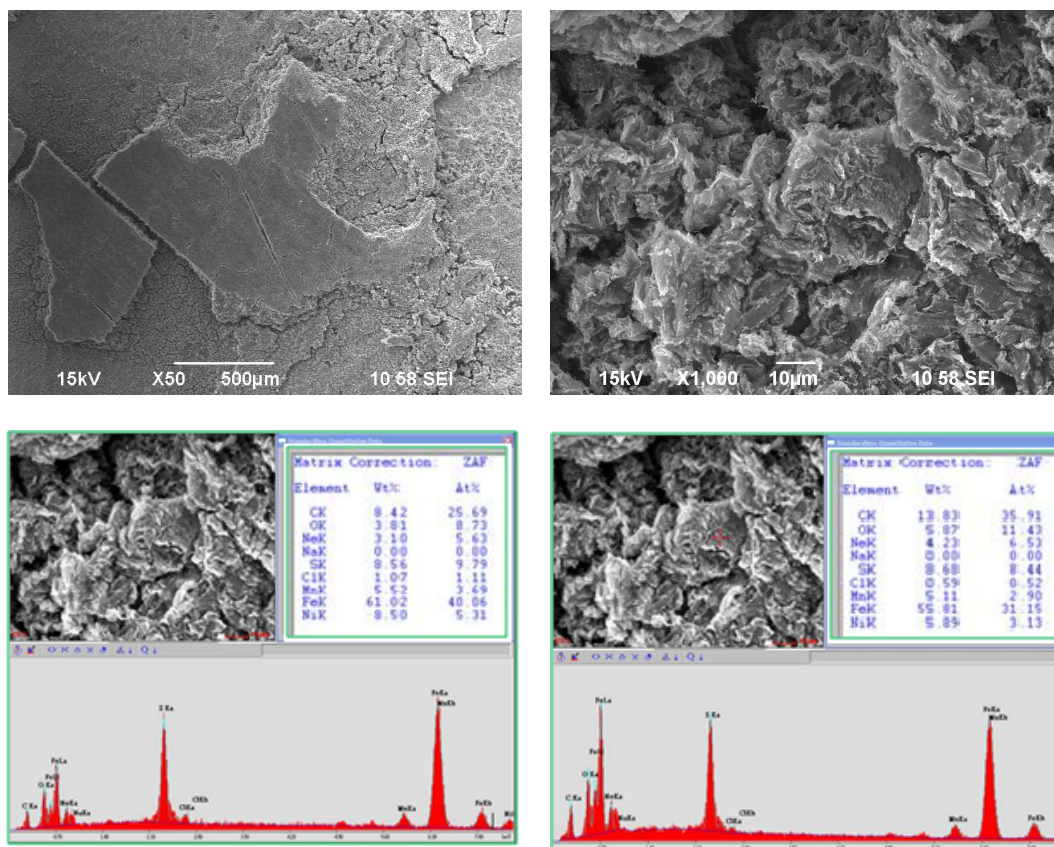


Figure 186. Surface morphology (SEM) and composition analysis (EDX) of steel sample.

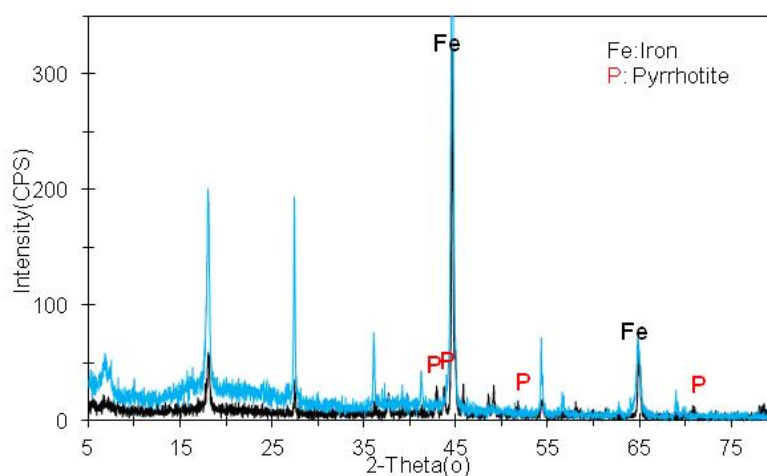


Figure 187. XRD pattern of corrosion product layer formed on the steel sample.

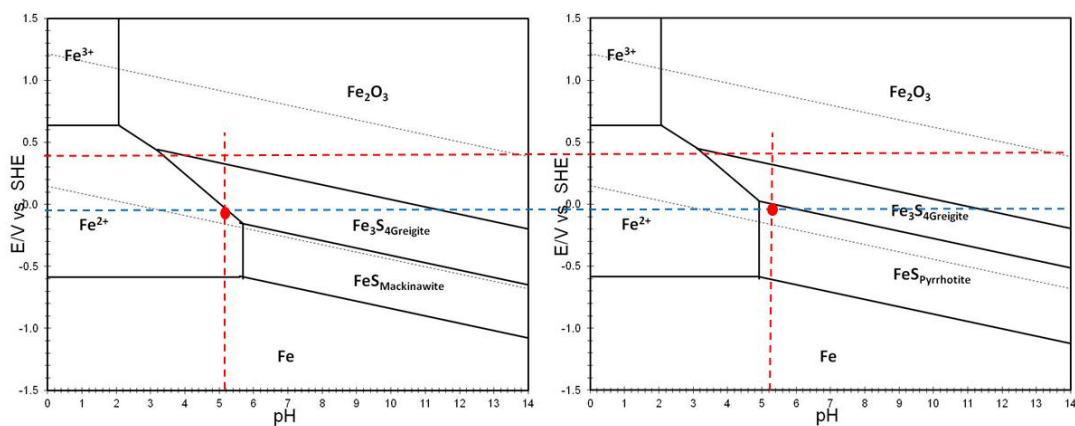


Figure 188. Verification of Pourbaix diagrams generated according to experimental conditions in the beginning of experiment (a) Mackinawite / Greigite; (b) Mackinawite / Greigite / Pyrrhotite (25 °C,  $p\text{H}_2\text{S} = 0.01$  bar,  $[\text{Fe}^{3+}] = 10^{-6}$  M,  $[\text{Fe}^{2+}] = 10$  ppm).

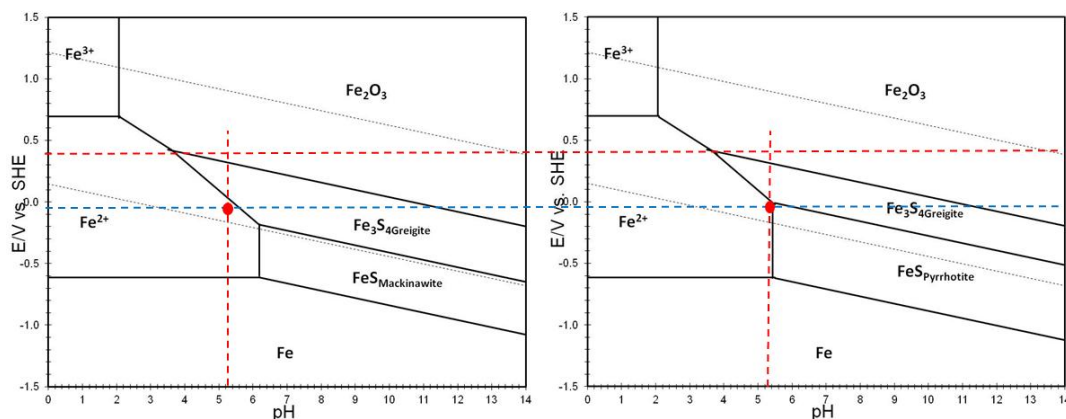


Figure 189. Verification of Pourbaix diagrams generated at the end of experiment (a) Mackinawite / Greigite; (b) Mackinawite / Greigite / Pyrrhotite (25 °C,  $\text{pH}_2\text{S} = 0.01$  bar,  $[\text{Fe}^{3+}] = 10^{-6}$  M,  $[\text{Fe}^{2+}] = 1.3$  ppm).

#### C.4 Conclusions

- Pourbaix diagrams for an  $\text{H}_2\text{S}$ - $\text{H}_2\text{O}$ -Fe system at 25 °C were constructed and verified with electrochemical polarization experiments (by controlling the potential and measuring surface pH at a corroding steel sample) and then by analyzing the corrosion product layer using XRD.
- Only pyrrhotite was detected as a corrosion product in all the experiments. Mackinawite was not detected probably due to it was transformed to pyrrhotite. Greigite could not form in the applied potential range. Pyrite did not form due to short exposures.
- The experimental results generally agreed well with the predictions made by Pourbaix diagrams.



**OHIO**  
UNIVERSITY

Thesis and Dissertation Services